UNIVERSITY OF CALIFORNIA SAN DIEGO

Galactic Archeology with Ultracool Dwarfs and Stellar Streams

A dissertation submitted in partial satisfaction of the
requirements for the degree
Doctor of Philosophy

in

Physics

by

Christian Aganze

Committee in charge:

Professor Adam J. Burgasser, Chair
Professor Javier Duarte
Professor Quinn Konopacky
Professor Michael Norman
Professor Lawrence Saul

2023

The dissertation of Christian Aganze is approved, and it is acceptable in quality and form for publication on microfilm and electronically.

University of California San Diego

2023

TABLE OF CONTENTS

LIST OF FIGURES

LIST OF TABLES

LIST OF SUPPLEMENTAL FILES

- Aganze_wispsi_Mdwarfs.txt
- Aganze_wispsi_lt.txt
- Aganze_wispsi_lateMadd.txt
- Aganze_wispsii_pointings.txt
- Aganze_simbad_sds.tex

ACKNOWLEDGEMENTS

I would like to thank my advisor Professor Adam Burgasser. My journey in Adam's lab began back in 2014 as a summer research student in the UC HBCU program. Throughout graduate school, Adam has been a patient and kind mentor who believed in me even when I didn't believe in myself. One (of many) particular incident that I remember fondly is Adam working out qualifying exam problems with me in his office, going above and beyond by offering additional resources for tutoring. I was truly lucky to have Adam as a my PhD advisor.

I would like to thank my committee members, Professor Quinn Konopacky, Professor Javier Duarte, Professor Michael Norman and Professor Lawrence Saul for supervising this dissertation. Professor Konopacky's group has been a second academic home to me through the "stars and planets" group. Also, thank you to Professor Konopacky for being generally kind to me and for providing me feedback on my postdoc applications.

I would also like to thank Professor Kathryn Johnston, Dr. Sarah Pearson and Dr. Tjitske Starkenburg for being my additional advisors over the last 2 years, for writing me letters of recommendation and for reviewing my postdoc applications. I am grateful to Professor Jonhston for sharing her extensive knowledge on galactic dynamics with me, to Dr. Pearson for being a kind mentor who gave me space to learn and to make mistakes and Dr. Tjitske Starkenburg for being generally smart and a superb mentor. I am also grateful to Dr. Gabriella Contardo and Dr. Adrian Price-Whelan for being kind to me.

I am thankful for our current and former lab members: Professor Daniella Bardalez Gagliuffi, Professor Christopher Theissen, Dr. Dino Hsu and Dr. Roman Gerasimov for being encouraging throughout my PhD journey. Professor Bardalez Gagliuffi was a graduate student when I started, she gave me lots of advice on how to best navigate the system. I have learned a lot from Professor Theissen who is not only a great

scientist but a wonderful mentor to many of us. I am grateful to Dr. Hsu, who was my lab mate who helped me with qualifying exam early in graduate school. I am also thankful to Dr. Gerasimov for letting me use his metal-poor models. I am also grateful to Dr. Kielan Hoch for helping me prepare for the qualifying exam.

I would also like to thank these people in no particular order, who helped review my postdoc job applications: Dr. Ivanna Escala, Dr. Maren Cosens, Dr. Emily Cunningham, Professor Kelle Cruz, Dr. Catherine Zucker, Dr. Alexander Riley and Dr. Russell Ryan Jr. I would also like to thank my undergraduate advisors at Morehouse Professor Willie Rockward, Professor Thomas Searles, Professor AaKut Bak, Professor Duane Cooper and Professor Carlyle Moore. I wouldn't be here without their help. I extend my gratitude to all the undergraduate students in Adam's lab, in particular, to Malina Desai, Juan Diego Draxl Giannoni and Camille Dunning for choosing me as a summer mentor on their machine learning projects. I learned a lot from them. I am also thankful to Dr. Lucianne Walkowicz and Professor Adam Miller who gave me advice and guidance and helped me look for non-academic jobs when I was struggling during graduate school. I would also like to thank Professor Mathew Malkan for their support and for writing letters for my job applications.

Chapter 2, in full, is a reprint of the material as it appears in the Astrophysical Journal 2022, Volume 924, Number 114, authored by Christian Aganze, Adam J. Burgasser, Mathew Malkan, Christopher A. Theissen, Roberto A. Tejada Arevalo, Chih-Chun Hsu1, Daniella C. Bardalez Gagliuffi, Russell E. Ryan, Jr., and Benne Holwerda. The thesis author was the primary investigator and author of this paper.

Chapter 3 in full, is a reprint of the material as it appears in the Astrophysical Journal 2022, Volume 934, Number 73, authored by Christian Aganze, Adam J. Burgasser, Mathew Malkan, Christopher A. Theissen, Roberto A. Tejada Arevalo, Chih-Chun Hsu, Daniella C. Bardalez Gagliuffi, Russell E. Ryan, Jr., and Benne Holwerda. The thesis

author was the primary investigator and author of this paper.

Chapter 4 is being prepared for submission to the Astrophysical Journal, authored by Christian Aganze, Roman Gerasimov, Adam Burgasser, Christopher Theissen, Chih-Chun Hsu. The thesis author was the primary investigator and author of this paper.

Chapter 5 has been submitted to the Astrophysical Journal and is currently in review, authored by Christian Aganze, Sarah Pearson, Tjitske Starkenburg ; Gabriella Contardo; Kathryn Johnston, Kiyan Tavangar, Adrian Price-Whelan, Burgasser, Adam J. The thesis author was the primary investigator and author of this paper.

VITA

2016	B. S. in Physics, Morehouse College
2021	Ph. D. candidate in Physics, University of California San Diego

PUBLICATIONS

Aganze C., Pearson S., Starkenburg T., Contardo G., Johnston K. V., Tavangar K., Price-Whelan A. M., Burgasser A. J. 2023, Prospects for Detecting Gaps in Globular Cluster Stellar Streams in External Galaxies with the Nancy Grace Roman Space Telescope, arXiv e-prints, arXiv:2305.12045, doi: 10.48550/arXiv.2305.12045

Calissendorff P., De Furio M., Meyer M., Albert L., **Aganze C.**, Ali-Dib M., Bardalez Gagliuffi D. C., Baron F., Beichman C. A., Burgasser A. J., Cushing M. C., Faherty J. K., Fontanive C., Gelino C. R., Gizis J. E., Greenbaum A. Z., Kirkpatrick J. D., Leggett S. K., Martinache F., Mary D., N'Diaye M., Pope B. J. S., Roellig T., Sahlmann J., Sivaramakrishnan A., Thorngren D. P., Ygouf M., Vandal T. 2023, JWST/NIRCam Discovery of the First Y+Y Brown Dwarf Binary: WISE J033605.05-014350.4, ApJ, 947, L30

Dransfield G., Timmermans M., Triaud A. H. M. J., Dévora-Pajares M., **Aganze C.**, Barkaoui K., Burgasser A. J., Collins K. A., Cointepas M., Ducrot E., Günther M. N., Howell S. B., Murray C. A., Niraula P., Rackham B. V., Sebastian D., Stassun K. G., Zúñiga-Fernández S., Almenara J. M., Bonfils X., Bouchy F., Burke C. J., Charbonneau D., Christiansen J. L., Delrez L., Gan T., García L. J., Gillon M., Chew Y. G. M., Hesse K. M., Hooton M. J., Isopi G., Jehin E., Jenkins J. M., Latham D. W., Mallia F., Murgas F., Pedersen P. P., Pozuelos F. J., Queloz D., Rodriguez D. R., Schanche N., Seager S., Srdoc G., Stockdale C., Twicken J. D., Vanderspek R., Wells R., Winn J. N., de Wit J., Zapparata A. 2023, A 1.55 R habitable-zone planet hosted by TOI-715, an M4 star near the ecliptic South Pole, MNRAS, doi: 10.1093/mnras/stad1439

Schneider A. C., Burgasser A. J., Bruursema J., Munn J. A., Vrba F. J., Caselden D., Kabatnik M., Rothermich A., Sainio A., Bickle T. P., Dahm S. E., Meisner A. M., Kirkpatrick J. D., Suárez G., Gagné J., Faherty J. K., Vos J. M., Kuchner M. J., Williams S. J., Bardalez Gagliuffi D., **Aganze C.**, Hsu C.-C., Theissen C., Cushing M. C., Marocco F., Casewell S., Backyard Worlds: Planet 9 Collaboration. 2023, Redder than Red: Discovery of an Exceptionally Red L/T Transition Dwarf, ApJ, 943, L16

Pozuelos F. J., Timmermans M., Rackham B. V., Garcia L. J., Burgasser A. J., Kane S. R., Günther M. N., Stassun K. G., Van Grootel V., Dévora-Pajares M., Luque R., Edwards B., Niraula P., Schanche N., Wells R. D., Ducrot E., Howell S., Sebastian D., Barkaoui K., Waalkes W., Cadieux C., Doyon R., Boyle R. P., Dietrich J., Burdanov A.,

Delrez L., Demory B. O., de Wit J., Dransfield G., Gillon M., Gómez Maqueo Chew Y., Hooton M. J., Jehin E., Murray C. A., Pedersen P. P., Queloz D., Thompson S. J., Triaud A. H. M. J., Zúñiga-Fernández S., Collins K. A., Fausnaugh M. M., Hedges C., Hesse K. M., Jenkins J. M., Kunimoto M., Latham D. W., Shporer A., Ting E. B., Torres G., Amado P., Rodón J. R., Rodríguez-López C., Suárez J. C., Alonso R., Benkhaldoun Z., Berta-Thompson Z. K., Chinchilla P., Ghachoui M., Gómez-Muñoz M. A., Rebolo R., Sabin L., Schroffenegger U., Furlan E., Gnilka C., Lester K., Scott N., **Aganze C.**, Gerasimov R., Hsu C., Theissen C., Apai D., Chen W. P., Gabor P., Henning T., Mancini L. 2023, A super-Earth and a mini-Neptune near the 2:1 MMR straddling the radius valley around the nearby mid-M dwarf TOI-2096, AA, 672, A70

Delrez L., Murray C. A., Pozuelos F. J., Narita N., Ducrot E., Timmermans M., Watanabe N., Burgasser A. J., Hirano T., Rackham B. V., Stassun K. G., Van Grootel V., **Aganze C.**, Cointepas M., Howell S., Kaltenegger L., Niraula P., Sebastian D., Almenara J. M., Barkaoui K., Baycroft T. A., Bonfils X., Bouchy F., Burdanov A., Caldwell D. A., Charbonneau D., Ciardi D. R., Collins K. A., Daylan T., Demory B. O., de Wit J., Dransfield G., Fajardo-Acosta S. B., Fausnaugh M., Fukui A., Furlan E., Garcia L. J., Gnilka C. L., Gómez Maqueo Chew Y., Gómez-Muñoz M. A., Günther M. N., Harakawa H., Heng K., Hooton M. J., Hori Y., Ikoma M., Jehin E., Jenkins J. M., Kagetani T., Kawauchi K., Kimura T., Kodama T., Kotani T., Krishnamurthy V., Kudo T., Kunovac V., Kusakabe N., Latham D. W., Littlefield C., McCormac J., Melis C., Mori M., Murgas F., Palle E., Pedersen P. P., Queloz D., Ricker G., Sabin L., Schanche N., Schroffenegger U., Seager S., Shiao B., Sohy S., Standing M. R., Tamura M., Theissen C. A., Thompson S. J., Triaud A. H. M. J., Vanderspek R., Vievard S., Wells R. D., Winn J. N., Zou Y., Zúñiga-Fernández S., Gillon M. 2022, Two temperate super-Earths transiting a nearby late-type M dwarf, AA, 667, A59

Ryan R. E., Thorman P., **Aganze C.**, Burgasser A. J., Cohen S. H., Hathi N. P., Holwerda B., Pirzkal N., Windhorst R. A. 2022, A Self-consistent Model for Brown Dwarf Populations, ApJ, 932, 96

Gan T., Soubkiou A., Wang S. X., Benkhaldoun Z., Mao S., Artigau É., Fouqué P., Arnold L., Giacalone S., Theissen C. A., **Aganze C.**, Burgasser A., Collins K. A., Shporer A., Barkaoui K., Ghachoui M., Howell S. B., Lamman C., Demangeon O. D. S., Burdanov A., Cadieux C., Chouqar J., Collins K. I., Cook N. J., Delrez L., Demory B.-O., Doyon R., Dransfield G., Dressing C. D., Ducrot E., Fan J., Garcia L., Gill H., Gillon M., Gnilka C. L., Gómez Maqueo Chew Y., Günther M. N., Henze C. E., Huang C. X., Jehin E., Jensen E. L. N., Lin Z., Manset N., McCormac J., Murray C. A., Niraula P., Pedersen P. P., Pozuelos F. J., Queloz D., Rackham B. V., Savel A. B., Schanche N., Schwarz R. P., Sebastian D., Thompson S., Timmermans M., Triaud A. H. M. J., Vezie M., Wells R. D., de Wit J., Ricker G. R., Vanderspek R., Latham D. W., Seager S., Winn J. N., Jenkins J. M. 2022, TESS discovery of a sub-Neptune orbiting a mid-M dwarf TOI-2136, MNRAS, 514, 4120

Hsu, C.; Burgasser, A. J.; Theissen, C. A.; Gelino, C. R.; Birky, J. L.; Diamant, S. J. M.; Bardalez Gagliuffi, D. C.; **Aganze; C.**, Blake, C. H., Jacqueline K. Faherty,"The Brown Dwarf Kinematics Project (BDKP). V. Radial and Rotational Velocities of T Dwarfs From Keck/NIRSPEC High-Resolution Spectroscopy", ApJS 257, 45, December 2021.

Kiwy, Frank; Faherty, Jacqueline K.; Meisner, Aaron; Schneider, Adam C.; Kirkpatrick, J. Davy; Kuchner, Marc J.; Burgasser, Adam J.; Casewell, Sarah; Kiman, Rocio; Calamari, Emily; **Aganze, Christian**; Hsu, Chih-Chun; Sainio, Arttu; Thakur, Vinod; The Backyard Worlds: Planet 9 Collaboration, "Discovery of 34 low-mass comoving systems using NOIRLab Source Catalog DR2", accepted in ApJ, April 2022, arXiv:2204.09739

Aganze, Christian; Burgasser, Adam J ; Malkan, Mathew; Theissen, Christopher A; Tejada Arevalo, Roberto A; Hsu, Chih-Chun; Bardalez Gagliuffi, Daniella C; E Ryan, Russell, Jr; Holwerda, Benne, "Beyond the Local Volume II: Population Scaleheights and Ages of Ultracool Dwarfs in Deep HST/WFC3 Parallel Fields", accepted in ApJ, April 2022, arxiv:2204.07621

Softich, Emma; Schneider, Adam C.; Patience, Jennifer; Burgasser, Adam J.; Shkolnik, Evgenya; Faherty, Jacqueline K.; Caselden, Dan; Meisner, Aaron M.; Kirkpatrick, J. Davy; Kuchner, Marc J.; Gagne, Jonathan; Bardalez-Gagliuffi, Daniella; Cushing, Michael C.; Casewell, Sarah L.; **Aganze, Christian**; Hsu, Chih-Chun; Andersen, Nikolaj Stevnbak; Kiwy, Frank; Thevenot, Melina; The Backyard Worlds: Planet 9 Collaboration, "CWISE J014611.20-050850.0AB: The Widest Known Brown Dwarf Binary in the Field", ApJL, 922, L12, February 2022

Faherty, Jacqueline K; Gagne, Jonathan; Popinchalk, Mark; Vos, Johanna M.; Burgasser, Adam J.; Schumann, Jorg; Schneider, Adam C.; Kirkpatrick, J. Davy; Meisner, Aaron M.; Kuchner, Marc J.; Bardalez Gagliuffi, Daniella C.; Marocco, Federico; Caselden, Dan; Gonzales, Eileen C.; Rothermich, Austin; Casewell, Sarah L.; Debes, John H.; **Aganze, Christian**; Ayala, Andrew; Hsu, Chih-Chun; Cooper, William J.; Smart, R. L.; Gerasimov, Roman; Theissen, Christopher A.; The Backyard Worlds: Planet 9 Collaboration, "A Wide Planetary Mass Companion Discovered Through the Citizen Science Project Backyard Worlds: Planet 9", ApJ, 923, 48, December 2021

Aganze, Christian; Burgasser, Adam J ; Malkan, Mathew; Theissen, Christopher A; Tejada Arevalo, Roberto A; Hsu, Chih-Chun; Bardalez Gagliuffi, Daniella C; E Ryan, Russell, Jr; Holwerda, Benne, "Beyond the Local Volume I: Surface Densities of Ultracool Dwarfs in Deep HST/WFC3 Parallel Fields", ApJ, 924, 144, January 2022

Schneider, Adam C.; Meisner, Aaron M.; Gagne, Jonathan; Faherty, Jacqueline K.; Marocco, Federico; Burgasser, Adam J.; Kirkpatrick, J. Davy; Kuchner, Marc J.; Gramaize, Leopold; Rothermich, Austin; Brooks, Hunter; Vrba, Frederick J.; Bardalez Gagliuffi, Daniella; Caselden, Dan; Cushing, Michael C.; Gelino, Christopher R.; Line, Michael R.; Casewell, Sarah L.; Debes, John H.; **Aganze, Christian**, Ayala, Andrew; Gerasimov, Roman; Gonzales, Eileen C.; Hsu, Chih-Chun; Kiman, Rocio; Popinchalk,

Mark; Theissen, Christopher; Backyard Worlds: The Planet 9 Collaboration, “Ross 19B: An Extremely Cold Companion Discovered via the Backyard Worlds: Planet 9 Citizen Science Project”, ApJ, 921, 150, November 2021

Meisner, Aaron M.; Schneider, Adam C.; Burgasser, Adam J.; Marocco, Federico; Line, Michael R.; Faherty, Jacqueline K.; Kirkpatrick, J. Davy; Caselden, Dan; Kuchner, Marc J.; Gelino, Christopher R.; Gagne, Jonathan; Theissen, Christopher; Gerasimov, Roman; **Aganze, Christian**; Hsu, Chih-Chun; Wisniewski, John P.; Casewell, Sarah L.; Bardalez Gagliuffi, Daniella C.; Logsdon, Sarah E.; Eisenhardt, Peter R. M., “New Candidate Extreme T Subdwarfs from the Backyard Worlds: Planet 9 Citizen Science Project", ApJ, 915, 120, July 2021

J. Davy Kirkpatrick; Christopher R. Gelino; Jacqueline K. Faherty; Aaron M. Meisner; Dan Caselden; Adam C. Schneider; Federico Marocco; Alfred J. Cayago; R. L. Smart; Peter R. Eisenhardt; Marc J. Kuchner; Edward L. Wright; Michael C. Cushing; Katelyn N. Allers; Daniella C. Bardalez Gagliuffi; Adam J. Burgasser; Jonathan Gagne; Sarah E. Logsdon; Emily C. Martin; James G. Ingalls; Patrick J. Lowrance; Ellianna S. Abrahams; **Christian Aganze**; Roman Gerasimov; Eileen C. Gonzales; Chih-Chun Hsu; Nikita Kamraj; Rocio Kiman; Jon Rees; Christopher Theissen; Kareem Ammar; Nikolaj Stevnbak Andersen; Paul Beaulieu; Guillaume Colin; Charles A. Elachi; Samuel J. Goodman; Leopold Gramaize; Leslie K. Hamlet; Justin Hong; Alexander Jonkeren; Mohammed Khalil; David W. Martin; William Pendrill; Benjamin Pumphrey; Austin Rothermich; Arttu Sainio; Andres Stenner; Christopher Tanner; Melina Thevenot; Nikita V. Voloshin; Jim Walla; Zbigniew Wedracki; “The Field Substellar Mass Function Based on the Full-sky 20-pc Census of 525 L, T, and Y Dwarfs", ApJS, 253, 7, March 2021

Meisner, Aaron M.; Faherty, Jacqueline K.; Kirkpatrick, J. Davy; Schneider, Adam C.; Caselden, Dan; Gagné, Jonathan; Kuchner, Marc J.; Burgasser, Adam J.; Casewell, Sarah L.; Debes, John H.; Artigau, Étienne; Bardalez Gagliuffi, Daniella C.; Logsdon, Sarah E.; Kiman, Rocio; Allers, Katelyn; Hsu, Chih-Chun; Wisniewski, John P.; Allen, Michaela B.; Beaulieu, Paul; Colin, Guillaume Durantini Luca, Hugo A.; Goodman, Sam; Gramaize, Léopold; Hamlet, Leslie K.; Hinckley, Ken; Kiwy, Frank; Martin, David W.; Pendrill, William; Rothermich, Austin; Sainio, Arttu; Schümann, Jörg; Andersen, Nikolaj Stevnbak; Tanner, Christopher; Thakur, Vinod; Thévenot, Melina; Walla, Jim; Wędracki, Zbigniew; **Aganze, Christian**; Gerasimov, Roman; Theissen, Christopher; The Backyard Worlds: Planet 9 Collaboration, “Spitzer Follow-up of Extremely Cold Brown Dwarfs Discovered by the Backyard Worlds: Planet 9 Citizen Science Project", ApJ, 889, 123, August 2020

Burgasser A. J., Lopez M. A., Mamajek E. E., Gagné J., Faherty J. K., Tallis M., Choban C., Tamiya T., Escala I., **Aganze C.** 2016, The First Brown Dwarf/Planetary-mass Object in the 32 Orionis Group, ApJ, 820, 32

Aganze C., Burgasser A. J., Faherty J. K., Choban C., Escala I., Lopez M. A., Jin Y., Tamiya T., Tallis M., Rockward W. 2016, Characterization of the Very-low-mass

Secondary in the GJ 660.1AB System, AJ, 151, 46

ABSTRACT OF THE DISSERTATION

Galactic Archeology with Ultracool Dwarfs and Stellar Streams

by

Christian Aganze

Doctor of Philosophy in Physics

University of California San Diego, 2023

Professor Adam J. Burgasser, Chair

Galactic Archeologists reconstruct the formation and evolution of the Milky Way by studying its stars. Enabled by large-scale surveys over the past $\approx$ 5 decades (e.g Hipparcos, 2MASS, Pan-STARRS, SDSS, Gaia), they have constructed detailed and precise spatial, kinematic and chemical maps of the Galaxy using billions of stars. Through these maps, a rich structure has been revealed: a young metal-poor disk, an old metal-poor thick disk, an old stellar halo full of debris from disrupted satellite galaxies, a Galactic bar/bulge, and a dark matter halo. These observations offer opportunities for direct comparison with state-of-the-art galaxy formation models. However, the lowest-mass stars and brown dwarfs (Ultracool dwarfs, UCDs) have been overlooked

in these studies. These are low-mass (< 0.1 solar masses) objects that are not massive enough to sustain hydrogen fusion, hence they cool down with time. Additionally, they are more than $10,000$ times intrinsically fainter than the Sun, hence their detection has been limited to the local Solar neighborhood (> 100 pc). In this thesis, I present a sample of 164 distant ($1-2$ kpc) UCDs discovered in the Hubble Space Telescope WFC3 Infrared Spectroscopic Parallel (WISP) Survey and 3D-HST. I model the observed luminosity function using population simulations to place constraints on scaleheights, vertical velocity dispersions, and population ages as a function of spectral type, consistent with prior simulations that predict that L-type dwarfs are on average a younger and less dispersed population. I use this population simulation framework to predict the UCD yield in the JWST PASSAGES survey, a similar and deeper survey to WISPS and 3D-HST, and find that it will produce a comparably-sized UCD sample, albeit dominated by thick disk and halo sources. By adding a set of recently-developed metal-poor models of UCDs to my modeling framework, I predict the expected counts of UCDs in three upcoming surveys such as the Euclid Telescope, the Nancy Grace Roman Observatory, and the Vera Rubin Observatory. I find that these surveys will find millions of UCDs to 10 kpc, allowing us to better probe the Milky Way Structure. In the last chapter of this thesis, I explore the detectability of gaps in globular cluster streams with the Roman telescope as an avenue to constrain the nature of dark matter. I find that Roman will find gaps in Andromeda and other external galaxies up to 3 Mpc, allowing us to directly test galaxy formation models that include dark matter.

Chapter 1

Introduction

1.1 Galactic Archeology

1.1.1 Early Work

The study of the formation and the evolution of the the Milky Way through the chemical, spatial, and kinematic mapping of its stars is referred to as "Galactic archaeology" (Freeman & Bland-Hawthorn, 2002). Nancy Grace Roman (Roman, 1950) was first to propose the idea of grouping stars in kinematic and chemistry space. The development of galaxy formation models was tested by the discoveries of the main structures of the Milky Way through spatial, chemical, and kinematic maps of stars near the Sun and beyond. Piddington & Minnett (1951) was first to report the discovery of the Galactic center using radio observations; and while galactic bars had been observed in external galaxies, Hammersley et al. (2000) was first to report a bar structure in the Milky Way by counting star towards the Galactic center. Gilmore & Reid (1983) was first to propose that the Milky Way disk might be composed of two components based on data from a large-scale survey of 12,500 stars using photographic plates taken by UK Schmidt telescope over an area of 18.5 sq. deg. Through their modeling of the density

of stars, they derived a vertical scaleheight (e-folding scale) of 300 pc for a thin disk and a separate, older disk component with a scaleheight of 1350 pc. The *Hipparcos* mission, launched in 1989-1993, provided a high-precision catalog of 118,2000 stars and a lower-precision Tycho catalog of 2.5 million stars, which provided an astrometric a reference frame, discovered multiple clusters, mapped spirals, and Galactic rotation by surveying cepheids and constrained local kinematics. Ibata et al. (1994) discovered the Sagittarius dwarf galaxy and its associated stream and Helmi et al. (1999) discovered the “Helmi streams", a set of tidal debris in the Galactic halo, near the Sun believed to be signatures of an accreted satellite. These discoveries further supported the idea that the Milky Way was largely built from repeated accretion events. Foundational work include Eggen et al. (1962) who suggested that galaxies form from monolithic gas collapse, but Searle & Zinn (1978) and Tinsley & Larson (1979) and others showed that mergers play a significant role in building up galaxies, and mergers are more likely to happen at earlier times as the density in the universe is higher. In the current accepted paradigm, luminous galaxies are a result of condensed, cooled gas in dark matter halos, which formed from large-scale cosmological hierarchical assembly over time (λ-CDM, White & Rees 1978; Efstathiou & Silk 1983; White & Frenk 1991; Navarro & Benz 1991). In these models, the Milky Way was built up through series of accretion events (Helmi et al., 2018).

1.1.2 Modern Picture of the Milky Way

Modern surveys (year 2000 and later) of the Milky Way have revolutionized our understanding of its structure and evolution by detecting and accurately measuring stellar parameters for billions of stars. Examples include the on-going Sloan Digital Sky Survey (SDSS, Gunn et al. 2006; Abolfathi et al. 2018) which uses the 2.5 meter optical telescope at Apache Point in New Mexico. SDSS has significantly contributed to cosmology by acquiring spectra and images of galaxies in the local universe (e.g.

bayron acoustic oscillations), and distant quasars. It has benefited the field of Galactic archaeology by measuring precise abundances, kinematics and photometry of $> 100,000$ stars (e.g. SDSS/SEGUE Yanny et al. 2009, SDSS/APOGEE Majewski et al. 2017), surveying stellar clusters, and by finding and mapping stellar streams. SDSS was one of the first surveys to conduct stellar spectroscopy at an "industrial" scale. Other notable ground-based and space-based surveys include the 2-Micron All Sky Survey (2MASS, Skrutskie et al. 2006), the Wide-field Infrared Survey Explorer (WISE, Wright et al. 2010), the Geneva-Coppen Haggen Survey (GCS, Nordström et al. 2004), the GALactic Archeology with HERMES survey (GALAH, Buder et al. 2021), the Large Sky Area Multi-Object Fiber Spectroscopic Telescope (LAMOST, Zhao et al. 2012) surveys, the Dark Energy Survey (DES, The Dark Energy Survey Collaboration 2005), the H3 survey (Conroy et al., 2019) and many more. These surveys use telescopes operating in the optical and infrared regions of the electromagnetic spectrum for various science cases. A significant fraction of these surveys can measure precise abundances (via stellar stellar spectroscopy) which allows for mapping of large parts of the sky in a manner that couldn't be accomplished with the SDSS telescopes alone. Recently, the Gaia spacecraft (Gaia Collaboration et al., 2018) has revolutionized the field by proving precise 6-dimensional positions and velocities for $>$ 1 billion stars, with a photometry and spectra spanning the optical region (0.3-1 micron), precise astrometry , radial velocities (RV precisions of $\approx$1-30 km/s).

The Stellar Disk

These modern surveys reveal the general structure of the Milky Way's disks; a young metal-rich thin disk and an old metal-poor thick disk, with an exponentially-decaying density away from the plane and from the Galactic center. Early studies (Bahcall & Soneira, 1980; Gilmore & Reid, 1983) performed star count experiments near the

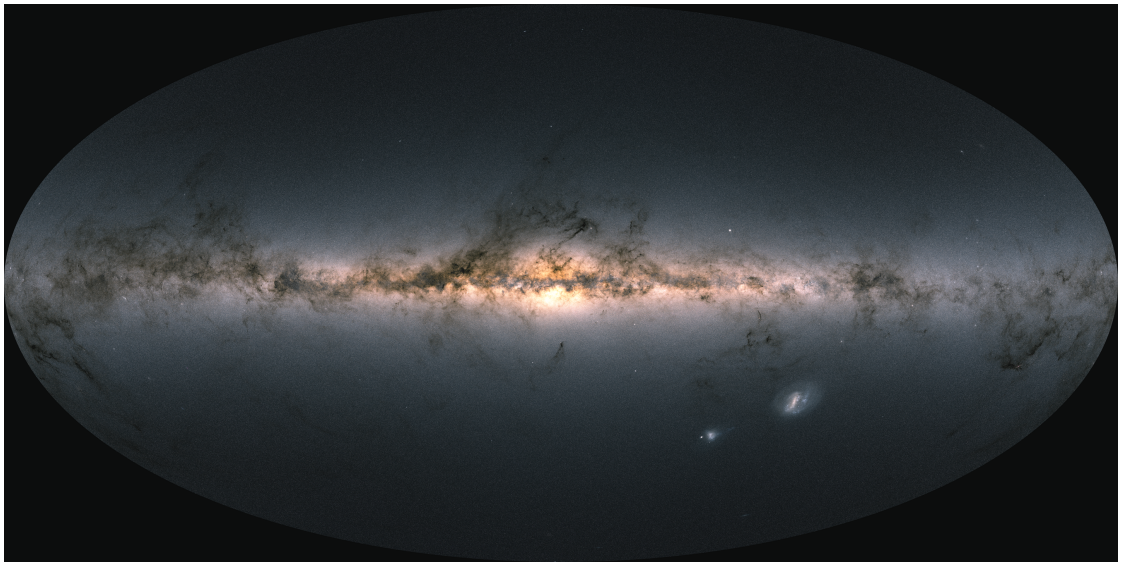

Figure 1.1 The Galactic plane is dominated by thin young, bright disk stars obscured by dust extinction in the Milky Way. The Small and Large Magellanic Clouds are visible in the lower right corner.

solar neighborhood to map the disk structure but they were limited by small samples, or imprecise photometry, or poor distance estimations. The most comprehensive analysis of the stellar density in the Milky Way disk was performed by Jurić et al. (2008) using 48 million M and K dwarfs selected by their precise colors in SDSS, covering an area over 6500 sq. deg. By fitting a 2-component exponential density law, they derived a scaleheight of 300 pc for the thin disk, a vertical scaleheight of 900 pc for the thick disk, and radial scalelengths of 2600 pc for the thin disk and 3600 pc for the thick disk, in agreement with the previous results (e.g Ruphy et al. 1996). They also determined the relative local fraction of thick stars to be 12 percent, in agreement with Gilmore & Reid (1983); but a recent meta-analysis of Bland-Hawthorn & Gerhard (2016) suggests that this value is $\approx$4 percent.

In addition to stellar density, disk structure can also be mapped by measuring precise elemental abundances. Bensby et al. (2003a) used high-resolution (R$\approx$48,000) spectra of $\approx$70 of F and G dwarfs coupled with kinematic and age information to show

that thin disk stars are older, more metal-poor and enhanced in α-elements compared to thin disk stars implying that they are formed in progressively-polluted gas with Type Ia supernovae. Subsequent studies (Haywood 2006; Bensby et al. 2014, and many more) have further confirmed this trend by using a variety of samples throughout the Milky Way. In particular, Ivezić et al. (2008) used over 2 million SDSS F and G-type main sequence stars with precisely-calibrated photometric metallicities to map the structure of the disk to distances up to 8 kpc. While they did not confirm the presence of a “thick disk", using a combination of kinematic and spatial information they found a bimodal distribution in metallicity: disk stars tend to peak at a higher metallicity compared to halo stars. With samples up to billions of stars from the APOGEE, RAVE, GALAH, LAMOST and Gaia surveys have established the presence two separate disk populations by their enrichment in [α/Fe] elements.

In addition to mapping the stellar density and abundance structure, large-scale surveys have also measured the precise kinematics of stars in the Milky Way disk. Early work by Wielen (1977) showed that the vertical and radial velocity dispersion of local disk stars increases with their age. This effect is known as the age velocity dispersion relation (AVR). It is attributed to the dynamical heating of stellar orbits due to fluctuations the smooth Galactic gravitational potential introduced by bars, large molecular clouds and spiral arms, or interactions with satellite galaxies (Spitzer & Schwarzschild, 1953; Sellwood & Binney, 2002; Binney & Tremaine, 2008; Quillen et al., 2009). The velocity distribution of disk stars can be modelled as Gaussians, broadening with age (Nordström et al., 2004; Aumer & Binney, 2009). The velocity dispersion as a function of time ($\sigma_v(\tau)$) and coordinate (R, ϕ, z) is given by a power law ($\sigma_v(R, \phi, z) \propto \sigma_0(R, \phi, z)\tau^{\beta(R,\phi,z)}$). In fully self-consistent models of Galactic disks, however, positions velocities, ages, and metallicities are more accurately modeled using general distributions functions of constants of motions (action-angles coordinates), with additional analytic prescriptions of

the enrichment and star formation history of the galaxy (Sanders & Binney, 2015; Binney & Vasiliev, 2023). While collision-less dynamics and analytic models provide useful frameworks for modeling the stellar disk, full-cosmological simulations are needed to better understand its formation and evolution. Hydrodynamical simulations show that the early Milky Way disk was born out of a turbulent star formation at early epochs ($>$ 6 Gyr ago) which explains the older, dispersed metal-poor thick disk. I further discuss formation scenarios for the disk in Section 1.1.3. Additionally, full cosmological contexts are needed because interactions with satellite galaxies (LMC, SMC, Sagittarius) can induce oscillations and disequilibrium in the disk evidenced by the recently-discovered Gaia phase-space spiral Antoja et al. (2018); Laporte et al. (2018) and a collective response of stars and dark matter Garavito-Camargo et al. (2021).

The Milky Way disk contains spiral arms. (Lin & Shu, 1966, 1964) proposed that spiral arms were density waves but other theories propose alternative mechanisms for forming and maintaining spirals, such as gravitational amplification in a differentially-rotating disk (Goldreich & Lynden-Bell, 1965; Julian & Toomre, 1966). The formation and evolution of spiral arms in galaxies also depend on the dynamics of gas and dark matter in galaxies, and it is an active field of research (Binney & Tremaine, 2008; D'Onghia et al., 2013). More generally, the full details of secular evolution and formation of structure in disk galaxies (including bars, spirals, etc.) are poorly-understood Sellwood (2014). The first maps of the Milky Way spiral structure was by Morgan et al. (1952) who used $\approx$30 stars. These structures have been mapped over time by various studies using a combination of gas and stellar kinematics, but some details on their morphology (e.g. the number of arms) are still unknown (Drimmel & Spergel, 2001; Quillen, 2002; Quillen et al., 2018). Additionally, there is evidence of disk flaring i.e. the continuous variation of vertical scaleheight with radius (López-Corredoira et al., 2002; Bovy et al., 2016), and the disk also "wraps" at $\approx$ 15 kpc (Carney & Seitzer, 1993; López-Corredoira et al.,

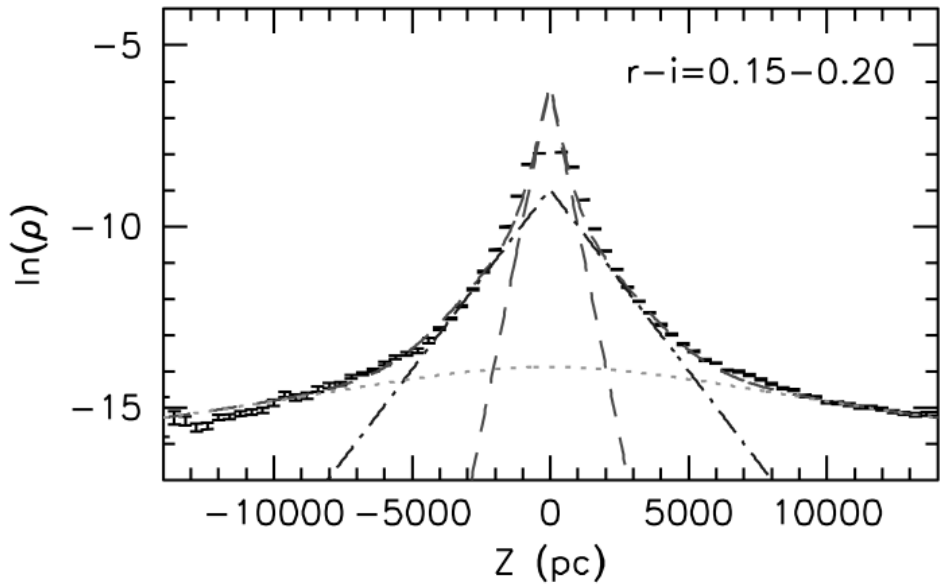

Figure 1.2 SDSS Stellar densities near the Sun (8 kpc) by Jurić et al. (2008). The dashed line is the sum of an exponential fit to the thin disk component, the dot-dashed line shows a thick disk fit, and the halo is shown as a dotted line.

2002). Flaring and wrapping are also seen using giants stars with Gaia (Chrobáková et al., 2022). These effects may be caused by a combination of radial migration or satellite interactions (Kazantzidis et al., 2009; Loebman et al., 2011).

The Stellar halo

The broad stellar density of the Milky Way halo fits a smooth spheroidal profile ($\rho(R) \propto R^{-n}$) with a power-law index of $n = 2.77$ (Jurić et al., 2008). However, the halo is almost entirely dominated by accreted substructure as predicted from cosmological models (Bullock & Johnston, 2005), as evidenced by the detection of tidally-disrupted streams (e.g Sagittarius stream, Majewski et al. 2003). Vivas & Zinn (2006) used a

sample of ≈ 450 RR Lyrae stars in a survey covering ≈ 300 degree^2 on the sky to map the density structure of the Galactic halo. Away from significant substructure, they fit a smooth spheroid with $n = 3$, a rediscovered prominent substructure (e.g the Sagittarius stream). The era of large-scale surveys has uncovered hundreds of streams in the Milky Way halo, which are signatures of tidally-disrupted satellite galaxies or globular clusters (Shipp et al., 2018).

By looking at kinematics, age, and metallicity, the stellar halo can be decomposed into two regions: an inner and an outer halo. Carollo et al. (2007) used $\approx$ 20,000 stars obtained with SDSS with precise kinematics and abundances. They found a population of inner halo stars extending from 10–15 kpc, following a nearly-prograde motion with Galactic rotation with high orbital eccentrics. Stars in the outer halo extend to 15–20 kpc and have a retrograde motion with a wide range of orbital eccentricities. They also found that halo stars are generally metal-poor, with the inner halo metallicities peaking at $[\mathrm{Fe/H}] = -1.6$ while outer halo stars metallicities peak at $[\mathrm{Fe/H}] = -2.2$. Subsequent studies (Carollo et al., 2010; Beers et al., 2012) with larger samples or different surveys have further confirmed these trends. Halo stars are generally older than > 10 Gyr (Jofré & Weiss, 2011a).

One highlight is the recent discovery of Gaia Enceladus (also called the Gaia Sausage, GCSE Helmi et al. 2018; Haywood et al. 2018; Deason et al. 2018). By examining the kinematics, spatial distributions, and metallicities of stars within 2 kpc of the Sun using Gaia and SDSS/APOGEE. Helmi et al. (2018) reported the discovery of a kinematic over-density in the Milky Way halo. GCSE stars have elevated [α/Fe] abundances, comparable to dwarf galaxies and ages that are consistent with the scenario of a single merger event with a stellar mass of 2-7$\times 10^8$ $M_\odot$ 10 Gyr ago (at a redshift of 2). In addition to forming the majority of eccentric inner halo stars, this merger is responsible for heating a pre-existing disk, which triggered new star formation. Subsequent studies

(Yuan et al., 2020; Naidu et al., 2020) have confirmed these findings; though others have proposed that the GCSE was rather a smaller merger (Lane et al., 2023). In addition to GCSE, Gaia has revealed a rich diversity of structure in the halo (Naidu et al., 2020; Myeong et al., 2018), all pointing to a complex accretion history, consistent with the idea that galaxies build up their masses from multiple accretion events.

Nuclear Star Cluster, the Galactic Center, the Bar and Bulge

A large fraction of massive galaxies host a nuclear star clusters at their center, with masses $> 10^6 M_\odot$, composed of a mixture of young and old stellar populations with a continuous star-formation process (Böker et al., 2002; Walcher et al., 2005, 2006). In the Milky Way, the Galactic center hosts a supermassive black hole (Sagittarius A*) with a mass of $\approx 4 \times 10^6 M_\odot$ at distance 8 kpc from the Sun(Ghez et al., 2008). The discovery was awarded the Nobel Prize in Physics in 2020. Sgr A* is surrounded by a nuclear star cluster with a mass of $\approx 3 \times 10^7 M_\odot$ (Launhardt et al., 2002). There is extreme dust extinction ($A_V \approx$40 mag, $A_K \approx$2 mag) in the cluster, hence most of the structure is best studied at infrared wavelengths. The dynamical model of the nuclear star cluster fits to a flattened density spheroid, with isotropic velocities (Chatzopoulos et al., 2015) and the nuclear star cluster is embedded inside a nuclear stellar disk covering a distance of 30–400 pc away from the center with a scale-height of ≈45 pc.

The nuclear star cluster lives inside the Galactic Bulge. Bulges are also seen in external galaxies and they are divided into two types: classical bulges which are rotationally-supported spherical distribution of stars with random motions, and pseudo-bulges (including disk-like bulges or boxy/peanut x-shaped bulges) which are stars orbiting in the same plane and extended in the vertical direction (Kormendy et al., 2006). Stars in the classical bulge are thought to come from mergers, or they are formed as part of monolithic collapse of primordial material (Aguerri et al., 2001). However, pseudo-

bulges are thought to be a product of secular evolution of the disk (Combes et al., 1990). The metallicity distribution of bulge stars in the Milky Way extends from metal-poor to metal-rich (-2 to +0.5, Zoccali et al. 2008). Ness et al. (2013) analyzed the metallicity and kinematic distribution of ≈28,000 stars in the Milky Way bulge. They found that metallicity distribution of stars in the Milky Way bulge extends from -2 to +0.15 with at least 5 different peaks associated with contamination from other Milky Way components (e.g thick disk halo) and they did not found a clear kinematic separation between a classical bulge and a pseudo-bulge. Bars are also observed in external galaxies (Sellwood & Wilkinson, 1993), and they are product of secular evolution of the disk (Combes & Sanders, 1981). The Milky Way's bar has been identified in gas (Blitz & Spergel, 1991; Binney et al., 1991). However, this feature is difficult to map with stars due to strong extinction towards the Galactic center and the Sun is embedded in the Galactic disk. The first identification of the bar from mapping densities of stars towards the Galactic center was done by Hammersley et al. (2000), who measured a half-length radius of ≈ 3.5 kpc. Just like spiral arms, bars are a major source of dynamical heating in the disk.

1.1.3 Outstanding Questions in Galactic Archeology

There are many unanswered questions in galactic archaeology, here are some topics that are most-relevant to this dissertation:

Dark Matter

The Milky Way's mass is dominated by dark matter, and the overall shape and dark matter content can be constrained by measuring the Galaxy rotation curve. Early work by Vera Rubin (Rubin et al., 1980) showed that edge-on spiral galaxies rotation curves did not match their mass profiles. Subsequent indirect evidence (e.g galaxy clusters, cosmic microwave background, strong lensing, baryonic acoustic oscillations)

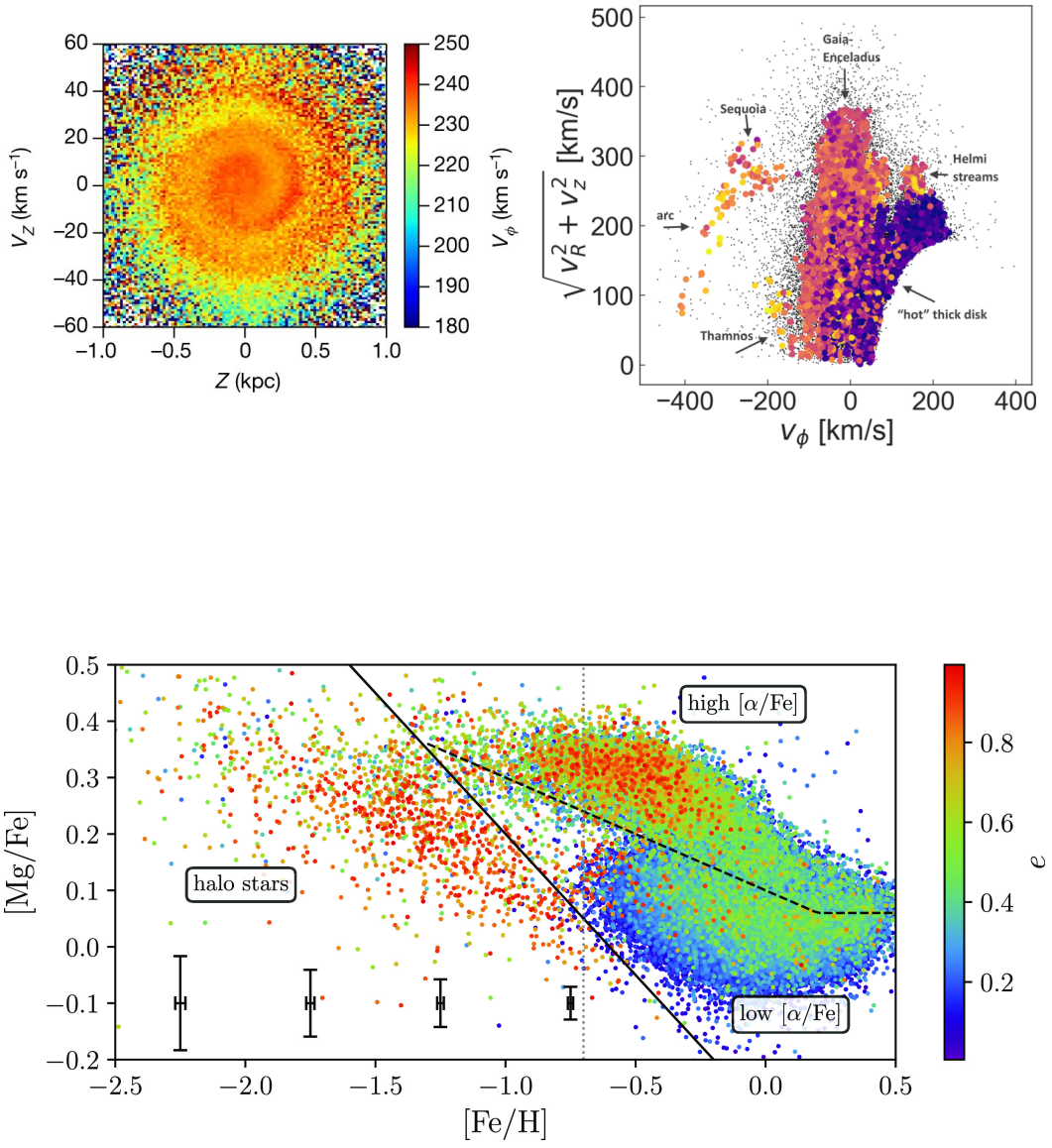

Figure 1.3 Top left: distributions of positions and velocities for 6 million disk stars within <1 kpc from the Sun from Antoja et al. (2018). The phase-spiral is the signature of dynamical disequilibrium in the disk caused by interactions with satellite galaxies (Hunt et al., 2022). Top Right: identification of kinematic substructure in the Milky Way halo by Helmi et al. (2018). GCSE which merged with the Milky Way $\approx$ 10 Gyr ago is the largest contributor. Bottom: APOGEE Stellar abundances of Gaia stars by Mackereth et al. (2019a) colored by orbital eccentricities. Halo stars and thick disk are metal-poor and move on eccentric orbits compared to thin disk stars consistent with the merger hypothesis.

show that non-luminous dark matter is indeed a large component of the mass of galaxies. The nature of dark matter remains unknown. There are many proposed models including, cold dark matter, warm dark matter and fuzzy dark matter which predict a different abundance of dark matter subhalos, dark matter halo shape (e.g cores vs cusps) and orientations (Bose et al., 2017; Spergel & Steinhardt, 2000; Rocha et al., 2013; Tulin & Yu, 2018; Hui et al., 2017; Glennon et al., 2022). Major advances in measuring precise motions of various tracers (e.g. stars, gas) in the Milky Way has allowed the measurement of the rotation curve out to$\approx$ 30 kpc from the center of the Galaxy (Gunn et al., 1979; Bovy et al., 2012b; Eilers et al., 2019). However, distance measurements at larger galacto-centric radii become uncertain. Detecting gaps in globular cluster streams in the Milky Way is a complementary technique. Globular cluster streams are dynamically cold, physically thin, and extended over large areas of the sky, hence they are sensitive to perturbations from encounters with small dark halos (Johnston et al., 2002; Yoon et al., 2011; Bovy, 2016; Bovy et al., 2017). The next generation of ground-based and space-based telescopes will offer an opportunity to constrain the nature of dark matter from various astrophysical tracers, in conjunction of ongoing direct detection methods.

Star Formation History and Initial Mass Function

Most of the star formation in galactic disks happens at early times where mergers dominate, the gas density is high which makes the early disks turbulent with variability in their star formation rates (Kereš et al., 2005; Hopkins et al., 2014; Somerville & Davé, 2015). It is probable that the Milky Way disk assembled in three stages as summarized by Semenov et al. (2023): a proto-galaxy made of metal-poor([Fe/H]< -1.5) stars with random motions, with abundances resembling globular clusters (Oser et al., 2010; Belokurov & Kravtsov, 2022; Conroy et al., 2022), followed by the formation of a thick disk $>$ 10 Gyr ago, evidenced by a steep metallicity gradient for metal-poor thick

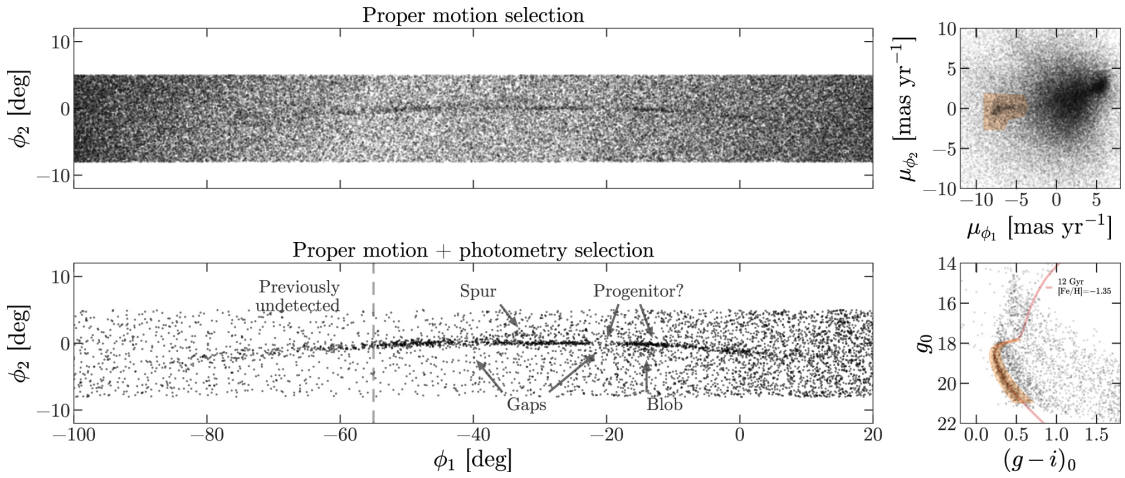

[Figure by Price-Whelan & Bonaca (2018) showing a gap induced in the globular cluster stream GD-1 from a dark matter subhalo.]Stars in the stream are selected by their Gaia proper motion and their Pan-STARRS photometry as shown in the upper and lower right subplots. Selected stars are plotted in angular coordinates along the stream, showing a feature (reproduced in simulations) created by an encounter with a dark matter subhalo with a mass between $10^6 - 10^8 M\odot$ (Bonaca et al., 2019)

disk stars, implying a rapid formation over 1 Gyr (Belokurov & Kravtsov, 2022); and finally the formation of a thin disk from secular evolution of the thin disk from angular momentum conservation (Bird et al., 2013; Agertz et al., 2021). The thick disk of the Milky Way may also have formed by the GCSE merger (Bonaca et al., 2020). However, hydrodynamical simulations show that mergers may only play minor role in shaping disk structure (Ma et al., 2017; Yu et al., 2022). Alternatively, the inner disk could also from an "inside-out" from processes such as radial migration (Schönrich & Binney, 2009; Loebman et al., 2011; Bovy et al., 2016). The full details of the formation and evolution of disks in the full cosmological context is still an open problem.

Stars are born in dense ($N_H \approx 10^{20}$cm^{-2}), cold ($\approx$ 10 K), turbulent molecular clouds, along filamentary structures (McKee & Ostriker, 2007). One fundamental distribution is the initial mass function (IMF) which is the probability density function for initial masses of stars right after formation. This distribution is usually parameterized as

a power-law

$$\frac{dN}{dM} \propto M^{-\alpha} \tag{1.1}$$

, also expressed as

$$\frac{dN}{d\log M} \propto m^{-\Gamma} \tag{1.2}$$

where $\Gamma = \alpha - 1$ or log-normal distributions

$$\frac{dN}{d\log M} \propto e^{(-\log M)^2} \tag{1.3}$$

A power-law IMF would emerge from a scale-free process while log-normal distributions are generally a result of a combination of multiple independent processes (Kirkpatrick et al., 2021). Salpeter (1955) uses $\alpha = 2.35$, while uses a broken power law $\alpha =$ 2.3Kroupa (2001) uses $\alpha = 2.3$for masses > 0.5 solar masses, $\alpha = 1.3$ between 0.08 and 0.5 solar masses $\alpha = 0.3$ below 0.08 solar masses, while Miller & Scalo (1979) and Chabrier (2005) use log-normal distribution. Many studies have estimated the IMF come from counting experiments in the field and clusters. Recently Kirkpatrick et al. (2021) derived $0.5 \leq \alpha \leq 0.7$ for field objects below < 0.1 solar masses. But, high-resolution simulations of star formation are needed to understand the origins of the IMF.

These studies have used main-sequence, and giant stars, but most abundance-sensitive stars are very low-mass stars and brown dwarfs. In the next section, I give a brief overview of these objects.

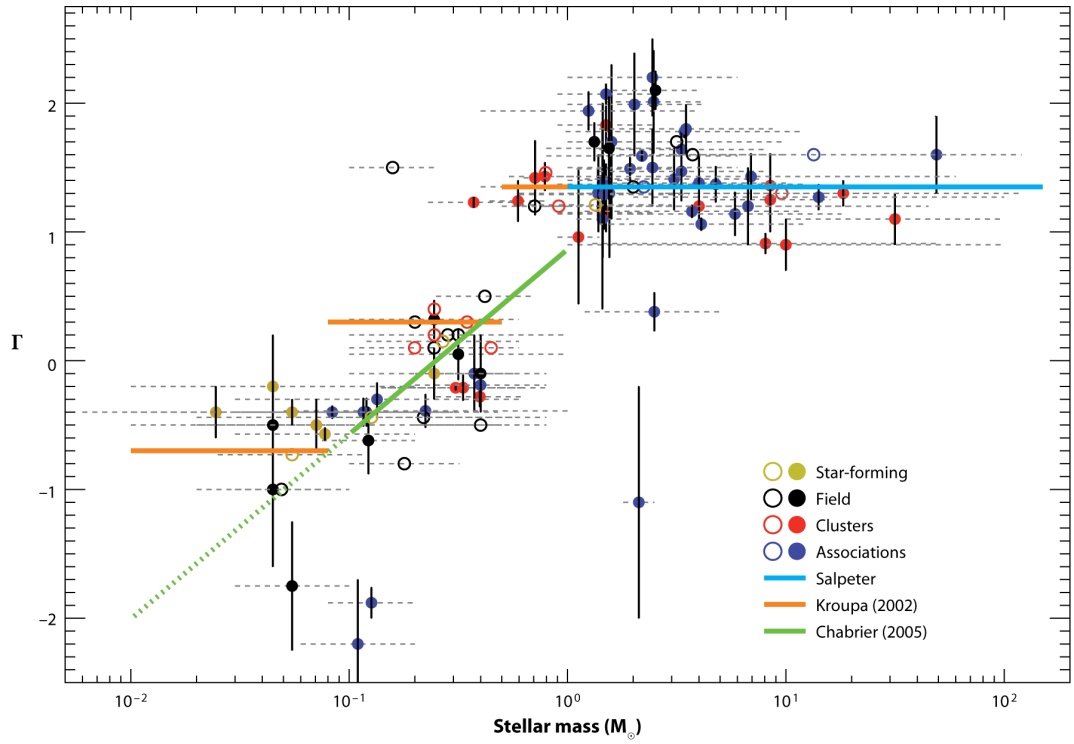

Figure 1.4 Figure by McKee & Ostriker (2007) showing constraints on the IMF in different environments. Note the lack of constraints for < 0.1 solar-mass objects.

1.2 Ultracool dwarfs as an Overlooked Tool for Galactic Archeology

1.2.1 Physical Characteristics

Ultracool dwarfs are the lowest-mass stars and brown dwarfs.Brown dwarfs were first hypothesized by Kumar (1962, 1963) who explored the internal structure of stars below $< 0.1M_{\odot}$ using numerical models. But, the first detection of a brown dwarf was done by Nakajima et al. (1995) who reported the discovery of GI 229B, a cool ($T_{\rm eff}< 1,500$K) companion to an M1 star. By measuring the brightness of the companion, they estimated a bolometric luminosity of $2 \times 10^{-6} L_{\odot}$, a radius of $0.1R_{\odot}$, which corresponds a model-dependent mass of 20-50 Jupiter masses. Generally, UCDs have effective temperatures of <3000 K, masses of $< 0.1M_{\odot}$, radii of $\approx 0.1R_{\odot}$, and encompass the spectral classes M,L,T and Y. The 2MASS, SDSS and other large-scale infrared surveys uncovered the first large samples (>100) of these objects, driving the definition of the L+T spectral classes (Kirkpatrick et al., 1999; Burgasser et al., 2006a). Subsequent deep surveys (WISE, PanSTARRS, DES, UKIDSS, CFHTLFS, HSP) have pushed this to thousands of thousands of objects Kirkpatrick et al. 1999, 2000; Hawley et al. 2002; Cruz et al. 2003; Burgasser et al. 2004), including the first Y dwarfs (Cushing et al., 2011). Currently, there are over $> 10,000$ spectroscopically-confirmed UCDs in the local neighborhood ($d < 100$ pc).

At younger ages ($< 1Myr$), UCDs interiors are well-described as an ideal gas and gravitational contract. Further contraction becomes then halted once these interiors reach electron-degenerate densities. Stars with masses $> 0.07M_{\odot}$ reach temperatures high enough to fuse Hydrogen and eventually reach temperature equilibrium. Lower-mass brown dwarfs do not sustain Hydrogen fusion and cool down with time, and they no

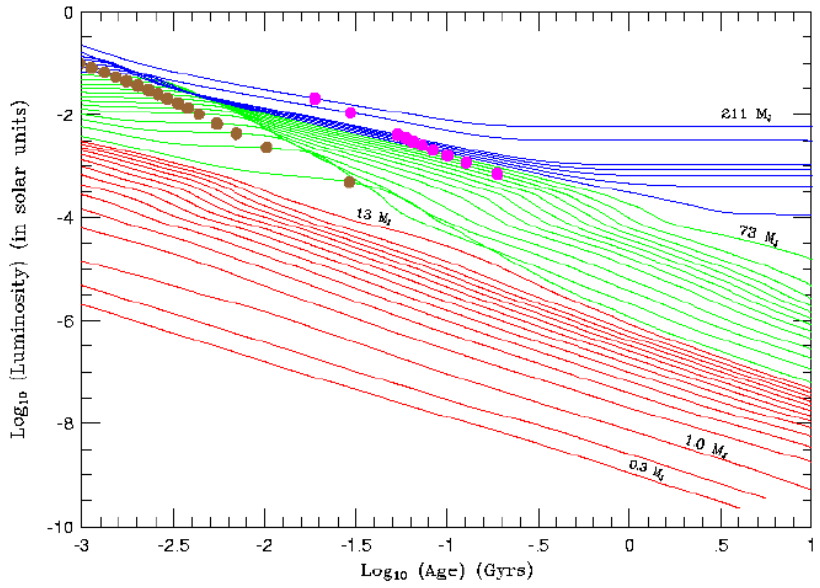

Figure 1.5 Blue curves show stars, brown dwarfs with masses above 13 Mj are shown in green and below 13 Mj are in red. Gold dots show the time where 50 percent of the deuterium has been burned and b;ue dots show where 50 percent of the lithium has been utilized.

further contraction as these objects are structurally supported by electron degeneracy pressure. This leads to the so-called “mass-age" degeneracy problem; unlike stars, it is impossible to determine the mass of a brown dwarf from the object’s luminosity alone. The details of the interior structure of a given UCD will depend on its mass and the metallicity (Burrows et al., 2001, 2006). More generally, whether a given UCD is a brown dwarf or low-mass star, its lifetime is $>$ 1 trillion years, exceeding the age of the currently-observable universe. Figure 1.5 shows the evolutionary track of UCDs of various masses as a function of age.

Atmospheres of UCDs are rich and complex, and show an strong dependence on surface temperature, gravity and metallicity. Major work on characterizing UCDs atmospheres has been undertaken over the last $\approx$25 years, starting with establishing “spectral standards" of low-mass stars and brown dwarfs. The process of standardizing

observed stars has a long tradition in observational astronomy, where the main goal just like animal taxonomy is to group “similar" objects in the same category. UCDs are divided into four spectral classes: M, L, T and Y dwarfs. M dwarfs cover a temperature range of 3,500-2,500 Kelvin, L dwarfs are 2,500–1,500 K, T dwarfs have temperatures ranges of 1,500 K-500 K and Y dwarfs are < 500 K (Kirkpatrick, 2005). Their spectra show signatures of absorption by molecular features, and they peak at 1 μm (near-infrared wavelengths). Late-M dwarf atmospheres show signatures of metal oxides (e.g VO, TiO), metal hydrides (e.g CaH, FeH, CrH, MgH) and alkali lines. As we reach low-temperature L dwarfs, we observe the strengthening of their metal hydride features and alkali features and weakening of their metal oxide bands. Additionally, as this objects cool down, there is the appearance of silicate clouds and a host of other condensates. Not only are these clouds evident in the spectral evolution of L dwarfs but they also explain their variability (Ackerman & Marley, 2001; Burgasser et al., 2002). Alternatively, Tremblin et al. (2015) have suggested that UCD spectral change can be explained by atmospheric mixing without invoking the presence of clouds. The spectra of L dwarfs are characterized by strong CO absorption and young L dwarfs show evidence of enhanced dust reddening. In the T dwarf regime, there is a conversion of CO to CH_4 which produces distinct features in the NIR. Finally, Y dwarf atmospheres are characterized by strengthened NH_3 features and the shift of the peak of their black bodies towards to mid-infrared ($\approx$ 5 microns). Figure 1.6 shows the spectral sequence of M, L, T dwarfs by Cushing et al. (2006).

1.2.2 Metal-Poor Subdwarfs

Metal-poor UCDs have significant spectral and color differences compared to typical solar-metallicity UCDs (Burgasser et al., 2003). Their spectra are dominated by collision-induced H_2 absorption features in the infrared(Linsky, 1969), which changes the slope of their spectral energy distribution, in addition to altering their overall signature of

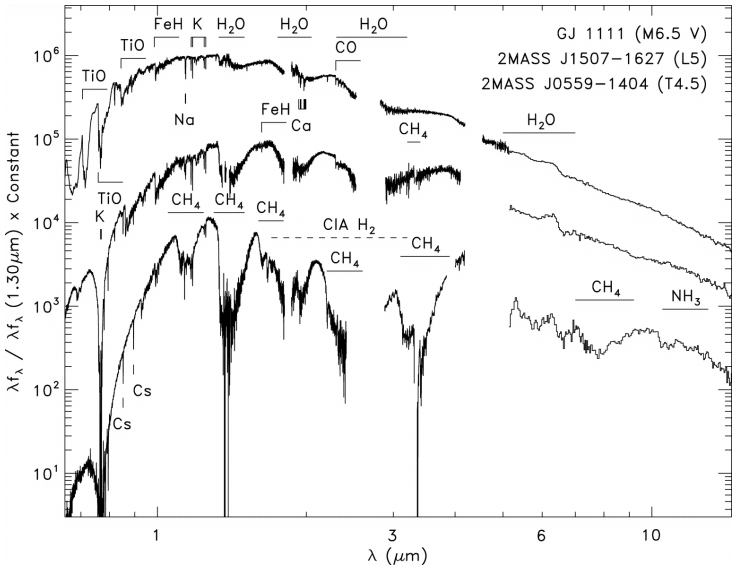

Figure 1.6 Spectral sequence of M, L, T dwarfs showing prominent absorption features in the near-infrared (Cushing et al., 2006)

other molecular absorption features. Hence, low-metallicity UCDs are easily identifiable by their colors and spectra even at low-resolution. Current local samples of L and T subdwarfs are limited by their intrinsic rarity as they are more likely to be thick disk or halo objects. However, recent large-scale surveys have significantly increased sample of known metal-poor, lowest-temperature objects (e.g. Zhang et al. 2019; Schneider et al. 2020). Nevertheless, these samples remain extremely small. Additionally, recent progress has been made in modeling efforts motivated by the possible detection of UCDs in metal-poor environments (e.g globular clusters) requiring direct comparison with models (Gerasimov et al., 2022).

1.2.3 UCD Kinematics

Local 3D-kinematic samples of UCDs are also dominated by thin disk sources, as these samples require bright sources (therefore extremely local < 20 pc) to measure

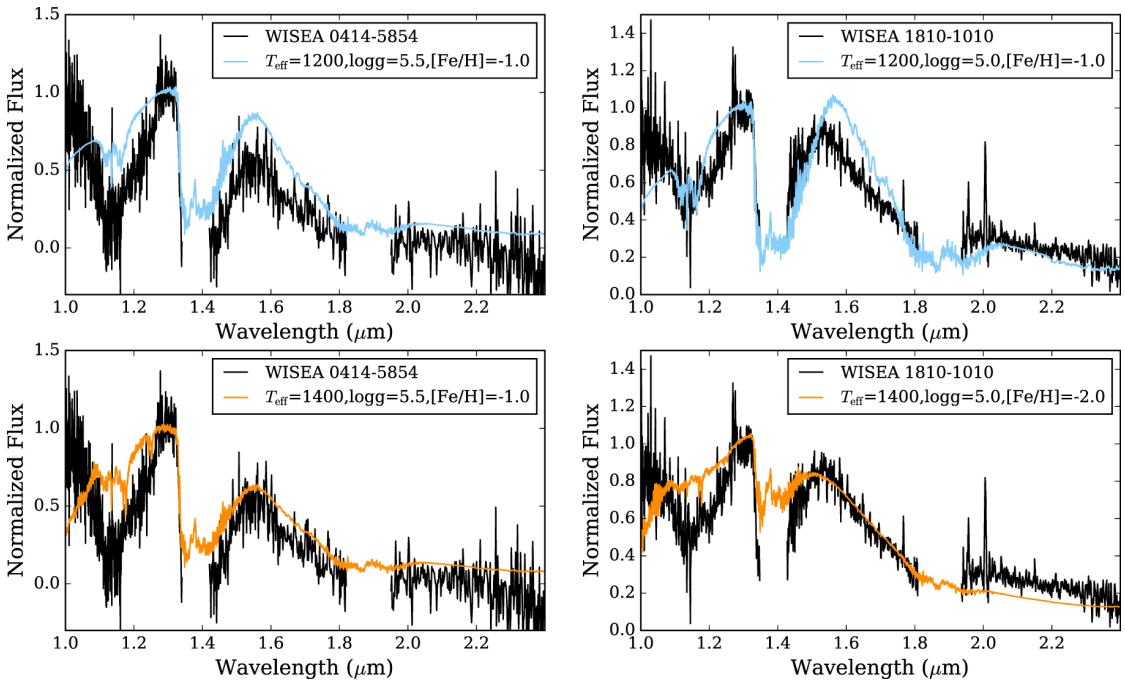

Figure 1.7 Examples of spectra of metal-poor T dwarfs identified by Schneider et al. (2020)

their radial velocities. Predictions from Monte-Carlo simulations (Burgasser, 2004; Robertson, 2021) show that the velocity dispersion as a function of UCD spectral type is a combination of effects, including of UCD evolution and Galactic dynamics. The Brown Dwarfs Kinematic Project series (Faherty et al., 2009, 2012; Hsu et al., 2021) has conducted precise monitoring of proper motions and radial velocities for a large sample of local M, L and T dwarfs. They found that thin disk L dwarfs are less-dispersed than T and M dwarfs, inline with disk heating models of (Aumer & Binney, 2009). Their respective velocity dispersion translate into population ages of 2-4 Gyr which are comparable to the median age of thin disk stars in the Galaxy. By further examining the population trend Hsu et al. (2021) found a break in kinematic dispersion corresponding to the Hydrogen burning limit.

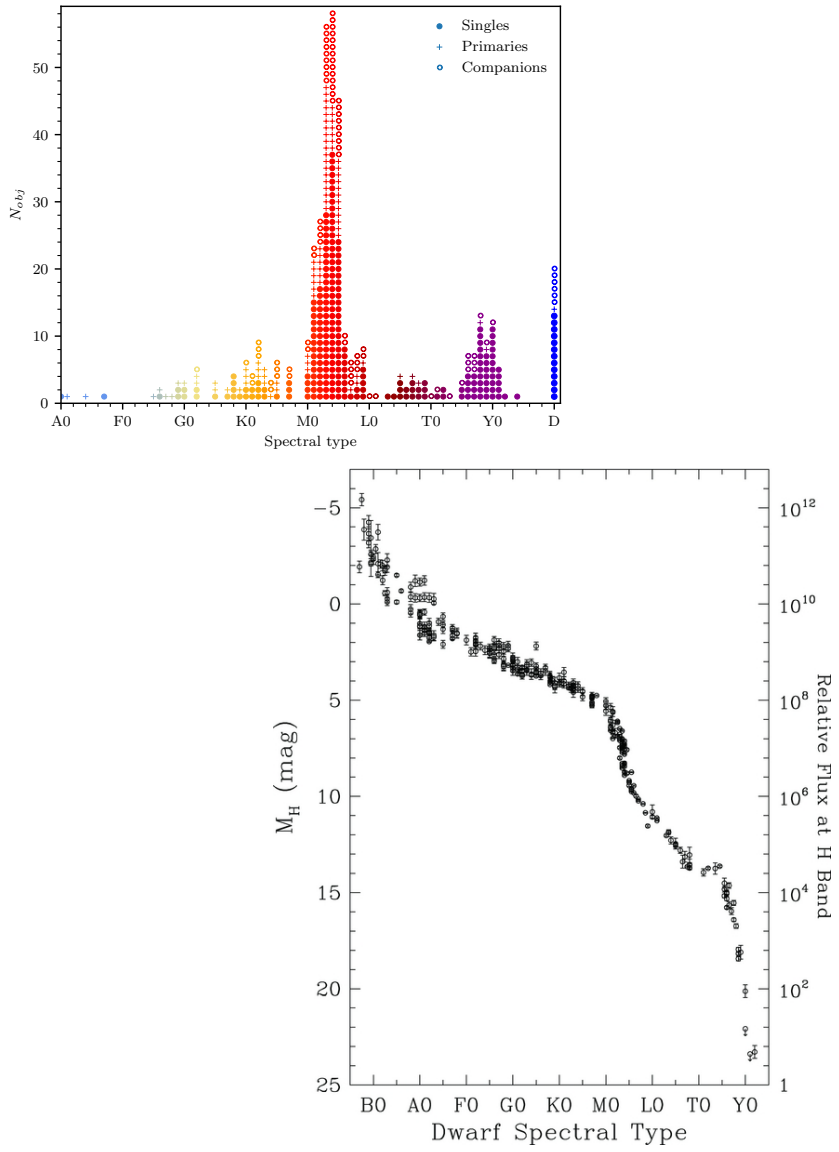

Figure 1.8 Top: Distribution of stars identified by Gaia, grouped by specytral type by spectral class within 10 pc of the solar neighborhood byReylé et al. (2021). M, L, T, Y (UCDs classes) dominate. Bottom: Intrinsic brightness (magnitudes and luminosities) of stars as a function of spectral type by Kirkpatrick et al. (2012). UCDs are a factor of $10,000$ fainter than the Sun.

1.2.4 UCDs as Probes for Galactic Structure

With the properties listed above, UCDs are an excellent/complimentary probe for Galactic archaeology. One of the primarily challenges in using ultracool dwarfs for galactic archaeology is their intrinsic faintness, and surveys to date have been largely limited to the immediate "Solar Neighborhood" (distances d $\lesssim$ 100 pc from the Sun). Local samples probe the Milky Way's thin disk and nearby young clusters and associations (Cruz et al., 2007b; Reyle et al., 2010; Kirkpatrick et al., 2021; Gagné et al., 2015), but fail to sample the thick disk and halo populations with sufficient numbers to measure population properties (Aganze et al., 2022a). Local samples also fail to reach UCDs in globular clusters which are located $>$1000 pc from the Sun and which formed in the earliest stages of the Milky Way's history (10–14 Gyr ago); and the bulge, a dense and metal-enriched environment surrounding the core of the Milky Way.

Next generation observatories will dramatically expand our view of the cosmos, enabling robust study of ultracool dwarfs in these environments. New facilities include the *James Webb Space Telescope* (*JWST*) which recently started science operations, the soon-to-be-completed Vera Rubin Observatory, and forthcoming space-based survey missions (e.g., *Euclid*, *Nancy Grace Roman Space Telescope*) and 30m-class ground-based telescopes (the Thirty Meter Telescope, the Giant Magellan Telescope, and Europe's Extremely Large Telescope). All of these facilities will have the capability to reach and characterize UCDs throughout the Milky Way, producing large samples of thick disk and halo UCDs, and making the first detections of UCDs in globular clusters, satellite streams, and the bulge.

1.3 Organization of the Dissertation

Chapter 2 lays out our work on finding 164 distant UCDs (> 2 kpc) in deep HST/WFC3 surveys. In Chapter 3, I present a follow-up paper that uses this sample to constrain the scaleheights and population ages of disk UCDs. In Chapter 4, I predict the expected counts of UCDs in the with the Roman telescope, the Vera Rubin Observatory and the Euclid Telescope. In Chapter 5, I predict the detectability of gaps in the Globular cluster streams with the Roman Telescope. Chapter 6 summarizes the main conclusions of every chapter.

Chapter 2

Surface Densities of Ultracool Dwarfs in Deep HST/WFC3 Parallel Fields

2.1 Introduction

The structure and evolution of the Milky Way is largely informed from the spatial and kinematic distributions of its luminous stars, an area of study known as Galactic archaeology (Freeman, 1987; Ivezić et al., 2012). Large imaging, astrometric, and spectroscopic surveys such as the the Sloan Digital Sky Survey (SDSS; York et al. 2000) have been critical for building our model of the Milky Way through 6-dimensional position and velocity data, and detailed spectroscopic characterization of large-scale stellar populations. Star-count data spanning decades have revealed that our Milky Way Galaxy contains multiple stellar populations, including a kinematically young population spatially distributed into two exponential disks (the thin and thick disks); a centrally-concentrated and spherically distributed population of metal-rich rich stars (the bulge), and a widely-dispersed old and metal-depleted population (the halo; e.g., de Vaucouleurs & Pence 1978; Bahcall & Soneira 1981; Jurić et al. 2008). Analysis of the stellar

evolutionary states of these populations suggest that the Galactic disk population has been continuously forming stars over the past 8–11 Gyr, while halo stars were largely formed 10–13 Gyr ago (Leggett et al., 1998; Tolstoy et al., 2009; Haywood et al., 2013a).

More recently, the *Gaia* astrometric mission (Gaia Collaboration et al., 2018), combined with large-scale spectroscopic surveys such as SDSS, the Large sky Area Multi-Object fiber Spectroscopic Telescope (LAMOST; Zhao et al. 2012), the Apache Point Observatory Galactic Evolution Experiment (APOGEE; Majewski et al. 2017), and GALactic Archaeology with HERMES (GALAH; De Silva et al. 2015; Martell et al. 2017), has greatly refined this picture of the Milky Way. Notable insights include the inference of major merger events that likely formed the inner stellar halo and thick disk populations (Gaia-Enceladus/Gaia sausage: Helmi et al. 2018; Belokurov et al. 2018; Myeong et al. 2018; Gallart et al. 2019; and the Sequoia event: Myeong et al. 2018, 2019); phase-space substructure and mixing among stars in the Solar Neighborhood, indicative of past perturbations of the Milky Way by satellite systems (Antoja et al., 2018); an ensemble of stellar streams that trace the tidal disruption of, and stellar accretion from these satellites (Boubert et al., 2018; Malhan et al., 2018; Koppelman et al., 2019a); and the detection of dozens of hypervelocity stars ejected through encounters with central supermassive black holes in the Milky Way and Large Magellanic Cloud (Boubert et al., 2018; Erkal et al., 2019a). These results show the Milky Way and its environment to be a complex and dynamically evolving system.

All of these studies have focused on the brightest red giants and main sequence stars, which provide both reach and reliability in the inference of stellar properties. Ultracool dwarfs (UCDs; $M \lesssim 0.1\ M$, $T_{\rm eff} \lesssim 3000$ K; Kirkpatrick 2005) provide an alternative, and potentially more enriching, population for studying the Milky Way system (Burgasser, 2004; Ryan et al., 2017). Ultracool dwarfs constitute $\sim$50% of stars by number in the immediate Solar Neighborhood ($d < 100$ pc), and are abundant in every

environment in the Galaxy (Reid et al., 1999; Chabrier & Baraffe, 2000; Cruz et al., 2007b; Bochanski et al., 2010; Kirkpatrick et al., 2019). Stellar UCDs have lifetimes far in excess of the age of the Galaxy (>10^3 Gyr, Laughlin et al. 1997), while substellar UCDs (brown dwarfs) do not fuse hydrogen and have effectively limitless lifetimes (Kumar, 1962, 1963; Hayashi & Nakano, 1963). Brown dwarfs also cool and dim as they age, developing distinct spectra shaped by strong molecular absorption features that are highly sensitive to atmospheric temperature, surface gravity, and metallicity. The thermal and chemical evolution of stellar and substellar UCDs provide age diagnostics that have been exploited in stellar cluster studies (Stauffer et al., 1998; Jeffries & Oliveira, 2005; Martín et al., 2018), coeval binary systems (Song et al., 2002; Burgasser & Blake, 2009), and searches of new members of young moving groups near the Sun (Lopez-Santiago et al., 2006; Gagné et al., 2015; Mamajek, 2015; Faherty et al., 2018).

Ultracool dwarfs have historically been uncovered in wide-field red optical and infrared sky surveys, including SDSS, the Deep Near-Infrared Survey of the Southern Sky (DENIS; Epchtein et al. 1997), the Two Micron All-Sky Survey (2MASS; Skrutskie et al. 2006), the United Kingdom Infra-Red Telescope Infrared Deep Sky Survey (UKIDSS; Lawrence & Others 2007), the Canada-France Brown Dwarf Survey (CFBDS; Reylé et al. 2010), the *Wide-field Infrared Survey Explorer (WISE*; Wright et al. 2010), and the Panoramic Survey Telescope and Rapid Response System (Pan-STARRS; Chambers et al. 2016), among others. The intrinsic faintness of UCDs means that these surveys only reach the immediate Solar Neighborhood ($d \leq 100$ pc). While these surveys have enabled study of the local UCD luminosity and mass functions (Cruz et al., 2007b; Metchev et al., 2008; Reyle et al., 2010; Bardalez Gagliuffi et al., 2019; Kirkpatrick et al., 2019, 2021) they cannot probe Galactic structure or UCD halo populations, of which relatively few examples are currently known (Burgasser et al., 2003; Lépine & Scholz, 2008; Zhang et al., 2019).

Deep, narrow-field imaging surveys provide one approach to investigate more distant ultracool dwarf populations. Many of these surveys have exploited the sensitivity and imaging resolution of the *Hubble Space Telescope*, often in parallel with searches for high-redshift galaxies for which UCDs are a "contaminant" population (Reid et al., 1996; Ryan et al., 2005; Ryan et al., 2011; Holwerda et al., 2014). Very deep, multi-band, ground-based surveys have also expanded our reach for UCDs (Kakazu et al., 2010; Sorahana et al., 2019; Carnero Rosell et al., 2019). However, these imaging surveys are subject to contamination and inaccuracies in spectral classification, which inhibits a detailed evaluation of completeness and analysis of population composition in terms of mass, temperature, metallicity, and other properties. Deep spectral surveys, notably those deploying the slitless grism modes of *HST*/ACS and *HST*/WFC3 instruments, have provided more robust and well-characterized samples of distant UCDs, but are shallower and small in sample size ($\lesssim$50 sources; Pirzkal et al. 2005, 2009; Masters et al. 2012).

In this paper, we present a new analysis of *HST*/WFC3 slitless grism spectra from the WISPS (Atek et al., 2010) and 3D-HST (Momcheva et al., 2016; Brammer et al., 2012; Skelton et al., 2014) surveys, expanding both the areal coverage and spectral types evaluated in these deep spectroscopic datasets. In Section 3.2 we describe the survey data used. In Section 2.3 we describe our selection process, including a robust analysis of three independent procedures using spectral indices and template fitting: selection by predefined index ranges and by two supervised machine learning methods. In Section 3.4 we review the properties of the 164 UCDs identified in this sample, including classifications and spectrophotometric distance estimates. In Section 5.6 we summarize the main results of our study. Further analysis of this sample is presented in a companion paper (Aganze et al., in prep, 2021; hereafter Paper II).

2.2 Data

The WISPS and 3D-HST surveys used the infrared channel of the WFC3 camera (Kimble et al., 2008), obtaining low-resolution G102 (λ = 0.8–1.17 μm, $\lambda/\Delta\lambda \approx 200$) and G141 ($\lambda$ = 1.11–1.67 μm, $\lambda/\Delta\lambda \approx 130$) grism spectra. Removal of the slit mask allows for overlapping spectra across the 136×123 (3.1×10^{-4} arcmin^2) inner field of view of the WFC3 camera.

2.2.1 WISPS survey data

WISPS is a 1000-orbit, *HST* pure-parallels survey covering 390 fields ($\sim$1500 arcmin^2), obtained concurrent with observations made with the Cosmic Origins Spectrograph (COS) or Space Telescope Imaging Spectrograph (STIS). The goal of WISPS is to conduct a census of star-forming, high-redshift galaxies; hence, WISPS fields are typically at high Galactic latitudes ($|b| \gtrsim 20^\circ$). Grism data in G102 and G141 settings were obtained with an exposure time ratio of 2.4:1, although the individual exposure times varied. For G141 data, exposures ranged over 600–1400 seconds and 3000–9000s for G102 data. Data were reduced using a combination of `aXe` (Kümmel et al., 2009) and custom software, the latter to remove residual background and to flag bad pixels. Reference images were used to determine source location, and contamination corrections for overlapping spectra were computed from `aXe`. Direct images were also obtained in the broad-band F110W, F140W, and F160W filters, with source catalogs generated using SExtractor (Bertin & Arnouts, 1996). We analyzed reduced grism and photometric data provided in WISPS release version 6.2 (Atek et al., 2010).

2.2.2 3D-HST survey data

3D-HST is an *HST* parallels survey of 248 orbits covering $\sim$600 arcmin^2. The goal of 3D-HST is to understand the physical processes that shape galaxies in the high-redshift universe. This survey targeted four standard deep extra-galactic fields: the All-wavelength Extended Groth strip International Survey (AEGIS; Davis et al. 2007), the Cosmic Evolution Survey (COSMOS, Scoville et al. 2007); the UKIDSS Ultra-Deep Survey (UKIDSS-UDS; Lawrence & Others 2007), and the Great Observatories Origins Deep Survey (GOODS-South and GOODS-North; Giavalisco et al. 2004). These fields are also covered by the Cosmic Assembly Near-infrared Deep Extragalactic Legacy Survey (CANDELS; Grogin et al. 2011; Koekemoer et al. 2011). Spectral data were obtained using both the ACS/G800L grism covering 0.5–0.9 μm with a resolution of $\lambda/\Delta\lambda \approx 100$, and the WFC3/G141 grism. We focused on the WFC3 data for this study. WFC3 exposures were obtained over two orbits, with exposure times varying between 2500–6600 s per pointing. Data were reduced using custom software, including generation of a contamination model, as described in Momcheva et al. (2016); we used these data for our spectral analysis[1]. Note that the extracted 1D spectra reported in Momcheva et al. (2016) are not corrected for the sensitivity; we therefore applied the sensitivity curves provided in the same 3D-HST data products to recover each spectrum's continuum shape.

[1]Data were retrieved from the survey's website, https://3dhst.research.yale.edu/Home.html, on August 12, 2016.

2.3 Selection of UCDs

2.3.1 Spectral Calibration Sample

To anchor our identification of new UCDs in the WISPS and 3D-HST datasets, we first created a spectral calibration sample composed of known UCDs with similar spectral coverage and resolution to the *HST* spectra. This sample was drawn from nearly 3,000 low-resolution ($\lambda/\Delta\lambda \approx 75$–$120$), near-infrared (0.9–2.5 μm) spectra of nearby UCDs observed with the SpeX spectrograph on the NASA InfraRed Telescope Facility (IRTF; Rayner et al., 2003), all contained in the SpeX Prism Library (SPL[2]; Burgasser, 2014). We selected all spectra with median signal-to-noise (S/N) > 10, and visually inspected these spectra to remove background contaminants, which are retained for our random forest classification as non-UCDs (Section 2.3.5). We also used 22 Y dwarf spectra from Schneider et al. (2015) and 77 UCD spectra from Manjavacas et al. (2019), all obtained with *HST*/WFC3. The resulting sample of 2,197 spectra of UCDs with spectral types M7 and later is referred hereafter as the UCD spectral template sample.

2.3.2 Pre-selection Constraints

Point-Source Selection We combined all grism and photometric data from the WISPS and 3D-HST datasets, an initial sample of 254,264 sources. To refine our selection of UCDs, point sources in the WISPS survey were selected using the SExtractor stellarity index `CLASS_STAR` $\neq 0$. 3D-HST provides a different flag, `star_flag`, that identifies point sources based on F160W imaging data. However, this flag rejected 3 visually-confirmed UCDs from the 3D-HST sample that were not rejected with the SExtractor stellarity index, so we used a different selection criteria based on the half-light radius parameter `FLUX_RADIUS` (r). Following Skelton et al. (2014), we required $r \geq 1.5$ and

[2]https://cass.ucsd.edu/~ajb/browndwarfs/spexprism/library.html

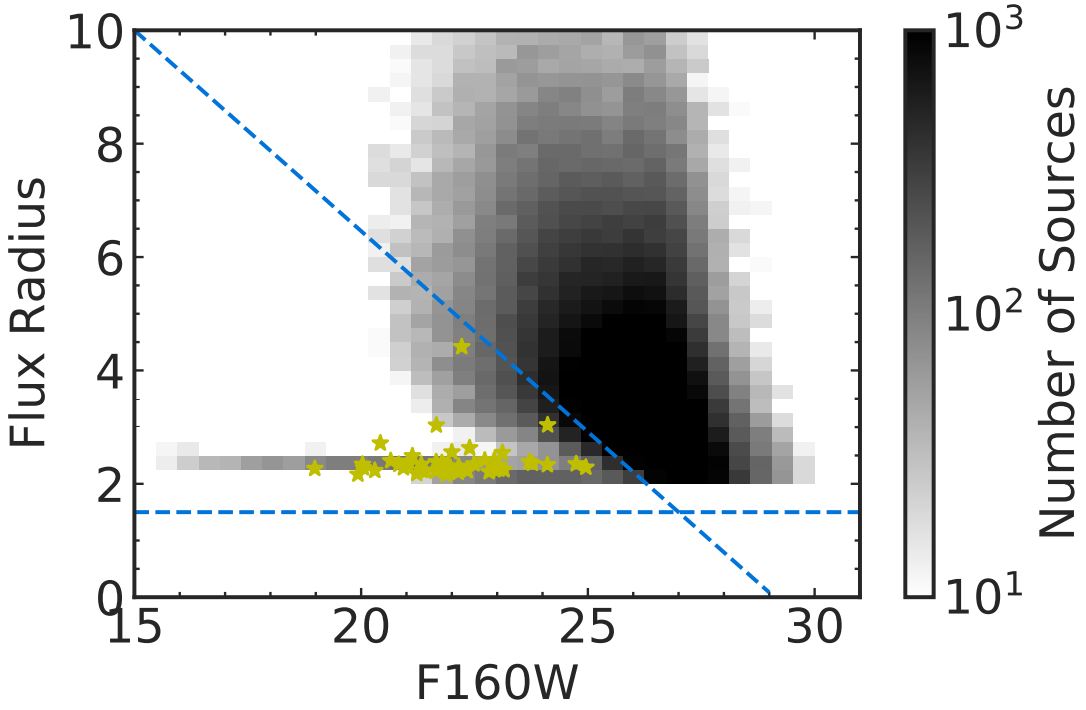

Figure 2.1 Point-source selection cut for the 3D-HST survey. The shaded 2D histogram shows the density of sources in 3D-HST, while our final sample is shown as yellow stars set by the criteria $r \geq 1.5$ and $r < -0.7 \times \mathrm{F140W} + 20.6$.

$r < -0.7 \times \mathrm{F140W} + 20.6$ (Figure 2.1). Point-source selection reduced the sample down to 104,346 sources, or 40.7% of the initial spectral sample.

J-band Signal-to-Noise Rejection To eliminate low S/N spectra that may be too ambiguous to identify or classify as UCDs, we applied a S/N cut on the WFC3 spectral data. UCDs display strong H_2O and CH_4 molecular absorption features in the J and H bands (1.1–1.6 μm), so a S/N calculation that encompasses the full spectral range will produce different results for different spectral types. Therefore, we defined S/N ratios for the J-band continuum in the range 1.2 $\mu\mathrm{m} \leq \lambda \leq 1.3$ μm (hereafter J-SNR), the H-band continuum in the range 1.52 $\mu m \leq \lambda \leq 1.65$ μm (hereafter H-SNR), and an overall median S/N in the range 1.1 $\mu m \leq \lambda \leq 1.65 \mu m$ (hereafter MEDIAN-SNR).

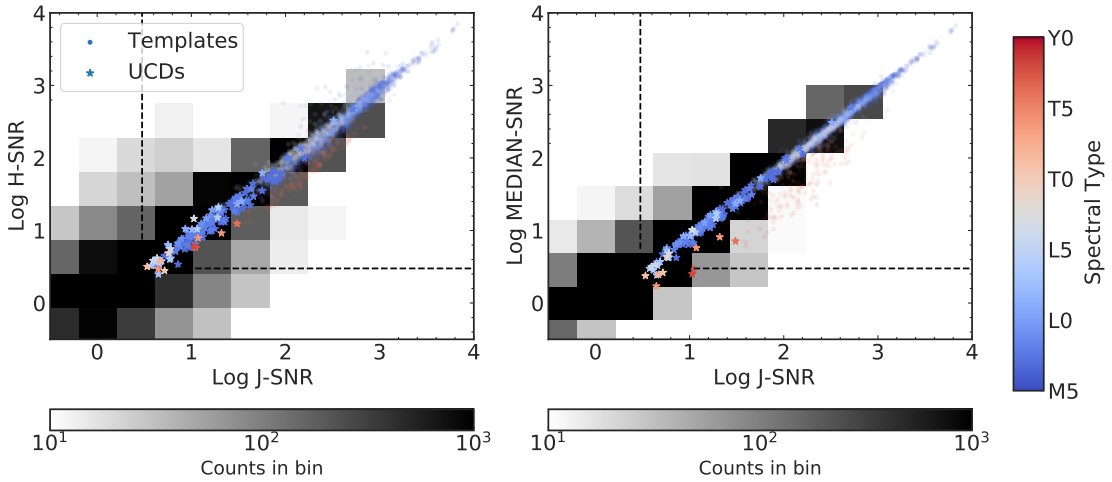

Figure 2.2 Comparison between H-SNR, MEDIAN-SNR, and J-SNR signal-to-noise ratios for objects in our final sample of UCDs (stars), point-sources in both surveys (grey background) and objects in our calibration sample colored by spectral type. Making a cut in J-SNR allows for a selection of late-type objects that would be missed from a comparable MEDIAN-SNR cut. Dashed lines indicate a signal-to-noise ratio of 3.

We also computed an average of the J-band and H-band S/N ratios (herafter JH-SNR). Figure 2.2 shows that a J-SNR cut at 3 allows us to effectively probe a deeper sample of later-type objects. We rejected the lowest S/N spectra by requiring J-SNR ≥ 3, which retained 46,561 spectra, or 18% of the initial spectral sample.

Spectral Template and Line Fitting Visual inspection of the remaining spectral data identify some common contaminants, including emission line sources, featureless spectra with low S/N, spectra with absorption or emission features outside the primary H_2O and CH_4 bands, and other artifacts. To distinguish featureless spectra from UCDs, we fit each WFC3 spectrum to the full UCD spectral template sample and to a straight line using χ^2 minimization. The χ^2 for each template fit was computed as

$$\chi^2_T = \sum_{\lambda=1.15\ \mu\mathrm{m}}^{1.65\ \mu\mathrm{m}} \frac{[\mathrm{Sp}(\lambda) - \alpha T(\lambda)]^2}{\sigma(\lambda)^2}, \tag{2.1}$$

where $\mathrm{Sp}(\lambda)$ is the WFC3 spectrum, $\sigma(\lambda)$ is its uncertainty, $T(\lambda)$ is the UCD template spectrum, and α is a scale-factor that minimizes χ^2_T,

$$\alpha = \frac{\sum_{\lambda=1.15\ \mu\mathrm{m}}^{1.65\ \mu\mathrm{m}} \frac{\mathrm{Sp}(\lambda)\times T(\lambda)}{\sigma(\lambda)^2}}{\sum_{\lambda=1.15\ \mu\mathrm{m}}^{1.65\ \mu\mathrm{m}} \frac{T(\lambda)^2}{\sigma(\lambda)^2}} \tag{2.2}$$

(cf. Cushing et al. 2005). The χ^2 for each line fit was similarly computed as:

$$\chi^2_L = \sum_{\lambda=1.15\ \mu\mathrm{m}}^{1.65\ \mu\mathrm{m}} \frac{[\mathrm{Sp}(\lambda) - a - b\lambda]^2}{\sigma(\lambda)^2} \tag{2.3}$$

where a and b are linear parameters determined through least-squares minimization.

To distinguish between these fits, we used an F-test statistic to determine if the best-fit template was a significant improvement over the line fit, by requiring $F(\chi^2_T/\chi^2_L, \mathrm{DOF}_T, \mathrm{DOF}_L) < 0.02$, where DOF is the effective degrees of freedom of each fit, equal to the number of pixels in the wavelength range 1.15–1.65 μ m (N = 108), minus 1 for the template fit or minus 2 for the line fit. This constraint imposes the condition that the probability that the UCD template is a worse fit than a line is less than 0.5%, a limit chosen based on the distribution of F statistics for similar fits to the spectral templates. This selection cut retained 98% of the templates and 5,946 of point-sources or 2.3% of the initial full sample, and provided a first-order estimate of the spectral classification of true UCDs in our sample.

2.3.3 Spectral Index Selection

2.3.4 Defining Spectral Indices

Our final selection criteria was based on the measurement of spectral indices which sample the strong CH_4 and H_2O molecular features present in the J- and H-band regions. Spectral indices are commonly used to classify UCD spectra, and are typically

tailored to the spectral resolution and region sampled (e.g., Tokunaga & Kobayashi, 1999; Cushing et al., 2000; Testi et al., 2001; Allers et al., 2007; Burgasser et al., 2007). We selected five wavelength regions bracketing the primary absorption features (Table 2.1), measuring the median flux in these regions. Uncertainties were estimated by Monte Carlo sampling of the individual flux measurements, assuming normal distributions scaled by the spectral uncertainties. Ten index ratios were then defined from these band fluxes, each of the form

$$\mathrm{A/B} = \frac{\langle F(\lambda_{A,l} < \lambda < \lambda_{A,h})\rangle}{\langle F(\lambda_{B,l} < \lambda < \lambda_{B,h})\rangle}, \tag{2.4}$$

where $\langle F \rangle$ denotes the median flux value in the wavelength range $\lambda_l < \lambda < \lambda_h$. To select for Y dwarfs, which have extremely low levels of flux in the H_2O and CH_4 absorption bands, we defined six additional indices that averaged flux measurements in multiple absorption bands, e.g., (H_2O-1+CH_4)/J-cont, (H_2O-2+CH_4)/H-cont. Figure 2.4 displays the trends in these spectral indices among dwarf and subdwarf spectral standards.

The spectral indices were measured on both the WFC3 data and our UCD spectral template sample. The latter were used to determine selection criteria for UCD subtype groups of M7–M9, L0–L4, L5–L9, T0–T4, T5–T9, Y dwarfs, and late-M/L subdwarfs. For each possible index-index pairing, we evaluated the distribution of index measurements for calibration templates within each of these subtype groupings, and defined parallelogram regions in which these templates clustered. The parallelograms were determined by first measuring a linear trend ($I_2 = aI_1 + b$) in the index-index data for a given subtype group, then defining a perpendicular range about that line that encompasses 5 times the standard deviation (STD) of template values. This process produces four vertices encompassing each template cluster in each of the possible index-index spaces.

Completeness and Contamination To quantify the effectiveness of these selection regions to identify UCDs in a given subtype group and exclude contaminants, we defined

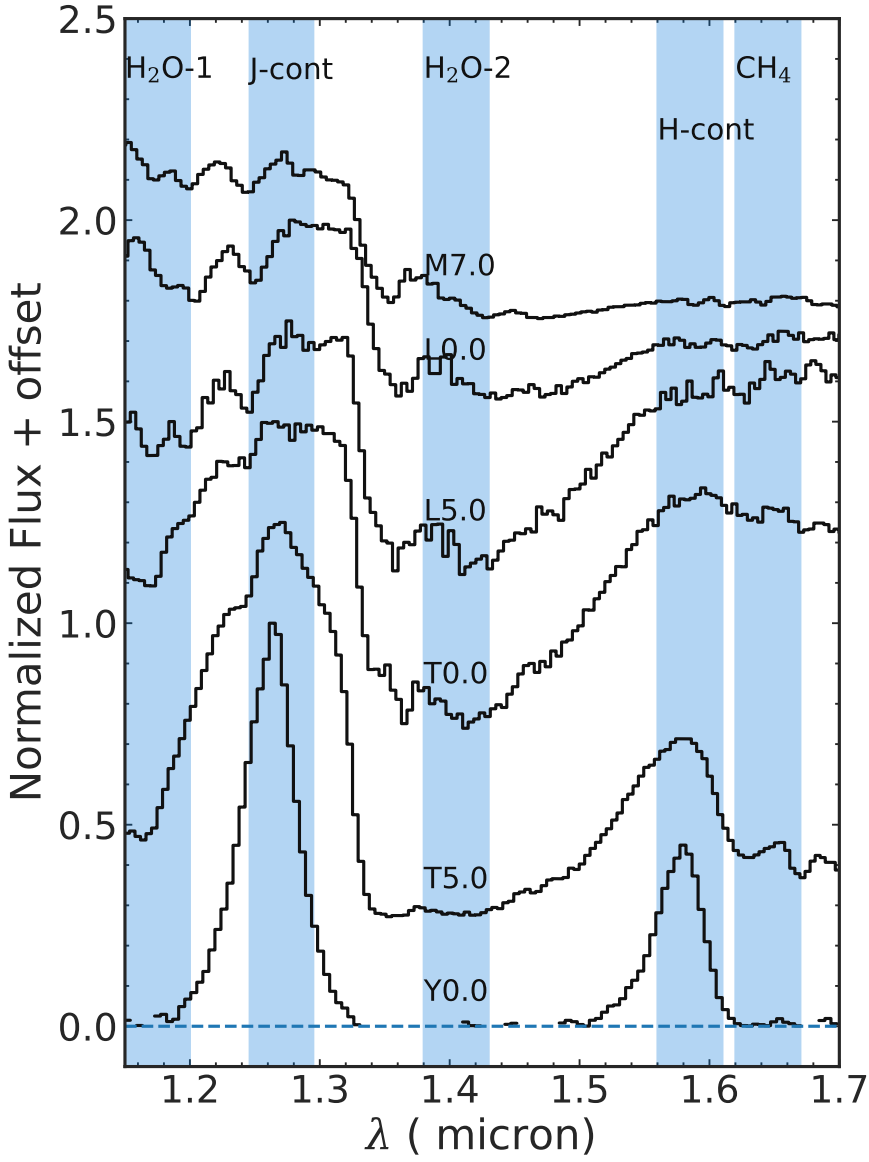

Figure 2.3 Illustration of spectral bands used to define spectral indices in this study (blue bands). The black lines are normalized low-resolution late-M, L, and T dwarf spectral standards defined in Burgasser et al. (2006a) and Kirkpatrick et al. (2010), and the Y0 dwarf WISE J1738+2732 from Cushing et al. (2011).

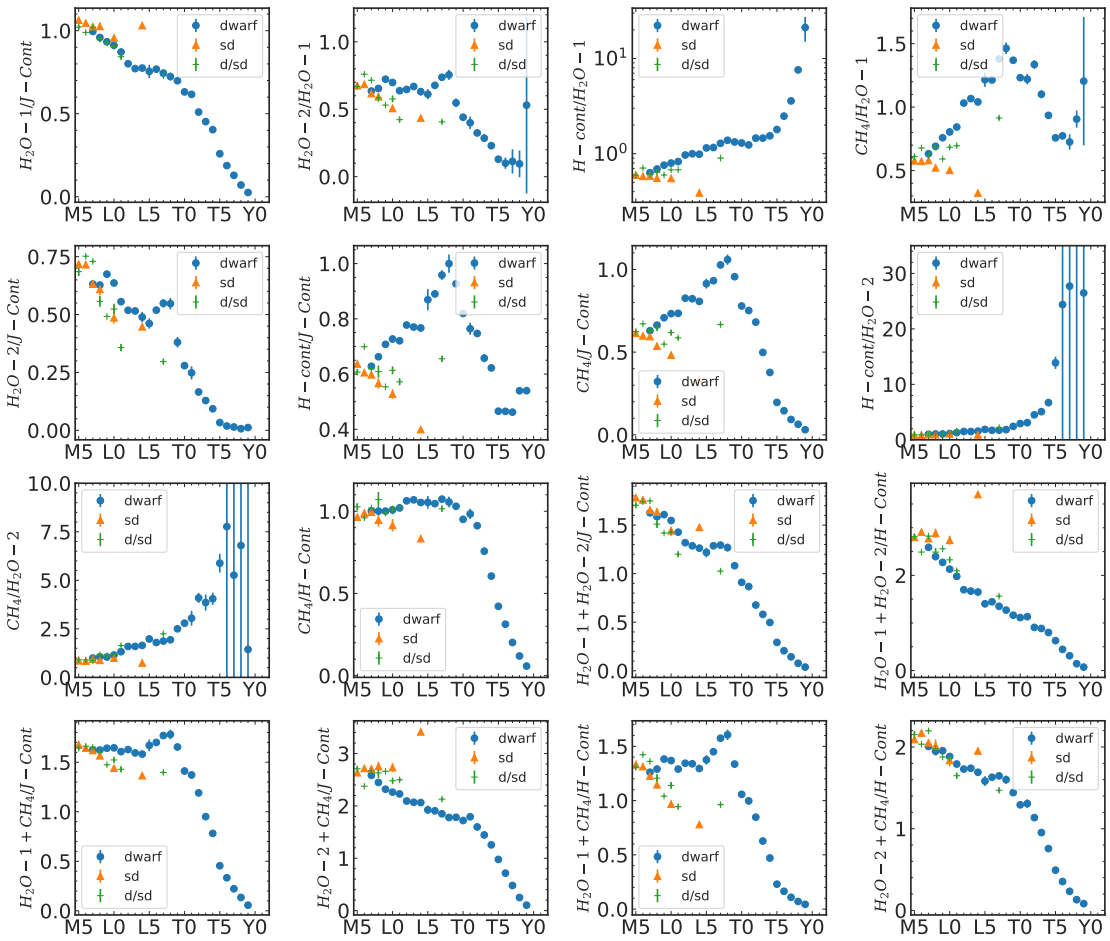

Figure 2.4 Spectral index values as a function of spectral type. Dwarf standards are indicated by blue dots, mild subdwarf (d/sd) standards by green crosses, and subdwarfs (sd) standards by orange triangles.

two statistical metrics measuring completeness (CP) and contamination (CT):

$$CP(SG,R) = \frac{N^*_{\rm T}(SG,R)}{N_{\rm T}(SG)} \tag{2.5}$$

,

$$CT(R) = \frac{N^*_{\rm WFC3}(R)}{N_{\rm WFC3}}. \tag{2.6}$$

In Equation (2.5), $N_{\rm T}(SG)$ is the total number of templates in subtype group SG, while $N^*_{\rm T}(SG,R)$ is the number of templates within an index-index selection region R; CP = 1 indicates selection of all templates. In Equation (2.6), $N_{\rm WFC3}$ is the total number of WFC3 spectra, while $N^*_{\rm WFC3}(R)$ is the number of these spectra within an index-index selection region R. As our expected number of UCD discoveries is assumed to be much smaller than $N_{\rm WFC3}$, a high selection rate of WFC3 spectra is consistent with a high level of contamination; CT $\ll 1$ indicates minimum contamination.

To maximize UCD selection (high CP) and minimize contamination (low CT) for each spectral subgroup, we rank-ordereded by CT those index-index pairs with CP ≥ 0.9, and chose the pair with the lowest contamination value; these are listed in Table 2.3. The best indices for each subtype group generally reflects the strongest molecular features present in those spectra. The greatest contamination was found in the selection regions for late-type M and early-type L dwarfs, and late-M/L subdwarfs, due to the relative weakness of molecular absorption features for these spectral types and hence greater similarity to background objects. Conversely, the late-type T and Y dwarf groups had the lowest contamination due to their distinct spectral morphologies.

Applying the single best index-index selection criteria to the sources that passed the prior cuts yielded 3,400 unique objects, primarily identified as late-M dwarfs and subdwarfs (Table 2.3). The subdwarf selection criterion appear to be most highly contaminated, as it identified 2,042 objects, while visual inspection ruled out the detection

of any unambiguous ultracool subdwarfs (Section 2.5.1).

Visual Selection After the preceding selection criteria were applied, we visually inspected the remaining spectra to confirm their UCD nature and spectral classifications. Keeping only those sources whose spectra were a clear visual match to an UCD spectral standard (including d/sd and sd subdwarf standards), we identified a total of 164 UCDs, provided as supplemental materials.

Retrospectively, we estimated the false positive rates (FP) for each subtype group as

$$FP(SG) = 1 - \frac{N^T_{WFC3}(SG)}{N^*_{WFC3}(SG)}, \tag{2.7}$$

where N^T_{WFC3} is the number of WFC3 spectra visually confirmed as UCDs. With the exception of the late-T and Y dwarfs, the best index selection criteria have FP values of nearly 100%, indicating significant contamination remains after these selection steps, although in terms of numbers these late-T and Y dwarfs only select < 15 objects each. Nevertheless, the cumulative selection process reduces the number of spectra requiring visual inspection by over 99%, and spot checks of the rejected sample indicate that few if any UCDs were missed by this process.

2.3.5 Selection by Random Forest Classifier

Despite a high completeness and a significant reduction in the contaminants with the spectral index selection, this methods selects more than 3,000 objects candidates for visual inspection. To further reduce this number, we explored a different selection: a random forest classifier. A random forest (Breiman, 2001) is a set of decision trees constructed on randomized samples of a dataset. A decision tree is model that recursively splits the sample into two parts until a pre-defined stopping criterion is reached. For example, if values of a feature j are $\{X_j\}$, the decision tree could split this dataset into

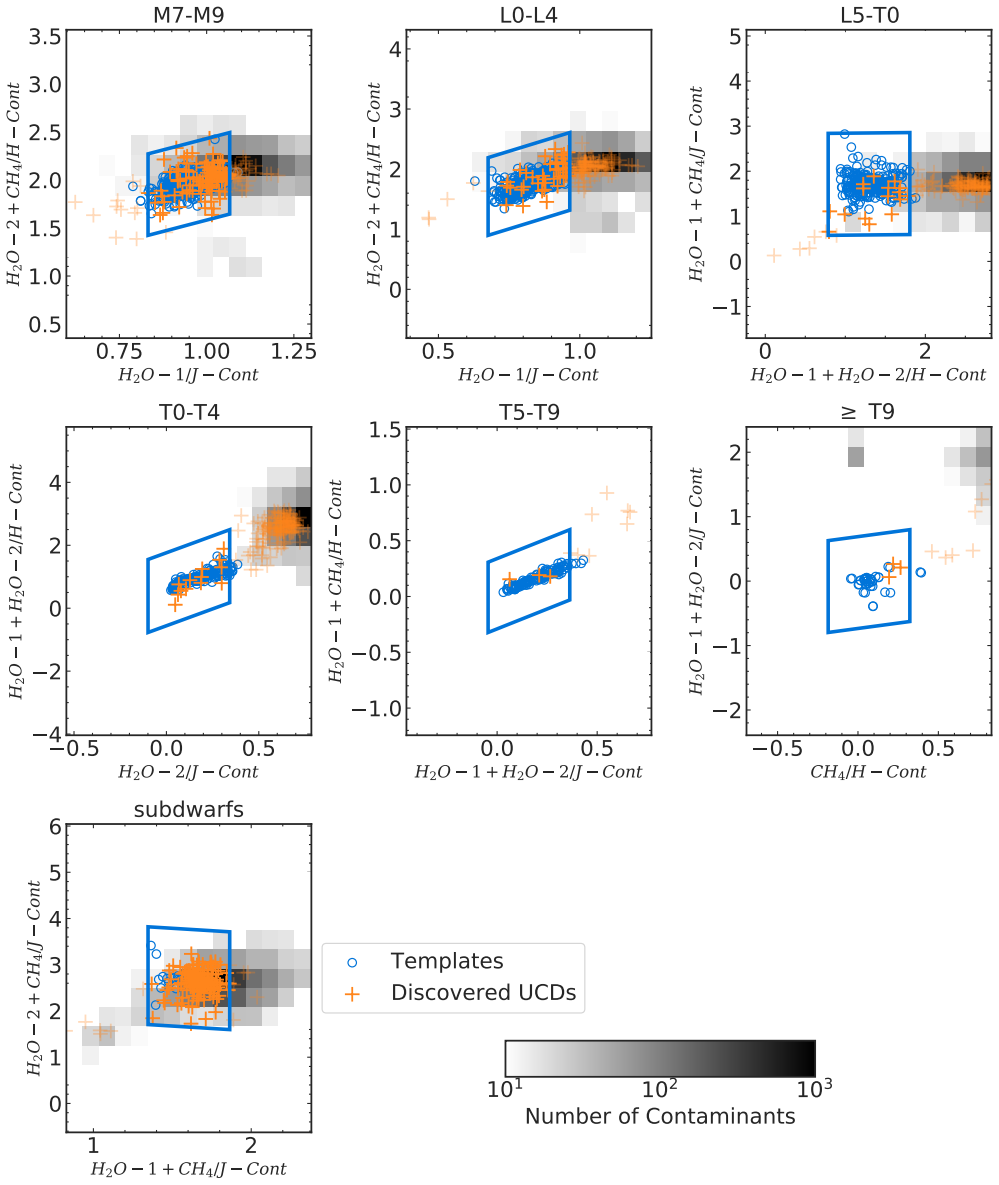

Figure 2.5 Optimal index-index selection regions for the subtype groups defined in this study. The shaded 2D histograms show the density of WISPS and 3D-HST point sources after applying both S/N and line-fit cuts. The blue circles are the appropriately-classified UCD spectral templates used to define the selection regions. The orange pluses are all visually-confirmed UCDs from the WISPS and 3D-HST samples.

two parts, $\{X|X_j < s\}$ and $\{X|X_j \geq s\}$, based on a threshold value s.

These steps are repeated on the new sub-spaces until a stopping criterion (e.g., minimum set size) is reached. For supervised classification, the optimal parameters for this tree (e.g., the stopping criterion, the structure of each tree) are chosen to minimize some pre-defined error function based on a set of pre-classified training data. Individual decision trees can be highly variant, since the final classifications at the end of the tree depends on where splits are made. Random forests seek to reduce this variance by using statistical methods such as bootstrap aggregation (Breiman, 1996).

The final classifications are determined by a majority vote of all of the decision trees. Random forests are a popular machine learning algorithm as they are fast, can be parallelized, and do not require large training datasets to be constructed. They have been used to reliably predict M dwarf subtypes based on photometric colors (Hardegree-Ullman et al., 2019), perform star-galaxy photometric classification in wide-field and transient surveys (Miller et al., 2017; Clarke et al., 2020), and conduct other photometric classification tasks (e.g., Richards et al., 2011; Dubath et al., 2011; Bloom et al., 2012; Brink et al., 2013). Random forests have also been used in a regression form to infer atmospheric parameters from brown dwarf and exoplanet spectra (Márquez-Neila et al., 2018; Oreshenko et al., 2020).

We used the `RandomForestClassifier` implementation of the random forest algorithm provided in the `scikit-learn` package (Pedregosa et al., 2011). Our pre-classified training data (all with J-SNR > 3) come from two sources: 3D-HST and WISPS spectra for non-UCD sources and the UCD template sample (Section 2.3.1). For the latter, we selected the 20 highest signal-to-noise spectra for each spectral subtype, smoothed and resampled these spectra to match the WFC3 resolution and wavelength range, and added Gaussian noise to encompass the range of J-SNR values present in the WFC3 dataset down to the J-SNR = 3 limit. The training data we organized into

five classes: a contaminants class composed of WFC3 spectra of non-point-sources and point-sources visually confirmed to not be UCDs (138,214 spectra total), M7–M9 dwarfs (4,686 spectra), L dwarfs (23,140 spectra), T dwarfs (13,479 spectra), Y dwarfs(12,871 spectra) and subdwarfs (14,977 spectra)

Choosing an appropriate set of features to classify a dataset is a critical design choice of any machine learning model. We used the five spectral indices and four signal-to-noise statistics defined in Section 2.3.2, the best-fit spectral type obtained from the spectral template fitting, and the F-test statistic comparing the template and line fits. In cases where features were not measurable due to small/zero denominators (common for noisy spectra), we assigned an extreme value of -99 to indicate missing data. The initial pre-classification dataset was shuffled and split into a training set (75%) and a testing set (25%) for constructing, optimizing, and evaluating the random forest model.

The parameters describing the random forest model (Table 2.5) were optimized using the randomized search cross-validation algorithm (Bergstra & Bengio, 2012). We used the K-fold cross-validation method in which the data is randomly split into K equally-sized sub-samples, the model is fit to $K-1$ of these sub-samples, and the model is then validated on the last sub-sample. The cross-validation algorithm conducts a random search over distributions of the tree parameters, weighting those with the smallest classification error highest. We assumed an initially uniform distribution of parameters, and utilized the default K = 5-fold cross-validation implemented in `RandomizedSearchCV`.

Classification error, and hence model convergence, was determined by evaluating four metrics[3] that compare the rates of true positives (TP), true negatives (TN), false positives (FP), and false negatives (FN):

$$\text{Accuracy} : Ac = (TP+TN)/(TN+TP+FN+FN) \tag{2.8}$$

[3]https://scikit-learn.org/stable/modules/model_evaluation.html

$$\text{Precision} : Pr = TP/(TP+FP) \tag{2.9}$$

$$\text{Recall} : Re = TP/(TP+FN) \tag{2.10}$$

$$\text{F}_1 \text{ Score} : F_1 = (Pr \times Re)/(Pr+Re) \tag{2.11}$$

These metrics were historically developed for information retrieval tasks in linguistics (Chinchor, 1992). Accuracy measures the model's ability to correctly classify all sources, both positive and negative classifications. Precision measures the model's ability to distinguish true positives from false positives. Recall measures the model's ability to correctly select members of a particular class, and the F_1 score combines the precision and recall measures. We computed these metrics for individual classes and averaged across classes. Our model was constructed in the Google Colab environment[4] (Carneiro et al., 2018). The final model was selected as the one with the highest F_1 score in order to minimize the false negative rate and maintain accuracy; its parameters are summarized in Table 2.4.

Figure 2.6 displays the "confusion matrix" of our random forest model, the matrix of true and false positives and negatives as determined by the test set. Our best model has an $>$97% accuracy score across all classes, but varies between classes (Table 2.5). The precision, recall, and F_1 scores are generally above 90% with the exception of M7–M9 class precision. In terms of performance, there is little confusion between UCD classes; the percentage of M7–M9, L dwarfs, and T dwarfs classified as another UCD class is below 1%. The primary loss in accuracy and precision stems from early M dwarfs ($< M7$) being classified as galaxies, likely due to their weak molecular features.

Figure 2.6 shows the distribution of feature importance among the features used for classification. Feature importance captures the sensitivity of classification to a particular feature by measuring the decrease in classification error due to splits on that

[4]https://colab.research.google.com/

feature. The most important feature is the classification spectral type from the standard template fits. However, this feature alone cannot distinguish between contaminants and UCD types. For example, low signal-to-noise contaminants with strong emission features (active galaxies) are often classified as T dwarfs. Features combining H_2O and continuum flux ratios therefore have high importance, as these are the highest S/N ratio features and enable segregation of UCDs and contaminants. The least important features tend to be those sampling the noisiest parts of the data; e.g., CH_4 and H_2O-2 indices.

In traditional RF models, the final classification of a source is based on the highest probability class across all decision trees in the random forest. To further reduce contamination, particularly in the M7–M9 dwarf class, we examined an alternative classification strategy in which classified UCDs were required to have classification probabilities >80%; all other sources were classified as contaminants. This 80% cutoff is determined from distribution the class probabilities for UCDs selected by the index method.

Table 2.5 shows that this additional classification criterion generally increases the precision of detecting UCDs, particularly for the M7–M9 class, while significantly reducing the recall. In effect, this criterion produces a trade-off between minimizing contamination and maximizing the recovery of true UCDs. Given the rarity of UCDs in the overall sample, we find this trade-off to be warranted, as it can be modeled out when evaluating the overall sample (Paper II).

Following the optimization of our model parameters, we built and trained a final random forest model using the entire pre-classified training set (with the 80% classification threshold), and applied it to the 46,561 WFC3 spectra of point sources with J-SNR > 3. In total, the random forest model classified 143 spectra as late-M, L, T or Y dwarfs including 2 objects identified as subdwarfs. Visual inspection confirmed 89 of these spectra as bona-fide UCDs. The random forest classifier did not select 72 with

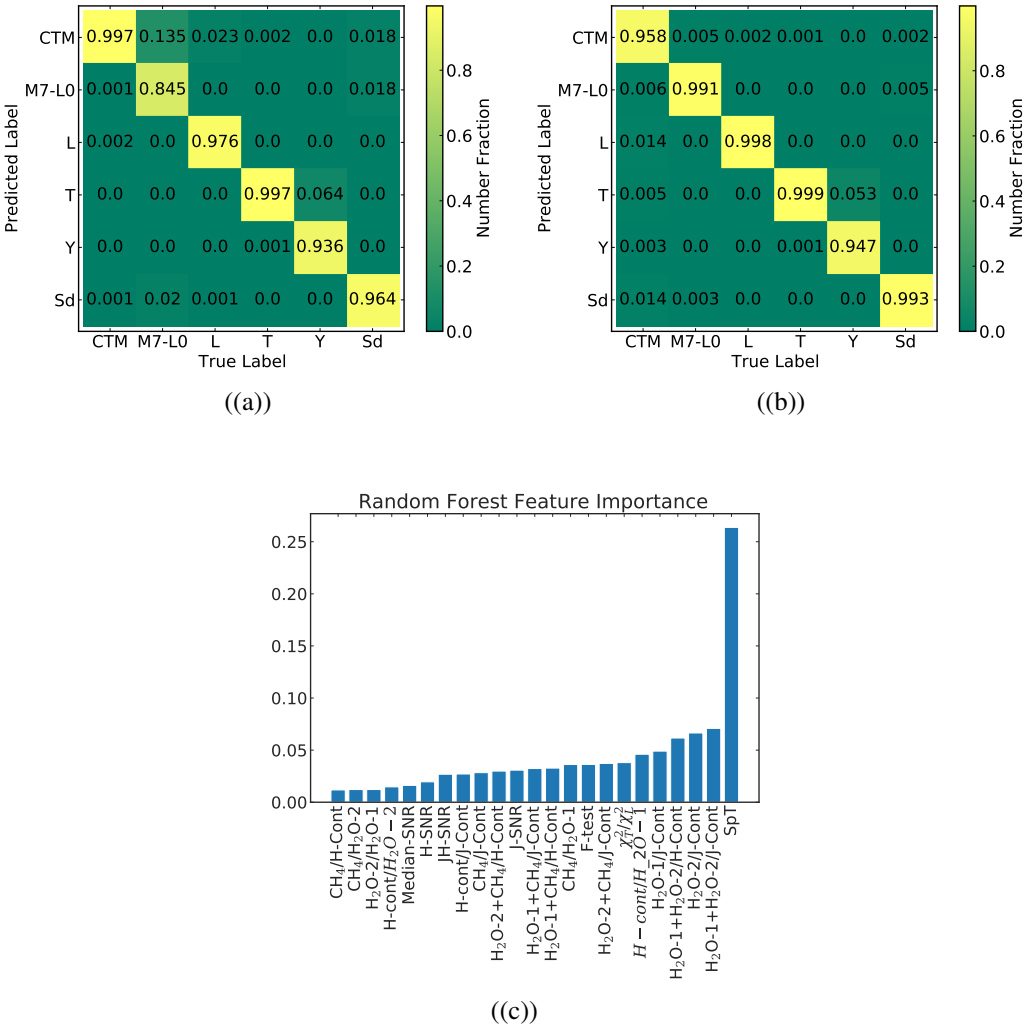

Figure 2.6 *Top*: Random forest confusion matrix based on the test set. Numbers along the diagonal indicate the number of correctly classified spectra (true positives), while off-diagonals indicate false positives and false negatives. Predicted labels/classes in (a) were determined as the label with the maximum probability, while labels in (b) were determined by requiring a minimum classification probability for M7–M9, L dwarf, and T dwarf classes. *Bottom*: Bar plot showing the relative feature importance for classification on the training set. Low-importance features tend sample the noisier regions of the spectra.

spectral types of M7–L8 previously selected by the index selection as they fall below the threshold classification probability of 80%. On the other hand, the random forest method identified one additional M7 UCDs that was missed by the index selection. While finding fewer UCDs overall compared to the visual index selection, this method (at 80% probability cutoff) provided a more than ten-fold reduction in contamination.

2.3.6 Selection by a Deep Neural Network

We explored a second machine learning classification approach using artificial neural networks (NNs; Schmidhuber 2014; LeCun et al. 2015; Shrestha & Mahmood 2019). Although the random forest method provided significant reduction in contamination, feed-forward artificial neural networks out-perform random forests in large-scale empirical studies (Caruana & Niculescu-Mizil, 2006). In the simplest design, a multi-layer, feed-forward NN with L hidden layers, each of dimensionality N, is a set of functions that transform an input vector $\vec{X}$ of dimensionality M into an output vector $f_k(\vec{X})$ of dimensionality K. Following the notation of Hastie et al. (2009), the set of transformations from $\vec{X}$ to $f_k(\vec{X})$ are given by

$$\vec{Z} = \sigma_0(\alpha \cdot \vec{X}), \tag{2.12}$$

$$\vec{A_1} = \sigma_1(\beta_1 \cdot \vec{Z}), \tag{2.13}$$

$$\vec{A_2} = \sigma_2(\beta_2 \cdot \vec{A_1}), \tag{2.14}$$

$$\vdots \tag{2.15}$$

$$f_k(\vec{X}) = g_k(\vec{A_L}). \tag{2.16}$$

Here, σ_0, σ_1, $\sigma_2 \ldots \sigma_L$, and g_k are scale functions also known as activation functions; while the matrices α of dimension $N \times M$ and β of dimension $K \times N$ are the neural network weights that linearly combine the various nodes between the layers. Train-

ing a neural network entails optimizing the neural network weights in order to minimize a classification convergence criterion $R(\theta)$ for a network model parameter set $\theta = \{\alpha, \beta_1, \beta_2, \ldots \beta_L, \vec{\Gamma}\}$, were $\vec{\Gamma}$ are design parameters for the network (Table 2.6). A convergence criterion commonly used is cross-entropy (Hastie et al. 2009),

$$R(\theta) = -\sum_{m=1}^{M}\sum_{k=1}^{K} Y_k \log f_k(X_m), \tag{2.17}$$

where Y_k represents the expected label for input variable $\vec{X}$. Minimizing $R(\theta)$ can be achieved numerically using a stochastic gradient descent algorithm (Kiefer & Wolfowitz, 1952).

While the mathematics behind NNs have been understood for decades, the recent emergence of large datasets in science and industry, and significant improvements in computational hardware, have contributed to their increased application in general and toward astrophysical problems in particular. Examples include the use of convolutional neural networks (CNNs) to model stellar properties based on lightcurves (Blancato et al., 2020), to predict galaxy spectra from their broad-band images (Wu & Peek, 2020), and to discover extra-solar planets (Shallue & Vanderburg, 2018); and the use of Generative Adverserial Networks (GANs) to extract features from noisy galaxy images (Schawinski et al., 2017). Baron (2019) provides a review of machine learning applications, including NNs, in astronomy.

To train our NN, we used the same features and pre-classified training set as the random forest classifier. Our neural network model is a simple Deep Neural Network (DNN) consisting of a series of fully-connected layers (see Figure 2.7), implemented using the `Keras` library (Chollet et al., 2015). To converge to optimal parameters, we use Adaptive Moment Estimation (Adam, Kingma & Ba 2014), a type of gradient descent algorithm. We used two forms of activation functions; for the input and hidden layers we

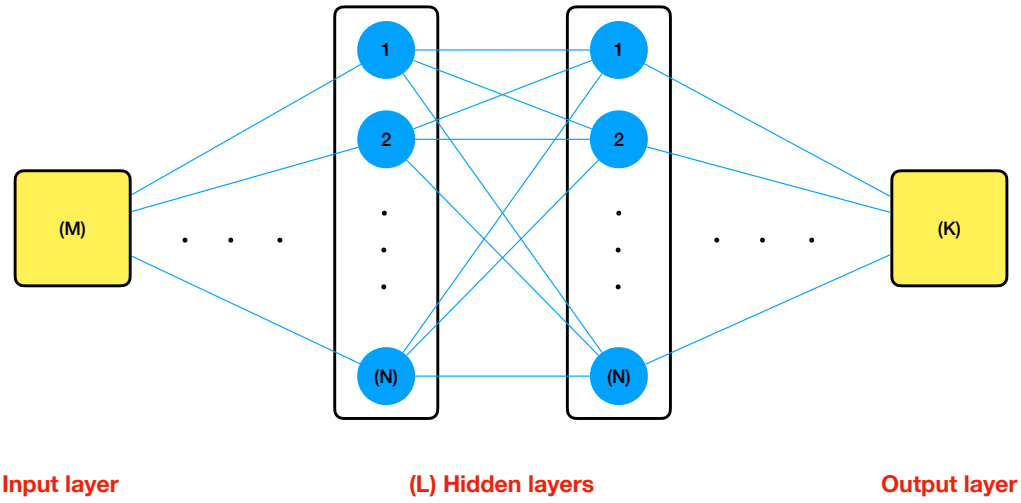

Figure 2.7 Schematic illustrating the DNN architecture used on this work. We summarize the model properties in Table 2.6

used the rectified linear unit (ReLU, Nair & Hinton (2010)) given by

$$\sigma(\vec{X})_i = \max(0, X_i), \tag{2.18}$$

while for the output layer we used the normalized exponential function (softmax) given by

$$\sigma(\vec{X})_i = \frac{e^{X_i}}{\sum_{j=1}^{M} e^{X_j}}. \tag{2.19}$$

The number of layers and nodes for the input and hidden layers are left as parameters to be determined through optimization.

To find the optimal parameters for the DNN model, we split our pre-classified spectral data into a training set, a validation set, and a test set with proportions of 40%, 40%, and 20%. The training and validation sets are used to find and train the best model, while the test set is used to evaluate the network performance on new data. We used a

random search algorithm to optimize the model parameters listed in Table 2.6. We varied the number of nodes N in each of the input and hidden layers, as well as the learning rate (η), which is a scale factor used to update model parameters from (θ) to (θ').

The parameter optimization was done on data samples (batches) of 300 spectra for each training epoch. We evaluated the same four performance metrics as used for the random forest (accuracy, precision, recall, and F_1 score), as well as cross-entropy, which was used to optimize the performance of the DNN model. As shown in Figure 2.8, model convergence as traced by the performance metrics occurs within 150 update cycles. Our best-performing model has $L = 6$ hidden layers of $N = 64$ nodes each, for a total of 118,085 trainable weights. Analysis of the test set indicates an overall accuracy, precision, recall, and F_1 score of $\sim 98\%$ (Table 2.7).

After re-building the DNN model from the optimal parameters and training it with the full pre-classified training set, we determined class probabilities for each of the six classes—contaminants, M7–M9 dwarfs, L dwarfs, T dwarfs, Y dwarfs, and subdwarfs—for the full WFC3 spectral sample. To reduce the number of false positives, we again imposed a classification probability threshold of $>80\%$ on the UCD classes. Figure 2.9 displays the probability distribution of point sources in the full WFC3 spectral sample. We identified a total of 537 UCD candidates including 158 objects classified as subdwarfs, of which 128 were visually confirmed. Like the random forest classifier, the DNN classifier provided a substantial reduction in contamination, but missed 36 UCDs identified by the index selection. On the other hand, the DNN classifier identified 3 additional UCDs (with spectral types of M7-M8) that were missed by the other two methods.

Combining the outcomes of all three selection methods, we identified 164 unique UCDs in the 3D-HST and WISPS surveys, listed in supplemental Tables and subdivided into half-class subgroups in Table 2.8. Field images, 2D, and 1D spectra are shown

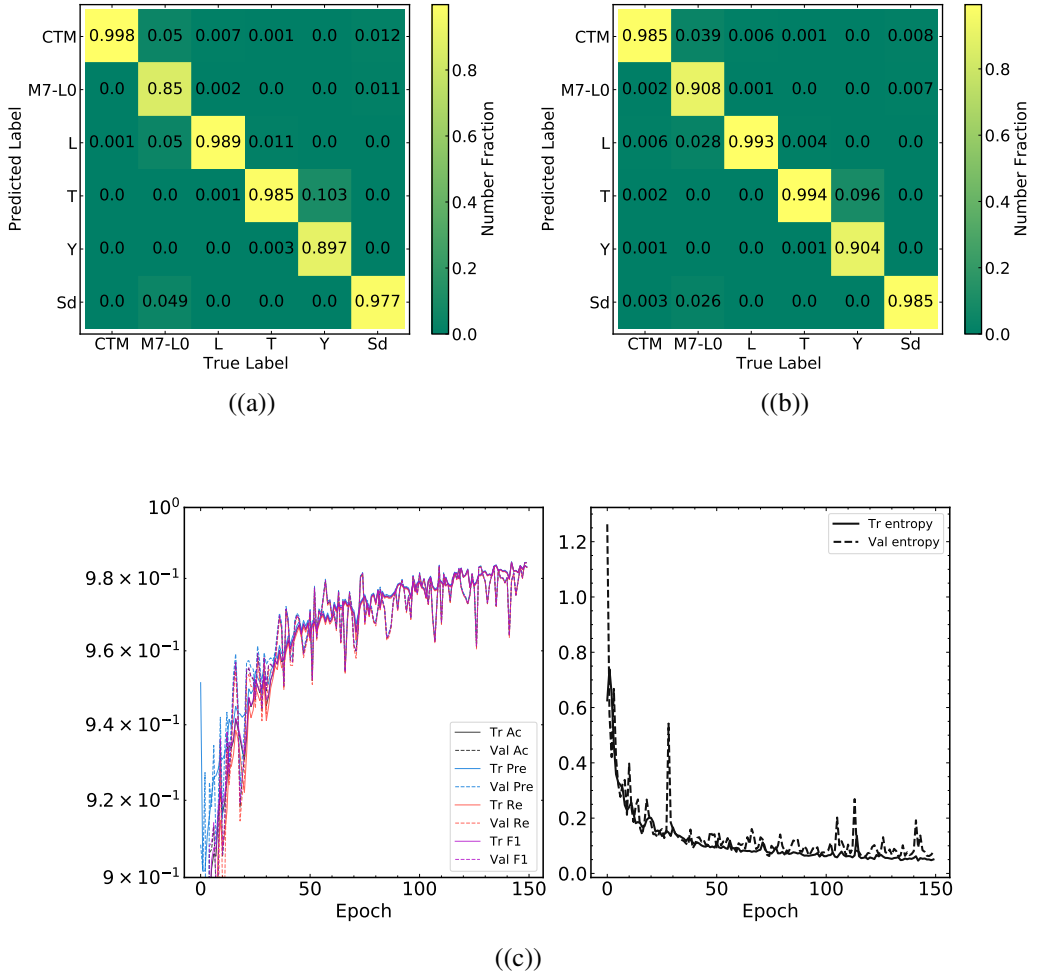

Figure 2.8 *Top*: Confusion matrix for the DNN showing the performance on the test set. Predicted labels in (a) are computed from the maximum probability, while labels (b) are computed by first making our selection cuts and then computing the maximum probability. Here, objects classified as <M7 and/or not satisfying our selection cuts are labelled as contaminants. *Bottom*: DNN performance metrics of accuracy (Ac), precision (Pre), recall (Re), cross-entropy, and F_1 on the training and validation sets. We achieve high performance after roughly 120 epochs. Beyond 120 epochs, the performance on validation set and training set start to deviate.

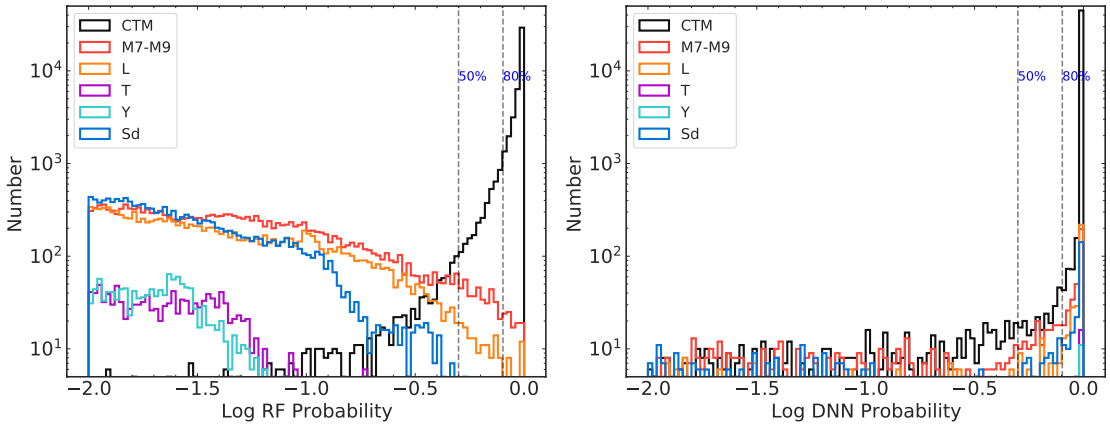

Figure 2.9 Log probability distributions of the random forest and neural network on the prediction set for each class. We also mark the 50% and 80% cutoff as dashed lines. The majority of sources have low probabilities of being UCDs and high probabilities of being contaminants

in Figure 2.14. While each method selected roughly the same number of UCDs, the index-selection method had over 10 times the number of contaminants compared to the random forest classifier and over 5 times the number of contaminants compared to the DNN classifier. The contamination rate was largely reduced by the application of a classification probability threshold, which cannot be equivalently computed for the index selection method. In total, we found 113 UCDs in the WISPS fields and 51 UCDs in 3D-HST.

2.4 Sample Characterization

2.4.1 Spectral Classifications

Classifications for our targets are based on comparisons to spectral standards using the method described in Section 2.3.2. We used the best-fit matches to determine the spectral types. Classification uncertainties were estimated using a weighted standard deviation, with weights computed from the F-test cumulative density distribution

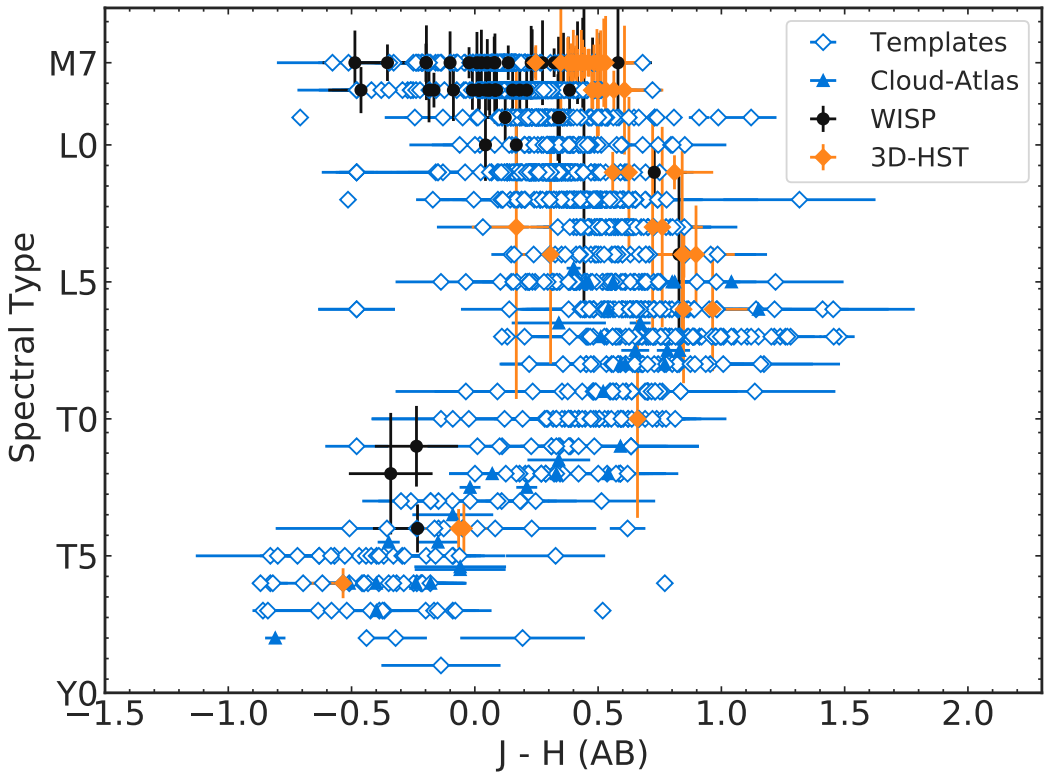

Figure 2.10 $J-H$ colors of UCDs in WISPS (black circles) and 3D-HST (orange diamonds) as a function of spectral type. These are compared to colors of sources in our template sample (blue diamonds) and from sources in Cloud-Atlas sample (Manjavacas et al. 2017; blue triangles)

$W_i = F(\chi^2_{T,i}/\min(\{\chi^2_T\}), DOF, DOF)$, with χ^2_T defined in equation (2.1). The median classification uncertainty is 1.4 subtypes, but varies between 0.5 and 9 subtypes. The largest classification uncertainties arise from the lowest S/N spectra, particularly for M-type UCDs. Figure 2.12 displays the distribution of spectral types, showing that our sample is heavily weighted toward late-M dwarfs (128 sources), as expected given their relatively bright intrinsic magnitudes and corresponding larger volumes sampled in this magnitude-limited survey. We identified 26 L dwarfs (primarily L0–L4) and 10 T dwarfs, but no Y dwarfs or subdwarfs.

2.4.2 Color-Spectral Type and Absolute Magnitude-Spectral Type Relations

All of the sources identified in the WISPS and 3D-HST surveys have apparent F110W, F140W, or F160W magnitudes from imaging data, which can be used in conjunction with source classifications to estimate distances. We determined new absolute magnitude/spectral type relations for M5–Y2 dwarfs in the F110W, F140W and F160W filters by bootstrapping to the 2MASS J- and H-band relations of Pecaut & Mamajek (2013). For T7-Y2 dwarfs, we shifted to the absolute H magnitude/spectral type relation of Kirkpatrick et al. (2021).

We first computed color offsets between 2MASS (Vega magnitudes) and *HST*/WFC3 photometry (AB magnitudes) by computing spectrophotometric colors from our UCD template sample (Section 2.3.1). To assure fidelity, we selected only those M5–T9 dwarfs with precise ($\leqslant$1 subtype uncertainty) red optical (late-M and L dwarfs) or infrared (late-L and T dwarfs) classifications; small 2MASS J- and H-band magnitude uncertainties ($\sigma < 0.4$); and spectra with median S/N $>$ 100 for M dwarfs, S/N $>$ 70 for L dwarfs, and S/N $>$ 10 for T dwarfs. We also included all of the Y dwarfs from the template sample, and removed known binaries.

Magnitudes were computed by convolving the spectra with the appropriate filter profiles (*HST*[5]) or response functions (2MASS; Cohen et al. 1992), and uncertainties in spectral fluxes were propagated by random sampling. Figure 2.11 shows the resulting color offsets as a function of spectral type. Variations in color offsets are largest when the 2MASS and *HST* filters are more widely separated, reflecting the substantial evolution in spectral morphology across UCD spectral classes. We chose those colors that minimized spectral type variation, and hence bootstrapped the F110W and F140W relations to J-band and the F160W relation to H-band. Adding the relevant correction for each individual

[5]https://www.stsci.edu/hst/instrumentation/wfc3/performance/throughputs

source to its absolute 2MASS magnitude from the absolute magnitude relation, we fit the entire spectral sequence with a 6th-order polynomial using least-squares fitting, masking sources that were more than 5σ outliers. Fit coefficients and corresponding absolute magnitude uncertainties are listed in Table 3.9. The scatter in these absolute magnitude relations is approximately 0.4–0.6 mag, comparable to other absolute magnitude/spectral type relations (e.g., Dupuy & Liu, 2012; Best et al., 2018).

The 2MASS colors of UCDs compared to colors of UCDs in our calibration samples are shown in Figure 2.10. These colors are computed using our relations in Table 3.9 and incorporating the intrinsic scatter in these relations. They tend to generally follow the trend from our calibration samples. However, objects with fairly large uncertainties in subtyping are offset from the general trend.

2.5 Distances and Galactic Coordinates

Distance estimates were computed for each source based on the relations in Table 3.9 and measured *HST*/WFC3 photometry. We assume for simplicity that all sources are single, although magnitude-limited surveys of ultracool dwarfs typically have a $\sim$20% multiplicity rate (Bouy et al., 2003; Burgasser et al., 2003, 2006b; Fontanive et al., 2018). Uncertainties in spectral classifications, source photometry, and the absolute magnitude relations were propagated by random sampling. In cases where more than one distance estimate was available from the absolute magnitude relations, we computed an uncertainty-weighted average. The distance of our UCD discoveries range over 60–3000 pc for late-M dwarfs, 40–2000 pc for L dwarfs, and 82–800 pc for T dwarfs (Figure 2.12). The most distant UCD with $< 50\%$ distance uncertainty is the M7$\pm$1 J23450092-4239288 at a distance of 2.1 ± 0.8 kpc; the closest is the L1.0$\pm$0.7 J09275744+6027467 at a distance of 48 ± 11 pc. J09275744+6027467 is also detected in

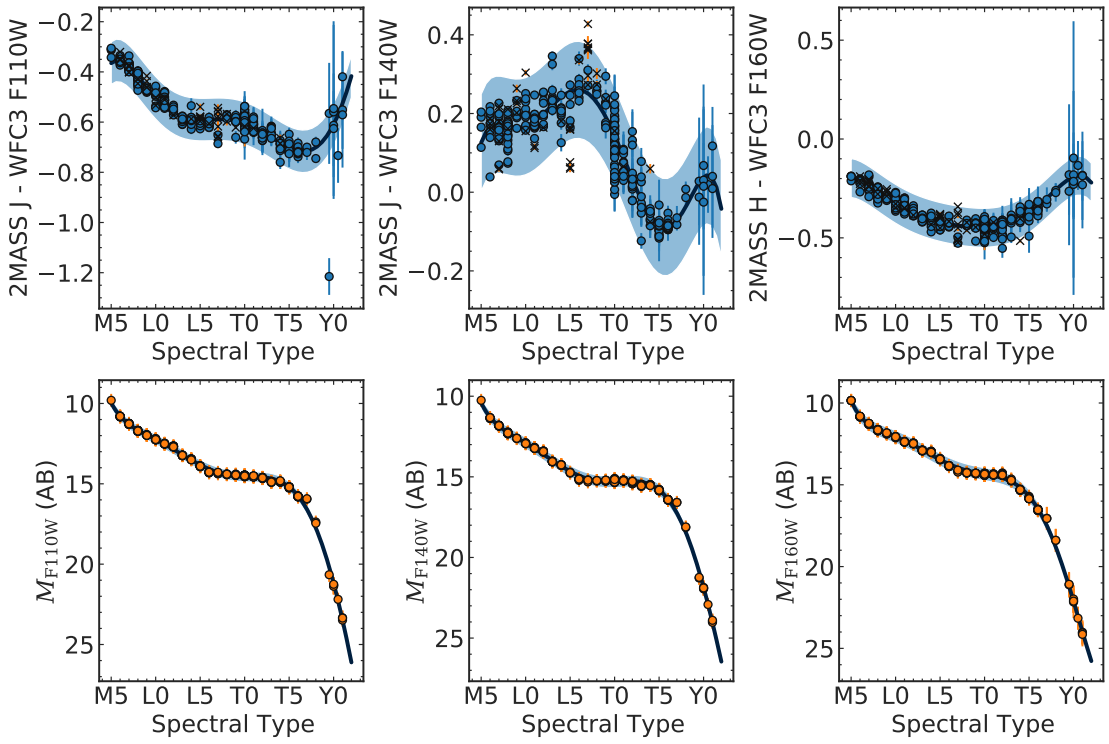

Figure 2.11 *Top*: Offsets between 2MASS *J*- and *H*-band magnitudes and *HST*/WFC3 F110W, F140W and F160W magnitudes as a function of spectral type, based on spectrophotometry of spectral templates. *Bottom*: Derived absolute magnitude-spectral type relations for *HST* filters. Orange points show relations bootstrapped to 2MASS *J*-band photometry, blue points show relations bootstrapped to 2MASS *H*-band photometry. The solid lines delineate the 6th-order polynomials whose coefficients are listed in Table 3.9.

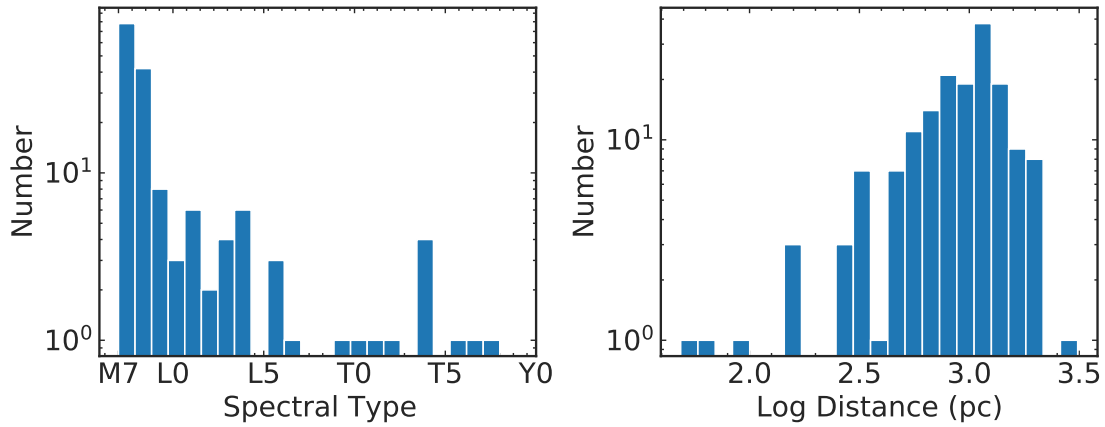

Figure 2.12 Spectral type and distance distributions of UCDs in the WISPS and 3D-HST surveys. (Left panel): Distribution of spectral types based on the spectral template fits. (Right panel); Distribution of spectrophotometric distances. The sample is dominated by late M dwarfs at distances $\gtrsim$ 1 kpc.

Gaia at parallax of 19.497±0.567 mas putting it at a distance of 51.4±1.5 pc, consistent with our estimate.

Figure 2.13 displays the distribution of source Galactic angular and spatial coordinates[6]. The angular distribution of the UCDs follows the *HST* pointings, with more sources identified in Galactic northern fields where there are more pointings. The average surface density of objects is 0.0813 arcmin^{-2} at low Galactic latitudes ($15^\circ \leq |b| \leq 30^\circ$), 0.0801 arcmin^{-2} at intermediate Galactic latitudes ($30^\circ \leq |b| \leq 60^\circ$), and 0.0625 arcmin^{-2} at high Galactic latitudes ($|b| \geq 60^\circ$). We observe 38 objects with $|Z| > 1$ kpc compared to 126 objects with $|Z| \leq 1$ kpc in the sample.

[6]We assume a right-handed, heliocentric Cartesian galactic coordinate system (X,Y,Z), where X points towards the Galactic center $(l,b) = (0^\circ,0^\circ)$, Y points in the direction of Galactic rotation ($l = 90^\circ$), and Z points towards the North Galactic Pole ($b = 90^\circ$). For cylindrical coordinates (R,Z), we assume R to be galactocentric, with the Sun located at $R_\odot$ = 8300 pc and $Z_\odot$ = 27 pc (Gillessen et al., 2009; Chen et al., 2001).

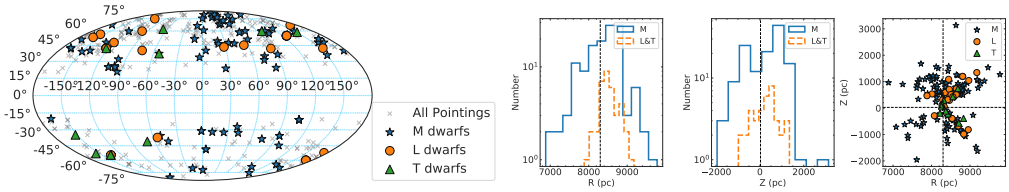

((a)) ((b))

Figure 2.13 *Top panel*: Distribution of observed UCDs in galactic angular coordinates (l,b). Grey X symbols indicate *HST* pointings without any UCDs. *Bottom panel*: Distribution of observed UCDs in cylindrical galactic coordinates $(R,Z$; left and middle) and scatter plot of (right) these coordinates. Sources are color-coded according to spectral type. Later-type UCDs are concentrated around the Solar neighborhood while earlier-type M dwarfs are located further into the Galactic disk.

2.5.1 Detailed Discussion of Sample UCDs

Late-M dwarfs We identified 128 sources with estimated spectral types of M7 $\leq$ SpT $<$ L0. Most of these classifications are robust, in that the major H_2O absorption feature between 1.3–1.45 μ m is clearly distinguishable from noise. For many of the WISPS spectra, we were able to confirm classification with additional G102 grism spectra (0.8–1.15 μ m) which encompasses additional H_2O, FeH, and TiO absorption features characteristic of M dwarf spectra. As the G102 and G141 spectra sample distinct, non-overlapping wavelength ranges, we were unable to converge on a correct scaling to merge these spectra, so we retain the classifications based on the G141 spectra alone. We visually inspected all source images to confirm our UCDs are point sources unblended with other sources in the field, although a handful of sources with misaligned imaging data prevented this verification[7].

One notable late-M dwarf discovery is the M8$\pm$1.5 dwarf WISPS J2333+3921, which appears to have stronger H_2O bands compared to its best-fit standard, which may be a signature of subsolar metallicity (Aganze et al., 2016). WISPS J2333+3921 G141

[7]These sources were GOODSS J0332$-$2749, COSMOS J1000+0227, GOODSN J1237+6210, WISPS J2005$-$4139, WISPS J2038$-$2021, and WISPS J2248$-$8011.

spectrum is better fit to a d/sd M9 standard despite its weaker FeH in the G102 spectrum. We also note that M7±2 dwarf WISPS J1242+3538, located at a distance just over 3 kpc, is very close to an adjacent bright source, and its spectrum may be partly contaminated. The closest M dwarf is M8±1 WISPS J2333+3925 at a distance of 67±17 pc also detected in Gaia at a parallax of 19.498±0.567 mas putting at at 50.5±0.5 pc, and a high proper motion (μ_α, μ_δ) of (389.688±0.203, -60.328±0.178) mas/yr.

L Dwarfs We identified 26 L dwarfs, nearly half of which (12 sources) have classifications between L0–L2, however, the fraction of sources per subtype throughout L0–L4 is nearly constant. Note that given the classification uncertainties, some of the earliest-type L dwarfs may be late M dwarfs, and similarly several classified late M dwarfs could be early L dwarfs. Most of these spectra are well-matched to the L dwarf spectral standards, and several are confirmed by additional G102 grism data. This sample contains a relatively nearby L2±1.1 dwarf, WISPS J0927+6027 at a distance of 48±11 pc, which is sufficiently bright ($F140W$ = 16.697±0.001) that it is amenable for further ground-based follow-up. The Gaia parallax of this object puts it a 51.4±1.5 pc and Gaia proper motion (μ_α, μ_δ) of (-6.780±0.550, 28.435±0.544) mas/yr.

T dwarfs T dwarfs are readily distinguished from other sources by their strong H_2O and CH_4 absorption features. We identified 10 T dwarfs which match well with spectral templates. These include the three T dwarfs previously identified in WISPS by Masters et al. (2012): WISPS J0307-7243 (T4±0.5 at ∼320 pc), WISP J1232-0033 (T7±.9 at ∼150 pc), and WISPS J1305-2538 (T8±0.7 at ∼80 pc); and AEGIS J1418+5242 (T4 at ∼330 pc), first identified in 3D-HST data by Brammer et al. (2012). One of the early T dwarf discoveries, WISP J0326−1643 (T1±1.4 at 740 pc), is also closely aligned with a brighter source, although its spectrum is a good fit to standards.

Ultracool Subdwarfs & Y dwarfs Despite creating specific selection criteria, we did not identify any obvious Y-type dwarfs or metal-poor subdwarfs in our sample. The lack of Y dwarfs is likely a consequence of the relatively small volume sampled for these intrinsically faint brown dwarfs. The lack of subdwarfs may be due to their low abundance and selection biases. In Paper II, we estimate an expected number of Y dwarfs in these samples to be <1. Ultracool subdwarfs are known to exist in the Solar Neighborhood (Burgasser et al., 2003; Zhang et al., 2019; Schneider et al., 2020), but are rare compared to solar-metallicity disk dwarfs ($\sim$0.25% in the Solar Neighborhood; Pirzkal et al. 2009). However, subdwarf members of the halo and thick disk populations should be more common at the larger distances probed by this survey (cf., Ryan & Reid 2016). Lodieu et al. (2017) measured a surface density of $\geq$M5 subdwarfs of 0.04 deg^{-2} to a depth of J = 18.8. For an average limiting depth of $F110W = 22$ this corresponds to $\approx$ 16 deg^{-2}, or roughly 10 $\geq$M5 subdwarfs over our total search area of $\approx$ 0.6 deg^2. Nevertheless, no subdwarfs were identified by our index selection, random forest classifier, or DNN classifier. There are several possible reasons that these sources were missing. First, subsolar metallicity is known to suppress the strength of molecular features, notably H_2O, in the near-infrared spectra of UCDs, largely through the presence of enhanced collision-induced H_2 absorption (Linsky, 1969; Burgasser et al., 2007; Zhang et al., 2017). Relatively featureless late-M subdwarf spectra would have been rejected by our line fitting test, while more structured L subdwarf spectra would have been exceedingly rare in our sample. In Paper II, we model the full selection function of our selection methods applied to our calibration samples. Thus, a measurement of the density and distribution of ultracool subdwarfs likely requires the inclusion of the shorter-wavelength red optical data to capture characteristic features in this region (e.g., red optical slope and TiO, VO, FeH, and CrH bands), but the data remains incomplete for these short wavelengths.

Table 2.1 Spectral Indices

Band	Wavelength Range (μ m)
J-Cont	1.15–1.20
H_2O-1	1.246–1.295
H_2O-2	1.38–1.43
H-Cont	1.56–1.61
CH_4	1.62–1.67

2.6 UCD Discovery Images and Spectra

This figure set displays the *HST*/WFC3 images and spectra for the 164 UCD discoveries reported in this study, sorted by Right Ascension. Each panel shows the *HST*/WFC3 image of the source in either $F140W$, $F160W$ or $F110W$ filters (top left); the 2D G141 grism image centered of the source (top right); and the extracted 1D spectrum and its uncertainty (black lines), compared to its closest-match spectral standard (yellow line), with estimated contamination contributions (blue lines) and regions sampled by spectral indices (grey bands) highlighted (bottom).

Table 2.2 Absolute magnitude and color vs spectral type relations used in this work.

x	y	rms	c6	c5	c4	c3	c2	c1	c0
SpT[a]	WFC3 M_{F110W}	0.32	-1.02260887E-06	1.78936774E-04	-1.25922122E-02	4.57612828E-01	-9.0880526E+005	9.41111020E+01	-3.88061925E+02
SpT	WFC3 M_{F140W}	0.37	-1.26911098E-06	2.18686594E-04	-1.51959378E-02	5.46285038E-01	-1.07472467E+01	1.10362962E+02	4.52949443E+02
SpT	WFC3 M_{F160W}	0.40	-1.47948519E-06	2.52178047E-04	-1.74232042e-02	6.25600790E-01	-1.23318793E+01	1.26978487E+02	-5.24118111E+02
SpT	2MASS J - F110W	0.084	-8.51745562E-08	1.56700496E-05	-1.16134203E-03	4.43613741E-02	-9.19918196E-01	9.78676767E+00	-4.20410372E+01
SpT	2MASS J - F140W	0.12	-2.36588003E-07	3.91245500E-05	-2.62006105E-03	9.08427011E-02	-1.7201058E+00	1.68859410E+01	-6.70968425E+01
SpT	2MASS H- F160W	0.097	-7.35527084e-08	1.20431676E-05	-8.06167351E-04	2.8249569E-02	-5.45254603E-01	5.45750570E+00	-2.22166138E+01

[a] Decimal spectral type, with 10 = M0, 20 = L0, 30 = T0, etc.
[b] Empirical relations are computed as $y = \sum_{n=1}^{m} c_n x^n$ where m is the power of the polynomial. Coefficients are written in decimal exponent notation.

Table 2.3 Selection Criteria

SpT Range	X-axis	Y-axis	v1	v2	v3	v4	CP	CT	FP
M7–M9	H_2O-1/J-Cont	H_2O-2+CH_4/H-Cont	(0.83, 2.27)	(1.07, 2.49)	(1.07, 1.65)	(0.83, 1.42)	0.99	0.164	0.890
L0–L4	H_2O-1/J-Cont	H_2O-2+CH_4/H-Cont	(0.68, 2.19)	(0.96, 2.61)	(0.96, 1.32)	(0.68, 0.9)	1.0	0.070	0.903
L5–L9	H_2O-1+H_2O-2/H-Cont	H_2O-1+CH_4/J-Cont	(0.79, 2.84)	(1.81, 2.86)	(1.81, 0.6)	(0.79, 0.58)	1.0	0.037	0.928
T0–T4	H_2O-2/J-Cont	H_2O-1+H_2O-2/H-Cont	(-0.1, 1.55)	(0.34, 2.5)	(0.34, 0.18)	(-0.1, -0.77)	1.0	0.013	0.831
T5–T9	H_2O-1+H_2O-2/J-Cont	H_2O-1+CH_4/H-Cont	(-0.04, 0.31)	(0.36, 0.6)	(0.36, -0.03)	(-0.04, -0.32)	1.0	0.0007	0.25
Y dwarfs	CH_4/H-Cont	H_2O-1+H_2O-2/J-Cont	(-0.19, 0.63)	(0.32, 0.8)	(0.32, -0.63)	(-0.19, -0.8)	0.95	0.0007	0.25
subdwarfs	H_2O-1+CH_4/J-Cont	H_2O-2+CH_4/J-Cont	(1.35, 3.82)	(1.86, 3.71)	(1.86, 1.6)	(1.35, 1.71)	1.0	0.503	1.0

[a] v1-v4 denote the (x, y) positions of the vertices of the selection box for the given index-index pair; CP, CT, and FP are the completeness, contamination, and false positive rates defined in Equations 2.5, 2.6 & 2.7.

Table 2.4 Random Forest Model Parameters

Parameter[a]	Description	Best value
`class_weight`	Weight of each class	balanced
`bootstrap`	Using bootstrap samples[b]	True
`oob_score`	Using out-of-the-bag samples to compute accuracy[b]	False
`n_estimators`	Number of trees	947
`min_impurity_split`	Minimum value of classification error to split the tree node on	1.2E-8
`max_leaf_nodes`	The maximum number of nodes for each leaf	526
`max_depth`	Maximum depth of a tree	889
`min_samples_split`	Minimum number of objects needed to split on an internal node	53
`criterion`	Measure of the quality of the split (node purity) on each tree	entropy[c]

[a] Parameter name in the scikit-learn `RandomForestClassifier` object

[b] Bootstrapping was done by splitting the training set into two randomly-assigned 50% partitions, training the random forest on one partition, and using this to classify the second partition (see for example Miller et al. 2017). Out-of-the-bag (OOB) samples are the data that were not used when fitting a tree to the bootstrapped samples

[c] The entropy is defined as $-\sum_{k=1}^{K} p_{mk} \log p_{mk}$, where p_{mk} is the proportion of k-class objects classified m-class, where $K = 5$ is the total number of classes.

Table 2.5 Random Forest Metrics on Test Set

Class	Accuracy	Precision	Recall	F_1	TP	FP	TN	FN	Sample
Contaminants	0.991	0.997	0.989	0.993	34304	101	17055	382	34686
M7–M9	0.994	0.845	0.918	0.880	1067	196	50484	95	1162
L	0.996	0.976	0.990	0.983	5666	141	45978	57	5723
T	0.996	0.997	0.933	0.964	3084	8	48528	222	3306
Y	0.996	0.936	0.999	0.966	3192	220	48428	2	3194
Sd	0.996	0.964	0.988	0.976	3724	139	47932	47	3771
Classification Probability >80%[b]									
Contaminants	0.970	0.958	0.999	0.978	34662	1526	15630	24	34686
M7–M9	0.995	0.991	0.799	0.885	929	8	50672	233	1162
L	0.990	0.998	0.910	0.952	5206	12	46107	517	5723
T	0.993	0.999	0.896	0.944	2961	4	48532	345	3306
Y	0.995	0.947	0.967	0.957	3090.000	172	48476	104	3194
Sd	0.990	0.993	0.862	0.923	3250.000	22	48049	521	3771

[a] Predicted class is based on the highest probability class for that particular object.

[b] Predicted class must have a >80% classification probability; sources that do not satisfy this constrained are classified as contaminants.

Table 2.6 Deep Neural Network Model Parameters

Parameter	Description	Parameter range	Best value
L	Number of layers	(1, 10)	10
N	Number of nodes per layer	(1, 640)	348
η	Learning rate	0.1, 0.01, 0.001, and 0.0001	0.0001
⋯	Batch size	⋯	300
⋯	train, validation, test split	⋯	0.4, 0.4, 0.2

Table 2.7 Deep Neural Network Metrics on the Test Set

Class	Accuracy	Precision	Recall	F_1	TP	FP	TN	FN	Sample
Contaminants	0.996	0.998	0.996	0.997	27594	62	13696	122	27716
M7-M9	0.944	0.850	0.944	0.895	876	154	40392	52	928
L	0.975	0.989	0.975	0.982	4532	49	36778	115	4647
T	0.886	0.985	0.886	0.933	2359	36	38776	303	2662
Y	0.997	0.897	0.997	0.944	2584	297	38585	8	2592
Sd	0.978	0.977	0.978	0.977	2864	67	38478	65	2929
Classification Probability >80%[b]									
Contaminants	0.997	0.985	0.997	0.991	27630	411	13347	86	27716
M7-M9	0.913	0.908	0.913	0.910	847	86	40460	81	928
L	0.954	0.993	0.954	0.973	4431	33	36794	216	4647
T	0.875	0.994	0.875	0.931	2329	14	38798	333	2662
Y	0.990	0.904	0.990	0.945	2565	273	38609	27	2592
Sd	0.960	0.985	0.960	0.973	2813	42	38503	116	2929

[a] Predicted class is based on the highest probability class for that particular object.
[b] Predicted class must have a >80% classification probability; sources that do not satisfy this constrained are classified as contaminants.

Table 2.8 Number of UCDs Identified in the 3D-HST and WISPS Surveys

	Initial	Visually Confirmed					
Selection		M7–M9	L0–L4	L5–L9	T0–T4	T5–T9	Total
Index Selection	3,400	125	21	5	7	3	161
Random Forest (80%)	143	62	13	4	7	3	89
Deep Neural Network (80%)	537	101	15	4	7	3	128
Random Forest (50%)	550	120	21	5	7	3	156
Deep Neural Network (50%)	753	124	19	5	7	3	158
TOTAL (Any Method)	⋯	128	21	5	7	3	164

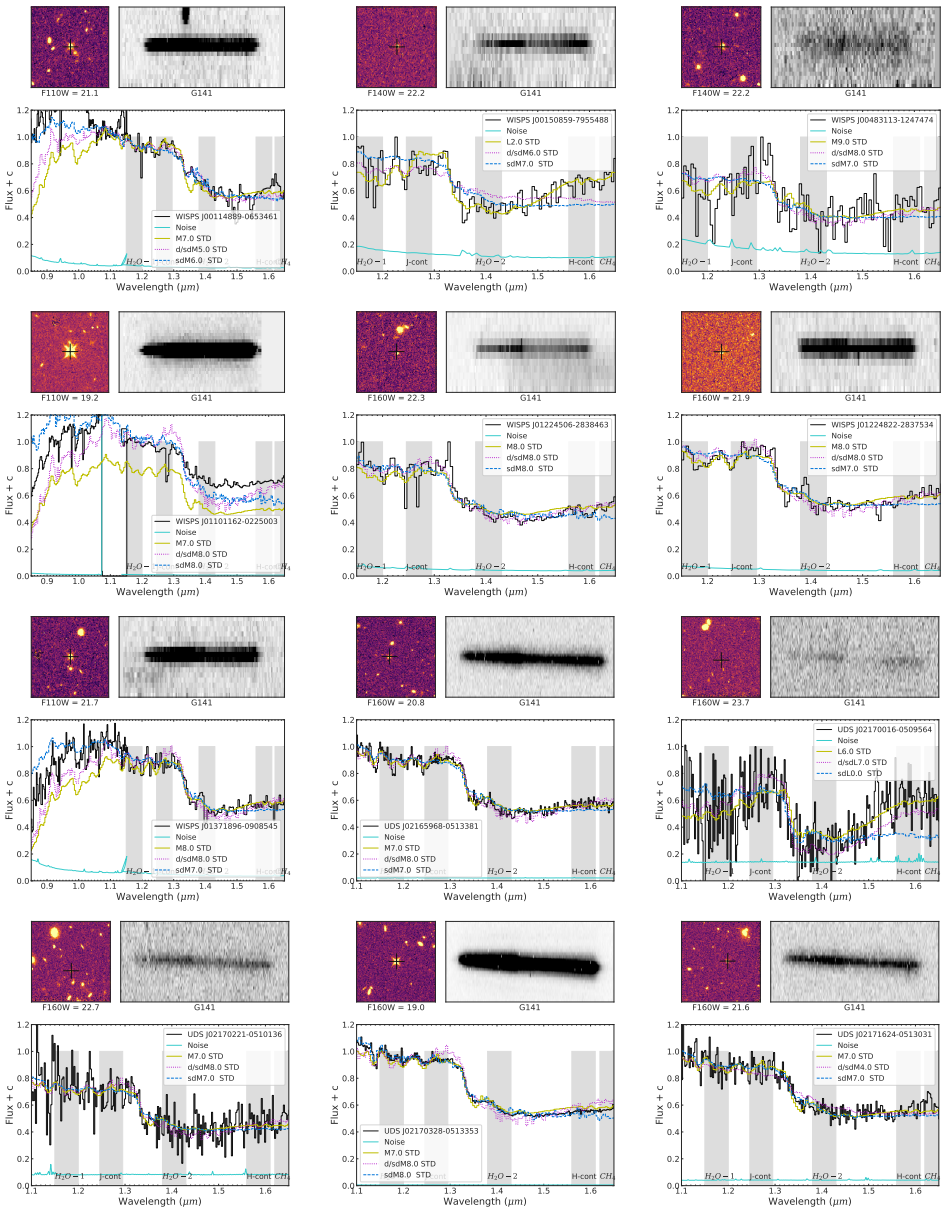

Figure 2.14 Spectra of UCD discoveries in order of Right Ascension. The top left panel displays a cutout of the F110W, F140W, or F160W image of the field near the object; the top right panel displays a cutout of the G141 dispersed spectral image centered on the object; the bottom panel displays the 1D-extracted spectrum (solid black line), compared to the best fit dwarf (yellow solid line), mild-subdwarf standard (d/sd; magenta dotted line) and subdwarf (sd; dashed blue line) spectral standards. Note that d/sd and sd standards do not extend into the T dwarf regime. In some panels, the 1D spectral axis is extended to include G102 grism data, when available.

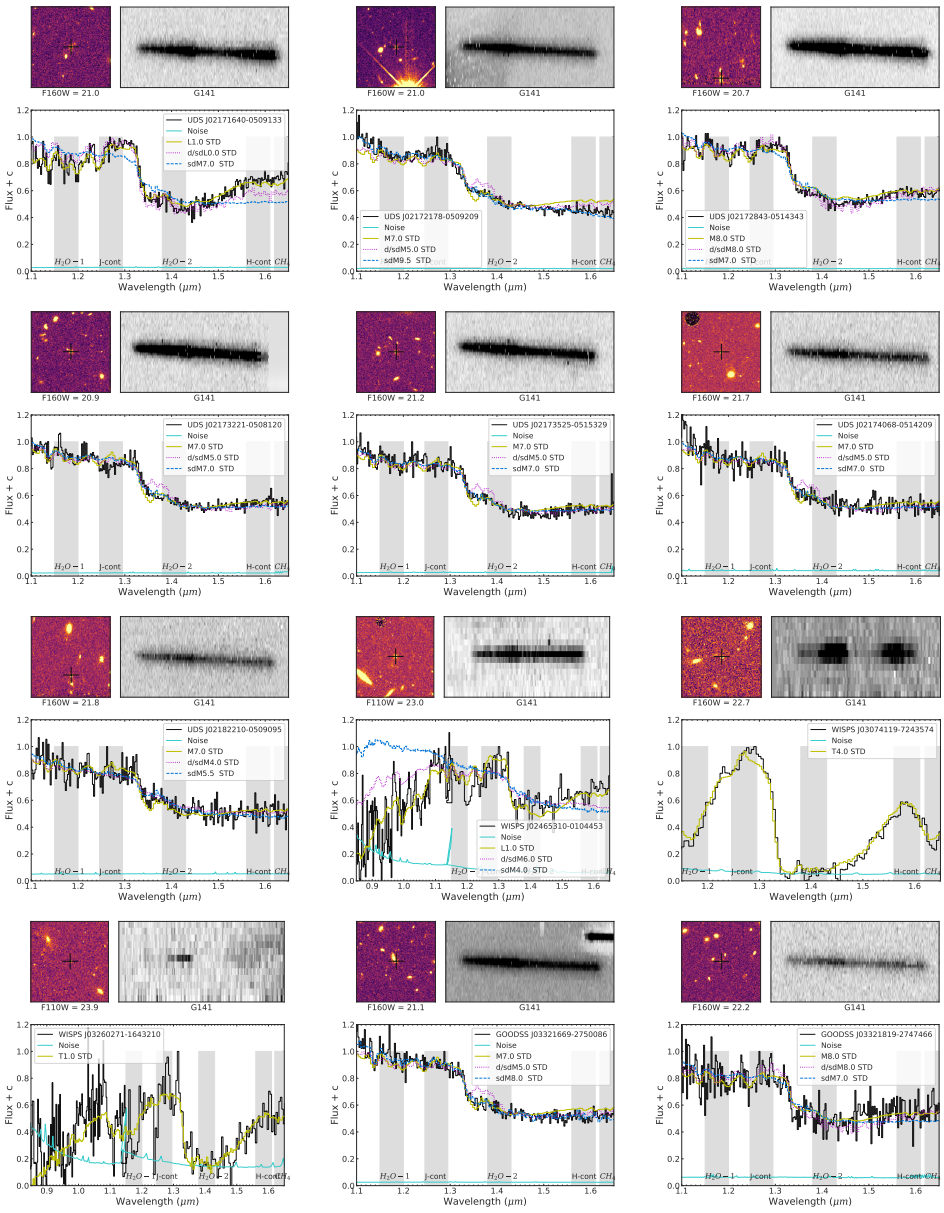

Figure 2.14 Spectra of UCD discoveries in order of Right Ascension. The top left panel displays a cutout of the F110W, F140W, or F160W image of the field near the object; the top right panel displays a cutout of the G141 dispersed spectral image centered on the object; the bottom panel displays the 1D-extracted spectrum (solid black line), compared to the best fit dwarf (yellow solid line), mild-subdwarf standard (d/sd; magenta dotted line) and subdwarf (sd; dashed blue line) spectral standards. Note that d/sd and sd standards do not extend into the T dwarf regime. In some panels, the 1D spectral axis is extended to include G102 grism data, when available (Continued).

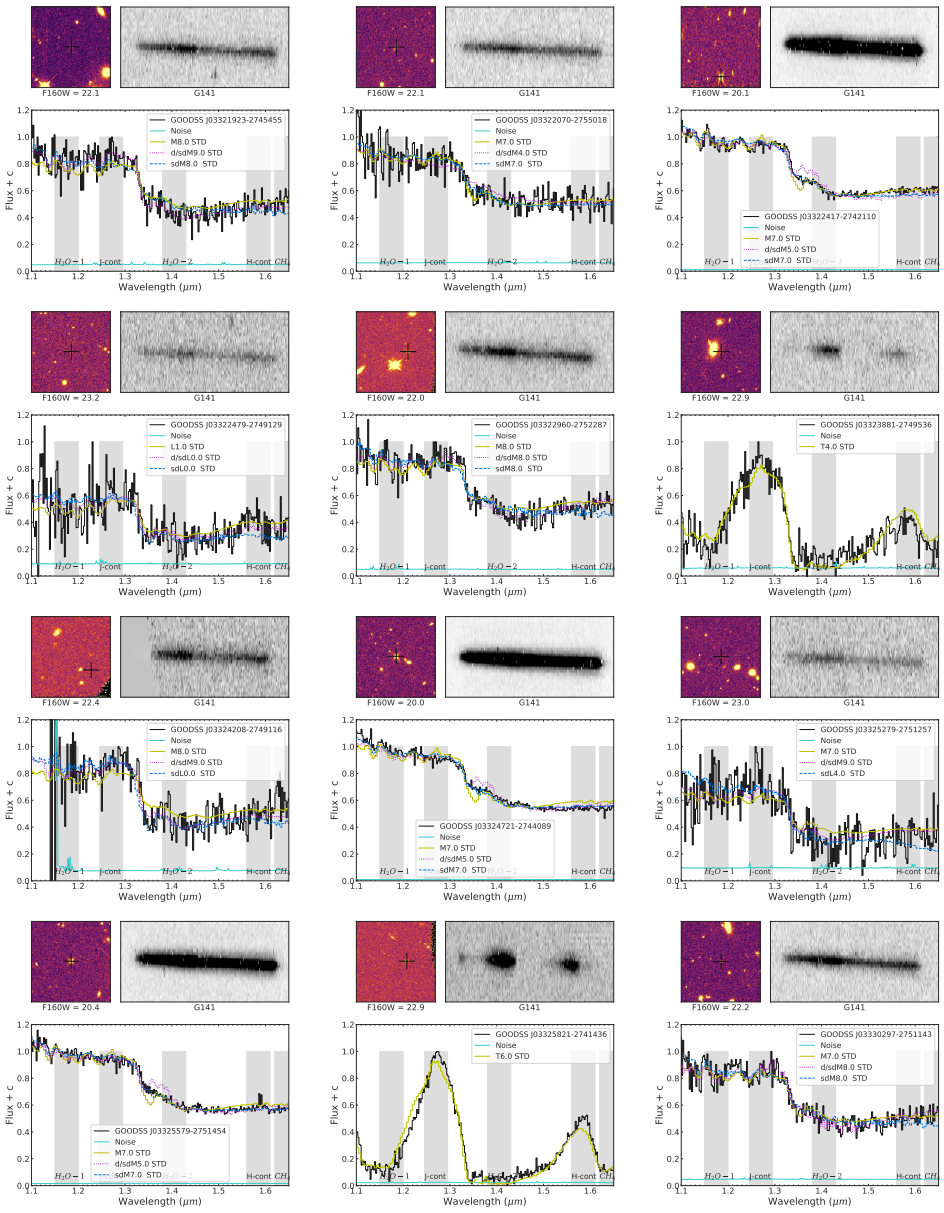

Figure 2.14 Spectra of UCD discoveries in order of Right Ascension. The top left panel displays a cutout of the F110W, F140W, or F160W image of the field near the object; the top right panel displays a cutout of the G141 dispersed spectral image centered on the object; the bottom panel displays the 1D-extracted spectrum (solid black line), compared to the best fit dwarf (yellow solid line), mild-subdwarf standard (d/sd; magenta dotted line) and subdwarf (sd; dashed blue line) spectral standards. Note that d/sd and sd standards do not extend into the T dwarf regime. In some panels, the 1D spectral axis is extended to include G102 grism data, when available (Continued).

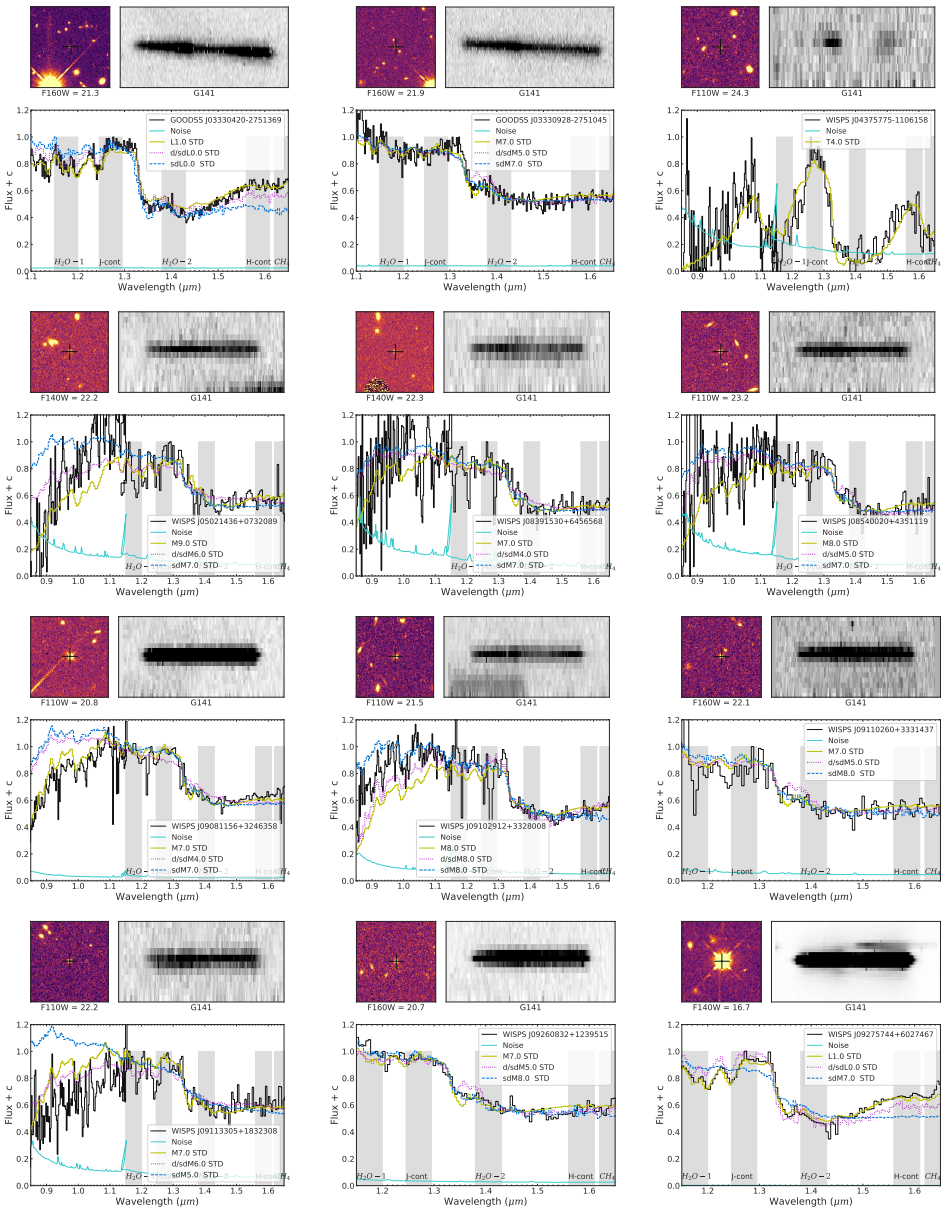

Figure 2.14 Spectra of UCD discoveries in order of Right Ascension. The top left panel displays a cutout of the F110W, F140W, or F160W image of the field near the object; the top right panel displays a cutout of the G141 dispersed spectral image centered on the object; the bottom panel displays the 1D-extracted spectrum (solid black line), compared to the best fit dwarf (yellow solid line), mild-subdwarf standard (d/sd; magenta dotted line) and subdwarf (sd; dashed blue line) spectral standards. Note that d/sd and sd standards do not extend into the T dwarf regime. In some panels, the 1D spectral axis is extended to include G102 grism data, when available (Continued).

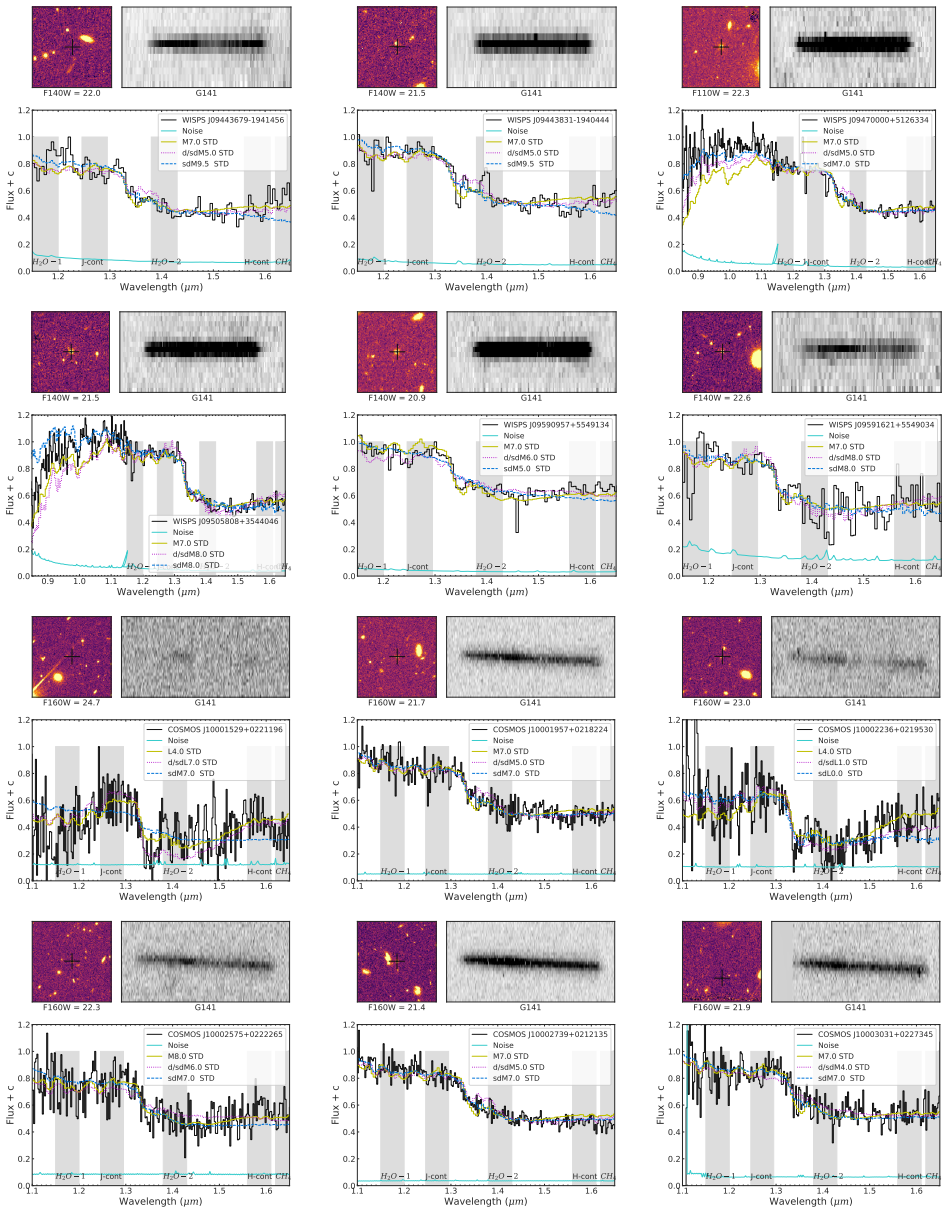

Figure 2.14 Spectra of UCD discoveries in order of Right Ascension. The top left panel displays a cutout of the F110W, F140W, or F160W image of the field near the object; the top right panel displays a cutout of the G141 dispersed spectral image centered on the object; the bottom panel displays the 1D-extracted spectrum (solid black line), compared to the best fit dwarf (yellow solid line), mild-subdwarf standard (d/sd; magenta dotted line) and subdwarf (sd; dashed blue line) spectral standards. Note that d/sd and sd standards do not extend into the T dwarf regime. In some panels, the 1D spectral axis is extended to include G102 grism data, when available (Continued).

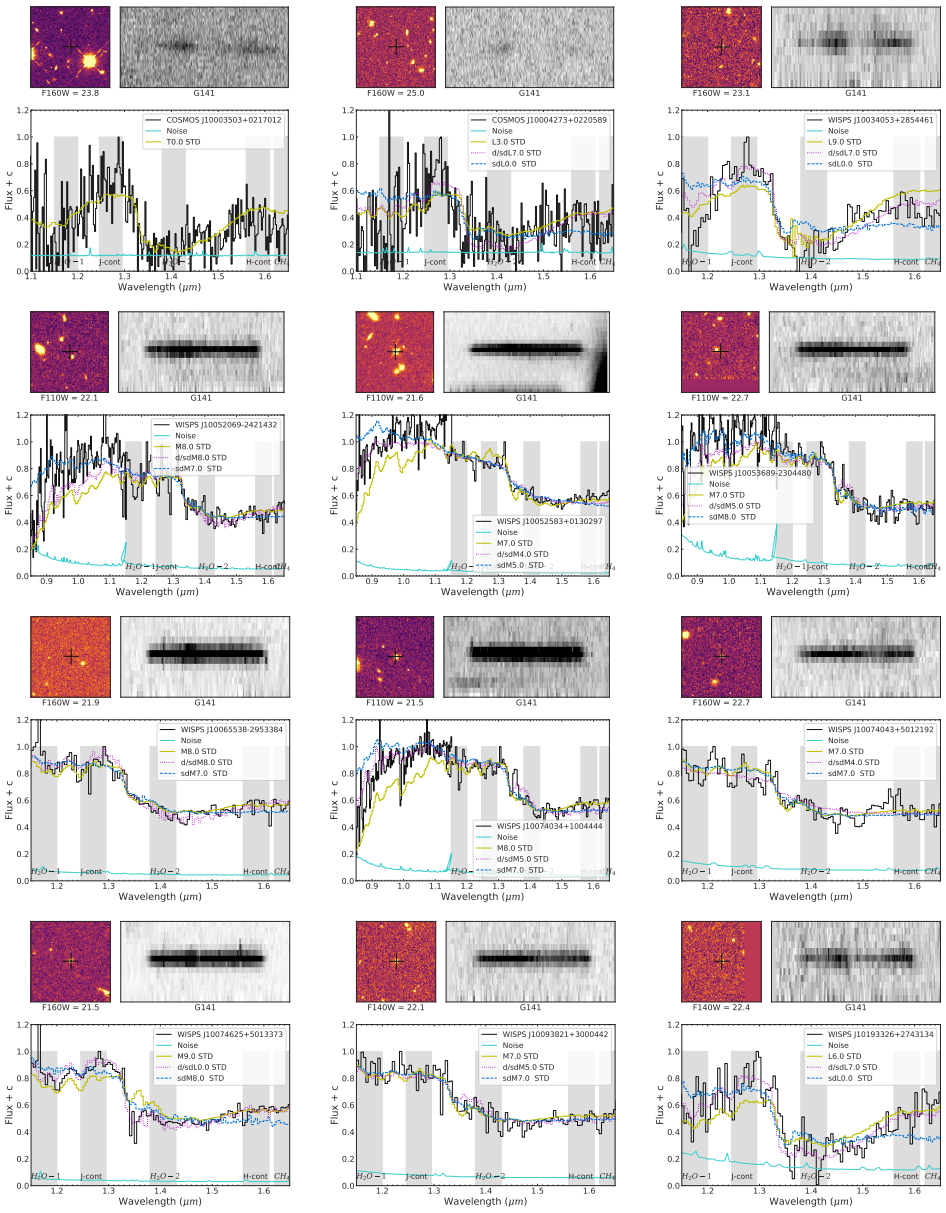

Figure 2.14 Spectra of UCD discoveries in order of Right Ascension. The top left panel displays a cutout of the F110W, F140W, or F160W image of the field near the object; the top right panel displays a cutout of the G141 dispersed spectral image centered on the object; the bottom panel displays the 1D-extracted spectrum (solid black line), compared to the best fit dwarf (yellow solid line), mild-subdwarf standard (d/sd; magenta dotted line) and subdwarf (sd; dashed blue line) spectral standards. Note that d/sd and sd standards do not extend into the T dwarf regime. In some panels, the 1D spectral axis is extended to include G102 grism data, when available (Continued).

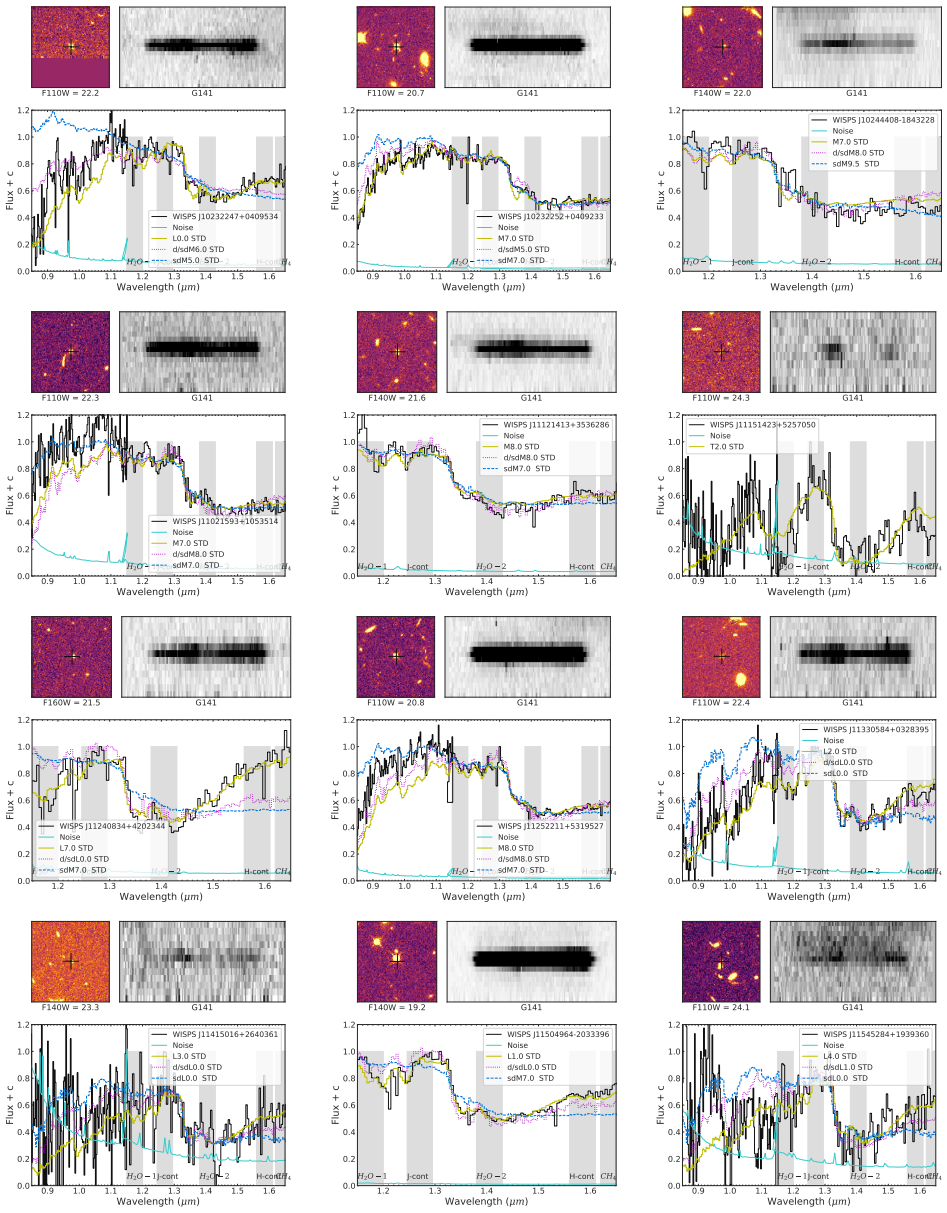

Figure 2.14 Spectra of UCD discoveries in order of Right Ascension. The top left panel displays a cutout of the F110W, F140W, or F160W image of the field near the object; the top right panel displays a cutout of the G141 dispersed spectral image centered on the object; the bottom panel displays the 1D-extracted spectrum (solid black line), compared to the best fit dwarf (yellow solid line), mild-subdwarf standard (d/sd; magenta dotted line) and subdwarf (sd; dashed blue line) spectral standards. Note that d/sd and sd standards do not extend into the T dwarf regime. In some panels, the 1D spectral axis is extended to include G102 grism data, when available (Continued).

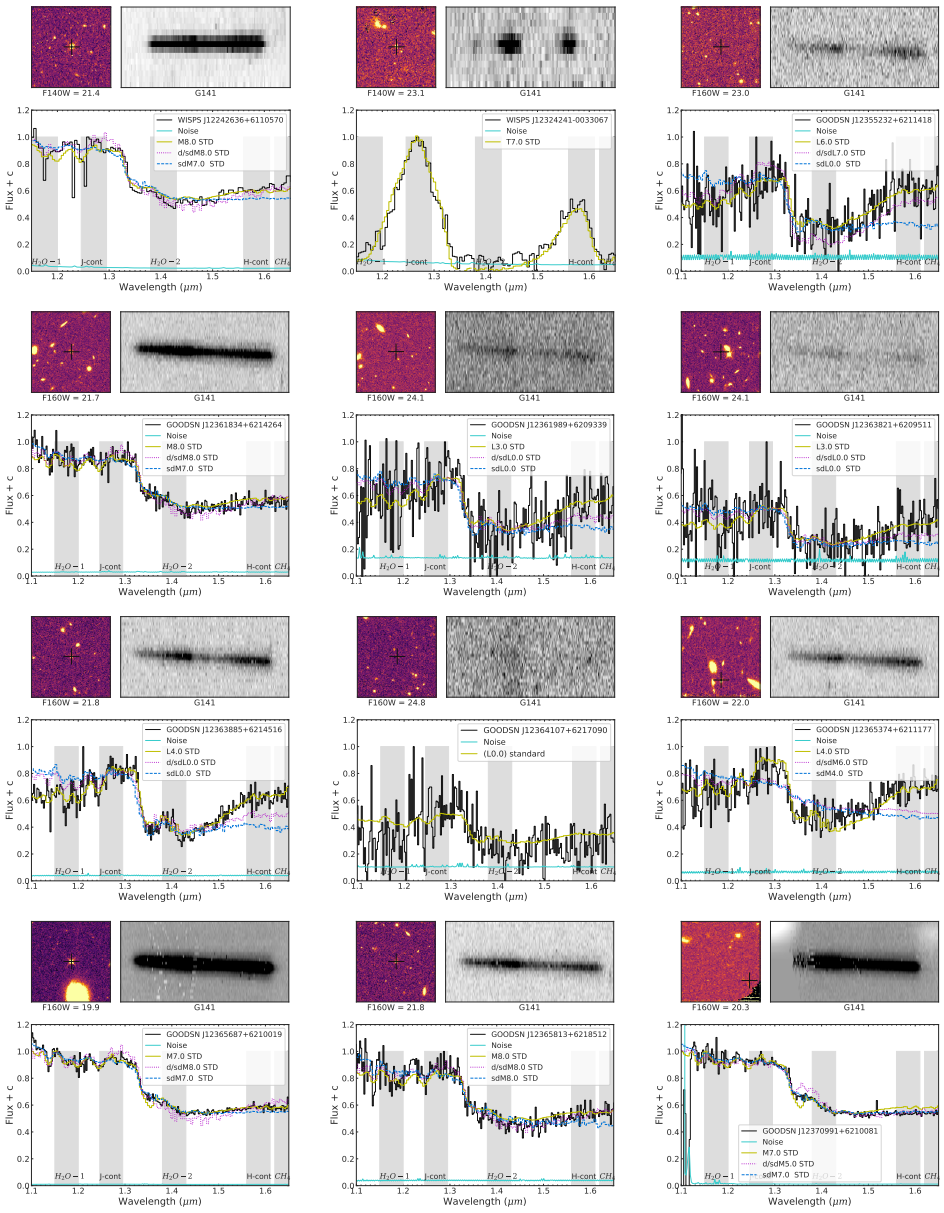

Figure 2.14 Spectra of UCD discoveries in order of Right Ascension. The top left panel displays a cutout of the F110W, F140W, or F160W image of the field near the object; the top right panel displays a cutout of the G141 dispersed spectral image centered on the object; the bottom panel displays the 1D-extracted spectrum (solid black line), compared to the best fit dwarf (yellow solid line), mild-subdwarf standard (d/sd; magenta dotted line) and subdwarf (sd; dashed blue line) spectral standards. Note that d/sd and sd standards do not extend into the T dwarf regime. In some panels, the 1D spectral axis is extended to include G102 grism data, when available (Continued).

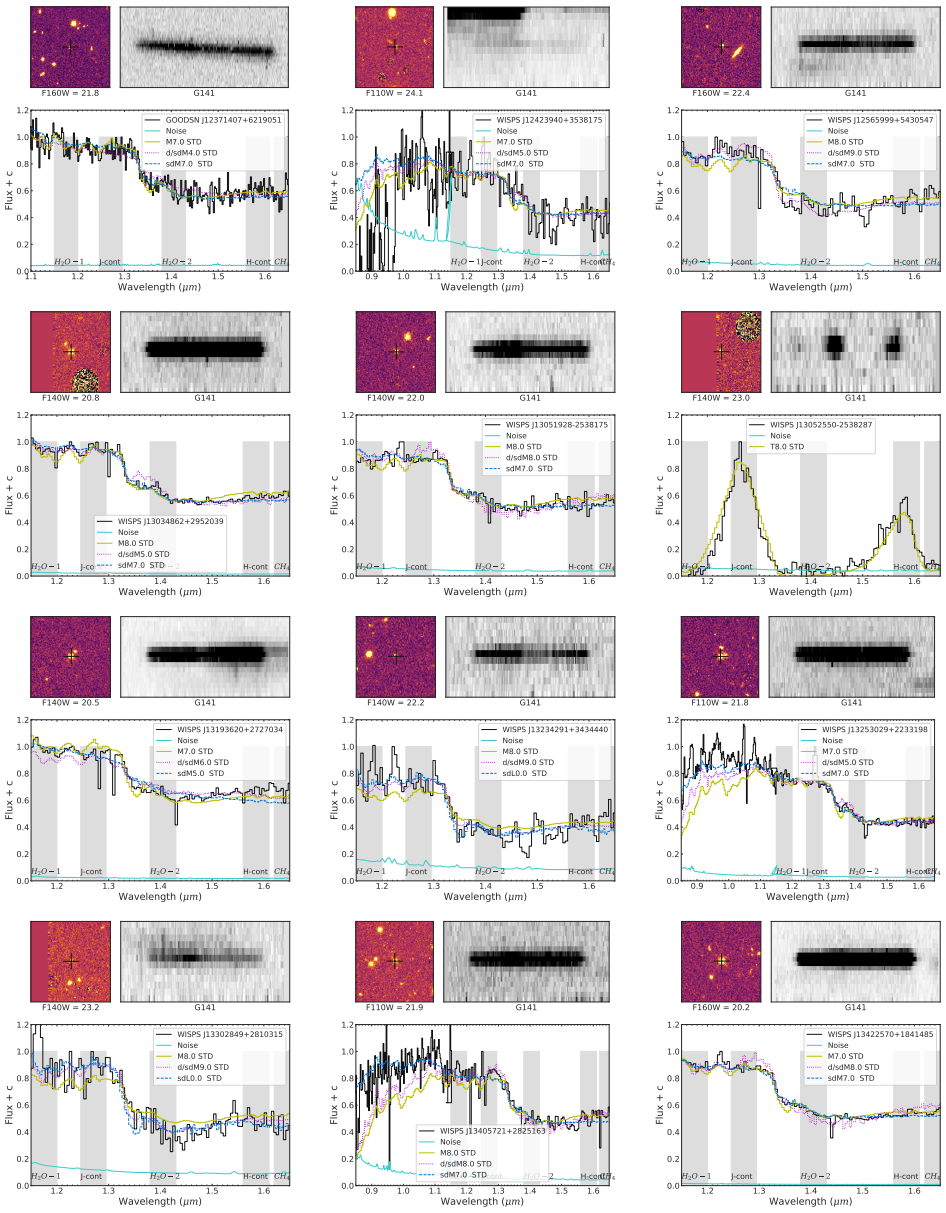

Figure 2.14 Spectra of UCD discoveries in order of Right Ascension. The top left panel displays a cutout of the F110W, F140W, or F160W image of the field near the object; the top right panel displays a cutout of the G141 dispersed spectral image centered on the object; the bottom panel displays the 1D-extracted spectrum (solid black line), compared to the best fit dwarf (yellow solid line), mild-subdwarf standard (d/sd; magenta dotted line) and subdwarf (sd; dashed blue line) spectral standards. Note that d/sd and sd standards do not extend into the T dwarf regime. In some panels, the 1D spectral axis is extended to include G102 grism data, when available (Continued).

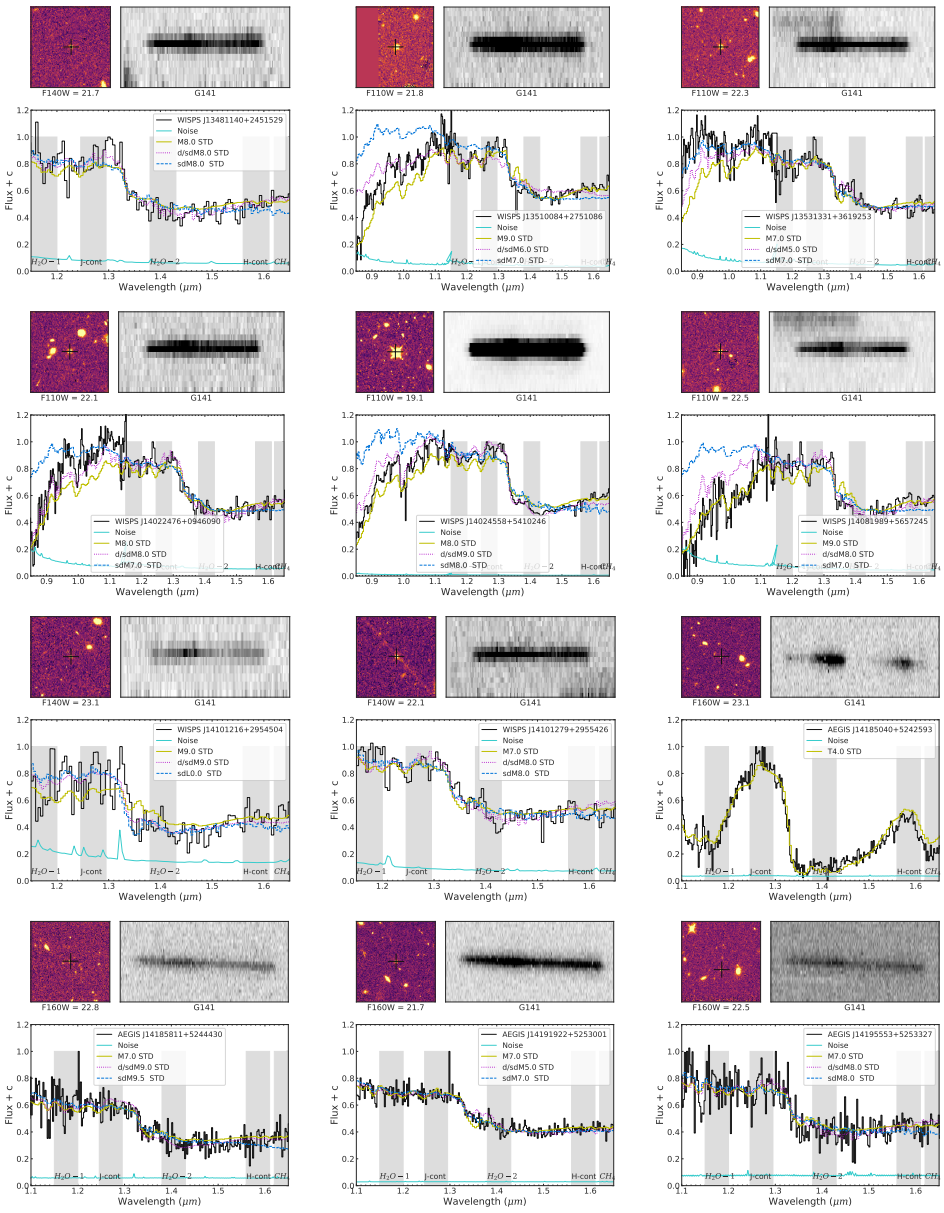

Figure 2.14 Spectra of UCD discoveries in order of Right Ascension. The top left panel displays a cutout of the F110W, F140W, or F160W image of the field near the object; the top right panel displays a cutout of the G141 dispersed spectral image centered on the object; the bottom panel displays the 1D-extracted spectrum (solid black line), compared to the best fit dwarf (yellow solid line), mild-subdwarf standard (d/sd; magenta dotted line) and subdwarf (sd; dashed blue line) spectral standards. Note that d/sd and sd standards do not extend into the T dwarf regime. In some panels, the 1D spectral axis is extended to include G102 grism data, when available (Continued).

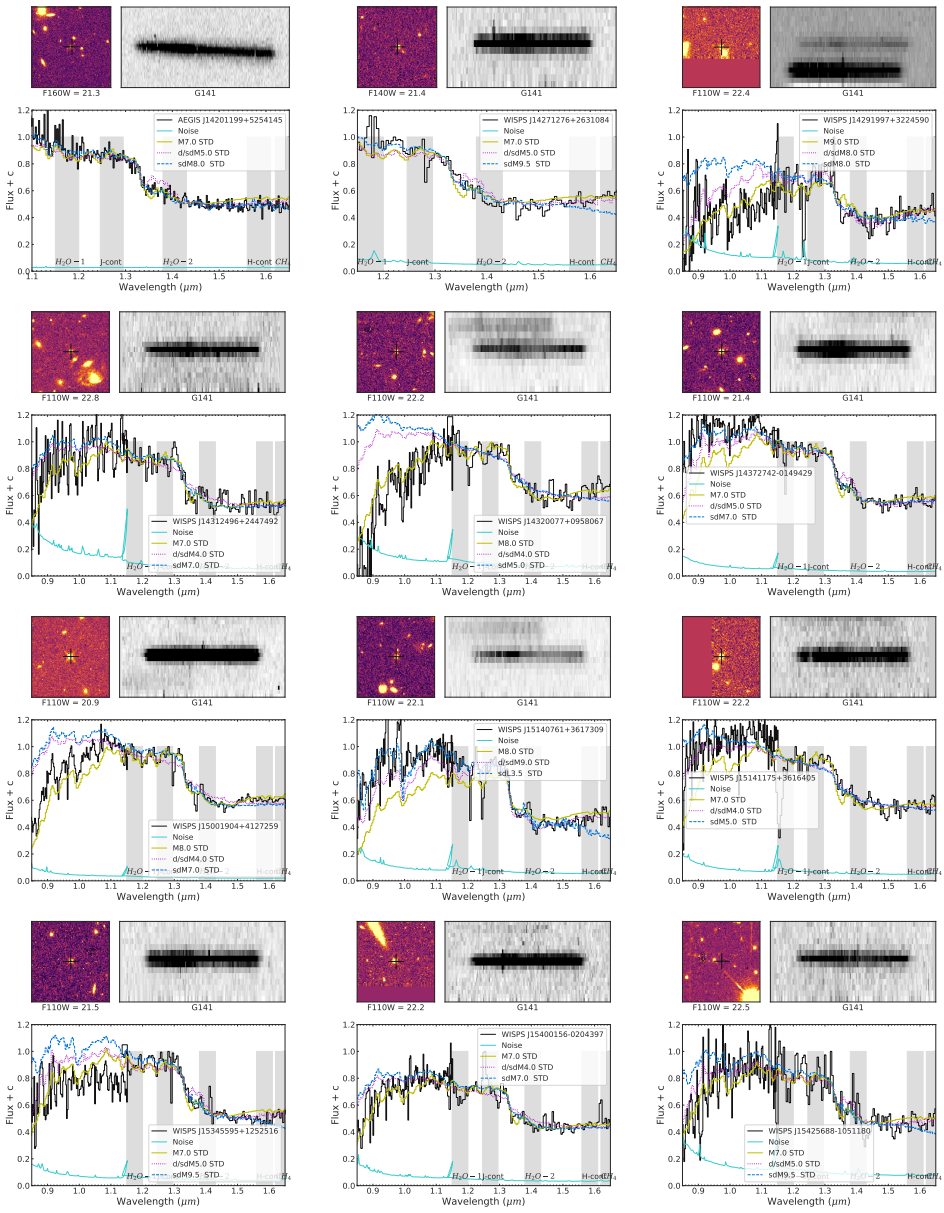

Figure 2.14 Spectra of UCD discoveries in order of Right Ascension. The top left panel displays a cutout of the F110W, F140W, or F160W image of the field near the object; the top right panel displays a cutout of the G141 dispersed spectral image centered on the object; the bottom panel displays the 1D-extracted spectrum (solid black line), compared to the best fit dwarf (yellow solid line), mild-subdwarf standard (d/sd; magenta dotted line) and subdwarf (sd; dashed blue line) spectral standards. Note that d/sd and sd standards do not extend into the T dwarf regime. In some panels, the 1D spectral axis is extended to include G102 grism data, when available (Continued).

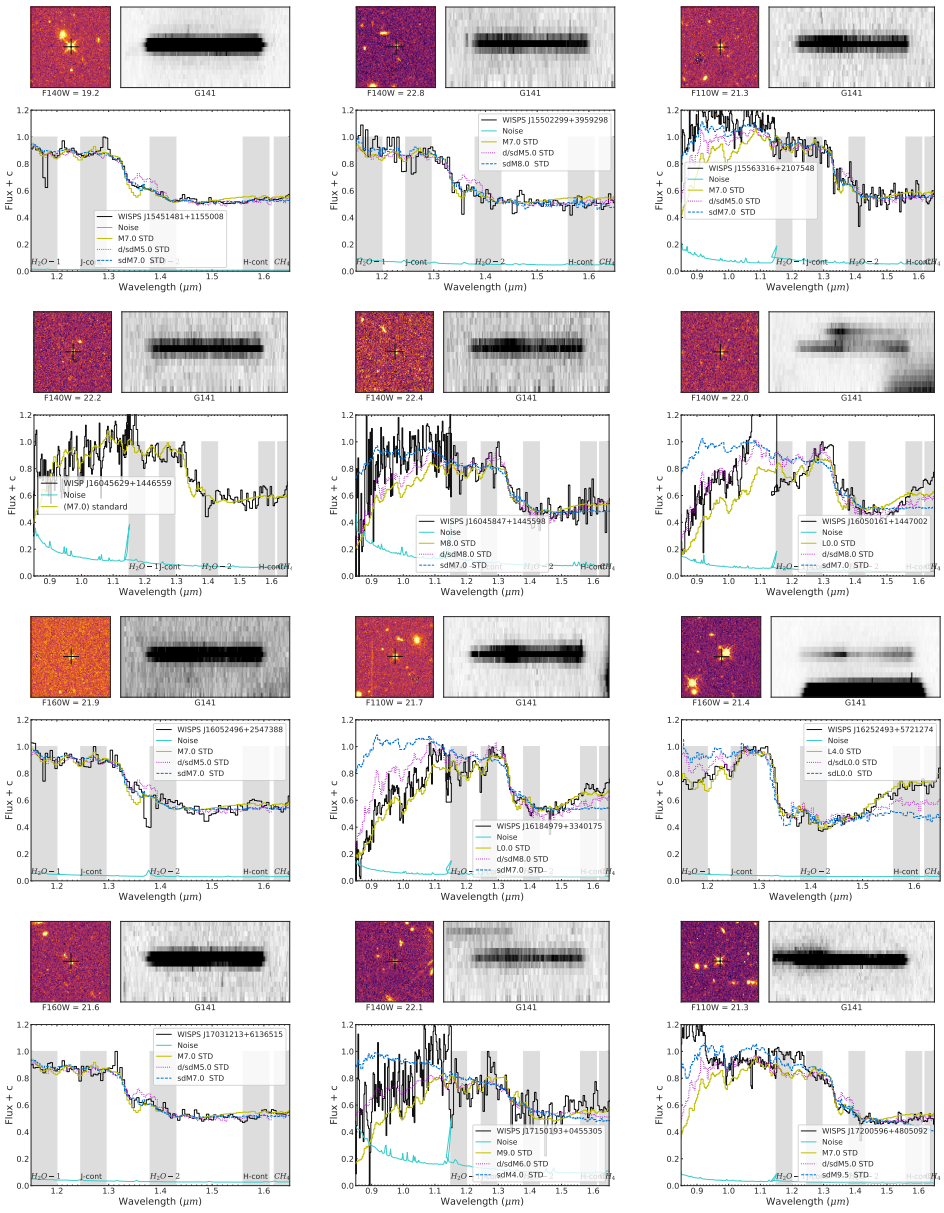

Figure 2.14 Spectra of UCD discoveries in order of Right Ascension. The top left panel displays a cutout of the F110W, F140W, or F160W image of the field near the object; the top right panel displays a cutout of the G141 dispersed spectral image centered on the object; the bottom panel displays the 1D-extracted spectrum (solid black line), compared to the best fit dwarf (yellow solid line), mild-subdwarf standard (d/sd; magenta dotted line) and subdwarf (sd; dashed blue line) spectral standards. Note that d/sd and sd standards do not extend into the T dwarf regime. In some panels, the 1D spectral axis is extended to include G102 grism data, when available (Continued).

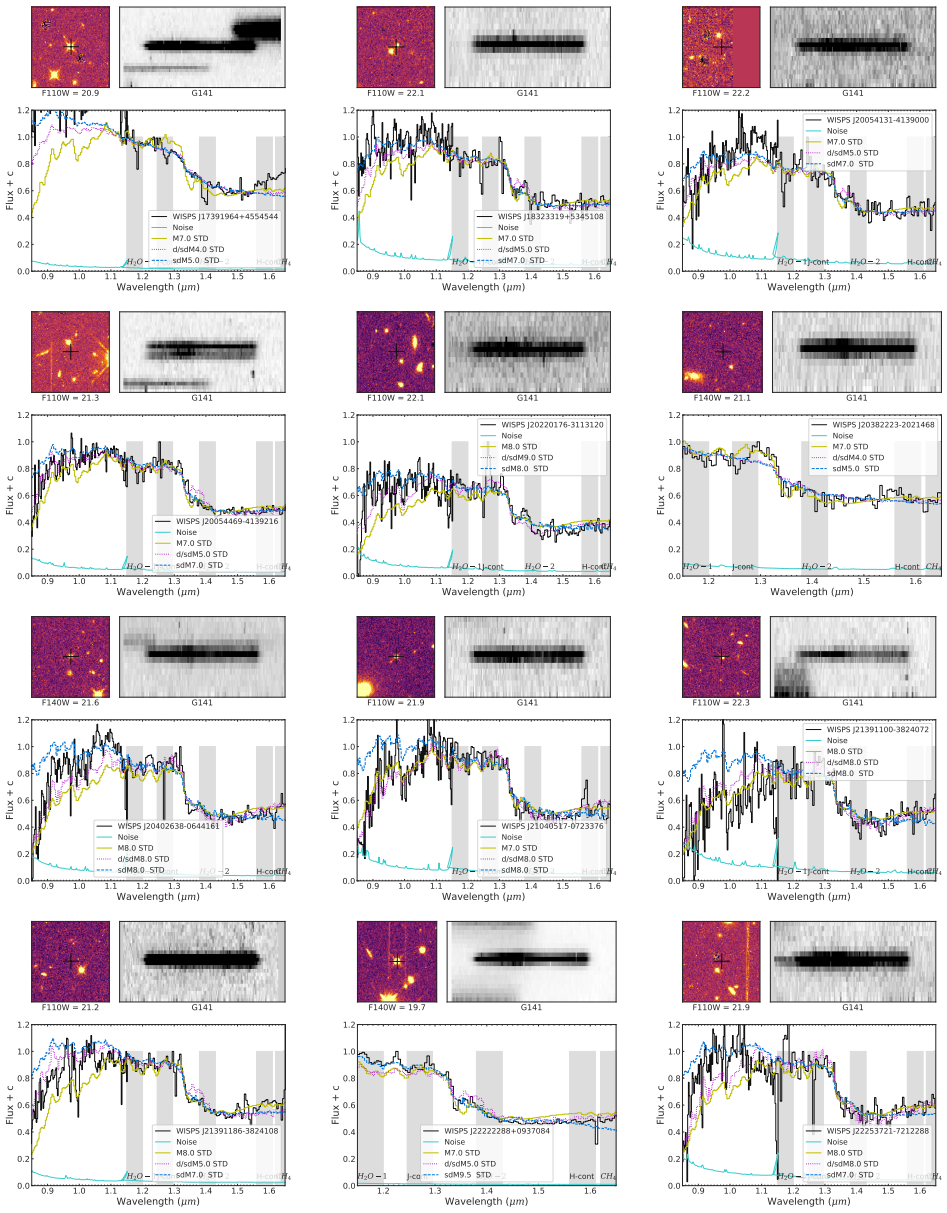

Figure 2.14 Spectra of UCD discoveries in order of Right Ascension. The top left panel displays a cutout of the F110W, F140W, or F160W image of the field near the object; the top right panel displays a cutout of the G141 dispersed spectral image centered on the object; the bottom panel displays the 1D-extracted spectrum (solid black line), compared to the best fit dwarf (yellow solid line), mild-subdwarf standard (d/sd; magenta dotted line) and subdwarf (sd; dashed blue line) spectral standards. Note that d/sd and sd standards do not extend into the T dwarf regime. In some panels, the 1D spectral axis is extended to include G102 grism data, when available (Continued).

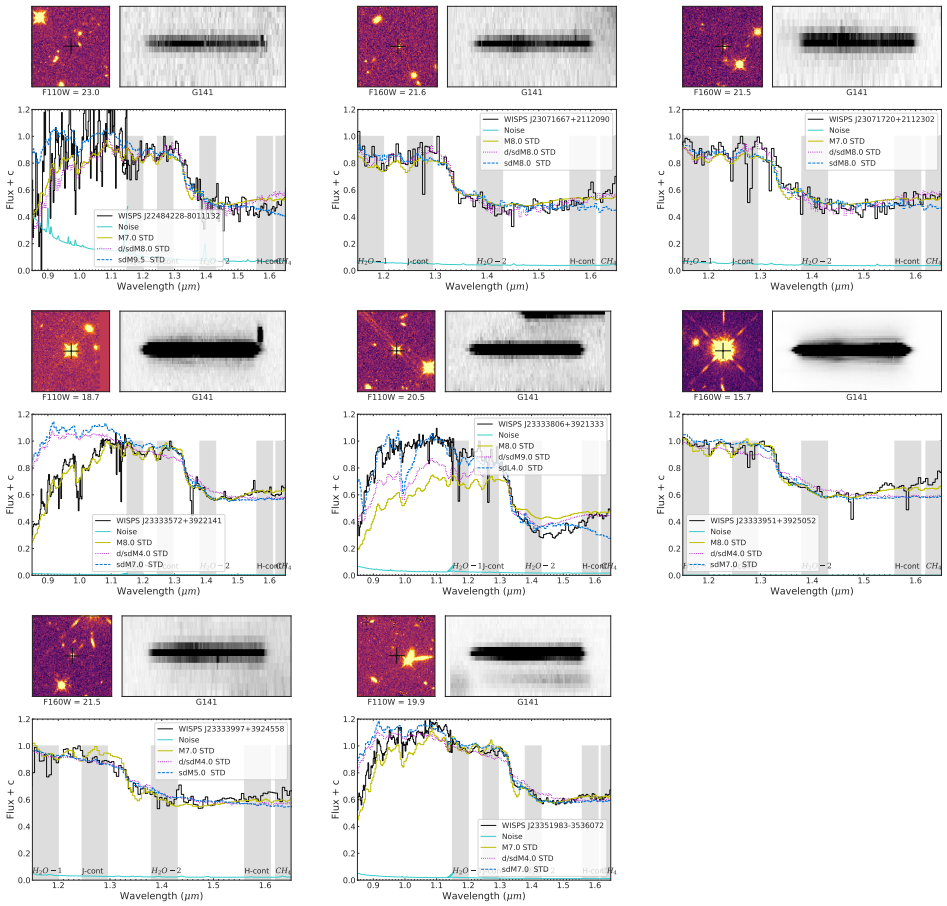

Figure 2.14 Spectra of UCD discoveries in order of Right Ascension. The top left panel displays a cutout of the F110W, F140W, or F160W image of the field near the object; the top right panel displays a cutout of the G141 dispersed spectral image centered on the object; the bottom panel displays the 1D-extracted spectrum (solid black line), compared to the best fit dwarf (yellow solid line), mild-subdwarf standard (d/sd; magenta dotted line) and subdwarf (sd; dashed blue line) spectral standards. Note that d/sd and sd standards do not extend into the T dwarf regime. In some panels, the 1D spectral axis is extended to include G102 grism data, when available (Continued).

2.7 Additional Late M Dwarf Discoveries

Here, we provide a table of 83 additional UCD candidates that were classified earlier than spectral type M7 based on comparison to spectral standards, but matched to high signal-to-noise UCD spectral templates classified M7 or later (Section 2.3.1). These sources were not included in the main sample, but are likely to be mid- to late-M dwarfs.

Chapter 2, in full, is a reprint of the material as it appears in the Astrophysical Journal 2022, Volume 924, Number 114, authored by Christian Aganze, Adam J. Burgasser, Mathew Malkan, Christopher A. Theissen, Roberto A. Tejada Arevalo, Chih-Chun Hsu1, Daniella C. Bardalez Gagliuffi, Russell E. Ryan, Jr., and Benne Holwerda. The thesis author was the primary investigator and author of this paper.

Chapter 3

Population Scaleheights and Ages of Ultracool Dwarfs in Deep HST/WFC3 Parallel Fields

3.1 Introduction

The spatial and kinematic structure, chemical composition, formation, and evolutionary history of the Milky Way—an area of study known as Galactic archaeology (Bland-Hawthorn & Gerhard, 2016)—is probed by its stellar components (Freeman, 1987; Ivezić et al., 2012). Recent advances in large-scale imaging, spectroscopic, and astrometric surveys have allowed the characterization of our Galaxy at unprecedented detail. These surveys have confirmed that the stellar population of the Milky Way is grouped into four principal components: a young, metal-rich exponential thin disk; an older exponential thick disk; a diffuse, old, and metal-poor halo; and a metal-rich central bulge and bar (de Vaucouleurs & Pence 1978; Bahcall & Soneira 1981; Jurić et al. 2008; Leggett et al. 1998; Tolstoy et al. 2009; Haywood et al. 2013b). These main components

contain various subpopulations and substructures, sculpted by major mergers such as Gaia-Enceladus (Belokurov et al., 2018; Helmi et al., 2018), and interactions with satellites such as Sagittarius (Price-Whelan et al., 2015; Laporte et al., 2019) and the Large and Small Magellanic Clouds (Erkal & Belokurov, 2020). Other kinds of substructures can be found in abundance and kinematic patterns, including distinct chemo-kinetic populations in the halo (Helmi et al., 1999, 2018; Myeong et al., 2018; Koppelman et al., 2019b; Naidu et al., 2020; Yuan et al., 2020), spatial and velocity phase-space spiral structure in the disk (Antoja et al., 2018), and numerous stellar streams (Boubert et al., 2018; Malhan et al., 2018; Shipp et al., 2018), all evidence of the complex and ongoing dynamical interactions between the Milky Way and its satellites.

Galactic spatial, kinematic, and abundance structure is typically probed through bright main sequence FGK stars and red giants, as these stars are intrinsically bright and well-distributed throughout the Galaxy. Ultracool dwarfs (UCDs), which encompass stars and brown dwarfs with $T_{\rm eff}$<3500K, mass <0.1 M, and spectral classes late-M, L, T, and Y (Kirkpatrick, 2005), offer an alternative and complementary approach for studying the Galaxy's formation history. UCDs constitute a significant fraction of stars in the Milky Way, comprising at least 20% of all the stars in the vicinity of the Sun (Reylé et al., 2021; Kirkpatrick et al., 2021). Stellar UCDs have stable main-sequence lifetimes that far exceed the age of the Universe ($\gtrsim 10^{12}$ years), while non-fusing substellar UCDs cool continuously over time. The distinct evolution of stellar and substellar UCDs allows them to serve as "standard clocks" in young stellar associations (Stauffer et al., 1998; Martín et al., 2018) and potentially in older globular clusters and the Galaxy at large (Burgasser, 2004; Caiazzo et al., 2017; Gerasimov et al., 2022). Their fully-convective interiors and cool, molecule-rich photospheres allow for sensitive measurement of metallicity (Rojas-Ayala et al., 2012; Veyette et al., 2017; Zhang et al., 2017), ideal for studies of chemical enrichment history. Since UCDs are more numerous and longer lived than FGK

stars and red giants, they potentially offer a higher phase-space resolution of ancient spatial, kinematic, and abundance substructures, allowing us to study the early history of the Milky Way in exquisite detail.

The challenge in using ultracool dwarfs for Galactic Archaeology is their intrinsic faintness. UCD population studies based on wide-field imaging surveys have been largely limited to the nearby Solar Neighborhood (d$\lesssim$ 100 pc), and have focused on measuring the local luminosity function and velocity dispersions (Cruz et al., 2007b; Metchev et al., 2008; Reyle et al., 2010; Bardalez Gagliuffi et al., 2019; Kirkpatrick et al., 2019, 2021; Burgasser et al., 2015; Hsu et al., 2021). Local studies also fail to sample the metal-poor thick disk and halo population in sufficient abundance to measure population properties; only few dozen nearby ultracool subdwarfs have been identified to date (Burgasser et al., 2003; Lépine & Scholz, 2008; Kirkpatrick et al., 2014; Zhang et al., 2019; Schneider et al., 2020).

In contrast, deep narrow-field surveys can reach more distant UCD populations, enabling measurement of disk structure and a greater proportion of halo and thick disk sources. The majority of deep surveys for UCDs (Table 3.8) have been undertaken with the *Hubble Space Telescope* (*HST*), as these objects often comprise a "foreground" to extragalactic surveys. Early work in this area includes measurement of M dwarf number counts in the *HST* Deep Field and Large Area Multi-Color Survey Groth Strip (Gould et al., 1997; Kerins, 1997; Chabrier & Mera, 1997). Analysis of these samples determined M dwarf thin and thick disk vertical scaleheights of $\sim$325 pc and $\sim$650 pc, respectively, and ruled out very low mass stars as being an appreciable component ($< 1\%$) of Galactic halo dark matter. Ryan et al. (2005) performed one of the first deep photometric surveys of distant UCDs, identifying 28 candidate L and T dwarfs in 135 arcmin^2 of deep imaging data obtained with the *HST* Advanced Camera for Surveys (ACS) instrument, selected by their $i-z$ colors to a limiting magnitude of $z < 25$. They determined a thin disk vertical

scaleheight of $\sim$350 pc, similar to prior measurements of deep M dwarf star counts. Ryan et al. (2011) subsequently identified 17 candidate late M, L, and T dwarfs in 232 arcmin^2 of *HST*/Wide Field Camera 3 (WFC3) imaging of the Great Observatories Origins Deep Survey (GOODS; Giavalisco et al. 2004) using optical and near-infrared color selection, and determined a thin disk vertical scaleheight for these sources of 290 ± 40 pc. Deep ground-based surveys have also identified samples of distant UCDs. Kakazu et al. (2010) identified 7 late-L and T dwarfs in 9.3 deg^2 of optical and infrared imaging data from the Subaru Suprime-Cam Hawaii Quasar and T dwarf survey to a limiting magnitude of $z < 23.3$, spectroscopically confirming several of the targets. From this small sample Kakazu et al. (2010) inferred a thin disk vertical scaleheight of $\sim$400 pc for brown dwarfs. Sorahana et al. (2019) used the larger (130 deg^2) and deeper ($z < 24$) Hyper Suprime-Cam Subaru Strategic Program survey (HSC-SSP; Aihara et al. 2018) to photometrically identify 3,665 L dwarfs, and inferred an average thin disk vertical scaleheight of 340–420 pc. Carnero Rosell et al. (2019) used multi-band imaging data from the Dark Energy Survey (DES; The Dark Energy Survey Collaboration 2005), combined with photometry from wide-field imaging surveys, to photometrically identify and classify 11,745 L0–T9 dwarfs to a limiting magnitude of $z \leqslant 22$, and estimated a thin disk vertical scaleheight of $\sim$450 pc. Recently, Warren et al. (2021) compiled a sample of 34,000 M7-L3 UCDs by searching over a large area of 3,070 deg^2 in the Sloan Digital Sky Survey (SDSS, York et al. 2000) and UKIRT Infrared Deep Sky Survey (UKIDSS) down to J = 17.5, and measured a scaleheight of $\sim$ 270 pc. These last three studies, which comprise the largest compilations of UCDs to date, use multiple colors to segregate UCDs from other background sources (Skrzypek et al., 2016).

Deep imaging surveys, typically based on optical photometry, generally probe scaleheights for only the most massive (stellar) ultracool dwarfs, and are subject to significant contamination from Galactic and extragalactic populations studies. A com-

plementary approach is to use deep spectroscopic surveys, which enable greater fidelity in both the confirmation and classification of UCDs. Pirzkal et al. (2005) identified 18 M dwarfs and 2 L dwarfs in the *Hubble* Ultra Deep Field with ACS imaging data and GRism ACS Program for Extragalactic Science (GRAPES, Pirzkal et al. 2004) spectroscopy. Using a single-component disk model and a halo population with a halo fraction of 0.25%, they derived a thin disk scaleheight of 400±100 pc for their >M4 population. In a follow-up paper, Pirzkal et al. (2009) found 203 M0-M9 dwarfs in the Probing Evolution And Reionization Spectroscopically (PEARS) fields, based on ACS spectra and additional photometry down to z = 25 (AB). They found that an exponential model with two disk components was required to reproduce the observed number counts, and derived a thin disk scaleheight of 370^{+60}_{-65} pc for M4-M9 spectral types, a thick disk scaleheight of ∼1000 pc, and halo-to-thin disk and thick disk-to-thin disk number ratios of 0.25% and 2%, respectively, values consistent with Sloan Digital Sky Survey (SDSS) results (Jurić et al., 2008). Pushing to lower temperatures, Masters et al. (2012) spectroscopically identified 3 late T dwarfs in the WFC3 Infrared Spectroscopic Parallels survey (WISP; Atek et al. 2010) based on the presence of strong CH_4 and H_2O absorption features in 1.1–1.7 μm *HST*/WFC3 spectra. This small sample was sufficient to constrain the power-law index of the substellar mass function of the thin disk but not its vertical scaleheight. In Aganze et al. (2022a) (hereafter Paper I), we reported the discovery of 164 late M, L, and T dwarfs in WISP and 3D-HST (Momcheva et al., 2016; Brammer et al., 2012; Skelton et al., 2014) *HST*/WFC3 spectroscopic data. In this study, we transform these data into the first measurement of vertical scaleheight as a function of spectral type in the UCD mass regime.

Measurement of the vertical scaleheight of UCDs as a function of spectral type or temperature is a key step toward exploring both the formation history and evolution of these objects. Vertical scaleheight is a proxy for population age (Bird et al., 2013;

Mackereth et al., 2017), driven by the dynamical heating of stellar populations through encounters with Galactic structures or dispersion induced by to satellite interactions (Spitzer & Schwarzschild, 1953; Lacey, 1984; Sellwood & Binney, 2002; Hopkins et al., 2008; Ma et al., 2017). Because UCDs are a mixture of long-lived, stable stars and cooling brown dwarfs, their ages, dispersions, and scaleheights are all predicted to show complex trends with temperature depending on formation and evolutionary history (Burgasser, 2004; Ryan et al., 2017). While kinematic trends can be discerned from the local sample (Zapatero Osorio et al., 2007; Blake et al., 2010; Burgasser et al., 2015; Hsu et al., 2021), variations in scaleheights requires a well-characterized, large sample of UCDs out to kpc distances, including low temperature L, T, and Y dwarfs.

Section 3.2 describes the survey contents, including limiting magnitudes, distances, and effective volume probed. Section 3.2.1 describes the Monte-Carlo population simulations used to model our star counts. Section 3.4 summarizes the results of our analysis, which places constraints on the scaleheights of late-M, L, and T dwarfs in the Galactic disk population. Section 3.5 presents predictions for the surface densities of UCDs that will be observed as part of the *James Webb Space Telescope* (*JWST*) Parallel Application of Slitless Spectroscopy to Analyze Galaxy Evolution survey (PASSAGE, *JWST* Cycle 1 GO-1571, PI Malkan, Malkan et al. 2021). We summarize our main conclusions in Section 5.6.

3.2 Characterizing the $HST/WFC3$ Ultracool Dwarf Sample

Observational Data

The sources and data considered in this investigation are described in Paper I. In brief, we analyzed spectral and photometric data of 164 late-M, L, and T dwarfs identified in 0.6 deg^2 of slitless grism spectral data obtained with *HST*/WFC3 in the WISP and 3D-HST surveys. The spectral data consist of low-resolution near-infrared measurements primarily spanning 1.11 $\mu m \leq \lambda \leq 1.67 \mu m$ at an average resolution of $\lambda/\Delta\ \lambda \approx 130$. The photometric data include measurements in the wide-band F110W (0.8-1.4 μm), F140W (1.2-1.6 μm), and F160W (1.4-1.7 μm) filters. We also used the spectral calibration sample described in Paper I, a set of approximately 3,000 near-infrared (0.7-2.5 μm)$low-resolution(\lambda/\Delta\lambda \approx 75$–120) spectra from the SpeX Prism Library (Burgasser, 2014), 22 *HST*/WFC3 Y dwarf spectra from Schneider et al. (2015), and 77 *HST*/WFC3 UCD spectra from Manjavacas et al. (2019). These data and the source properties are described in detail in Paper I.

Survey Limiting Magnitudes, Distances & Effective Volumes The number of stars present in a given field of view is equal to the number density of stars as a function of Galactic position integrated over the total volume along an observed line of sight. The volume observed is determined by the angular area of the field and the limiting distance probed, which depends on both the survey sensitivity and the intrinsic brightness of our targets. Since the latter varies as a function of spectral type in different ways between different imaging filters, it is necessary to compute these volumes as a function of spectral type and filter, in addition to considerations of varying integration times, photometric noise, and intrinsic variance in stellar brightness within a given spectral class, including

unresolved multiplicity.

For the 3D-HST survey, Skelton et al. (2014) report the effective limiting magnitudes of each pointing based on the point-source selection criteria described in Paper I. For the WISP survey, while Atek et al. (2010) does not provide a complete list of limiting magnitudes for all pointings, they do report an average depth of F110W = 26.8 and F140W = 25.0 across the survey. Given the additional selection criteria imposed on our sample, and the differing exposure times between individual WISP and 3D-HST pointings, we chose to re-estimate the limiting magnitudes for each individual pointing and imaging filter for the WISP data. These limits were determined for a subset of pointings by fitting a Gaussian kernel density estimator (KDE, Parzen 1962) to the distribution of apparent magnitudes of point-sources with spectral J-SNR > 3 (see Paper I) in each pointing and filter. This fitting procedure was applied to pointings that had more than 50 qualifying point sources (dense fields) to obtain a statistically robust limit, which was estimated as maximum of the KDE distribution. Pointings with fewer than 50 qualifying point sources (sparse fields) had faint magnitude limits estimated from linear relationships between the limiting magnitude and the logarithm of the G141 spectral exposure time from the dense pointings (see Table 3.6 and Figure 3.1). The faint magnitude limits for all fields and filters are listed in supplemental tables. We also adopted a bright limiting magnitude of 16 for all pointings and filters, based on the bright tails of the point source magnitude distributions as illustrated in Figure 3.1.

In Paper I, we found that several of our UCD discoveries had apparent magnitudes fainter than the defined limiting magnitudes, particularly among the late-L and T dwarfs. These "deep sources" arise from the redistribution of flux within each imaging filter by strong molecular absorption from H_2O and CH_4, in contrast to the flat, featureless spectra of most sources. The structured spectra imply that, at a given magnitude, a late-type UCD has a higher peak spectral flux density and higher J-SNR than the equivalent

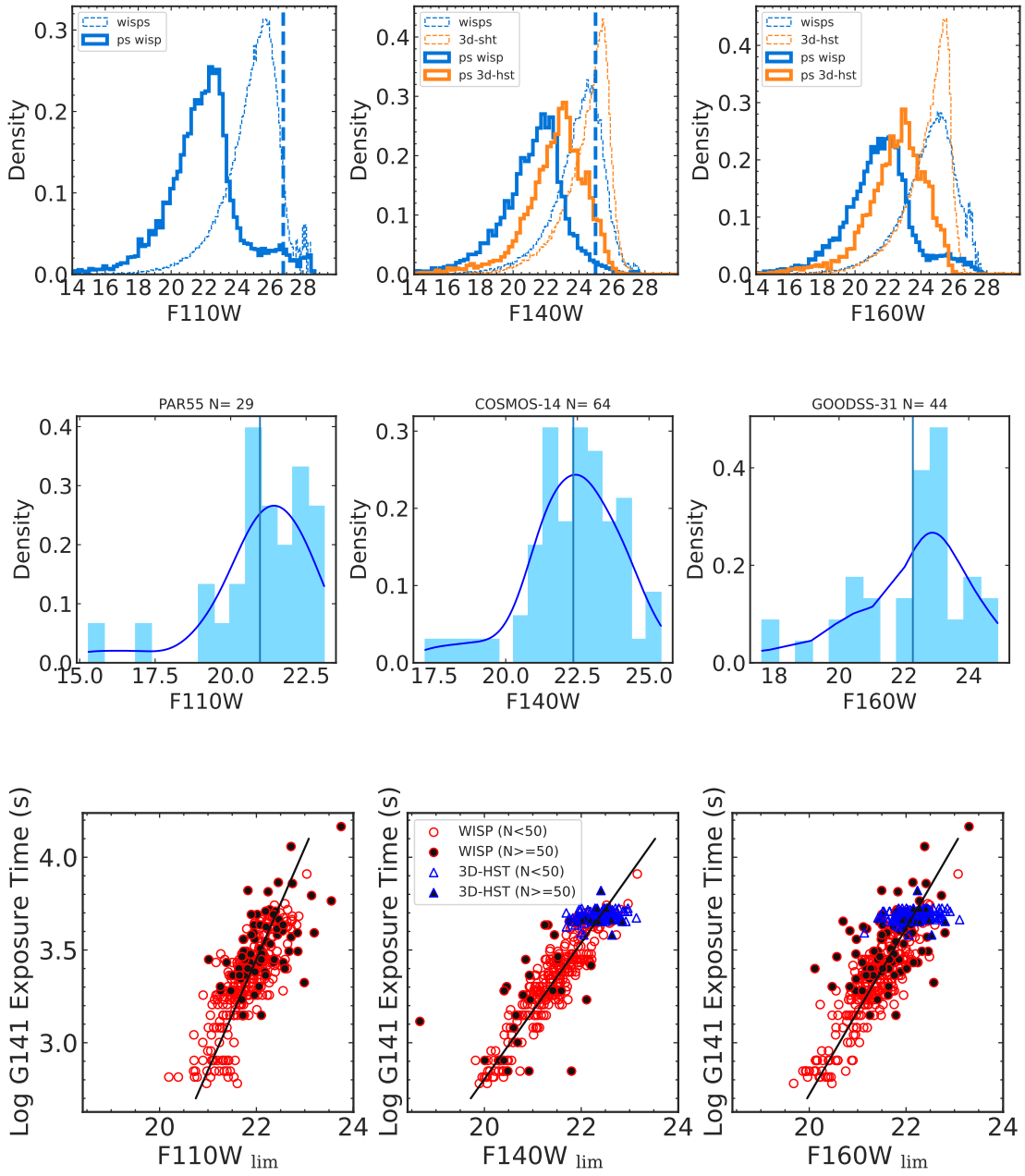

Figure 3.1 (a) Distributions of magnitudes for sources in the WISP and 3D-HST surveys across all pointings. Dotted lines show all sources, solid lines show point sources with J-SNR > 3. Blue vertical dashed lines shows magnitudes limits of Atek et al. (2010) (b) Estimation of the limiting magnitude for a select set of pointings. The smooth blue line shows the KDE, while the vertical black line indicates the adopted faint magnitude limit based on the KDE peak. (c) Faint magnitude limits for all pointings as a function of log spectral exposure time, separated into dense (filled symbols) and sparse (open symbols) fields. Linear fits between the dense field limits and log exposure time (black lines) were used to estimate the limiting magnitudes for the sparse fields, taking intrinsic scatter into account.

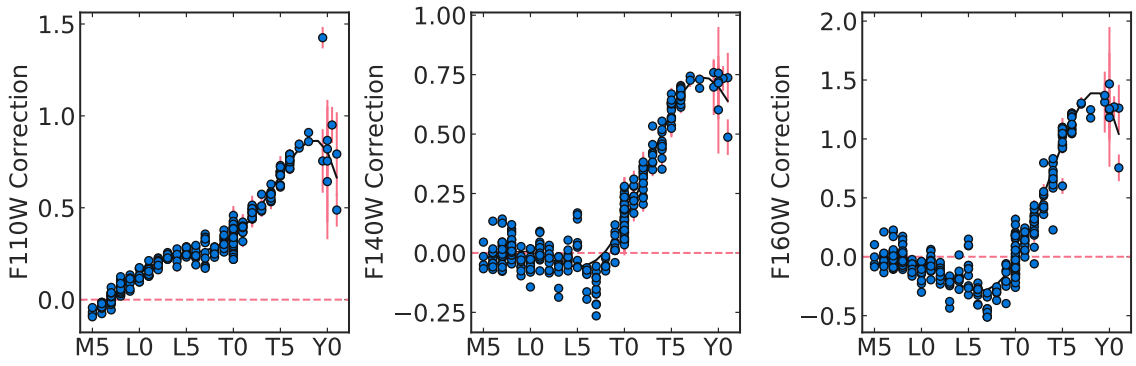

Figure 3.2 Magnitude offsets as a function of spectral type assuming a fixed J-SNR constraint. Black lines are fourth-order polynomial fits that take into account photometric uncertainties.

background source. In effect, we are able to probe to deeper magnitudes (and hence larger volumes) using a spectral, rather than photometric, selection criterion. To quantify this effect, we determined a limiting magnitude offset that varies with spectral type using the UCD template sample defined in Paper I. We scaled each spectrum to match the median flux in the J-SNR window of a standard M7 spectrum, which was assumed to have a negligible filter correction; then computed the relative magnitude in the $F110W$, $F140W$, and $F160W$ filters. Figure 3.2 displays these offsets with their corresponding polynomial fits. Magnitude offsets increase with later spectral type, reaching up to $\sim$1.5 mag difference among late T dwarfs in the $F160W$ band. These offsets were added to the limiting magnitudes per pointing and per spectral type in our subsequent analysis.

3.2.1 UCD Population Simulation

With the search volumes defined for each pointing, star counts can now be related to the luminosity function (LF), the number density of stars as a function of luminosity, brightness, temperature, or spectral type;[1] and its spatial variation (Galactic structure).

[1]Luminosity functions reported in the literature are variously measured with respect to luminosity ($\frac{dN}{d\log L}$ with units of pc^{-3} dex^{-1}), absolute magnitude ($\frac{dN}{dM_x}$ with units of pc^{-3} mag^{-1}), effective temperature ($\frac{dN}{dT_{\rm eff}}$

These functions in turn probe UCD formation mechanisms through the mass function and birthrate; UCD thermal evolution, particularly important for brown dwarfs; and UCD dynamical evolution in the Milky Way potential. All of these factors are interdependent; hence, we follow the approach of Burgasser (2004) in simulating UCD populations through a Monte Carlo approach.

3.3 Simulating the UCD Luminosity Function

The luminosity function of UCDs in the immediate Solar Neighborhood ($d \lesssim$ 20 pc), which largely samples the thin disk population, has been measured by several groups (Reid, 2003; Cruz et al., 2003; Cruz et al., 2007a; Bochanski et al., 2010; Metchev et al., 2008; Reyle et al., 2010; Kirkpatrick et al., 2012, 2019, 2021; Burningham et al., 2013; Bardalez Gagliuffi et al., 2019). These studies reveal a UCD LF that declines from the late-M to L dwarfs as we approach the hydrogen burning minimum mass; a minimum among the mid- and late-L dwarfs, composed primarily of warm and rapidly cooling brown dwarfs; and a rise among the T and Y dwarfs as brown dwarf evolution slows. A sharp peak in the observed LF at the L dwarf/T dwarf transition reported in Kirkpatrick et al. (2019) may be a consequence of delayed evolution due to thick condensate clouds (Saumon & Marley, 2008) or blended-light binaries (Burgasser 2007; see below). Integrated space densities in these samples range from $(12.6 \pm 0.6)\times10^{-3}$ pc^{-3} for M7–L5 dwarfs, $(0.5 \pm 0.3)\times10^{-3}$ pc^{-3} for L5–T6 dwarfs, and $\approx 10^{-3}$ pc^{-3} for T6–Y0 dwarfs (Kirkpatrick et al., 2012, 2021; Bardalez Gagliuffi et al., 2019). The observed LFs are qualitatively and quantitatively consistent with population simulations like those described here, albeit with continued uncertainty in the form of the underlying mass function, age distribution, and role of binaries due to small samples and persistent

with units of pc^{-3} K^{-1}), or spectral type ($\frac{dN}{d\mathrm{SpT}}$ with units of pc^{-3} subtype^{-1}) depending on implementation. We clarify the form of the LF used with a subscript; i.e., $\mathrm{LF}_{\mathrm{SpT}} = \frac{dN}{d\mathrm{SpT}}$.

incompleteness, even in the local volume.

In this analysis, we explicitly simulate the observed LF using assumptions of the mass function, age distribution, multiplicity, and evolutionary models. We note that Ryan & Reid (2016) use an alternative parameterized form of the local LF in their predictive study of UCDs in *JWST* pointings; however, this approach does not allow for evaluation of dependencies of the LF on the mass function or age distribution, nor the coupling between spatial and age distributions which can significantly modify the observed LF in deep samples.

For our baseline LF model, we generated a sample of 10^6 objects from a single power-law mass function parameterized by index α for masses nominally between $M_{\rm low}$ = 0.01 M and $M_{\rm high}$ = 0.15 M$\odot$:

$$P(M) = \frac{dN}{dM} \propto \left(\frac{M}{M_\odot}\right)^{-\alpha}. \tag{3.1}$$

We adopted $\alpha = 0.6$ based on results from Kirkpatrick et al. (2021) for the local field population, which is also consistent with the mass functions of UCDs in young clusters (Bastian et al., 2010). Masses were drawn from this distribution by inverting the cumulative distribution function

$$\mathrm{CDF}(M) = \int_{M_{\rm low}}^{M} P(m)dm \tag{3.2}$$

for $M \in [M_{\rm low}, M_{\rm high}]$, such that $M = \mathrm{CDF}^{-1}(x)$ for $x \in$ [0, 1]. We assigned ages using a uniform age distribution spanning 0.1–8 Gyr, which reasonably encompasses the local stellar population (Fouesneau et al., 2019).

To include the effects of multiplicity on our simulation, we assumed an overall binary fraction of 20% (Basri & Reiners, 2006; Burgasser, 2007; Fontanive et al., 2018),

and mass ratios $q \equiv M_2/M_1$ drawn from a power-law distribution

$$P(q) \propto q^{\gamma}. \tag{3.3}$$

We adopted $\gamma = 4$ based on the observed statistical distribution of resolved UCD binaries (Burgasser et al., 2006b) with $q \in [0,1]$. The 20% of simulated sources identified as binaries were assigned a secondary companion with mass $M_2 = qM_1$, and all binaries were assumed to be are unresolved and coeval.

Present-day physical parameters of effective temperature ($T_{\rm eff}$ in K), luminosity ($\log L_{\rm bol}/L_{\odot}$), surface gravity ($\log g$ in cm s^{-2}), and radius ($R/R_{\odot}$) were determined for all simulated sources and secondary components using a logarithmic interpolation of six evolutionary model grids: Burrows et al. (1997, hereafter B97), Burrows et al. (2001, hereafter B01), Baraffe et al. (2003, hereafter B03), the hybrid cloud models of Saumon & Marley (2008, hereafter SM08), the Sonora models of Marley et al. (2018, hereafter M18), and the equilibrium chemistry ATMOS models of Phillips et al. (2020, hereafter P20). A summary of the model set assumptions and parameter limits is given in Table 3.3. Note that some model parameter limits result in incomplete simulation samples (see discussion below). All models considered assume solar metallicity, which is appropriate given the dominance of field objects in our sample (Paper I).

Our observed sample is characterized by directly measurable quantities of spectral type and apparent magnitude; hence, it is necessary to convert simulated physical parameters into observable quantities. We used empirical relationships established from local UCD populations, specifically the spectral type to effective temperature scale of Pecaut & Mamajek (2013)[2] for objects earlier than L0; and that of Kirkpatrick et al. (2021) for L, T, and Y dwarfs. We accounted for the intrinsic scatter in these relations by

[2]https://www.pas.rochester.edu/~emamajek/EEM_dwarf_UBVIJHK_colors_Teff.txt.

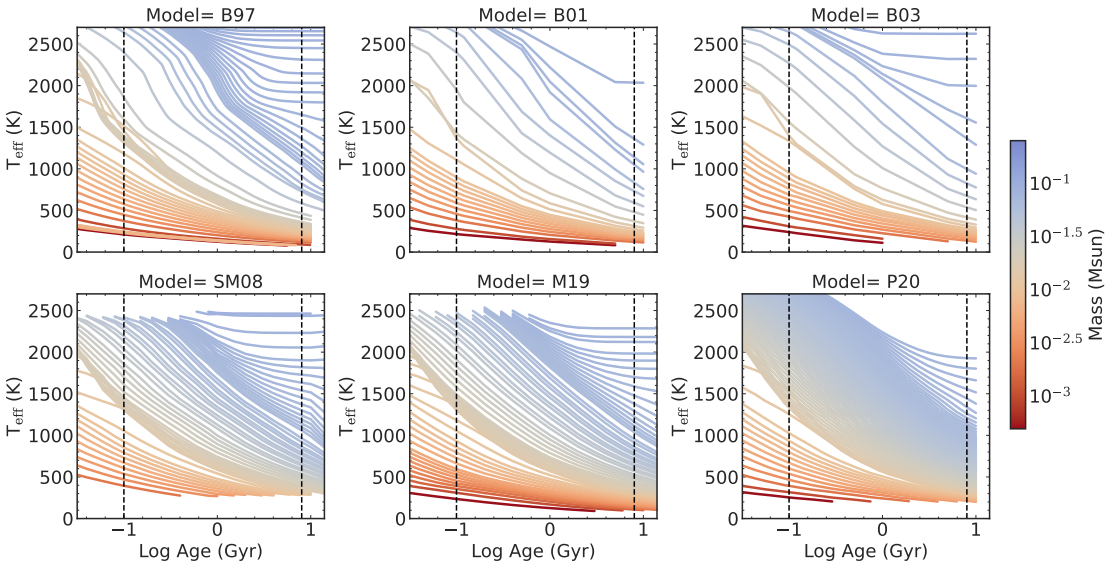

Figure 3.3 Evolutionary model grids used in this work plotted as effective temperature ($T_{\rm eff}$) versus age, with evolutionary isomass tracks color-coded by mass. Parameter limits of these models are listed in Table 3.3. Dashed lines show age limits for thin disk populations from 0.1 Gyr to 8 Gyr

random sampling.

For binary systems, we determined composite spectral types following the methodology of Burgasser (2007). We generated a sample of 104,776 binary templates from our SpeX template sample, scaling all spectra by their absolute MKO J magnitudes using the M_J/spectral type relations from Dupuy & Liu (2012) for M6-T8 dwarfs and from Kirkpatrick et al. (2021) for T8-Y1 dwarfs. All possible pairs for which a secondary is classified as late or later than the primary were added together. Each binary template's spectral type was then determined by comparing to spectral standards, as done for our observed targets (see Paper I).

Figure 3.4 compares the mean primary, secondary, and composite classifications based on this analysis. Composite spectral types are typically $\lesssim$0.5 subtypes later than the primary type for most spectral types, with the notable exception of early T dwarf composite systems, which are up to 2.5 subtypes later. This difference is the result of

the well-documented 1 μm "flux reversal" phenomenon at the L/T transition (Burgasser et al., 2002; Liu et al., 2006; Looper et al., 2008).

To scale our simulated distributions to accurately predict sample numbers, we compared our simulated effective temperature distributions[3] $\widetilde{\mathrm{LF}}_T$ to that reported by Kirkpatrick et al. (2021) for the local UCD population, sampling temperatures between 400 K and 2000 K in $\Delta T_{\rm eff}$ = 150 K bins. We computed a scale factor (α) that minimizes the χ^2 residuals between simulated and observed LFs based on the observational uncertainties σ_{LF}:

$$\alpha = \sum_{T_i=450\ K}^{T_i=2100\ K} \frac{\widetilde{\mathrm{LF}}_T \times \mathrm{LF}_T}{\sigma^2_{\rm LF}} \Big/ \sum_{T_i=450\ K}^{T_i=2100\ K} \frac{\widetilde{\mathrm{LF}}^2_T}{\sigma^2_{\rm LF}} \tag{3.4}$$

(cf. Cushing et al. 2005).

Figure 3.5 compares the observed and scaled simulated LF_T distributions for all six evolutionary models. There is general agreement between the models, with the exception of an extra peak in the SM08 models in the 1200–1350 K bin, which is detected in the observed LF_T of Kirkpatrick et al. (2021), as noted above. The absence of this feature in other evolutionary models suggests it more likely attributed to delayed evolution at the L/T transition than multiplicity. The simulations match the observed L dwarf and late-T/Y dwarf source densities, but slightly over-predict the number of mid-type T dwarfs (1000 K $\lesssim T_{\rm eff} \lesssim$ 1500 K). We also compared the J-band absolute magnitude luminosity functions (LF_J) of our simulations to measurements from Cruz et al. (2007b) and Bardalez Gagliuffi et al. (2019), after normalizing the simulations to the latter; and to the parameterized LF_J of Ryan & Reid (2016). Here we see significant differences between the model predictions at the brightest magnitudes, $M_J < 11$ (corresponding to spectral types <L0), largely due to parameter limits (e.g. the lack of stellar models in P20); and at the faintest magnitudes, $M_J > 13$, due to the restricted range of spectral types included in the Cruz et al. (2007b) and Bardalez Gagliuffi et al. (2019) samples.

[3]We denote simulated distributions with the $\widetilde{\mathrm{LF}}$ notation.

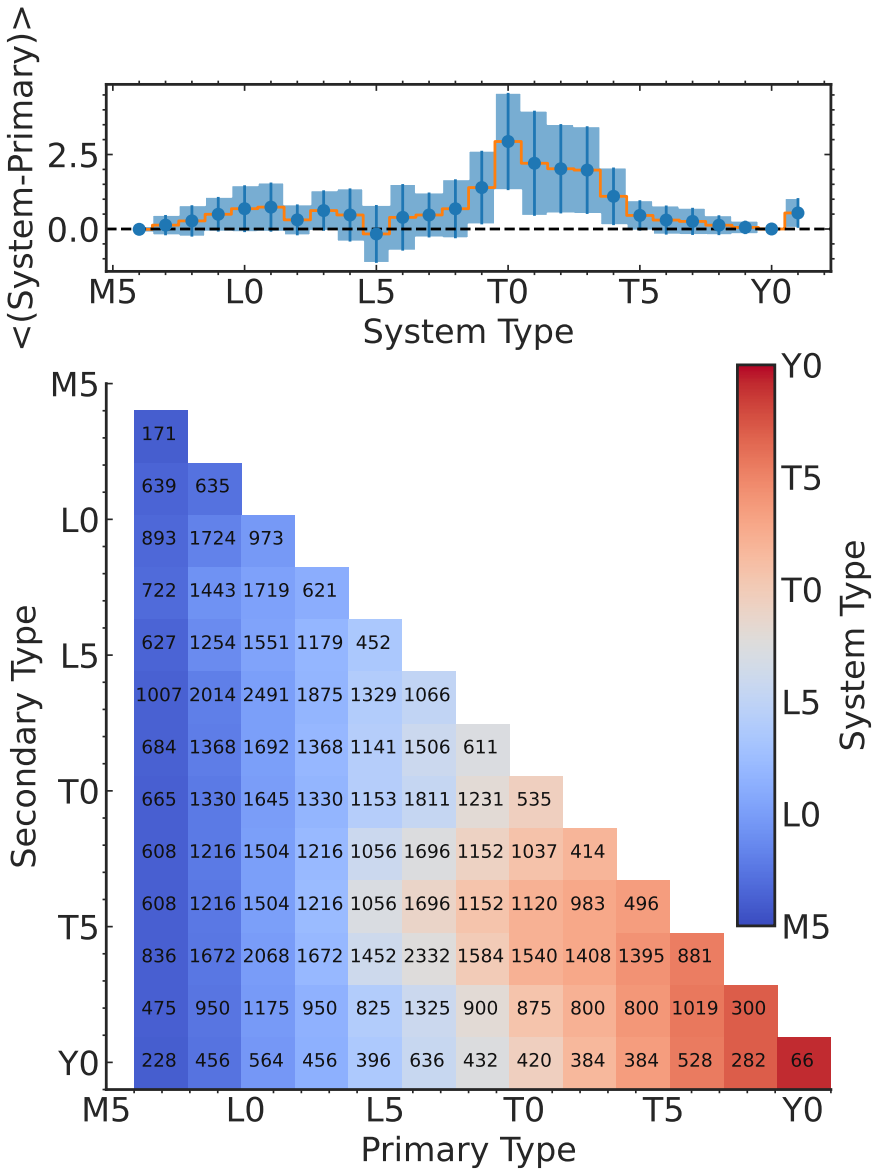

Figure 3.4 The larger deviation of system types at T0–T2 reflects the onset of CH_4 absorption and the well-documented 1 μm flux reversal at the L/T transition. Uncertainties (shaded region and error bars) reflect standard deviations among the simulated binaries. *Bottom panel*: Average near-infrared composite system spectral types for spectral binary templates as a function of primary and secondary classification. Note the shift toward later composite system types for mid-/late-L primaries and early-/mid-T secondaries. The number of template spectra in each bin is reported. Template spectra are scaled to their absolute M_J magnitudes.

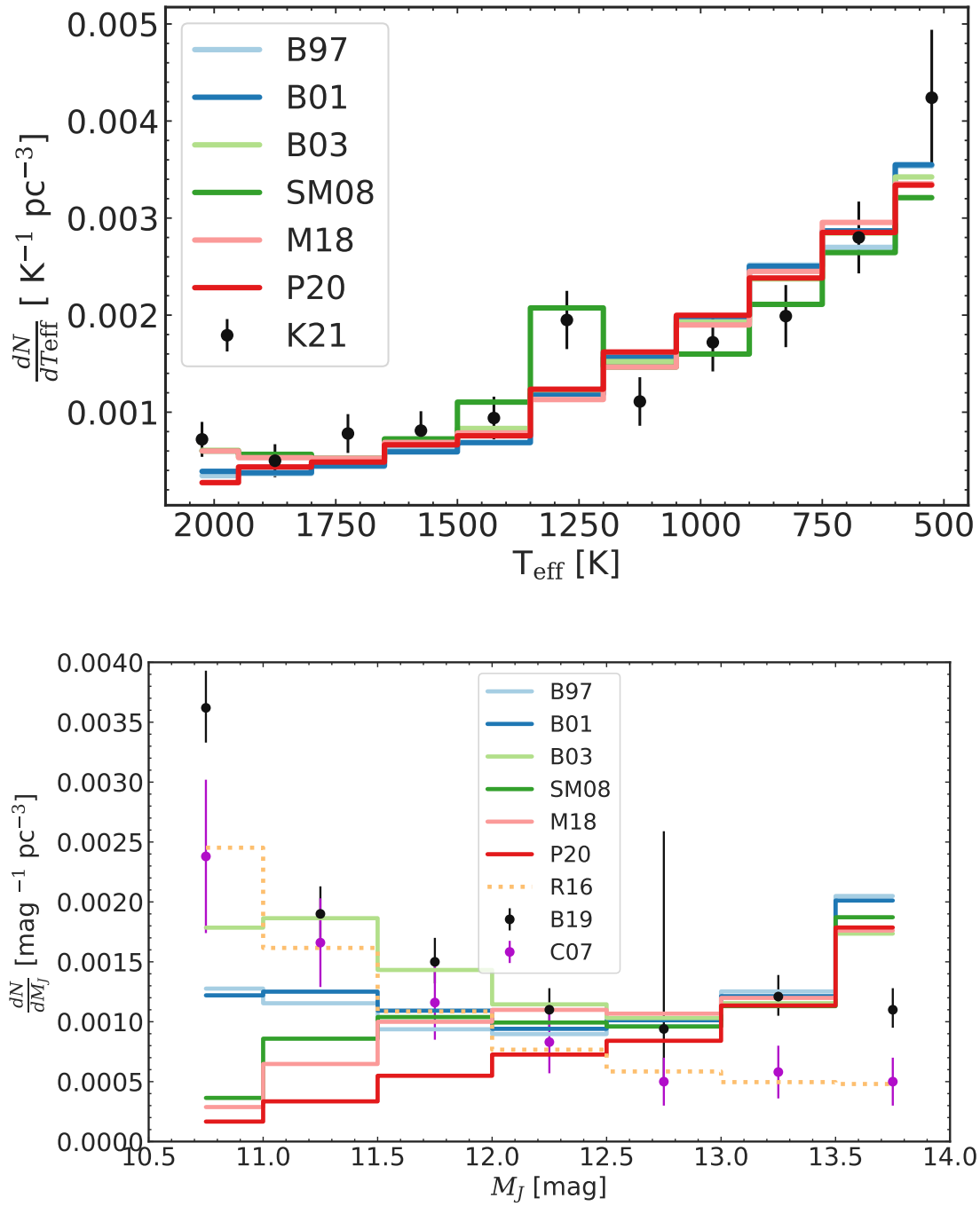

Figure 3.5 [(a) Comparison between our simulated luminosity functions as a function of $T_{\rm eff}$ ($\widetilde{LF}_T$) for different evolutionary models to the measured LF_T of Kirkpatrick et al. (2021, data points with error bars). Models correspond to Burrows et al. (1997, B97); Burrows et al. (2001, B01), Baraffe et al. (2003, B03); Saumon & Marley (2008, SM08); Marley et al. (2018, M18); and Phillips et al. (2020, P20). (b) Comparison between our simulated luminosity functions as a function of absolute J magnitude ($\widetilde{LF}_J$) to the observed LF_Js of Cruz et al. (2007b, magenta points with error bars) and Bardalez Gagliuffi et al. (2019, black point with error bars). The empirical relation of Ryan & Reid (2016) is also shown as a dashed line.

Absolute $F110W$, $F140W$, and $F160W$ magnitudes were assigned to each simulated source using the absolute magnitude/spectral type relations developed in Paper I. We accounted for scatter in these relations by including random offsets in the assigned magnitudes following a normal distribution. For binary systems, we computed combined-light magnitudes, by adding the fluxes of the individual primary and secondary to obtain a combined magnitude in all filters.

3.3.1 Effective Volumes

The number of sources $N(\mathrm{SpT})$ of a given spectral type detected in a field of view can be expressed as the product of the local number density of sources, $\rho_{\odot}(\mathrm{SpT})$, and the effective volume of that field, $V_{\mathrm{eff}}(\mathrm{SpT})$. The effective volume is defined here as the density-weighted volume probed in a given radial direction based on the underlying stellar density field $\rho(\vec{r})$,

$$V_{\mathrm{eff}}(\mathrm{SpT}) = \int_V \frac{\rho(\vec{r})}{\rho_{\odot}(\mathrm{SpT})}\, dV \approx \Delta\Omega \int_{d_{\min}(\mathrm{SpT})}^{d_{\max}(\mathrm{SpT})} \frac{\rho(\vec{r})}{\rho_{\odot}(\mathrm{SpT})} r^2 dr, \tag{3.5}$$

where $\vec{r}$ is the galactocentric position vector

$$\vec{r} = (X,Y,Z) = \big(R_{\odot} - r\cos(b)\cos(l), -r\cos(b)\sin(l), Z_{\odot} + r\sin(b)\big), \tag{3.6}$$

with $R_{\odot}$ = 8300 pc and $Z_{\odot}$ = 27 pc (Gillessen et al., 2009; Chen et al., 2001). $\Delta\Omega$ is the (assumed small) solid angle of the imaged field, equal to 4.1 arcmin^2 = 3.47$\times$ 10^{-7}radian^2 for each WFC3 infrared grism image; and r is heliocentric radial distance in the direction of Galactic latitude b and longitude l. This line integral is computed between limiting heliocentric radial distances $d_{\min}(\mathrm{SpT}) \leq r \leq d_{\max}(\mathrm{SpT})$ which are determined from the bright and faint magnitude limits of the image ($m_{\mathrm{bright,faint}}$; see §3.2)

and the absolute magnitude of the source, $M(\mathrm{SpT})$, in a given filter:

$$\log\left(\frac{d_{\mathrm{min,max}}}{10\ \mathrm{pc}}\right)(\mathrm{SpT}) = \frac{1}{5}(m_{\mathrm{bright,faint}} - M(\mathrm{SpT})) \tag{3.7}$$

with $M(\mathrm{SpT})$ in $F110W$, $F140W$, and $F160W$ based on the relations derived in Paper I (see above). We ignored reddening effects as all of the WISP and 3D-HST pointings are at high Galactic latitudes ($|b| > 15^{\circ}$). For each pointing, we adopted the smallest outer distance limit among the imaging filters used in that pointing.

We adopted as our stellar density field a single-component, axisymmetric, exponential disk model:

$$\rho(\vec{r}) = \rho(R,Z) = \rho_{\odot}\exp\left(-\frac{R-R_{\odot}}{L}\right)\exp\left(-\frac{|Z-Z_{\odot}|}{H}\right), \tag{3.8}$$

where R, Z are galactocentric cylindrical coordinates ($R^2 = X^2 + Y^2$); and L and H are the radial and vertical scaleheights, respectively. We adopted L = 2600 pc (Jurić et al., 2008), while stellar densities were computed for H = 100 pc, 150 pc, 200 pc, 250 pc, 300 pc, 350 pc, 400 pc, 450 pc, 500 pc, 600 pc, 800 pc, and 1000 pc. Figure 3.6 illustrates how the total effective volume varies as a function of spectral type and vertical scaleheight.

With effective volumes computed for each pointing, spectral type, and vertical scaleheight, we assigned specific pointings to each simulated source using V_{eff} as a weight factor. Specifically, we constructed cumulative distribution functions (CDFs) of the pointings by rank ordering the V_{eff}s for each spectral type and vertical scaleheight model. We conducted uniform draws from these CDFs to appropriately weight source locations with pointings that had larger effective volumes; i.e., those with longer exposure times (larger d_{max}) and lower Galactic latitudes (smaller $|Z - Z_{\odot}|$).

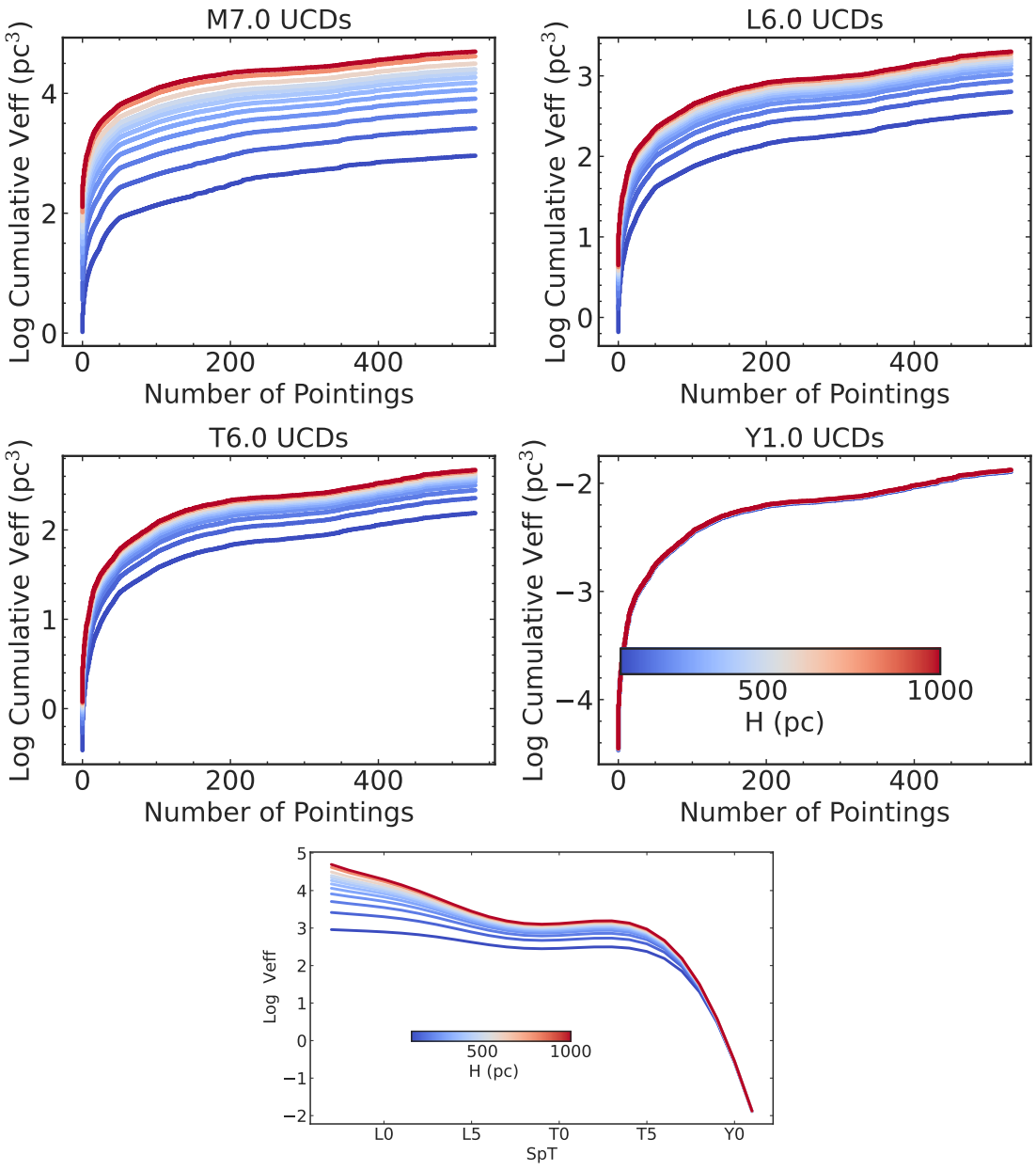

Figure 3.6 These were constructed as a rank ordering of $V_{\rm eff}$, such that pointings with larger effective volumes are toward the right of the distributions. The normalized forms of these distributions were used to assign pointings to our simulated sources. Note that the Y1 dwarfs show little Galactic scaleheight dependence as they are detected at close distances ($d < 10$ pc). (b) Total effective volume over all WISP and 3D-HST pointings as a function of spectral type for various vertical scaleheights.

Distances were assigned using the likelihood function

$$P(r,b,l) = \rho(\vec{r})r^2, \tag{3.9}$$

which was initially evaluated over the range $0.5d_{\rm min} < d < 2d_{\rm max}$ for each pointing and spectral type to account for sources scattered into the observed volume by photometric uncertainty or unresolved multiplicity. For each pointing and scaleheight, samples of $N = 10^5$ distances were generated by inverting the CDF associated with Equation 3.9 along a selected line of sight, which is equivalent to the normalized effective volume given by

$$\mathrm{CDF}(0.5d_{\rm min} < r < 2d_{\rm max}, b, l) = \frac{\int_{0.5d_{\rm min}}^{r} P(r,b,l)dr}{\int_{0.5d_{\rm min}}^{2d_{\rm max}} P(r,b,l)dr} \tag{3.10}$$

With these distances,individual apparent $F110W$, $F140W$, and $F160W$ magnitudes were computed and assigned.

To account for measurement uncertainties, we fit a linear relation to the magnitude uncertainties σ_m of all the point sources in the WISP and 3D-HST surveys as a function of filter magnitude (m) and log image exposure time (t_I),

$$\log\sigma_m = \alpha\left(m - m_0\right) - \beta\log\left(\frac{t_I}{1000\mathrm{s}}\right) + \log\sigma_0, \tag{3.11}$$

where m_0 = 19 and α, β, and σ_0 are fit parameters (Table 3.7). The magnitudes of each simulated source in all three filters are then estimated by drawing from a normal distribution with a spread equal to the appropriate magnitude uncertainty.

To appropriately model the observed spectra, we first determined a relationship between the source photometric magnitudes, grism integration times (t_{G141}), and J-SNR

values (Figure 3.7):

$$\log \text{J-SNR} = a\ (m - m_0) + b \log \frac{t_{\text{G141}}}{1000s} + \log J\text{-SNR}_0 \tag{3.12}$$

where again m_0 = 19 and a, b, and $J-\text{SNR}_0$ are the fit parameters. Here, m is the simulated magnitude with uncertainty included (Eqn. 3.11). Sources brighter than 15 mag were assigned a ceiling value of J-SNR = 500, while sources fainter than 25 were assigned a floor value of J-SNR = 1, matching the properties of the data. We assigned the minimum J-SNR value among the three imaging filters to each simulated source. The simulated apparent magnitudes and J-SNR ratios were both used to evaluate selection effects.

3.3.2 Selection Effects

Our selection of UCDs in the WFC3 sample using indices and line and spectral template fits, and the criteria used to narrow down the sample for visual confirmation, makes it likely that we rejected some fraction of UCDs present in the sample, particularly those with low S/N data. To quantify potential biases in this selection, we applied the selection criteria defined in Paper I to a sample of low-resolution UCD spectra of varying S/N to measure the recovery fraction as a function of spectral type and apparent magnitude. The simulation sample was generated from 20 of the highest S/N spectra (50 $<$ S/N $<$ 200) for each subtype between M7–T9 in our template sample. For Y dwarfs, we used all templates without a S/N cut. We reduced the S/N of each spectrum by adding uncorrelated Gaussian noise, creating 100 spectra per template with J-SNR $\geq$ 3.

For each of these test spectra, we computed the same indices and fit statistics, and applied the same selection criteria used to select UCDs from the WFC3 sample prior to visual confirmation, as described in Paper I. With perfect selection, we would expect to

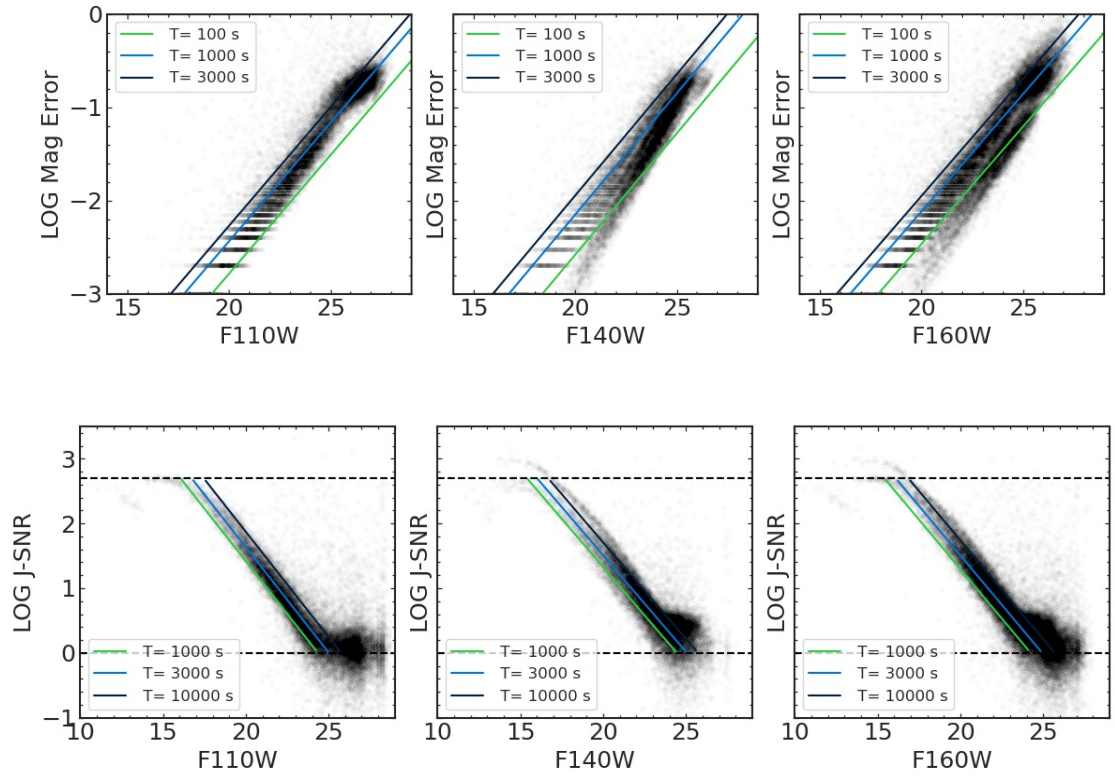

Figure 3.7 (a) Fits (straight lines) to apparent magnitude uncertainties for point sources in the WISP and 3D-HST surveys (black points) as function of magnitude for representative exposure times of 100 s (green), 1000 s (turquoise), and 3000 s (dark blue), for F110W (left), F140W (middle), and F160W (right) imaging data. (b) Fits (straight lines) to $J - SNR$ values for point source spectra (black points) as a function of apparent magnitude for representative exposure times and the three filters (same color scheme as panel a). The horizontal dashed lines indicate the minimum (J-SNR = 1) and maximum (J-SNR = 500) ranges over which the fits were made.

recover all spectra down to J-SNR = 3; in practice, we expect to lose some fraction of the noisiest spectra, which may depend on spectral subtype.

We defined a selection probability function ($\mathscr{S}$) as a function of J-SNR and spectral type as

$$\mathscr{S}(J\text{-SNR}_i, \text{SpT}) = \frac{N_{s,i}}{N_{tot,i}}, \tag{3.13}$$

where $N_{s,i}$ is the number of test spectra selected in a given spectral type and J-SNR bin i (bin sizes of 1 subtype and 2 steps in S/N, respectively), and $N_{tot,i}$ is the total number of test spectra in that bin. "Selection" in this case means that a source is selected as any kind of UCD; e.g, a simulated M7 selected as an M9 was counted as a successful selection. For the random forest and neural network models, we used the requirement of 80% classification probability to be selected (see Paper I).

Selection probability functions for the index-based, random forest, and neural network approaches are illustrated in Figure 3.8. As expected, the highest S/N spectra are selected across all spectral types, but we increasingly lose objects at lower S/N values as indices become unreliable. This is particularly true for earlier spectral classes where absorption features are weaker. Sources that did not reach any of the probability cutoffs for UCDs in our selection contribute to the low-selection regions for our machine learning methods. Note that a combination of selection criteria (as an "or" selection) reduces selection biases considerably, although this may result in much greater contamination.

With a selection probability assigned to each simulated source based on its estimated J-SNR and SpT, we computed the expected number of objects per spectral type in given pointing as

$$N_{\text{sim}}(\text{SpT}) = \rho_{\odot}(\text{SpT}) \cdot V_{\text{eff}}(\text{SpT}) \cdot \sum_i \mathscr{S}(J\text{-SNR}_i, \text{SpT}) \tag{3.14}$$

where the sum is over all values of simulated J-SNR for a given SpT.

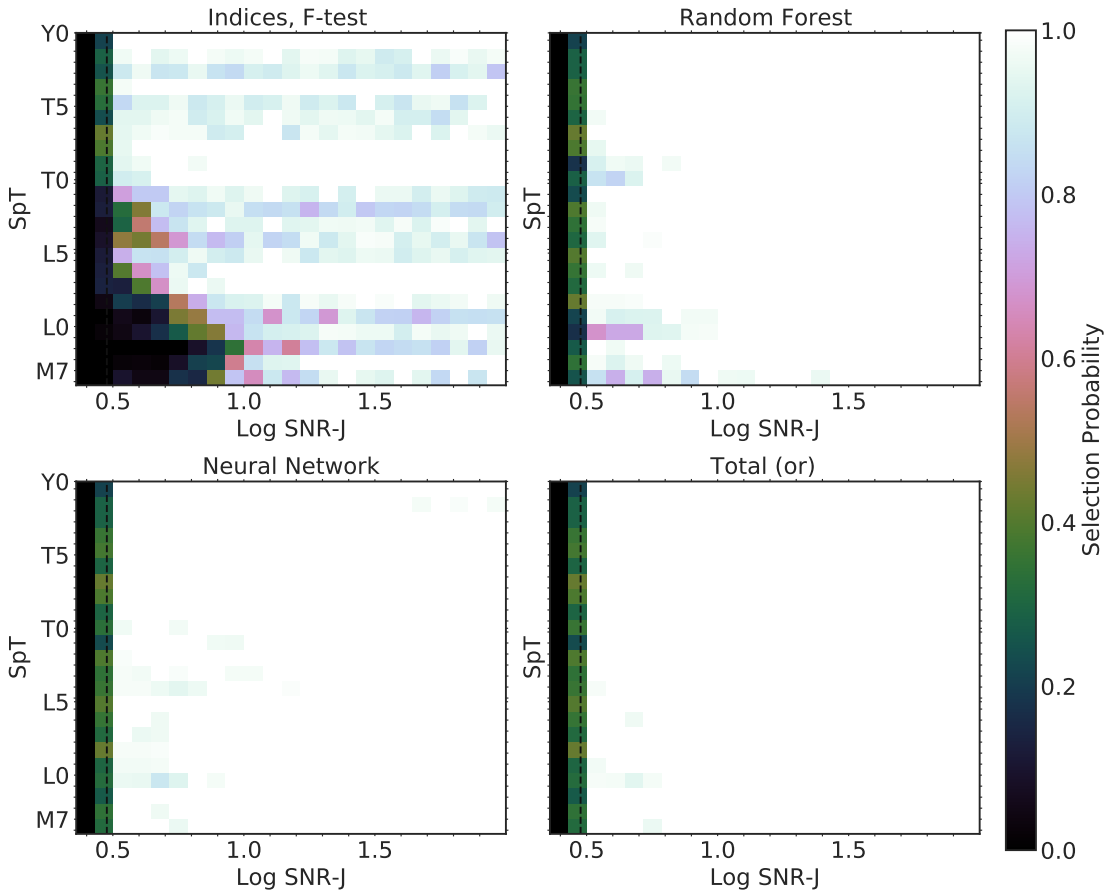

Figure 3.8 Selection probability functions for the index-based, random forest, and neural network selection methods as a function of spectral type and J-SNR. For the random forest and neural network models, we assumed a classification probability of 80% is required.

We compare these predicted number counts to the observed numbers of UCDs for each model and scaleheight in Figure 3.9. The observed number of UCDs in this case is not the full sample of 164 reported in Paper I, but only those sources with magnitudes brighter than the completeness limits of their respective fields in at least one of the $F110W$, $F140W$ or $F160W$ filters, accounting for the spectral type-based correction described in Section 2.2 and displayed in Figure 3.2. The resulting comparison sample is composed of 98 UCDs, including 76 late-M dwarfs, 18 L dwarfs, and 4 T dwarfs, and has the same selection criteria imposed as our simulated sample.

3.3.3 Contamination from the Thick Disk Population

Our population simulations are designed specifically for the thin disk population, and hence will not account for thick disk or halo sources in the WFC3 survey data. To assess the contribution of the thick disk population to our sample, we performed a parallel population simulation, assuming the same mass range and distribution, a uniform age distribution spanning 8–10 Gyr (Kilic et al., 2017), and a fixed vertical scaleheight of $H = 900$ pc (Jurić et al., 2008). While thick disk stars are typically metal-poor and older than 10 Gyr (Gilmore et al., 1995; Haywood et al., 2013b; Hawkins et al., 2015; Mackereth et al., 2017; Sharma et al., 2019), we use these solar-metallicity B03 evolutionary models and locally-defined empirical calibrations as a first-order assessment. Scaling the local number density to be 12% that of the thin disk (Jurić et al., 2008), we estimate 36.7 M7–M9 dwarfs, 6.9 L0–L4 dwarfs, 0.3 L5–L9 dwarfs, and $\lesssim$1 T and Y dwarfs in the WFC3 sample. We note that none of the UCDs identified in Paper I were matched to metal-poor subdwarf templates ([M/H] $\lesssim -1$) in the index selection analysis, although modest degrees of metal deficiency ([M/H] $\lesssim -0.5$) are likely undetectable in these data (Aganze et al., 2016). The lack of proper motion information for the vast majority of the sample also prevents us from assessing the thick disk contribution through

kinematics (Bensby et al., 2003b). Hsu et al. (2021) finds that the fraction of intermediate thin-disk/thick disk objects for UCDs ranges from 3-8% based on the 3D-kinematics of the nearby (d<20 pc) UCD sample. However, these data are limited to the local volume and we expect to see a larger fraction of thick disk stars at larger distances and high galactic latitudes. Pirzkal et al. (2009) and van Vledder et al. (2016) estimate a local thick disk fraction of M dwarfs to be 5%–7.5% (Table 3.8). Because of their small contribution to the sample, we chose to account for potential thick disk contamination by statistically removing these sources from our sample, rather than explicitly modeling in thick disk stars. We also ignore the contribution of halo UCDs in our sample given that the local ratio of halo to thin disk stars is smaller still (0.25%–0.75%; Pirzkal et al. 2009; van Vledder et al. 2016).

3.4 Results

3.4.1 Number Counts

Figure 3.9 compares the predicted number of ultracool dwarfs in the combined WISP and 3D-HST samples for different evolutionary models and assumed scaleheights to our observed number counts. The number counts for each subtype range is a result of competing effects between the effective volume and luminosity function, as illustrated in Figures 3.6 and 3.5. Number counts of earlier-type UCDs (late-M and L dwarfs) are higher due to their greater limiting distances and larger volumes, while the number counts of later-type UCD (T and Y dwarfs) are determined by their smaller volumes and the rise in the luminosity function. The overall trend is a monotonic decrease in number counts as a function of increasing spectral type, with a slight bump for early T dwarfs.

We see general agreement between the observed number counts and the predictions from the various evolutionary models, particularly for the L and T dwarfs. For the

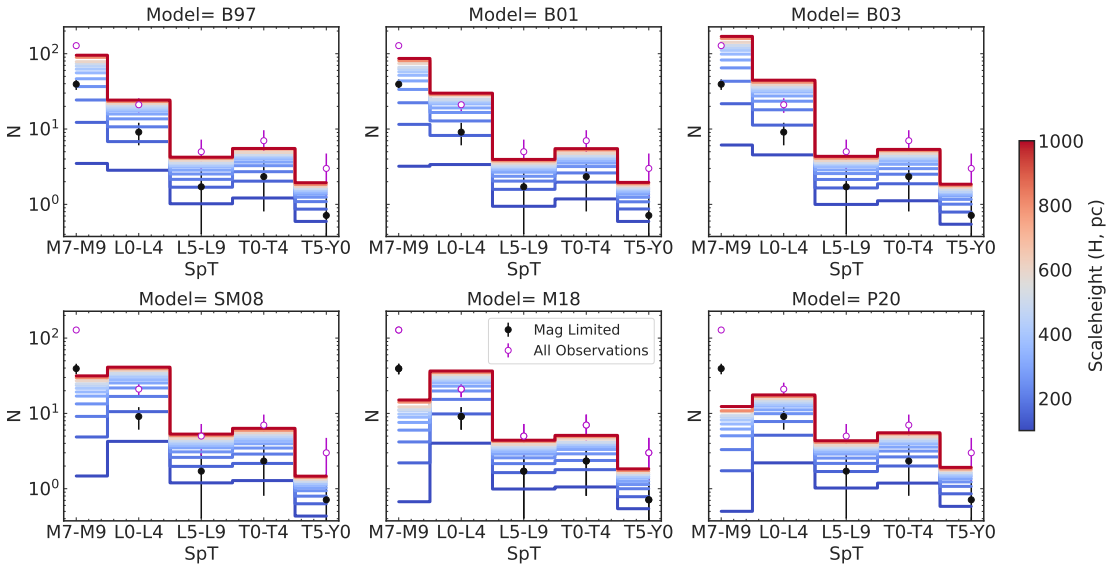

Figure 3.9 Measured ultracool dwarf source counts in the combined WISP and 3D-HST fields (points with error bars) compared to predicted counts from our population simulations (histograms) for various evolutionary models (different panels) and assumed scaleheights (color scale). Number counts of for our comparison sample of 98 UCDs with magnitudes brighter than the field completeness limits are shown in black points, while the full sample of 164 UCDs are shown as white points. In both cases, the estimated number of contaminating thick disk objects, assuming a thin:thick ratio of 12%, has been subtracted to focus only on the thin disk predictions. Models correspond to Burrows et al. (1997, B97); Burrows et al. (2001, B01); Baraffe et al. (2003, B03); Saumon & Marley (2008, SM08); Marley et al. (2018, M18); and Phillips et al. (2020, P20)

M7–M9 dwarfs, there are pronounced mismatches between the data and predictions from some of the models, which can be attributed to model mass and temperature parameter limits. Only the B97, B01 and B03 models encompass objects massive enough and hot enough to fully cover this spectral type range, so we restrict our analysis of the M7–M9 subtype group to these models.

3.4.2 Vertical Scaleheight

To quantify estimates of the ultracool dwarf scaleheight, for each evolutionary model and spectral type subgroup, we computed a mean scaleheight by convolving the probability distribution of observed number counts with a monotonic interpolation of scaleheight as a function of predicted number counts $H(N)$, as illustrated in Figure 3.10. The distribution of number counts was modeled as a continuous Poisson distribution[4] assuming the observed number of thin disk sources ($N_{\rm thin}$) to be an accurate estimate of the expected number of sources (N):

$$P(N) \propto \frac{N^{N_{\rm thin}-1}}{\Gamma(N_{\rm thin})} \exp(-N) \tag{3.15}$$

where Γ is the Gamma function.

Note that the observed number of thin disk sources N_{thin} is equal to number of observed sample sources minus the predicted number of thick disk stars, $N_{thin} = N_{obs} - N_{thick}$ (Section 3.3.3). Drawing 10^5 samples per model and spectral type subgroup, we inferred the distribution of scaleheights as

$$P(H) = H(P(N)) \tag{3.16}$$

The median values and 16% and 84% quantile uncertainties of these distributions are

[4] https://docs.scipy.org/doc/scipy/reference/generated/scipy.stats.gamma.html#scipy.stats.gamma

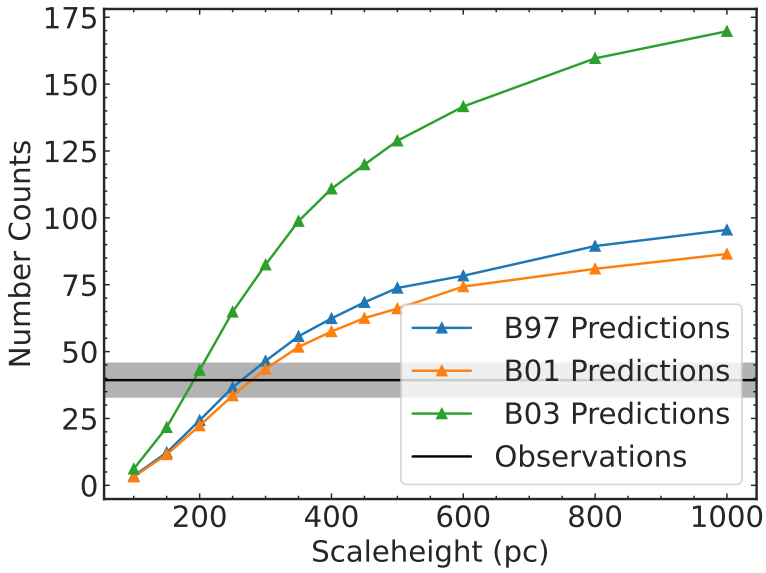

Figure 3.10 Interpolation of predicted number counts as a function of scaleheight for M7–M9 dwarfs. Predicted number counts are shown for the Burrows et al. (1997, B97; blue triangles), Burrows et al. (2001, B01; orange triangles); and Baraffe et al. (2003, B03; green triangles) evolutionary models. The black line and gray band indicates the measured number count of M7–M9 dwarfs and Poisson error.

given in Table 3.4 for each model and spectral type group. We also computed median values for scaleheights per spectral type group across all models, with the exception of the M7–M9 subtype group for which we combined only the B97, B01 and B03 models.

We observe overall consistency between model predictions, with differences generally smaller than the Poisson uncertainties of the sample. One exception is the P20 model predictions for L0–L4 dwarfs, caused by the substellar upper mass limit of these models and corresponding absence of evolutionary tracks for $T_{\rm eff} \gtrsim 2000$ K at ages $\gtrsim 1$ Gyr (Figure 3.3). These models were excluded in determining median values for this spectral subgroup. We also find significant differences in the inferred values of the M7–M9 dwarfs between the B97 and B01 models and the B03 models, which likely arise from differences in the evolutionary models themselves, rather than parameter limits. Since we have no *a priori* reason to prefer one model set over the other (however, see

Section 3.4.4), we retain values from all three models, and our median values integrate the systemic uncertainty arising from the model differences. Finally, although the local luminosity function predicts a bump at 1350 K (early T subtypes) specifically for SM08 models, we see a small rise in numbers for all models, so this model-dependent effect does not play a measurable role in the predicted scaleheights for our coarse subtype groupings.

Comparing our results to previously reported measurements, for the M7–M9 dwarfs we infer a vertical scaleheight of $H = 249^{+48}_{-61}$ pc, which is low but statistically consistent with values reported for late-M dwarf samples in deep *HST* fields by van Vledder et al. (2016, $H = 290 \pm 20$ pc for 274 M dwarfs), Ryan et al. (2005, $H = 350 \pm 50$ pc for >M6 dwarfs), Pirzkal et al. (2009, $H = 370 \pm 60$ pc for M4–M9 dwarfs), and Holwerda et al. (2014, $H = 400 \pm 100$ pc for M5–M9 dwarfs). Our results are also consistent with measurements from ground-based SDSS data reported in Bochanski et al. (2010, $H = 300 \pm 15$ pc for M0–M8 dwarfs) and SDSS-UKIDSS data reported in Warren et al. (2021, $H \approx 270$ pc for 32,942 M dwarfs). One explanation for the lower values of thin disk scaleheights for late-M dwarfs inferred in this study compared to other deep *HST* fields is a potential overestimation of the local fraction of thick disk objects in our sample. Additional constraints assuming a thick disk fraction of 5% are provided Table 3.5. These latter values, averaging to 361^{+112}_{-125} pc, are more in agreement with previous deep *HST* field results, and indicates an inherent degeneracy between the thick disk fraction and inferred thin disk scaleheight. We will see later, however, that a small thick disk contamination is not favored in our age analysis, and for the remainder of this study, we report results that assume a thick disk fraction of 12%.

Our overall scaleheight estimates for L dwarfs ($H = 153^{+56}_{-30}$ pc) and T dwarfs ($H = 175^{+149}_{-56}$ pc) are considerably smaller than those previously inferred from deep *HST* ($H = 350 \pm 50$ pc; Ryan et al. 2011) and ground-based ($H \approx 450$ pc; Carnero Rosell

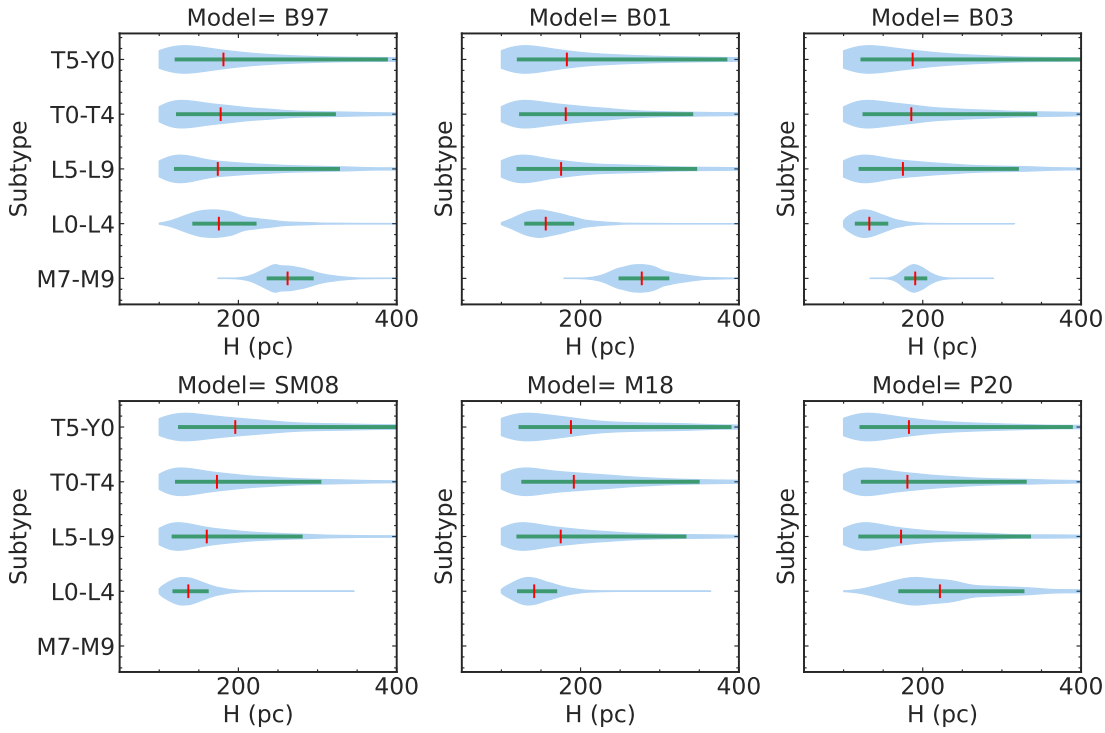

Figure 3.11 Probability distributions of scaleheights inferred from our sample (red violin plots) based on Poisson errors and scaleheight/number count relation. Median values are indicated by vertical red bars and their 16% to 84% quantile range are displayed as red horizontal bars. The extended shapes of these distributions for spectral types $>$ L5 reflects the intrinsic sampling uncertainty from the small numbers of these bins.

et al. 2019) photometric surveys of these objects. Our results are in qualitative agreement with the predictions of Burgasser (2004) and Ryan et al. (2017) who argued that brown dwarf evolutionary effects would drive down the vertical scaleheight of late-L and early-T dwarfs compared to late-M dwarfs. The large uncertainties on our scaleheights for these cooler objects, driven by the small sample of L and T dwarfs identified, limit our ability to explore these differences with this sample.

3.4.3 Velocity Dispersions

The scaleheight, velocity dispersion, and age of a stellar or substellar population in the Galaxy are inter-dependent. Older stars tend to have larger kinematic dispersions

and occupy a disk with a larger scaleheight (Sanders & Das, 2018; Bovy, 2017). This trend can be explained by cumulative dynamic interactions with structures in the Galaxy such as giant molecular clouds or spiral arms (Spitzer & Schwarzschild, 1953; Lacey, 1984; Sellwood & Binney, 2002), or dynamical heating due to past merger events (Toth & Ostriker, 1992; Hopkins et al., 2008; Martig et al., 2014; Minchev et al., 2015; Ma et al., 2017; Buck et al., 2020).

To infer population ages for each of our spectral subgroups, we first converted scaleheights into total velocity dispersions using a relationship based on the analytical model of van der Kruit (1988),

$$H = \zeta_n \frac{\sigma_{20}^2}{\Sigma_{68}} \tag{3.17}$$

where σ_{20} is the vertical velocity dispersion in units of 20 km s^{-1}, Σ_{68} is the surface mass density of the Galactic disk in units of 68 M pc^{-2} (Bovy & Rix, 2013), and ζ_n is a normalization constant based on the parametric form of the vertical mass density $\rho(z)$:

$$\rho_n(z) = 2^{-2/n} \rho_0 \, \mathrm{sech}^{2/n} \left(\frac{nz}{2H} \right). \tag{3.18}$$

Our simple exponential disk corresponds to $n = \infty$ and ζ_n = 435 pc (Ryan et al., 2017).

Converting our scaleheights into velocity dispersions using these relations (Table 3.4), we compared these inferred dispersions to dispersion measurements from local UCD samples ($d < 20$ pc). Our median estimate of σ_W = $15.1^{+1.4}_{-2.0}$ km s^{-1} for M7–M9 dwarfs is consistent with dispersions reported by Burgasser et al. (2015, $\sigma_W = 13.8 \pm 0.3$ km s^{-1}) and Hsu et al. (2021, $\sigma_W = 16.3 \pm 0.3$ km s^{-1}). In contrast, our median estimate of σ_W = $11.6^{+1.5}_{-1.1}$ km s^{-1} for L0–L4 dwarfs is significantly lower than the measured dispersion reported by Burgasser et al. (2015, $\sigma_W = 19.5 \pm 0.4$ km s^{-1}) for this subtype group. In this case, there is evidence that the local population of L dwarfs is significantly contaminated by older, thick disk sources, and Hsu et al.

(2021) report a smaller thin disk L dwarf dispersion, $\sigma_W = 15.3 \pm 0.3$ km s^{-1} which is still higher than our estimate of σ_W = $11.8^{+2.0}_{-1.2}$ km s^{-1} for our overall L dwarf sample. We find agreement between our median estimate of σ_W= $12.7^{+4.6}_{-2.2}$ km s^{-1} for T dwarfs and the local measurement of $\sigma_W = 13.3 \pm 0.4$ km s^{-1} by Hsu et al. (2021), albeit with substantial uncertainties in our value due to small number statistics.

3.4.4 Ages

We transformed velocity dispersions into ages using a power-law age-velocity dispersion relation (AVR) of the form;

$$\sigma_W(\tau) = \sigma_0 \left(\frac{\tau + \tau_{\rm min}}{\tau_{\rm min} + \tau_{\rm max}} \right)^{\beta_z} \tag{3.19}$$

where σ_0 is the velocity dispersion at $\tau_{\rm max}$, $\tau_{\rm min}$ and $\tau_{\rm max}$ define the epochs of initial and maximal velocity dispersions, and β_z is a power-law index that quantifies the rate of dispersion increase. We used the best-fit model parameters from Aumer & Binney (2009) without a low-metallicity tail: $(\beta, \sigma_0, \tau_{\rm min}, \tau_{\rm max})$ =(0.445, 23.831 km s^{-1}, 0.001 Gyr, 10 Gyr).

Inferred ages and associated uncertainty distributions (based on Monte Carlo sampling) for each spectral subgroup and model are listed in Table 3.4 and illustrated in Figure 3.12. In the Figure, we also show the distribution of the median age from the original simulations. To estimate this distribution, we randomly sampled N_{thin} objects from the simulation for a given spectral type range and computed the median age, where N_{thin} corresponds to the observed sample N_{obs} minus the estimated thick disk contamination N_{thick} (Tables 3.4 and 3.5). This process was repeated 10^4 times to estimate the sampling uncertainty in the simulated median age. Different evolutionary models display similar patterns in age versus spectral type grouping, with M7–M9 dwarfs

(mostly stars) and T5–Y1 dwarfs (all brown dwarfs) having near-uniform ages, while L0–L4 dwarfs (mixed stars and brown dwarfs) are skewed toward younger ages.

To test more generally whether the distributions of simulated ages agree with age distributions inferred from number counts, we computed the overlapping probability using Kolmogorov–Smirnov (KS) test, which measures the probability that two distributions are distinct. We find *KS* values are generally $\leq$0.5, indicating good to modest agreement between simulated and inferred age distributions. There are significant deviations between simulated and inferred ages for M7–M9 and L0–L4 subtypes which may indicate errors in the evolutionary models themselves, with some models having smaller inferred ages compared to simulated ages (B03, SM03, M18) and others larger ages (B97, B01, P20). These systematic differences between the models are worse when a lower thick disk fraction is considered (Table 3.5), favoring a 12% fraction. We note that the largest deviation between inferred and simulated ages occurs for the P20 models applied to the L0–L4 dwarf sample, and for all models applied to the M5-M9 sample. We attribute these mismatches to the parameter limits in the models, an incorrect assumption of the thick disk fraction or systematic uncertainties in age-velocity dispersion relations. Nevertheless, we find reasonable agreement between the inferred and the median simulated ages for L and T dwarfs, albeit with significant uncertainties due to small number statistics among the latest spectral class groups.

Our age estimates for UCDs based on scaleheights can be compared to kinematic age estimates from the local population. Our median M7–M9 dwarf age estimate of $3.6^{+0.8}_{-1.0}$ Gyr based on the Aumer & Binney (2009) AVR is consistent with kinematic estimates from Burgasser et al. (2015, 4.0 ± 0.2 Gyr) and Hsu et al. (2021, 4.1 ± 0.3 Gyr).

For L0–L4 dwarfs, our estimate of $2.0^{+0.6}_{-0.4}$ Gyr is substantially lower than the (likely contaminated) 6.5$\pm$0.4 Gyr kinematic age inferred by Burgasser et al. (2015), and our age estimate for all L dwarfs, $2.1^{+0.9}_{-0.5}$ Gyr, is also significantly lower than the

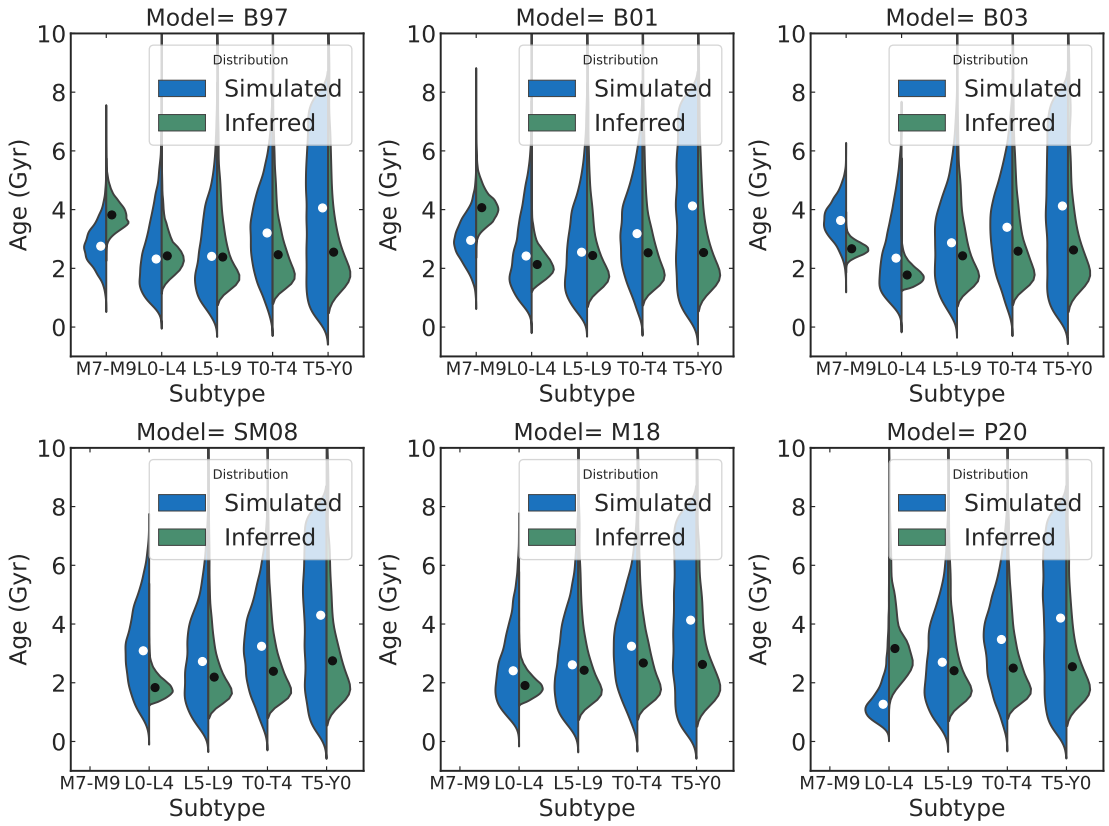

Figure 3.12 Comparison between the distribution of simulated median ages (blue shaded regions on left) and the median age estimates for our *HST* ultracool dwarf sample based on scaleheight determinations (olive shaded regions on right) and the Aumer & Binney (2009) AVR. Median values for each distribution are indicated by white and black circles, respectively. Note that the SM08, M18 and P20 number count predictions are unreliable for M7–M9 dwarfs due to model parameter limits, and are not displayed.

kinematic age of thin disk L dwarfs of 4.2 ± 0.3 Gyr from Hsu et al. (2021). Our estimate of $2.4^{+2.4}_{-0.8}$ Gyr for T dwarfs is lower than but formally in agreement with the kinematic age of 3.5 ± 0.3 Gyr from Hsu et al. (2021), albeit again with significant uncertainties.

The absolute kinematic ages reported here and in other population studies must be considered carefully, as they are significant systematic issues to be considered when mapping spatial or kinematic distributions to population ages. Generally, these arise from the fact that populations formed in distinct environments and residing in different regions of the Galaxy undergo different kinematic heating histories (Aumer et al., 2016;

Bovy et al., 2012a; Mackereth et al., 2019b; Sharma et al., 2021). Relations connecting quantities such as age, velocity dispersion, and spatial distribution measured locally may not apply to populations located at large vertical distances from the Galactic plane or in different radial zones. More succinctly, the AVRs derived from different stellar samples do have significant variations. The AVR of Aumer & Binney (2009), which is used in prior UCD population analyses (Burgasser et al., 2015; Ryan et al., 2017; Hsu et al., 2021), is based on ≈15,000 main-sequence stars with distances up to ∼300 pc from the Sun selected from the Geneva Copenhagen Survey (GCS, Nordström et al. 2004; Holmberg et al. 2007) and *Hipparcos* (van Leeuwen, 2007) catalogs, with isochronal ages based on the Bertelli et al. (2008) models. We examined the AVRs of two other stellar samples to examine systematic effects, both of which use a model of the same form as Equation 4.1. The AVR of Just & Jahreiß (2010, J10) is based on a sample of main-sequence GCS and *Hipparcos* stars, with additional sources from Jahreiß & Wielen (1997), sampling distances up to ∼200 pc from the Sun. Following a similar method as A09, J10 model the observed number counts, kinematics, ages and metallicities assuming an initial mass function, star formation rate, and metallicity distribution in a fully-consistent model of the Galaxy, but with different parameterizations of the star formation rate and gravitational potential. The resulting AVR best-fit parameters are $(\beta, \sigma_0, \tau_{\rm min}, \tau_{\rm max})$= (0.5, 29.9 km/s, 0.5 Gyr, 12 Gyr). The AVR of Sharma et al. (2021, S21) is based on a large sample of ∼840,000 main-sequence turnoff and red-giant stars out to distances of 2 kpc from the Sun (Sharma et al., 2018, 2019), with measurements from GALAH (De Silva et al., 2015), LAMOST (Zhao et al., 2012), APOGEE (Hayden et al., 2015), the Transit Exoplanet Survey Satellite (TESS, Ricker et al. 2014) catalog, the High Efficiency and Resolution Multi-Element Spectrograph (HERMES, Sheinis et al. 2015), and the *Kepler/K2* mission (Borucki et al., 2010; Howell et al., 2014). Ages were derived from isochronal fitting and astroseismology, and the resulting AVR best-fit

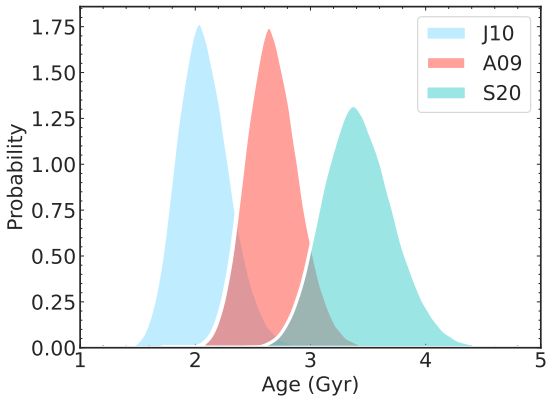

Figure 3.13 Comparison between the inferred age distributions for M7-M9 dwarfs in our sample based on the AVRs of Just & Jahreiß (2010, J10), Aumer & Binney (2009, A09), and Sharma et al. (2021, S21). The J10 relations tend to predict the youngest ages while the S21 relations tend to predict the oldest ages. These distributions are based on the Baraffe et al. (2003) evolutionary models.

parameters are $(\beta, \sigma_0, \tau_{\rm min}, \tau_{\rm max})$= (0.441±0.007, 21.1±0.2 km/s, 0.1 Gyr, 10 Gyr). As indicated in Tables 3.4 and 3.5, and illustrated in Figure 3.13, the J10 relation consistently yields ages that are older than A09 by ∼1–1.5 Gyr while the S21 relation consistently yields ages that are younger by ∼0.5–1 Gyr, implying an overall systematic uncertainty on absolute ages of 1–2 Gyr. Despite this, all three relations predict the same relative trends in inferred ages across UCD spectral subgroups; they all find that the late M dwarfs are older than the L and T dwarfs. Thus, while absolute ages of UCD populations may be uncertain, the relative age differences predicted by the simulations are confirmed by our scaleheight measurements.

3.5 Predictions for the *JWST* PASSAGE Survey

In this series, we have examined the largest deep UCD spectral sample compiled to date, composed of 164 late-M, L, and T dwarfs with 1.1–1.7 μm low-resolution spectra. While reaching to kpc distances for the warmest late-M and L dwarfs, this

sample nevertheless provides relatively weak constraints on the scaleheights and ages of the coldest brown dwarfs due to sensitivity and sample size limits. It is therefore useful to explore how deeper surveys planned for the recently launched *James Webb Space Telescope (JWST)* will improve upon these UCD population measurements. Ryan & Reid (2016) and Holwerda et al. (2018) have previously explored UCD source counts and identification in deep *JWST* imaging surveys; here we explore the expected yield from deep grism spectroscopic surveys, specifically the Parallel Application of Slitless Spectroscopy to Analyze Galaxy Evolution survey (PASSAGE, *JWST* Cycle 1 GO-1571, PI Malkan, Malkan et al. 2021). This survey aims to study star formation across cosmic time by obtaining slitless grism spectra and imaging data in the F115W (0.9-1.3 μm), $F150W (1.3 - 1.7 \mu m)$, and F200W (1.7-2.2 μm) passbands using the Near Infrared Imager and Slitless Spectrograph (NIRISS; Doyon et al. 2012; Willott et al. 2022) over various pointings at high Galactic latitudes ($|b| > 20^o$), with a goal of observing a total area of 0.16 deg^2. By increasing the depths to J = 27 (AB), this survey will produce a substantially deeper UCD sample. Several proposed programs with JWST are expected to reach comparable depths (Robertson, 2021).

To simulate the expected number counts of UCDs in this survey, we followed a similar procedure as outlined in Section 3.2.1. The PASSAGE survey pointings are yet to be determined, so we chose a set of 124 random pointing at Galactic latitudes $|b| > 20^o$. We computed absolute magnitude/spectral type relations in the *JWST*/NIRISS filters using the methods described in Paper I (see Table 3.9), and assume a limiting magnitude of 27 (AB) in all three filters. We adopted the simulation parameters for the thin and thick disk population detailed in Table 3.2, using two vertical thin disk scaleheights (200 pc and 400 pc) that grid our results, and a common mass function between the thin disk, thick disk, and halo populations.

For the halo population, we assumed a flattened spheroid density distribution

$$\rho_{\rm halo} = \left(\frac{R_{\odot}}{(r^2 + (z/q)^2)^{\frac{1}{2}}} \right)^n$$

with parameters q=0.64 and n=2.77, a halo/thin disk density ratio of of 0.25% (Jurić et al., 2008), and a uniform age distribution of 8-10 Gyr. Halo stars are typically older than 10 Gyr (Jofré & Weiss, 2011b; Guo et al., 2019); however, models do not cover this parameter range. Additionally, while both thick disk and halo stars and brown dwarfs are metal-depleted compared to the thin disk, there is a lack of publicly-available metal-poor evolutionary models for UCDs that span the late-M, L, T, and Y dwarf temperature range, so we deployed the solar-metallicity models of B01 and B03 to evolve our simulated sources. We follow the same procedure outlined in Section 3.2.1 by accounting for the binary fraction of UCDs, and the intrinsic scatter in the spectral type-temperature and absolute magnitude-spectral type relations. We do not account for additional selection effects; however, we require that all sources should be detectable in F115W and F150W filters down to a magnitude limit of 27 (AB).

Figure 3.14 and Table 3.1 summarize the results of our simulation, showing the surface density and maximum distances of UCDs in the full PASSAGE survey as a function of spectral type. The sensitivity of *JWST*/NIRISS will allow us to detect late M dwarfs to a limiting distance of $\sim$40 kpc, L dwarfs out to 10-30 kpc and T dwarfs out to 1-10 kpc, offering a 10-fold increase in the limiting distances compared to deep UCD samples observed with *HST* (Table 3.8). However, the total covered area in PASSAGES is about 4 times smaller than WISP & 3D-HST, resulting in a comparably sized sample as that examined here.

While not significantly improving overall sample statistics, PASSAGES will substantially improve our assessment of the thick disk and halo UCD population, with

surface densities of thin disk, thick disk, and halo objects being roughly constant from late M dwarfs to early T dwarfs. The higher proportion of thick disk and halo stars is due to the fact that *JWST* will easily reach the effective vertical edge of the thin disk. In addition, the longer cooling times for old thick disk and halo populations will boost their numbers among the late-L and T dwarfs. The exceptional distances probed results in a strong dependence of thin disk UCD surface densities as a function of vertical scaleheight, with a factor of 10 difference in L and T dwarf surface densities between H = 200 pc and H = 400 pc. We also find that thick disk UCDs will outnumber thin disk UCDs down to mid-T, and halo UCDs will outnumber thin disk UCDs among late-M and early L dwarfs, depending on the thin disk scaleheight. Beyond spectral type T7, there is a significant drop off in surface densities as the extreme faintness of the coldest brown dwarfs restricts their detection to with a vertical scaleheight or less. Our simulations predict $<$ 1 Y dwarf in PASSAGE data, although the luminosity function of these objects remains highly unconstrained (Kirkpatrick et al., 2021). We also note a small variation in predicted number counts among the late-M dwarfs between the B01 and B03 models, mirroring the discrepancies seen in our *HST* sample, and indicating an empirical path to explicitly testing the models.

Overall, our simulation predicts at least one thin disk, thick disk, or halo UCD per NIRISS imaging field (4.84 arcmin^2), with (depending on evolutionary model and scaleheight assumptions) 15-100 thin disk UCDs (cumulative surface densities 0.03-0.18 arcmin^{-2}), 70-90 thick disk UCDs (cumulative surface densities 0.12-0.15 arcmin^{-2}), and 50-90 halo UCDs (cumulative surface densities of 0.09-0.15 arcmin^{-2}), all relatively evenly distributed between late-M, L and (thin/thick disk) T dwarfs. For comparison, Ryan & Reid (2016) predict surface densities of 0.02-0.1 arcmin^{-2} for thin and thick disk M8–T5 dwarfs in *JWST* imaging down to J = 27 (AB), with thick disk objects dominating the sample. Our predictions indicate that UCDs in the PASSAGE fields will also be

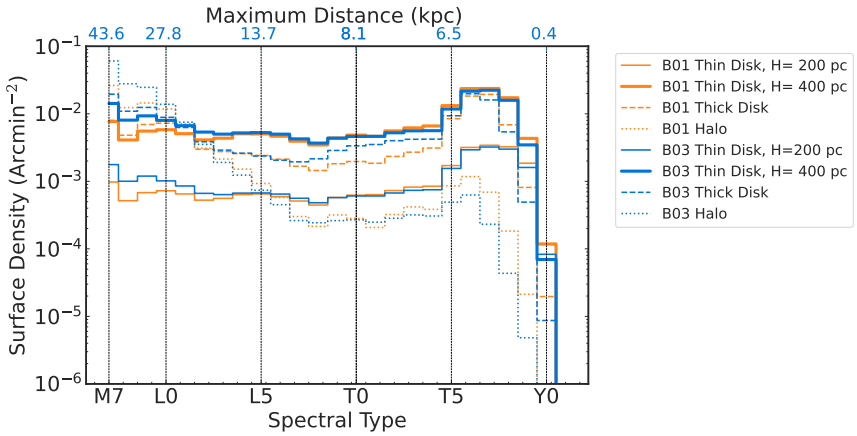

Figure 3.14 Surface density predictions in the PASSAGE survey for UCDs as function of spectral type for thin disk (solid lines), thick disk (dashed lines), and halo populations (dotted lines). We model two thin disk populations with H = 200 pc (thin solid lines) and H = 400 pc (thick solid lines). We show simulations based on the Burrows et al. (2001, B01; blue lines) and Baraffe et al. (2003, B03; orange lines) evolutionary models.

dominated by metal-poor thick disk and halo objects, so an appropriate simulation needs to take into account metallicity effects in both evolution and spectral energy distributions. A more complete study of these effects will be considered in a future study.

Table 3.1 Expected Surface Densities (arcmin^{-2}) of M7-Y1 UCDs in the PASSAGE Survey

Spectral Type	Thin Disk				Thick Disk		Halo	
	Model = B01		Model = B03		Model = B01	Model = B03	Model = B01	Model = B03
	H=200 pc	H=400 pc	H=200 pc	H=400 pc				
M7-M9	0.00217	0.0174	0.00397	0.0316	0.0198	0.0428	0.0531	0.113
L	0.00588	0.0459	0.00677	0.0528	0.0302	0.0359	0.0280	0.0299
T	0.0171	0.110	0.0156	0.100	0.0658	0.0704	0.00454	0.00283
Y0-Y1	<0.001	<0.001	<0.001	<0.001	<0.001	<0.001	<0.001	<0.001
Total	0.0252	0.173	0.0265	0.185	0.116	0.149	0.0856	0.146

3.6 Absolute Magnitude/Spectral Type Relations

Table 3.9 lists absolute magnitude/spectral type relations for M5-Y1 UCDs in *WST*/NIRISS filters. The derivation of absolute magnitude relations follows the

Table 3.2 Summary of main parameters for population simulations

Quantity	Parameterization	Parameter	Range of Quantity
Mass (M)	Power-law IMF	$\alpha = 0.6$	$0.01\ M_\odot \leq M \leq 0.15\ M_\odot$[a]
Thin disk age (τ)	Uniform SFH	$\cdots$	0.1 Gyr $\leq \tau \leq$ 8 Gyr
Binary fraction	Constant	20%	$\cdots$
Mass ratio ($q = M_2/M_1$)	Power law	$\gamma = 4$	$0 \leq q \leq 1$
Evolutionary models	Grid interpolation	Various[b]	$\cdots$ [c]
Thin disk vertical scale height (H)	Various	$\cdots$	100 pc $\leq H \leq$ 1000 pc
Thin disk radial scale height (L)	Constant	2600 pc[d]	$\cdots$
Thick disk age ($\tau_{\rm thick}$)	Uniform SFH	$\cdots$	8 Gyr $\leq \tau_{\rm thick} \leq$ 10 Gyr[e]
Thick disk vertical scale height ($H_{\rm thick}$)	Constant	900 pc[d]	$\cdots$
Thick disk radial scale height ($L_{\rm thick}$)	Constant	3600 pc[d]	$\cdots$
Thick/Thin disk ratio	Constant	12%[d]; 5%[f]	$\cdots$

[a] Some evolutionary models do not cover the full mass range, see Table 3.3.
[b] Evolutionary models included in this analysis are from Burrows et al. (1997), Burrows et al. (2001), Baraffe et al. (2003), Saumon & Marley (2008), Marley et al. (2018), and Phillips et al. (2020).
[c] See Table 3.3 for quantity ranges of individual evolutionary models.
[d] Based on Jurić et al. (2008).
[e] Based on Kilic et al. (2017).
[f] An average of the values reported by Pirzkal et al. (2009), van Vledder et al. (2016), and Hsu et al. (2021).

Table 3.3 List of available range of masses, $T_{\rm eff}$, ages, cloud treatment for evolutionary models

Model	Mass ($M_\odot$)	Age (Gyr)	$T_{\rm eff}$ (K)	Treatment
B97	$0.0005\ M_\odot \leq M \leq 0.237\ M_\odot$	0.0008 Gyr $\leq \tau \leq$ 20 Gyr	74 K $\leq T_{\rm eff} \leq$ 4363 K	Cloud-free
B01	$0.0005\ M_\odot \leq M \leq 0.2\ M_\odot$	0.001 Gyr $\leq \tau \leq$ 10 Gyr	82 K $\leq T_{\rm eff} \leq$ 4096 K	Cloud-free
B03	$0.0005\ M_\odot \leq M \leq 0.1\ M_\odot$	0.001 Gyr $\leq \tau \leq$ 10 Gyr	111 K $\leq T_{\rm eff} \leq$ 3024 K	Cloud-free
SM08	$0.002\ M_\odot \leq M \leq 0.09\ M_\odot$	0.003 Gyr $\leq \tau \leq$ 15 Gyr	270 K $\leq T_{\rm eff} \leq$ 2558 K	Hybrid
M18	$0.0005\ M_\odot \leq M \leq 0.08\ M_\odot$	0.001 Gyr $\leq \tau \leq$ 15 Gyr	91 K $\leq T_{\rm eff} \leq$ 2537 K	Cloud-free
P20	$0.0005\ M_\odot \leq M \leq 0.075\ M_\odot$	0.001 Gyr $\leq \tau \leq$ 10 Gyr	200 K $\leq T_{\rm eff} \leq$ 3075 K	Cloud-free

Table 3.4 Scaleheights, Velocity Dispersions, and Population Ages of HST Ultracool Dwarfs

SpT	Quantity	B97	B01	B03	SM08	M18	P20	Median[a]	N_{obs}[b]	N_{thick}[c]
M7-M9	H (pc)	262^{+36}_{-28}	277^{+39}_{-31}	191^{+16}_{-15}	···	···	···	249^{+48}_{-61}	76	36.7
	σ_w (km/s)	$15.5^{+1.0}_{-0.9}$	$16.0^{+1.1}_{-0.9}$	$13.2^{+0.6}_{-0.5}$	···	···	···	$15.1^{+1.4}_{-2.0}$	···	···
	Age (Gyr) (A09)	$3.8^{+0.6}_{-0.5}$	$4.1^{+0.6}_{-0.5}$	$2.7^{+0.3}_{-0.2}$	···	···	···	$3.6^{+0.8}_{-1.0}$	···	···
	Age (Gyr) (J10)	$3.2^{+0.6}_{-0.5}$	$3.5^{+0.7}_{-0.5}$	$2.1^{+0.3}_{-0.2}$	···	···	···	$3.0^{+0.8}_{-1.0}$	···	···
	Age (Gyr) (S21)	$4.9^{+0.8}_{-0.6}$	$5.3^{+0.9}_{-0.7}$	$3.4^{+0.4}_{-0.3}$	···	···	···	$4.6^{+1.1}_{-1.3}$	···	···
	Median Age (Gyr) (Simulation)	$2.8^{+0.8}_{-0.7}$	$3.0^{+0.8}_{-0.8}$	$3.6^{+0.8}_{-0.7}$	···	···	···	$2.7^{+1.2}_{-2.3}$	···	···
	KS (A09-Simulation)	**0.7**	**0.7**	**0.8**	···	···	···	···	···	···
	KS (J10-Simulation)	0.4	0.4	**0.9**	···	···	···	···	···	···
	KS (S21-Simulation)	**0.9**	**0.9**	0.3	···	···	···	···	···	···
L0-L4	H (pc)	175^{+53}_{-35}	156^{+39}_{-29}	132^{+26}_{-20}	137^{+28}_{-21}	141^{+32}_{-23}	222^{+118}_{-56}	146^{+41}_{-27}	16	6.9
	σ_w (km/s)	$12.7^{+1.8}_{-1.4}$	$12.0^{+1.4}_{-1.2}$	$11.0^{+1.0}_{-0.8}$	$11.2^{+1.1}_{-0.9}$	$11.4^{+1.2}_{-1.0}$	$14.3^{+3.4}_{-2.0}$	$11.6^{+1.5}_{-1.1}$	···	···
	Age (Gyr) (A09)	$2.4^{+0.8}_{-0.5}$	$2.1^{+0.6}_{-0.4}$	$1.8^{+0.4}_{-0.3}$	$1.8^{+0.4}_{-0.3}$	$1.9^{+0.5}_{-0.4}$	$3.2^{+2.0}_{-0.9}$	$2.0^{+0.6}_{-0.4}$	···	···
	Age (Gyr) (J10)	$1.8^{+0.8}_{-0.5}$	$1.5^{+0.6}_{-0.4}$	$1.2^{+0.4}_{-0.3}$	$1.3^{+0.4}_{-0.3}$	$1.3^{+0.5}_{-0.3}$	$2.6^{+2.1}_{-0.9}$	$1.4^{+0.6}_{-0.4}$	···	···
	Age (Gyr) (S21)	$3.1^{+1.1}_{-0.7}$	$2.7^{+0.8}_{-0.6}$	$2.2^{+0.5}_{-0.4}$	$2.3^{+0.6}_{-0.4}$	$2.4^{+0.6}_{-0.5}$	$4.1^{+2.6}_{-1.2}$	$2.5^{+0.8}_{-0.5}$	···	···
	Median Age (Gyr) (Simulation)	$2.3^{+1.6}_{-1.1}$	$2.4^{+1.8}_{-1.2}$	$2.4^{+1.7}_{-1.1}$	$3.1^{+1.6}_{-1.5}$	$2.4^{+1.6}_{-1.1}$	$1.3^{+0.9}_{-0.5}$	$2.5^{+1.7}_{-1.2}$	···	···
	KS (A09-Simulation)	0.2	0.3	0.4	0.6	0.4	**0.8**	···	···	···
	KS (J10-Simulation)	0.3	0.4	0.6	**0.7**	0.6	0.6	···	···	···
	KS (S21-Simulation)	0.4	0.3	0.3	0.4	0.2	**0.9**	···	···	···
L5-L9	H (pc)	172^{+172}_{-57}	176^{+199}_{-59}	175^{+166}_{-59}	160^{+139}_{-46}	175^{+179}_{-58}	174^{+190}_{-58}	172^{+175}_{-56}	2	0.3
	σ_w (km/s)	$12.6^{+5.2}_{-2.3}$	$12.7^{+5.8}_{-2.4}$	$12.7^{+5.0}_{-2.3}$	$12.1^{+4.4}_{-1.9}$	$12.7^{+5.4}_{-2.3}$	$12.6^{+5.6}_{-2.3}$	$12.6^{+5.3}_{-2.2}$	···	···
	Age (Gyr) (A09)	$2.4^{+2.8}_{-0.9}$	$2.4^{+3.3}_{-0.9}$	$2.4^{+2.7}_{-0.9}$	$2.2^{+2.2}_{-0.7}$	$2.4^{+2.9}_{-0.9}$	$2.4^{+3.1}_{-0.9}$	$2.4^{+2.9}_{-0.8}$	···	···
	Age (Gyr) (J10)	$1.8^{+3.0}_{-0.8}$	$1.8^{+3.5}_{-0.8}$	$1.8^{+2.8}_{-0.8}$	$1.6^{+2.3}_{-0.6}$	$1.8^{+3.1}_{-0.8}$	$1.8^{+3.3}_{-0.8}$	$1.8^{+3.0}_{-0.8}$	···	···
	Age (Gyr) (S21)	$3.0^{+3.7}_{-1.1}$	$3.1^{+4.4}_{-1.2}$	$3.1^{+3.6}_{-1.2}$	$2.8^{+3.0}_{-0.9}$	$3.1^{+3.9}_{-1.2}$	$3.1^{+4.1}_{-1.2}$	$3.0^{+3.8}_{-1.1}$	···	···
	Median Age (Gyr) (Simulation)	$2.4^{+1.8}_{-1.3}$	$2.6^{+1.8}_{-1.4}$	$2.9^{+1.8}_{-1.6}$	$2.7^{+1.8}_{-1.5}$	$2.6^{+1.9}_{-1.4}$	$2.7^{+1.8}_{-1.5}$	$2.6^{+1.8}_{-1.5}$	···	···
	KS (A09-Simulation)	0.2	0.2	0.1	0.2	0.2	0.2	···	···	···
	KS (J10-Simulation)	0.2	0.2	0.2	0.3	0.2	0.2	···	···	···
	KS (S21-Simulation)	0.3	0.3	0.2	0.2	0.2	0.2	···	···	···
T0-T4	H (pc)	178^{+162}_{-59}	182^{+183}_{-62}	185^{+180}_{-64}	173^{+150}_{-55}	191^{+180}_{-69}	180^{+165}_{-61}	181^{+169}_{-62}	3	0.7
	σ_w (km/s)	$12.8^{+4.9}_{-2.3}$	$12.9^{+5.4}_{-2.4}$	$13.0^{+5.3}_{-2.5}$	$12.6^{+4.6}_{-2.2}$	$13.2^{+5.2}_{-2.7}$	$12.9^{+4.9}_{-2.4}$	$12.9^{+5.0}_{-2.4}$	···	···
	Age (Gyr) (A09)	$2.5^{+2.6}_{-0.9}$	$2.5^{+3.0}_{-1.0}$	$2.6^{+3.0}_{-1.0}$	$2.4^{+2.4}_{-0.9}$	$2.7^{+3.0}_{-1.1}$	$2.5^{+2.7}_{-0.9}$	$2.5^{+2.8}_{-0.9}$	···	···
	Age (Gyr) (J10)	$1.9^{+2.8}_{-0.8}$	$1.9^{+3.2}_{-0.9}$	$2.0^{+3.2}_{-0.9}$	$1.8^{+2.6}_{-0.8}$	$2.1^{+3.2}_{-1.0}$	$1.9^{+2.8}_{-0.9}$	$1.9^{+2.9}_{-0.9}$	···	···
	Age (Gyr) (S21)	$3.1^{+3.5}_{-1.2}$	$3.2^{+4.0}_{-1.3}$	$3.3^{+3.9}_{-1.3}$	$3.0^{+3.2}_{-1.1}$	$3.4^{+4.0}_{-1.4}$	$3.2^{+3.6}_{-1.2}$	$3.2^{+3.7}_{-1.2}$	···	···
	Median Age (Gyr) (Simulation)	$3.2^{+1.7}_{-1.6}$	$3.2^{+1.8}_{-1.6}$	$3.4^{+1.8}_{-1.7}$	$3.2^{+1.8}_{-1.6}$	$3.2^{+1.8}_{-1.6}$	$3.5^{+1.8}_{-1.7}$	$3.3^{+1.8}_{-1.6}$	···	···
	KS (A09-Simulation)	0.2	0.2	0.2	0.2	0.1	0.2	···	···	···
	KS (J10-Simulation)	0.3	0.3	0.3	0.4	0.3	0.4	···	···	···
	KS (S21-Simulation)	0.1	0.1	0.1	0.1	0.2	0.1	···	···	···
T5-Y0	H (pc)	183^{+241}_{-66}	182^{+227}_{-65}	188^{+269}_{-69}	196^{+229}_{-75}	188^{+230}_{-69}	183^{+234}_{-65}	187^{+237}_{-68}	1	0.3
	σ_w (km/s)	$13.0^{+6.8}_{-2.6}$	$13.0^{+6.4}_{-2.6}$	$13.1^{+7.4}_{-2.7}$	$13.4^{+6.4}_{-2.9}$	$13.1^{+6.5}_{-2.7}$	$13.0^{+6.6}_{-2.6}$	$13.1^{+6.6}_{-2.7}$	···	···
	Age (Gyr) (A09)	$2.6^{+4.0}_{-1.0}$	$2.5^{+3.8}_{-1.0}$	$2.6^{+4.5}_{-1.0}$	$2.8^{+3.8}_{-1.2}$	$2.6^{+3.8}_{-1.0}$	$2.6^{+3.9}_{-1.0}$	$2.6^{+3.9}_{-1.0}$	···	···
	Age (Gyr) (J10)	$2.0^{+4.4}_{-1.0}$	$1.9^{+4.1}_{-0.9}$	$2.0^{+5.0}_{-1.0}$	$2.1^{+4.2}_{-1.1}$	$2.0^{+4.2}_{-1.0}$	$1.9^{+4.2}_{-0.9}$	$2.0^{+4.3}_{-1.0}$	···	···
	Age (Gyr) (S21)	$3.3^{+5.3}_{-1.3}$	$3.2^{+5.0}_{-1.3}$	$3.4^{+6.0}_{-1.4}$	$3.5^{+5.1}_{-1.5}$	$3.4^{+5.1}_{-1.4}$	$3.2^{+5.2}_{-1.3}$	$3.3^{+5.3}_{-1.4}$	···	···
	Median Age (Gyr) (Simulation)	$4.1^{+2.8}_{-2.7}$	$4.1^{+2.8}_{-2.7}$	$4.1^{+2.7}_{-2.7}$	$4.3^{+2.6}_{-2.8}$	$4.1^{+2.8}_{-2.7}$	$4.2^{+2.6}_{-2.8}$	$4.2^{+2.7}_{-2.7}$	···	···
	KS (A09-Simulation)	0.2	0.3	0.2	0.2	0.2	0.3	···	···	···
	KS (J10-Simulation)	0.3	0.3	0.3	0.3	0.3	0.3	···	···	···
	KS (S21-Simulation)	0.2	0.2	0.2	0.2	0.2	0.2	···	···	···
L	H (pc)	173^{+50}_{-35}	157^{+39}_{-29}	134^{+26}_{-20}	136^{+27}_{-21}	143^{+31}_{-23}	210^{+98}_{-52}	153^{+56}_{-30}	18	7
	σ_w (km/s)	$12.6^{+1.7}_{-1.3}$	$12.0^{+1.4}_{-1.2}$	$11.1^{+1.0}_{-0.9}$	$11.2^{+1.1}_{-0.9}$	$11.5^{+1.2}_{-1.0}$	$13.9^{+2.9}_{-1.8}$	$11.8^{+2.0}_{-1.2}$	···	···
	Age (Gyr) (A09)	$2.4^{+0.8}_{-0.5}$	$2.2^{+0.6}_{-0.4}$	$1.8^{+0.4}_{-0.3}$	$1.8^{+0.4}_{-0.3}$	$1.9^{+0.5}_{-0.4}$	$3.0^{+1.6}_{-0.8}$	$2.1^{+0.9}_{-0.5}$	···	···
	Age (Gyr) (J10)	$1.8^{+0.8}_{-0.5}$	$1.6^{+0.6}_{-0.4}$	$1.2^{+0.4}_{-0.3}$	$1.3^{+0.4}_{-0.3}$	$1.4^{+0.5}_{-0.3}$	$2.4^{+1.7}_{-0.8}$	$1.5^{+0.9}_{-0.4}$	···	···
	Age (Gyr) (S21)	$3.0^{+1.0}_{-0.7}$	$2.7^{+0.8}_{-0.6}$	$2.3^{+0.5}_{-0.4}$	$2.3^{+0.6}_{-0.4}$	$2.4^{+0.6}_{-0.5}$	$3.8^{+2.1}_{-1.1}$	$2.6^{+1.2}_{-0.6}$	···	···
	Median Age (Gyr) (Simulation)	$2.1^{+3.7}_{-1.6}$	$2.3^{+3.8}_{-1.7}$	$2.3^{+3.7}_{-1.8}$	$2.7^{+3.6}_{-2.1}$	$2.3^{+3.8}_{-1.8}$	$1.6^{+3.4}_{-1.2}$	$2.2^{+3.8}_{-1.7}$	···	···
	KS (A09-Simulation)	0.4	0.3	0.4	0.5	0.4	0.5	···	···	···
	KS (J10-Simulation)	0.3	0.4	0.5	0.6	0.5	0.4	···	···	···
	KS (S21-Simulation)	0.4	0.4	0.4	0.4	0.4	0.6	···	···	···
T	H (pc)	170^{+143}_{-52}	173^{+150}_{-55}	179^{+158}_{-59}	173^{+139}_{-55}	183^{+156}_{-62}	170^{+146}_{-53}	175^{+149}_{-56}	4	0.4
	σ_w (km/s)	$12.5^{+4.5}_{-2.1}$	$12.6^{+4.6}_{-2.2}$	$12.8^{+4.8}_{-2.3}$	$12.6^{+4.3}_{-2.2}$	$13.0^{+4.7}_{-2.4}$	$12.5^{+4.5}_{-2.1}$	$12.7^{+4.6}_{-2.2}$	···	···
	Age (Gyr) (A09)	$2.3^{+2.3}_{-0.8}$	$2.4^{+2.4}_{-0.8}$	$2.5^{+2.6}_{-0.9}$	$2.4^{+2.2}_{-0.8}$	$2.5^{+2.5}_{-1.0}$	$2.4^{+2.4}_{-0.8}$	$2.4^{+2.4}_{-0.8}$	···	···
	Age (Gyr) (J10)	$1.7^{+2.4}_{-0.7}$	$1.8^{+2.6}_{-0.8}$	$1.9^{+2.7}_{-0.8}$	$1.8^{+2.4}_{-0.8}$	$1.9^{+2.7}_{-0.9}$	$1.8^{+2.5}_{-0.8}$	$1.8^{+2.5}_{-0.8}$	···	···
	Age (Gyr) (S21)	$3.0^{+3.1}_{-1.0}$	$3.0^{+3.2}_{-1.1}$	$3.2^{+3.4}_{-1.2}$	$3.0^{+3.0}_{-1.1}$	$3.2^{+3.4}_{-1.2}$	$3.0^{+3.1}_{-1.1}$	$3.1^{+3.2}_{-1.1}$	···	···
	Median Age (Gyr) (Simulation)	$3.6^{+3.0}_{-2.4}$	$3.5^{+3.0}_{-2.4}$	$3.7^{+3.0}_{-2.5}$	$3.6^{+3.0}_{-2.4}$	$3.6^{+3.0}_{-2.5}$	$3.7^{+3.0}_{-2.6}$	$3.6^{+3.0}_{-2.5}$	···	···
	KS (A09-Simulation)	0.3	0.3	0.2	0.3	0.2	0.3	···	···	···
	KS (J10-Simulation)	0.4	0.3	0.3	0.3	0.3	0.4	···	···	···
	KS (S21-Simulation)	0.2	0.2	0.2	0.2	0.2	0.2	···	···	···

[a] Median values computed by combining all samples obtained from all models, not by standard error propagation formula. For M7–M9 dwarfs, only B97, B01, and B03 models are used; for L0–L4 dwarfs, the P20 models are excluded.

[b] The total number of UCDs in the magnitude-limited WISP and 3D-HST surveys analyzed in this study; simulations are compared to $N_{thin} = N_{obs} - N_{thick}$. [c] Estimated number of thick disk contaminants; see Section 3.3.3.

[d] Estimated probability that the age distribution of the simulated sample and that inferred from our measured number counts are distinct, as assessed through the Kolmogorov–Smirnov (KS) test. Values of KS $\geq$0.7 are considered significantly distinct.

Model notation: B97: Burrows et al. (1997); B01: Burrows et al. (2001); B03: Baraffe et al. (2003); SM08: Saumon & Marley (2008); M18: Marley et al. (2018); P20: Phillips et al. (2020).

Table 3.5 Scaleheights, Velocity Dispersions, and Population Ages of HST Ultracool Dwarfs Assuming 5-percent Thick Disk Fraction

SpT	Quantity	B97	B01	B03	SM08	M18	P20	Median[a]	N_{obs}[b]	N_{thick}[c]
M7-M9	H (pc)	385^{+72}_{-53}	429^{+108}_{-73}	240^{+22}_{-18}	···	···	···	361^{+112}_{-125}	76	15.3
	σ_W (km/s)	$18.8^{+1.7}_{-1.3}$	$19.9^{+2.4}_{-1.8}$	$14.8^{+0.7}_{-0.6}$	···	···	···	$18.2^{+2.6}_{-3.5}$	···	···
	Age (Gyr) (A09)	$5.9^{+1.2}_{-0.9}$	$6.6^{+1.9}_{-1.3}$	$3.4^{+0.4}_{-0.3}$	···	···	···	$5.5^{+1.9}_{-2.1}$	···	···
	Age (Gyr) (J10)	$5.5^{+1.5}_{-1.0}$	$6.4^{+2.3}_{-1.4}$	$2.9^{+0.4}_{-0.3}$	···	···	···	$5.1^{+2.3}_{-2.3}$	···	···
	Age (Gyr) (S21)	$7.7^{+1.7}_{-1.2}$	$8.7^{+2.6}_{-1.7}$	$4.4^{+0.5}_{-0.4}$	···	···	···	$7.1^{+2.6}_{-2.8}$	···	···
	Median Age (Gyr) (Simulation)	$2.8^{+0.6}_{-0.6}$	$3.0^{+0.7}_{-0.6}$	$3.6^{+0.6}_{-0.6}$	···	···	···	$2.7^{+1.0}_{-2.4}$		
	KS (A09-Simulation)	**1.0**	**1.0**	0.2	···	···	···	···	···	
	KS (J10-Simulation)	**1.0**	**1.0**	0.6	···	···	···	···	···	
	KS (S21-Simulation)	**1.0**	**1.0**	0.6	···	···	···	···	···	
L0-L4	H (pc)	235^{+104}_{-53}	199^{+59}_{-38}	161^{+31}_{-26}	168^{+35}_{-28}	177^{+42}_{-31}	344^{+238}_{-113}	182^{+63}_{-36}	16	2.9
	σ_W (km/s)	$14.7^{+3.0}_{-1.8}$	$13.5^{+1.9}_{-1.3}$	$12.2^{+1.1}_{-1.0}$	$12.4^{+1.2}_{-1.1}$	$12.8^{+1.4}_{-1.2}$	$17.8^{+5.3}_{-3.2}$	$13.0^{+2.1}_{-1.4}$	···	···
	Age (Gyr) (A09)	$3.4^{+1.7}_{-0.8}$	$2.8^{+1.0}_{-0.6}$	$2.2^{+0.5}_{-0.4}$	$2.3^{+0.5}_{-0.4}$	$2.4^{+0.7}_{-0.5}$	$5.2^{+4.2}_{-1.9}$	$2.5^{+1.0}_{-0.6}$	···	···
	Age (Gyr) (J10)	$2.8^{+1.8}_{-0.8}$	$2.2^{+1.0}_{-0.6}$	$1.6^{+0.5}_{-0.4}$	$1.7^{+0.5}_{-0.4}$	$1.8^{+0.7}_{-0.5}$	$4.7^{+5.0}_{-2.0}$	$1.9^{+1.0}_{-0.5}$	···	···
	Age (Gyr) (S21)	$4.4^{+2.3}_{-1.1}$	$3.6^{+1.3}_{-0.8}$	$2.8^{+0.7}_{-0.5}$	$2.9^{+0.7}_{-0.6}$	$3.1^{+0.9}_{-0.6}$	$6.8^{+5.6}_{-2.5}$	$3.2^{+1.4}_{-0.8}$	···	···
	Median Age (Gyr) (Simulation)	$2.3^{+1.4}_{-1.0}$	$2.5^{+1.4}_{-1.0}$	$2.4^{+1.4}_{-1.0}$	$3.1^{+1.3}_{-1.3}$	$2.4^{+1.4}_{-1.0}$	$1.3^{+0.7}_{-0.4}$	$2.5^{+1.4}_{-1.1}$	···	
	KS (A09-Simulation)	0.4	0.3	0.3	0.4	0.2	**0.9**	···	···	···
	KS (J10-Simulation)	0.2	0.2	0.5	0.6	0.3	**0.9**	···	···	···
	KS (S21-Simulation)	0.6	0.5	0.3	0.2	0.4	**1.0**	···	···	···
L5-L9	H (pc)	180^{+189}_{-62}	183^{+210}_{-65}	182^{+172}_{-63}	166^{+155}_{-51}	181^{+191}_{-63}	180^{+202}_{-62}	179^{+189}_{-61}	2	0.1
	σ_W (km/s)	$12.9^{+5.6}_{-2.5}$	$13.0^{+6.0}_{-2.5}$	$12.9^{+5.1}_{-2.5}$	$12.4^{+4.8}_{-2.1}$	$12.9^{+5.6}_{-2.5}$	$12.8^{+5.9}_{-2.5}$	$12.8^{+5.6}_{-2.4}$	···	···
	Age (Gyr) (A09)	$2.5^{+3.1}_{-1.0}$	$2.6^{+3.5}_{-1.0}$	$2.5^{+2.8}_{-1.0}$	$2.3^{+2.5}_{-0.8}$	$2.5^{+3.1}_{-1.0}$	$2.5^{+3.3}_{-0.9}$	$2.5^{+3.1}_{-0.9}$	···	···
	Age (Gyr) (J10)	$1.9^{+3.3}_{-0.9}$	$2.0^{+3.7}_{-0.9}$	$1.9^{+3.0}_{-0.9}$	$1.7^{+2.6}_{-0.7}$	$1.9^{+3.4}_{-0.9}$	$1.9^{+3.6}_{-0.9}$	$1.9^{+3.3}_{-0.9}$	···	···
	Age (Gyr) (S21)	$3.2^{+4.2}_{-1.3}$	$3.3^{+4.6}_{-1.3}$	$3.2^{+3.8}_{-1.3}$	$2.9^{+3.3}_{-1.0}$	$3.2^{+4.2}_{-1.3}$	$3.2^{+4.4}_{-1.3}$	$3.2^{+4.1}_{-1.2}$	···	···
	Median Age (Gyr) (Simulation)	$2.4^{+1.8}_{-1.3}$	$2.6^{+1.8}_{-1.4}$	$2.8^{+1.8}_{-1.6}$	$2.7^{+1.9}_{-1.5}$	$2.6^{+1.8}_{-1.4}$	$2.6^{+1.8}_{-1.4}$	$2.6^{+1.8}_{-1.4}$	···	···
	KS (A09-Simulation)	0.2	0.2	0.1	0.2	0.2	0.2	···	···	···
	KS (J10-Simulation)	0.1	0.1	0.2	0.3	0.2	0.2	···	···	···
	KS (S21-Simulation)	0.3	0.3	0.2	0.2	0.2	0.2	···	···	···
T0-T4	H (pc)	191^{+189}_{-68}	197^{+215}_{-72}	202^{+204}_{-76}	188^{+169}_{-66}	209^{+212}_{-81}	195^{+189}_{-71}	197^{+197}_{-72}	3	0.3
	σ_W (km/s)	$13.3^{+5.4}_{-2.6}$	$13.5^{+6.0}_{-2.8}$	$13.6^{+5.7}_{-2.8}$	$13.1^{+5.0}_{-2.6}$	$13.9^{+5.8}_{-3.0}$	$13.4^{+5.4}_{-2.7}$	$13.4^{+5.6}_{-2.8}$	···	···
	Age (Gyr) (A09)	$2.7^{+3.1}_{-1.0}$	$2.8^{+3.6}_{-1.0}$	$2.8^{+3.4}_{-1.2}$	$2.6^{+2.8}_{-1.0}$	$3.0^{+3.6}_{-1.3}$	$2.7^{+3.1}_{-1.1}$	$2.8^{+3.3}_{-1.1}$	···	···
	Age (Gyr) (J10)	$2.1^{+3.4}_{-1.0}$	$2.2^{+3.9}_{-1.1}$	$2.2^{+3.7}_{-1.1}$	$2.0^{+3.0}_{-1.0}$	$2.4^{+3.9}_{-1.2}$	$2.1^{+3.4}_{-1.0}$	$2.2^{+3.6}_{-1.1}$	···	···
	Age (Gyr) (S21)	$3.4^{+4.1}_{-1.4}$	$3.6^{+4.8}_{-1.5}$	$3.7^{+4.5}_{-1.6}$	$3.4^{+3.7}_{-1.3}$	$3.8^{+4.7}_{-1.7}$	$3.5^{+4.2}_{-1.4}$	$3.5^{+4.4}_{-1.5}$	···	···
	Median Age (Gyr) (Simulation)	$2.9^{+2.0}_{-1.4}$	$2.9^{+2.1}_{-1.5}$	$3.2^{+2.1}_{-1.7}$	$3.0^{+2.0}_{-1.6}$	$3.0^{+2.0}_{-1.6}$	$3.2^{+2.1}_{-1.6}$	$3.0^{+2.1}_{-1.6}$	···	···
	KS (A09-Simulation)	0.1	0.1	0.1	0.1	0.1	0.1	···	···	···
	KS (J10-Simulation)	0.2	0.2	0.2	0.2	0.2	0.3	···	···	···
	KS (S21-Simulation)	0.2	0.2	0.2	0.2	0.2	0.2	···	···	···
T5-Y0	H (pc)	189^{+247}_{-70}	189^{+246}_{-71}	193^{+277}_{-73}	204^{+235}_{-81}	194^{+238}_{-73}	187^{+238}_{-69}	193^{+247}_{-73}	1	0.1
	σ_W (km/s)	$13.2^{+6.8}_{-2.7}$	$13.2^{+6.8}_{-2.7}$	$13.3^{+7.5}_{-2.8}$	$13.7^{+6.4}_{-3.1}$	$13.4^{+6.6}_{-2.8}$	$13.1^{+6.6}_{-2.7}$	$13.3^{+6.8}_{-2.8}$	···	···
	Age (Gyr) (A09)	$2.6^{+4.1}_{-1.1}$	$2.6^{+4.1}_{-1.1}$	$2.7^{+4.7}_{-1.1}$	$2.9^{+3.9}_{-1.2}$	$2.7^{+4.0}_{-1.1}$	$2.6^{+4.0}_{-1.0}$	$2.7^{+4.1}_{-1.1}$	···	···
	Age (Gyr) (J10)	$2.0^{+4.5}_{-1.0}$	$2.0^{+4.5}_{-1.0}$	$2.1^{+5.2}_{-1.1}$	$2.3^{+4.4}_{-1.2}$	$2.1^{+4.4}_{-1.1}$	$2.0^{+4.3}_{-1.0}$	$2.1^{+4.5}_{-1.1}$	···	···
	Age (Gyr) (S21)	$3.4^{+5.5}_{-1.4}$	$3.4^{+5.5}_{-1.4}$	$3.5^{+6.2}_{-1.5}$	$3.7^{+5.2}_{-1.7}$	$3.5^{+5.3}_{-1.5}$	$3.3^{+5.3}_{-1.4}$	$3.5^{+5.5}_{-1.5}$	···	···
	Median Age (Gyr) (Simulation)	$4.2^{+2.7}_{-2.8}$	$4.1^{+2.8}_{-2.6}$	$4.1^{+2.8}_{-2.6}$	$4.3^{+2.7}_{-2.8}$	$4.2^{+2.7}_{-2.7}$	$4.1^{+2.7}_{-2.7}$	$4.1^{+2.7}_{-2.7}$	···	···
	KS (A09-Simulation)	0.2	0.2	0.2	0.2	0.2	0.2	···	···	···
	KS (J10-Simulation)	0.3	0.3	0.3	0.3	0.3	0.3	···	···	···
	KS (S21-Simulation)	0.2	0.2	0.2	0.2	0.2	0.2	···	···	···
L	H (pc)	227^{+87}_{-50}	198^{+56}_{-37}	162^{+31}_{-26}	166^{+33}_{-27}	176^{+41}_{-31}	313^{+199}_{-96}	190^{+100}_{-41}	18	3
	σ_W (km/s)	$14.5^{+2.5}_{-1.7}$	$13.5^{+1.8}_{-1.3}$	$12.2^{+1.1}_{-1.0}$	$12.3^{+1.2}_{-1.0}$	$12.7^{+1.4}_{-1.2}$	$17.0^{+4.7}_{-2.8}$	$13.2^{+3.1}_{-1.5}$	···	···
	Age (Gyr) (A09)	$3.2^{+1.4}_{-0.8}$	$2.8^{+0.9}_{-0.6}$	$2.2^{+0.5}_{-0.4}$	$2.3^{+0.5}_{-0.4}$	$2.4^{+0.6}_{-0.5}$	$4.7^{+3.4}_{-1.6}$	$2.7^{+1.6}_{-0.6}$	···	···
	Age (Gyr) (J10)	$2.7^{+1.5}_{-0.8}$	$2.2^{+0.9}_{-0.6}$	$1.6^{+0.5}_{-0.4}$	$1.7^{+0.5}_{-0.4}$	$1.8^{+0.6}_{-0.4}$	$4.2^{+4.0}_{-1.7}$	$2.0^{+1.7}_{-0.6}$	···	···
	Age (Gyr) (S21)	$4.2^{+1.9}_{-1.0}$	$3.6^{+1.2}_{-0.8}$	$2.8^{+0.6}_{-0.5}$	$2.9^{+0.7}_{-0.6}$	$3.1^{+0.9}_{-0.6}$	$6.1^{+4.6}_{-2.1}$	$3.4^{+2.1}_{-0.8}$	···	···
	Median Age (Gyr) (Simulation)	$2.1^{+3.7}_{-1.6}$	$2.3^{+3.8}_{-1.7}$	$2.3^{+3.7}_{-1.8}$	$2.7^{+3.6}_{-2.1}$	$2.3^{+3.8}_{-1.8}$	$1.6^{+3.4}_{-1.2}$	$2.2^{+3.8}_{-1.7}$	···	···
	KS (A09-Simulation)	0.5	0.4	0.4	0.4	0.4	0.6	···	···	···
	KS (J10-Simulation)	0.4	0.3	0.4	0.5	0.4	0.5	···	···	···
	KS (S21-Simulation)	0.5	0.5	0.4	0.4	0.4	**0.7**	···	···	···
T	H (pc)	187^{+170}_{-64}	190^{+183}_{-66}	197^{+187}_{-70}	191^{+164}_{-67}	203^{+191}_{-75}	189^{+168}_{-65}	193^{+178}_{-68}	4	0.4
	σ_W (km/s)	$13.1^{+5.0}_{-2.5}$	$13.2^{+5.3}_{-2.6}$	$13.4^{+5.3}_{-2.7}$	$13.3^{+4.8}_{-2.6}$	$13.7^{+5.4}_{-2.8}$	$13.2^{+4.9}_{-2.5}$	$13.3^{+5.2}_{-2.6}$	···	···
	Age (Gyr) (A09)	$2.6^{+2.8}_{-1.0}$	$2.7^{+3.0}_{-1.0}$	$2.8^{+3.1}_{-1.1}$	$2.7^{+2.7}_{-1.0}$	$2.9^{+3.2}_{-1.2}$	$2.6^{+2.8}_{-1.0}$	$2.7^{+2.9}_{-1.0}$	···	···
	Age (Gyr) (J10)	$2.0^{+3.0}_{-0.9}$	$2.0^{+3.2}_{-1.0}$	$2.2^{+3.4}_{-1.0}$	$2.1^{+2.9}_{-1.0}$	$2.3^{+3.5}_{-1.1}$	$2.0^{+3.0}_{-1.0}$	$2.1^{+3.2}_{-1.0}$	···	···
	Age (Gyr) (S21)	$3.3^{+3.7}_{-1.3}$	$3.4^{+4.0}_{-1.3}$	$3.5^{+4.1}_{-1.4}$	$3.4^{+3.6}_{-1.4}$	$3.7^{+4.2}_{-1.5}$	$3.4^{+3.7}_{-1.3}$	$3.4^{+3.9}_{-1.4}$	···	···
	Median Age (Gyr) (Simulation)	$3.6^{+3.0}_{-2.4}$	$3.5^{+3.0}_{-2.4}$	$3.7^{+3.0}_{-2.5}$	$3.6^{+3.0}_{-2.4}$	$3.6^{+3.0}_{-2.5}$	$3.7^{+3.0}_{-2.6}$	$3.6^{+3.0}_{-2.5}$	···	···
	KS (A09-Simulation)	0.2	0.2	0.2	0.2	0.2	0.2	···	···	···
	KS (J10-Simulation)	0.3	0.3	0.2	0.3	0.2	0.3	···	···	···
	KS (S21-Simulation)	0.2	0.2	0.2	0.2	0.2	0.2	···	···	···

Table 3.6 Linear fits to the limiting magnitudes of WISP fields as a function of G141 exposure time. Limiting magnitudes per filter are computed as $c_0 + c_1 \log t/1000\ s$ where t is the exposure time in seconds. These relations do not account for the sensitivity correction for late spectral types discussed in Section 3.2.

Filter	c_0	c_1	Scatter
F110W	18.06	1.26	0.23
F140W	17.14	1.50	0.29
F160W	17.37	1.36	0.22

Table 3.7 Fit Parameters for Simulated Magnitude Uncertainties and Spectral S/N

Fit quantity	Dependent quantities	Filter	Best fit parameters
σ_m	t_I, m	F110W	(α, β, σ_0)= (0.25, −0.35, 0.003)
σ_m	t_I, m	F140W	(α,β, σ_0)= (0.26,−0.43, 0.007)
σ_m	t_I, m	F160W	(α,β, σ_0) = (0.25,−0.35, 0.003)
log J-SNR	t_{G141}, m	F110W	(a,b, log J-SNR$_0$) = (−0.22, 0.40 , 1.32)
log J-SNR	t_{G141}, m	F140W	(a,b, log J-SNR$_0$) = (−0.24, 0.23, 1.33)
log J-SNR	t_{G141}, m	F160W	(a,b, log J-SNR$_0$) = (−0.24, 0.39, 1.53)

methodology in Aganze et al. (2022a). Magnitudes were measured by convolving NIRISS filter profiles with low-resolution spectra of M5-T9 UCDs from the SpeX Prism Library (SPL; Burgasser, 2014). Additional WFC3 spectra of Y0-Y1 were obtained from from Schneider et al. (2015). We computed color corrections between magnitudes in the NIRISS filters and magnitudes in either MKO J or 2MASS H filters, then applied these corrections to the absolute magnitude relations of Dupuy & Liu (2012) for spectral types earlier than T8 and Kirkpatrick et al. (2021) for spectral types T8-Y2. We propagated uncertainties by random sampling and derived polynomial coefficients by fitting a 6th-degree polynomial, clipping 3 σ outliers.

Table 3.8 Previous Deep Surveys for Ultracool Dwarfs.

Survey Reference & Methodology	Area (deg^2)	Limiting Magnitude	Limiting Distance (pc)	$\log_{10}$ Effective Volume (pc^3)[a]	Number Detected	Population Parameters
Ryan et al. (2005)	0.038	z (AB) < 25	1250 (L0)	3.1 (L0)	28 LT	$H = 350 \pm 50$ pc
HST/ACS imaging			250 (T0)	1.6 (T0)		
Pirzkal et al. (2005)	0.003	F775W (AB) < 27	500 (L0)	1.2 (L0)	18 late-M	$H = 400 \pm 100$ pc
HST/ACS spectra			170 (L5)	0.1 (L5)	2 L	
Pirzkal et al. (2009)	0.028	z (AB) < 25	1700 (M9)	2.8 (M9)	43 M4-M9	$H = 370^{+60}_{-65}$ pc
HST/ACS spectra						$H_{\rm TD} \approx 1000$ pc
						$f_h \approx 0.25\%$
Ryan et al. (2011)	0.064	F125W (AB) < 25.5	3000 (L0)	3.4 (L0)	17 MLT	$H = 290 \pm 40$ pc
HST/WFC3 imaging		F098M (AB) < 26.5	700 (T0)	2.5 (T0)		
Kakazu et al. (2010)	9.3	z (AB) < 23.3	570 (L0)	4.8 (L0)	7 LT	$H \approx 400$ pc
Suprime-Cam imaging			120 (T0)	3.1 (T0)		
Masters et al. (2012)	0.2	F125W (AB) < 23	400 (T0)	2.8 (T0)	3 T	...
HST/WFC3 spectra			120 (T8)	1.5 (T8)		
Sorahana et al. (2019)	130	z (AB) < 24	900 (L0)	6.2 (L0)	3,665 L	$H = 340 - 420$ pc
Suprime-Cam imaging			238 (L8)	5.1 (L8)		
Carnero Rosell et al. (2019)	2,400	z (AB) < 22	360 (L0)	6.7 (L0)	11,745 LT	$H \approx 450$ pc
Dark Energy Survey imaging			65 (T0)	4.8 (T0)		
Warren et al. (2021)	3,070	J (Vega) < 17.5	200 (L0)	6.3 (L0)	1,016 L	$H = 270 \pm 6$ pc
SDSS + UKIDSS + WISE imaging						
Aganze et al. (2022a) & This study	0.6	F140W (AB) < 21.8	1170 (M7)[b]	3.7 (M7)	128 late-M	$H = 249^{+48}_{-61}$ pc (late-M)
HST/WFC3 spectra			780 (L0)	3.5 (L0)[b]	26 L	$H = 153^{+36}_{-36}$ pc (L)
			280 (T0)	2.8 (T0)[b]	10 T	$H = 175^{+149}_{-56}$ pc (T)

[a] The effective volume of disk stars detectable in the survey, a statistic which accounts for the spatial distribution of the sample. See Section 3.2.1 for further details.
[b] Using $H = 200$ pc and one-component exponential disk model
[c] This collection of surveys assumes limiting distances $\gtrsim$400 pc to appropriately sample the vertical scaleheight of the thin disk.

Table 3.9 Absolute Magnitude/Spectral Type Relations for M5-Y1 UCDs in NIRISS Passbands.

x	y	rms	c6	c5	c4	c3	c2	c1	c0
SpT	M_{F115W}	0.39	4.29713588E-07	-5.04229648E-05	2.22068501E-03	-4.37392153E-02	3.02230231E-01	1.75203666E+00	-1.70701962E+01
SpT	M_{F150W}	0.40	3.81506552E-07	-4.80917601E-05	2.37805487E-03	-5.74753589E-02	6.67409384E-01	-2.38264132E+00	-1.22005576E+00
SpT	M_{F200W}	0.40	7.59609823E-07	-1.00377706E-04	5.31740074E-03	-1.43601133E-01	2.05416628E+00	-1.39462050E+01	3.72959094E+01

[a] Decimal spectral type, with 10 = M0, 20 = L0, 30 = T0, etc.
[b] Empirical relations are computed as $y = \sum_{n=1}^{m} c_n x^n$ where m is the power of the polynomial. Coefficients are written in decimal exponent notation.

Chapter 3 in full, is a reprint of the material as it appears in the Astrophysical Journal 2022, Volume 934, Number 73, authored by Christian Aganze, Adam J. Burgasser, Mathew Malkan, Christopher A. Theissen, Roberto A. Tejada Arevalo, Chih-Chun Hsu, Daniella C. Bardalez Gagliuffi, Russell E. Ryan, Jr., and Benne Holwerda. The thesis author was the primary investigator and author of this paper.

Chapter 4

Predictions for Future Ground-Based Facilities and Space Missions

4.1 Introduction

In previous chapters, we demonstrated how deep pencil beam surveys with HST/WFC3 provide a sufficiently-large sample of UCDs at distances of 1-2 kpc to constrain M and L dwarf scaleheights. However, not large enough to constrain T dwarfs nor detect significant numbers of halo objects. In this chapter, we explore possibilities for the next generation of surveys, with a particular focus on the Vera Rubin Observatory, the Euclid telescope, and the Nancy Grace Roman Space Telescope. We particularly focus on prospects for constraining the star formation history and the kinematic heating history of the Milky Way by measuring the stellar mass function index of the halo population and thin disk scaleheights down to substellar masses.

Early work by Reid et al. (1999) sought to constrain the substellar mass function using a sample of 25 photometrically-selected L dwarfs with the DENIS and 2MASS surveysThey incorporated evolutionary models by Baraffe et al. (1997) to simulate the

expected distribution of L dwarfs within the solar neighborhood. Their results were consistent with a power-law mass function of $dN/dM \propto M^{-\alpha}, 1 < \alpha < 2$, which ruled out a large contribution of undetected brown dwarfs as dark matter. Burgasser (2004) extended these simulations to include low-temperature T dwarfs, and found that the simulated luminosity function is sensitive to the age distribution of the population (among other things). With the 2MASS, WISE and SDSS surveys, thousands of UCDs have been spectroscopically confirmed Burgasser (2014), which has resulted in constraints of the stellar mass function ($0.5 \leq \alpha \geq 0.7$, Kirkpatrick et al. 2012, 2019, 2021), the binary fraction ($\leq 20\%$ (Gizis et al., 2003; Burgasser et al., 2003)), local kinematics Faherty et al. (2010); Hsu et al. (2021), and the discovery and characterization of local metal-poor UCDs (Burgasser et al., 2003; Zhang et al., 2017; Schneider et al., 2020). Still, these studies only detect the local field population. Deep space-based surveys have expanded to greater distances (100 pc-2 kpc) through photometric and spectroscopic samples (Ryan et al., 2005; Ryan et al., 2011; Aganze et al., 2022b) but they are limited by small samples and low spectral type precision.

The local population IMF down to substellar masses has been constrained down to substellar masses in the solar neighborhood ($<$20 pc, Kirkpatrick et al. 2012, 2021), it remains unconstrained in the thick disk and halo (or generally metal-poor) populations. Variations of the IMF include the suppression of the formation of UCDs in a young halo due to the lack of metal coolants in progenitor clouds. However, the effects of metallicities on star formation down to UCD masses remain unconstrained by observations (Bate & Bonnell, 2005; Bromm, 2013). To constrain the IMF and the star formation history of the halo down to substellar masses, samples of halo UCDs are needed. In both the halo and old globular cluster populations, the cooling of brown dwarfs is expected to produce a gap in the luminosity function and the color-magnitude diagram, between stars and brown dwarfs (Burgasser, 2004; Gerasimov et al., 2022), with variations caused

by stellar abundance effects on brown evolution and star formation histories. This gap provides a potential new age tracer for the halo and GCs. However, there are currently < 20 known metal-poor UCDs with kinematics that are consistent with the galactic halo (Lodieu et al., 2015). Recently, Li et al. (2023) constrained the variation in stellar mass function due to metallicity effects by using a catalog of 30,000 M dwarfs with distances between 100–300 pc, covering masses of 0.1-0.3 solar masses and metallicities between -0.8 and 0.4 using the LAMOST survey. They derived an IMF power law that decreases with metallicity ($dN/dM \propto M^{-\alpha}; \alpha$ between 1.3 and 2.3). While this study explores metallicity ranges, the sample is local, and lacks cooler UCDs whose evolution is sensitive to metallicity effects.

Large samples of UCDs can also constrain kinematic heating history in the Milky Way disk. It is well-established that orbits of stars in the disk are disrupted and kinematically heated with time by molecular clouds, spirals arms, bars or merger events (Aumer & Binney, 2009). UCDs provide an additional low-mass tracer that has not been fully utilized. A recent study by Medan & Lépine (2023) used a sample of 250,000 K dwarfs in the local neighborhood to re-discover kinematic substructure (clumps, ridges, streams, etc.) in the disk that was previously discovered with higher-mass, main-sequence stars. However, the dependence of these effects on solar mass and metallicity are yet to be explored. Radial migration and heating are responsible for the metallicity spread as a function of galacto-centric radius (Loebman et al., 2011), but little work has been done to characterize this effect down to substellar masses. Many spectroscopic surveys are focused on measuring precise stellar abundances (RAVE, SEGUE, GALAH, APOGEE, LAMOST) which combined astrometric information (Gaia) to provide a full chemo-dynamic picture of the disk. However, these surveys lack UCDs. Kinematic heating and radial migration result in age-scaleheight-velocity relations, and these relations vary with metallicity (Sharma et al., 2021). Additionally, the cooling and evolution of UCDs result

in the dependence of population age with spectral type (Burgasser et al., 2004; Ryan et al., 2017). In the absence of precise kinematic measurements, the spatial distribution of large samples of disk UCDs over large distances provides a snapshot of the disk structure down to substellar masses. Solano et al. (2021) predicted that Euclid will detect over 2 million L dwarfs and over 1 million T dwarfs, with variations up to a factor of 2 for vertical scale heights varying between 250 pc and 450 pc. In this study, we test these predictions by including metal-poor UCDs. Our primary goal is to generate specific predictions of UCD detection for these surveys using various assumptions about the underlying Galactic structure, UCD star formation history, and various evolutionary model considerations for different Galactic populations. We also analyze optimal search strategies and strengths of each survey to address fundamental science questions about UCDs, such as the relative abundances of thin disk, thick disk, and halo UCDs; the mass function and star formation history of the UCD halo; the effects of metallicity-dependent evolution in thick disk and halo UCDs; the low-mass limits of thin disk, thick disk, and halo UCDs.

4.2 Surveys

4.2.1 Euclid

The Euclid mission is a space-based infrared survey launched on Saturday, July 1st 2023 with the main goal of improving our understanding of dark energy and the nature of dark matter. The telescope is equipped with optical and near-infrared photometric and spectroscopic instruments (VIS, 0.5–1 micron; NISP 1.–2. micron), and slitless spectroscopy capabilities between 1.25-1.85 microns. The telescope will have a large $\approx$ 0.7 sq. degrees field of view, with an image resolution of 0.1–0.3 arcsec. The telescope is planned to be operational for 6 years. We discuss two surveys of interest: the Euclid wide-field survey, and the deep survey as outlined by Euclid Collaboration et al. (2022)

Euclid Wide Field Survey The Euclid Wide Survey will be the main program of the Euclid telescope, covering an area of 15,000 sq. deg with a magnitude depth of 24 (AB mag). In their observing strategy for a given field, NISP grism, and VIS will simultaneously take 570s exposures, then NISP images of 112s each will be taken, in addition to calibration exposures. 95 percent of the survey will have at least three VIS images, 90 percent will have NISP Y, J, and H band, 90 percent will have >3 spectroscopic images, and 50 percent will have 4 or more spectroscopic exposures at different orientations to minimize cross-contamination between objects and orders. The Euclid fields are chosen based on constraints from the spacecraft orbit, calibration exposures, minimizing zodiacal light, and Galactic extinction and blinding stars. As VIS is in the optical, these exposures and will be the most affected by Galactic extinction (reaching 0.15 mag at central wavelength). With these constraints, most of the galactic plane will be avoided $|\beta| > 23$degrees.

Euclid Deep and Auxiliary Fields In addition to the main wide survey, Euclid will target well-known fields that have archival ground-based and space-based data. These fields are the CDFS, COSMOS, SXDS, VVSS, CANDELS/AEGIS, CANDELS/GOODS-N covering about 0.5-2. sq. deg. Additional observations of the CPC (completeness purity calibration) field covering 20 sq. deg, deep observations of 10-20 sq. deg for Euclid deep fields (EDF North, EDF South and EDF Fornax). In total, the Euclid deep fields will cover over 40 sq. deg to a depth of 27 mag (AB).

4.2.2 Rubin Observatory & Other Ground-based surveys

The Rubin Observatory The Vera Rubin Observatory (previously known as the Large Synoptic Sky Survey Telescope, LSST, LSST Science Collaboration et al. 2009) is a ground-based observatory located in Chile (first light August 2024). The primary goal

of the Rubin Observatory is to conduct a synoptic survey of the sky which will probe the nature of dark energy and dark matter, map bodies in the solar system, survey the transient sky, and map the structure of the Milky Way. Its 6.7 meter telescope provides a 9.6 sq. deg field of view, and operates at optical wavelengths (0.3-1 micron, *ugrizy* filters). At full operation, the Rubin Observatory will deliver 15 TB of raw images per night over the next 10 years, totaling over 50 petabytes of data.

The main Rubin survey will cover 18,000 sq. deg of the Southern sky to acquire large samples of photometric redshifts for galaxies, discovering and characterizing supernovae, and performing weak lensing measurements in galaxy clusters to constrain cosmological models. These goals will require repeated and frequent observations probing various timescales in different optical filters. Additional astrometric measurements are required for solar system science and Milky Way science. The main survey will reach single visit depths of single visit of $u = 3.9, g = 25.0, r = 24.7, i = 24.0, z = 23.3, y = 22.1$ AB mag and the 10-year survey will reach depths of $u = 6.3(70\text{visits}), \text{g} = 27.5(100), \text{r} : 27.7(230), \text{i} : 27.0(230)\text{z} : 26.2(200), \text{y} = 24.9(200)$, and astrometric precisions of 3 mas and 1 may/r at $r = 24$, but it will be possible to reach to 0.6 mas or 0.2 mas/yr for $r = 21$ all calibrated to the Gaia reference frame.

In addition to the main survey, the Rubin observatory will survey probe deep fields, accounting for 10-20 percent of observing time with more frequent visits. These deep fields will reach depths of $u = 23.5, g = 25.3, r = 25.6, i = 25.4, z = 24.9, \text{and} y = 24.0$ and they are located at the following Galactic coordinates: ELAIS S1 (l=311., b=-72.9), XMM-LSS (171.2, -58.77), Extended Chandra Deep Field-South (l=224.07, -54.47), COSMOS (l=236.83, b=42.09).

LSST DP0 As we use the LSST Data Preview data (DP0) to validate our simulations for the Rubin survey, we briefly describe it here. The DP0 data was released in 2022

by the Rubin DESC collaboration, with the goal of providing simulated catalogs and images and testing the Rubin pipeline. These simulations include galaxies and stars in the Milky Way using large-scale N-body simulations, galaxy models, and Milky Way stellar populations models that account for dust extinction. For the Milky Way populations, they used the luminosity function and the stellar density model by Jurić et al. (2008), extrapolating the luminosity function $r \approx 27$. As a validation test, they their compared numbers to the Besancon model (Robin et al., 2003). Proper motions and 3D-kinematics were modeled based on Bond et al. (2010). To estimate magnitudes of individual sources, they convolved stellar SEDs by Kurucz (1993) for main-sequence stars and giants, and they used M L, T dwarfs models and spectra from Cushing et al. (2005); Bochanski et al. (2007); Burrows et al. (2006)Finally, they simulated Rubin observations (including the cadence) by generating mock images and processing them the Rubin pipeline. Here, we only use the final generated point-source catalog.

4.2.3 Nancy Grace Roman Telescope

The Nancy Grace Roman Telescope (Schneider et al., 2015) is expected to launch in 2025, its main goals are to explore the nature of dark matter and dark energy and to constrain theories about the formation of exoplanets. Many observing programs are proposed, but here we will only focus on the two relevant surveys.

The High-Latitude Wide-Area Survey (HLWAS) The main goal of this survey is to measure redshifts for galaxies early in the universe (z=1-3, look back times of 8-11 billion years) to constrain cosmological parameters. The Survey will consist of 1,700–2,000 sq. deg at depths of 25.8-26.7 (AB, depending on the filter) using the Y106, J129, H158, F184 filters, and Grism. Most of the surveyed areas (while not fully determined yet) will be at high galactic latitudes to avoid Galactic extinction.

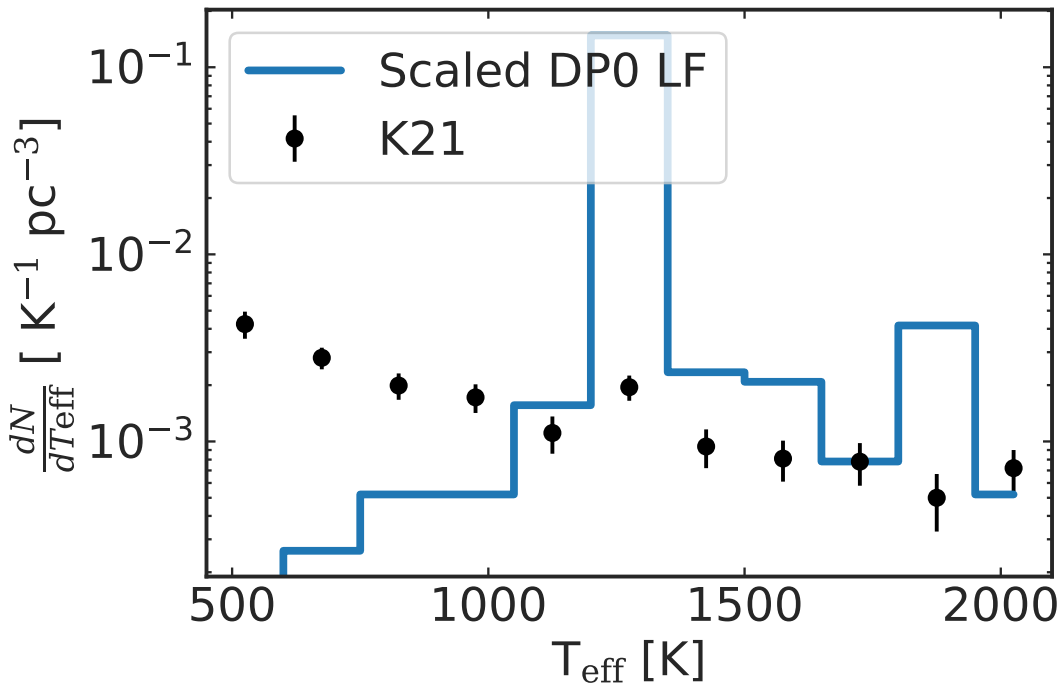

Figure 4.1 Luminosity function of ultracool dwarfs in 150 K bins inferred from the DP0 dataset (blue histogram) compared to the measured luminosity function within 20 pc Kirkpatrick et al. (2021). The DP0 sample includes "stars" with $i-z>1$ and $z<22$, assumes the $i-z$/SpT and SpT/M_i relations of Best et al. (2018), and is constrained to an estimated (volume-complete) distance of 30 pc. While the luminosity functions are in agreement down to 1500 K, these distributions diverge significantly in the cooler T and Y dwarf regime (note the log scale).

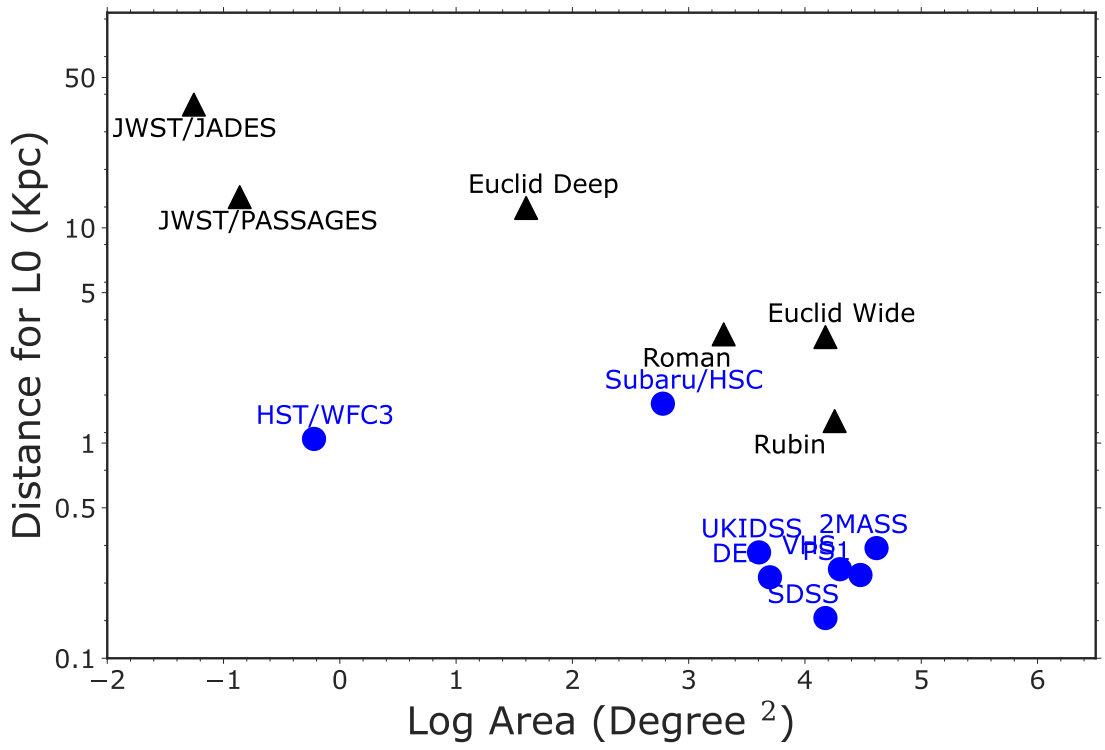

Figure 4.2 Comparison of depths and area between previous surveys (blue) and future surveys (black)

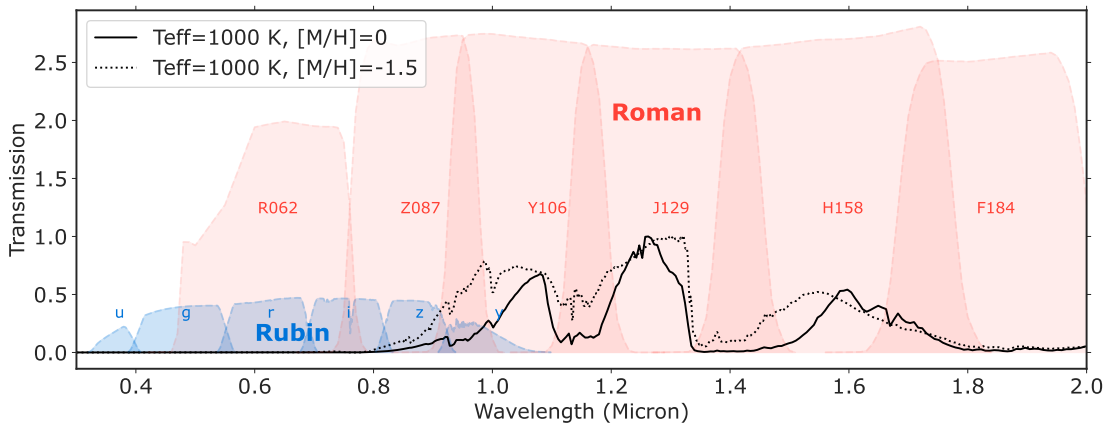

Figure 4.3 Model spectra by Gerasimov et al. (2022) for two objects with $T_{\rm eff}$=1000 K with metallicities of 0 and -1.5 showcasing the sensitivity of molecular absorption features of UCDs to metallicity effects. Filter profiles

The High-Latitude Time Domain Survey (HLTS) The main goal of HLTS is to detect bright high-z supernovae to constrain cosmological parameters. The survey will constitute 25 percent of all Roman observing time over two years. It will cover 5-20 sq. deg with filters that are yet to be determined and the Prism instrument. Each region will be re-imaged every 5 days, and while the locations of the fields has been confirmed, it will survey high galactic latitudes to minimize effects due to galactic extinction.

4.3 Methods

4.3.1 Population Simulations

Atmosphere and Evolutionary models :

To model the disk population, we used the set of evolutionary models provided by the Sonora grid (Marley et al., 2021). The Sonora models are solar metallicity, spanning effective temperature ($T_{\rm eff}$) range of 200 K to 2400 K, surface gravity (logg) range from 2.5 to 5.5 cm/s^2, (C/O) ratios ranging from -0.5 to 1.5 solar, and masses ranges 0.5 to 85

Jupiter masses. These utilize the latest set of molecular opacities to accurately capture atmospheric properties. We also used solar-metallicity atmosphere models by Line et al. (2014). For subsolar metallicities, we used the atmosphere and evolutionary models Gerasimov et al. (2022) models, which use the PHOENIX code (Hauschildt et al., 1997). Gerasimov models encompass a comprehensive set of physics, incorporating clouds based on BT-Settl (Allard et al., 2012; Helling et al., 2008)They also include 500 gases and 200 condensates, allowing for a detailed treatment of atmospheric composition.For our study, we focused two populations of metallicities ranging from -0.5 to -1.5 with [alpha/Fe]= 0.3, to model the thick disk and halo populations respectively.

Absolute Magnitude-Spectral Type Relations To transform model parameters to the observed properties of the sample, we constructed absolute magnitude relations based on a combination of empirical and theoretical spectra and photometry. Previous studies have devised absolute magnitude relations for subdwarfs, but they are usually not extended to the low-temperature regime due to the lack of parallax information for these faint objects. To address this issue, we collected spectral templates and photometric data for known dwarfs and subdwarfs in the literature. We used dwarf template spectra for dwarfs from the SpeX Prism Library (Burgasser, 2014) [1]$> 2,000$ M5$-$T8 spectra, and their compiled 2MASS J, H, and K magnitudes. Additionally, we collected Gaia DR2 parallax information and Pan-STARRS photometry for $> 7,000$ M0-T9 objects compiled by Best et al. (2021). We also used additional optical and infrared spectra by Lodieu et al. (2010) and Zhang et al. (2018)

For sources with parallax information, we computed Pan-STARRS g, r, i, z, y the 2MASS J, H, K_s and SDSS g,r,i,z absolute magnitudes. To magnitudes we first computed the color difference between filters and the closest-matched SDSS, PS1 or

[1] http://www.browndwarfs.org/spexprism/

2MASS filters, by convolving spectral templates (including subdwarfs) with filter profiles. We then fitted a 4th-degree polynomial to the absolute magnitude vs spectral type for all filters. Due to the lack of spectral templates for late-type objects, we used solar-metallicity atmosphere models by (Line et al., 2014) and metal-poor models by Gerasimov et al. (2020), restricting the templates to log g$=$ 4.5 or 5.0 to exclude young sources. For these models, we estimated spectral types based on spectral type-temperature relations by Gonzales et al. (2018) and Pecaut & Mamajek (2013). Absolute magnitudes were scaled to the SDSS z-band to account for any-zero point offsets. We report the absolute magnitude-spectral type relations in Table 4.3.

Simulating a Population Our method closely follows the process in derived Chapter 2. We modeled a Galactic population, assuming that all thin disk sources are dwarfs with solar metallicity, and thick disk sources are classified as sd or d/sd with [Fe/H]$= -0.5$, and all halo sources are classified as esd with [Fe/H]$= -1.5$.

We simulated 10^6 stars by drawing their masses a power-law initial mass function ($dN/dM = M^{-0.6}$, based on Kirkpatrick et al. 2021). We assumed uniform age distribution of $0-8$ Gyr for a thin disk population, $8-13$ Gyr for a thick disk population, and 10-14 Gyr for a halo population (Jurić et al., 2008; Jofré & Weiss, 2011a; Kilic et al., 2017). To account for binaries, we simulated masses of secondaries from a mass ratio ($q = M_2/M_1$) distribution $P(q) = q^4$ with and q$\in$[0, 1]. These parameters are based on the statistical distribution of resolved binaries (Burgasser, 2007). We estimated effective temperatures ($T_{\rm eff}$) using evolutionary models by Marley et al. (2021) for thin disk sources and Gerasimov et al. (2020) for thick disk and halo objects. The resulting temperature distribution to the measured luminosity function of Kirkpatrick et al. (2021).

Our goal is to model the expected counts, color, and proper motion selections in these surveys. To model wide-area surveys accounting for galactic structure, we

simulated distances assuming an exponential thin disk with a scale height of 300 pc, an exponential thick disk with a scale height of 900 pc, and a flattened spheroid halo based on Jurić et al. (2008)

We assigned absolute magnitudes based on our pre-computed absolute-magnitude vs spectral type relations. We then assigned apparent magnitudes from distances and absolute magnitudes. While the intrinsic scatter in our relations varies, we used a scatter of 0.1 for all our relations. We further discuss the limitations of these simulations below. Distances are assigned by randomly sampling from the integrated cumulative density of stars as a function of distance along a line of sight (l, b). To simplify these computations, we chose 1,000 random lines of sight from the positions of all candidates, sampling a given survey's footprint.

Simulating Kinematics We assigned heliocentric UVW kinematics for the thin disk, thick disk, and halo populations. For the thin disk, we drew UVW velocities as normal distributions, with the median velocities and the velocity dispersions given by the age-velocity dispersion relations by Aumer & Binney (2009):

$$\sigma(\tau) = \sigma_0 \left(\frac{\tau + \tau_{\rm min}}{\tau_{\rm min} + \tau_{\rm max}} \right)^{\beta} \tag{4.1}$$

$$(U,V,W) \propto \text{Normal}\left((U_0,V_0,W_0);\sigma(\tau)\right) \tag{4.2}$$

where σ_0 is the velocity dispersion for population of age τ between $\tau_{\rm max}$, $\tau_{\rm min}$ and $\tau_{\rm max}$ = 10Gyr and β is a power-law index that quantifies the rate of dispersion increase. We used the best-fit model parameters from Aumer & Binney (2009) without a low-metallicity tail, for σ_U velocities $(\beta, \sigma_0, \tau_{\rm min})$ =(0.307, 41.899 km s^{-1}, 0.001 Gyr), (0.43,28.823 km s^{-1}, 0.715 Gyr) for σ_V and (0.455, 23.381 km s^{-1}, 0.001 Gyr). We used (U_0, V_0, W_0)= (0 km/s, $-\sigma_V^2$/74 km/s, 0 km/s) based on the same study. For the thick disk, we used

a constant velocity dispersion of $(\sigma_U, \sigma_V, \sigma_W) = (67, 38, 35)$ km/s and $(U_0, V_0, W_0) = (0, 46, 0)$ km/s based on Bensby et al. (2013). For the halo we used the multiple halo models of Carollo et al. (2007) where $(\sigma_U, \sigma_V, \sigma_W) = (58, 52.5, 38)$ km/s and $(U_0, V_0, W_0) = (-2.5, -31, 2)$ km/s for galactic heights ($|z|$) $<$ 1kpc; $(\sigma_U, \sigma_V, \sigma_W) = (136, 105, 78)$ km/s and $(U_0, V_0, W_0) = (-10, -181, -4)$ km/s for ($1 < |z| <$ 2kpc); $(\sigma_U, \sigma_V, \sigma_W) = (163, 121, 95)$ km/s and $(U_0, V_0, W_0) = (-29, -209, 4)$ km/s for ($2 < |z| <$ 3kpc); and $(\sigma_U, \sigma_V, \sigma_W) = (152, 136, 109)$ km/s and $(U_0, V_0, W_0) = (-37, -237, 2)$ km/s for ($|z| >$ 3kpc. We then computed the reduced proper motions in respective filters from each object's positions and 3D kinematics.We also computed reduced proper motions H given a magnitude m in each respective defined as

$$H = m + 5 \times \log_{10}(\mu) - 10 \tag{4.3}$$

Number Counts To predict the expected counts in each survey, we first needed to estimate the effective volume, by accounting for the densities and selection effects along a given line of sight. We divided each survey footprint into small angle pointings. The total expected number of stars per spectral type and in a given Galactic direction (l, b) was then computed by integrating the local density, corrected by the selection function $\mathscr{S}$ as a function of spectral type and direction as

$$N(\mathrm{SpT, l, b}) = \int_{1\ \mathrm{pc}}^{\mathrm{d_{max}}} \rho(\mathrm{SpT, r, l, b}) \mathscr{S}((\mathrm{SpT, l, b}) \mathrm{r^2 drd}\Omega \tag{4.4}$$

where $d_{\max}$ is the maximum distance for a given spectral type (based on 1.5 times the distance obtained from the magnitude limits). As defined in Chapter 3, the local density from Kirkpatrick et al. (2021), and the total density is obtained by adding the thin disk density, thick disk and the halo. $d\Omega$ is the total angular area of the pointing which is assumed to be sufficiently small that the integral elements are independent of the areal

coverage in a given pointing. . We simulated 100 random pointings (except for the Euclid survey where the pointing is specified) at high Galactic latitudes (>20 degrees).

To compute the selection function (SpT, l, b) for a given spectral type and direction, we computed the fraction of sources within the selection criteria (including magnitude cuts, color and proper motion selections) compared to the number of the simulated population. We report the resulting number counts in the upcoming sections. We applied three basic "baseline surveys" for each observatory/facility that we simulated in our analysis (Summarized in Table 4.1). For the Rubin survey, we simulated the 10-year depths, and the single-visit depths, including our color selection and requiring a proper motion cut of > 1 mas/yr as described by the survey. For Euclid, we simulated the wide-fields survey and the deep fields, and for Roman, we simulated the HLTDS and the HLWAS survey.

Table 4.1 Table of Simulated Surveys

Survey	Area (sq. deg)	Simulated footprint	Selection
Rubin single visit	18,000	Decl.<0 deg.	$i<24.0$, $z<23.3, y<22.1, i-z>0.7$ $i-y>1, z-y>0.5$
Rubin 10 year	18,000	Decl.<0 deg.	$i<25.4$, $z<24.9, y<24, i-z>0.7, i-y>1$ $z-y>0.5, \mu>1\mathrm{mas/yr}, \pi>3\mathrm{mas}$
Roman HLWAS	2,000	$\lvert\beta\rvert>20$ deg	F087= 26.7, F106= 26.7 F129= 26.7 F158= 26.7, F184= 25.8
Roman HLTDS	20	$\lvert\beta\rvert>20$ deg	F087= 26.7, F106= 26.7 F129= 26.7, F158= 26.7, F184= 25.8
Euclid wide area	15,000	$\lvert\beta\rvert>20$ deg	NISP Y, J, H= 24
Euclid deep fields	40	R.A=189.2 deg, Decl.=62.2 deg	Y, J, H= 27

4.4 Results

4.4.1 Prediction for Future Surveys

Color and Proper Motion Selection To design selection criteria for UCDs in Rubin surveys, we computed synthetic colors by convolving relevant filters with the Low-Z

Table 4.2 Population simulation parameters

Population	Parameter	Distribution	Reference
All	IMF	Power law (α=-0.6)	Kirkpatrick et al. (2021)
Thin disk	Age	Uniform (0, 8) Gyr	Jurić et al. (2008)
	Metallicity	solar	Mackereth et al. (2019a)
	Evolutionary grid	–	Marley et al. (2021)
	Density	Exponential disk	Jurić et al. (2008)
	Local density	–	Kirkpatrick et al. (2021)
	Kinematics	Gaussian (as a function of age)	Aumer & Binney (2009)
Thick disk	Age	Uniform (8, 10) Gyr	Kilic et al. (2017)
	Evolutionary grid	–	Gerasimov et al. (2020)
	Metallicity	[Fe/H]=-0.5	Mackereth et al. (2019a)
	Density	Exponential disk	Jurić et al. (2008)
	Local thick disk fraction	0.12	Jurić et al. (2008)
	Kinematics	Gaussian	Bensby et al. (2013)
Halo	Age	Uniform (10, 14) Gyr	Jofré & Weiss (2011a)
	Evolutionary grid	–	Gerasimov et al. (2020)
	Metallicity	[Fe/H]=-1.5	Mackereth et al. (2019a)
	Density	Spheroid	Jurić et al. (2008)
	Local halo fraction	0.0025	Jurić et al. (2008)
	Kinematics	Gaussian	Carollo et al. (2007)

and Gerasimov et al. (2022) atmosphere models, without accounting for instrumental uncertainty. To design selection criteria for Rubin surveys, we compared the combination of $g-z, z-y, r-z, i-z,$ and $g-r$ colors of the models to the DP0 data. We did not account for the spread in colors due to binarity or uncertainties, but we used a broad set of criteria that distinguish most of the colder objects from the DP0 population. Hence, we required $z-y > 0.2, i-y > 1, i-z > 0.7$ for both the Rubin single visits and the Rubin 10 year survey. For the 10 year survey, we required parallaxes to be < 1 mas and 3 mas/yr cut for proper motions.

Expected Yields The Euclid wide area survey will find $> 10^6$ UCDs, with a nearly equal number of stars in the thin disk, disk. For the halo, we expect a similar number of UCDs at earlier types ($< L0$), but the number of halo L and T dwarfs drop to $10^4 - 10^5$.

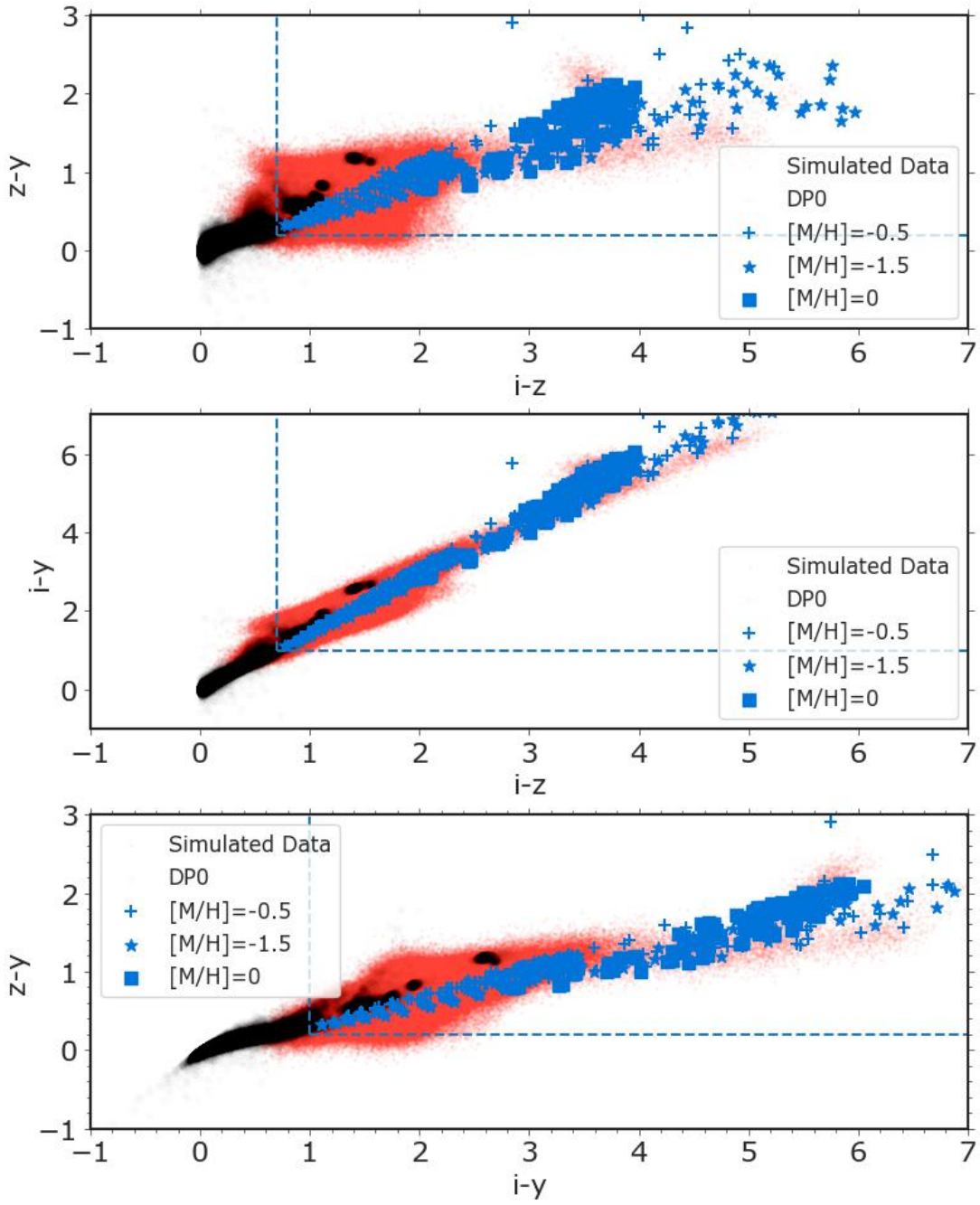

Figure 4.4 Color selection of UCDs in the Rubin Observatory. DP0 data are shown in black, metal-poor models are shown as crosses, and solar metallicity models are shown as circles.

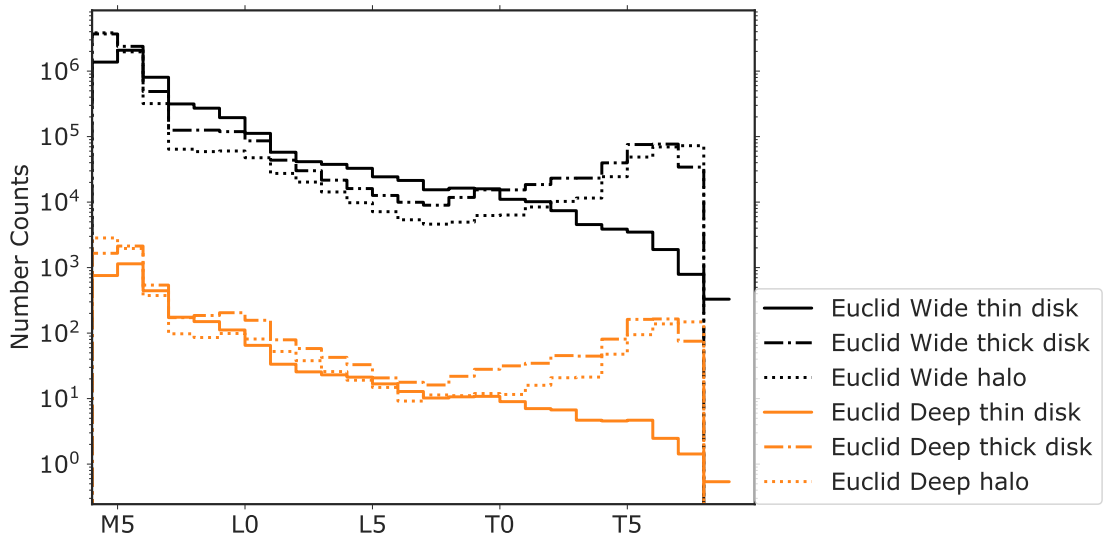

Figure 4.5 Expected number counts of UCDs for the baseline Euclid surveys for different Galactic populations

For the deep fields, we expect thousands (per type) of thin disk and thick disk sources and hundreds of halo L and T dwarfs. Our expected counts for the Euclid surveys are in agreement with Sharma et al. (2021). Additionally, as UCDs subdwarfs are typically intrinsically brighter, we expect to detect halo and thick disk UCDs in larger volumes at the same magnitude limit. Also, the deep fields probe volumes where the thick disk and halo sources dominate over thin disk sources as thin disk sources have a small scaleheight.

For the Roman survey, the wide-field survey will cover a smaller area compared to Euclid by a factor of ≈ 7, but 2-3 magnitude deeper (see Table of surveys). Hence, our simulations predict nearly a similar number compared to Euclid (i.e $> 10^5$ per type) of late M dwarfs in the thick disk and halo. There is a drop in the L/T transition and a peak back towards T dwarfs. Note that as we simulated both surveys have to have the same depths, hence the HLTDS survey expected counts show the same trend. Note that Roman surveys will detect more thick disk and halo objects compared to thin disk sources. Additionally, with proper motion information, it will be possible to separate thick disk, thin disk and halo objects in reduced proper motion -vs color space.

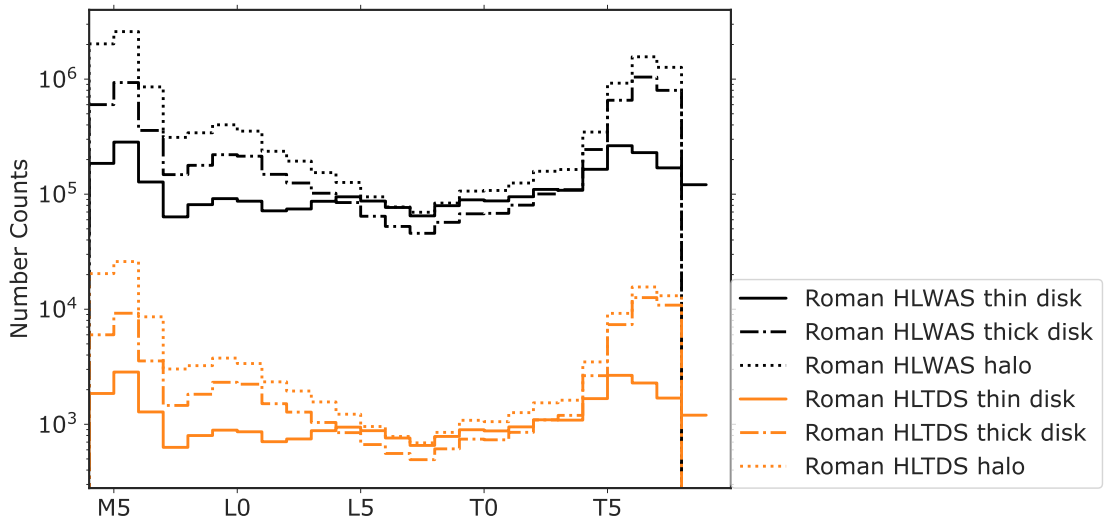

Figure 4.6 Expected number counts of UCDs for the baseline Roman surveys for different Galactic populations

Similarly, for the Rubin survey will predict $> 10^6$ >M5 objects but these numbers are suppressed towards T dwarfs reaching tens of objects per type for the thin disk. For the thick and halo, we still expects to detect thousands of sources, which is an at least 2 orders of magnitude improvement on the current number of known T subdwarfs. We also simulated the 10 year survey by applying the astrometric selection criteria shown in Figure 4.10. We find that the 10 year survey will detect thousands of subdwarfs (halo and thick disk) with detectable parallaxes and proper motions.

Finally, we examine the possibility to constrain the disk scaleheight and the halo mass function with these samples. Figures 4.8 and 4.9 show the expected number counts for thin disk scaleheigths between 100 pc–400 pc and the halo mass function power-law between -2.3–2.3. Roman and Euclid will provide sufficiently-large samples to differentiate the scaleheight with a precision < 50 pc. Rubin will provide millions of samples due its large but it is still unable deep in the halo and the disk. However, Rubin will provide precise parallaxes and proper motions, which will independently constrain the kinematics of the disk.

Table 4.3 Absolute magnitude and color vs spectral type relations used in this work.

x	y	rms	c6	c5	c4	c3	c2	c1	c0
spt	LSST g	0.24	-9.4754e-06	1.3335e-03	-7.0447e-02	1.7138e+00	-1.7917e+01	7.5084e+01	
spt	LSST r	0.23	-1.6833e-05	2.1536e-03	-1.0434e-01	2.3498e+00	-2.3426e+01	9.2152e+01	
spt	LSST i	0.22	-1.4762e-05	1.8217e-03	-8.5638e-02	1.8904e+00	-1.8634e+01	7.4120e+01	
spt	LSST z	0.21	-9.0376e-06	1.1847e-03	-5.8829e-02	1.3562e+00	-1.3695e+01	5.6959e+01	
spt	LSST y	0.21	-7.1508e-06	9.6091e-04	-4.8594e-02	1.1321e+00	-1.1416e+01	4.8178e+01	
spt	Roman R062	0.21	-9.3350e-06	1.2166e-03	-6.0073e-02	1.3774e+00	-1.3827e+01	5.6995e+01	
spt	Roman Z087	0.21	-9.3455e-06	1.2179e-03	-6.0131e-02	1.3786e+00	-1.3838e+01	5.7031e+01	
spt	Roman Y106	0.21	-7.3312e-06	9.7438e-04	-4.8560e-02	1.1069e+00	-1.0708e+01	4.2725e+01	
spt	Roman J129	0.22	-5.1804e-06	7.2067e-04	-3.7330e-02	8.7936e-01	-8.7845e+00	3.6274e+01	
spt	Roman H158	0.22	-7.6170e-06	9.9640e-04	-4.8919e-02	1.1061e+00	-1.0906e+01	4.3349e+01	
spt	Roman F184	0.23	-4.0883e-06	6.1539e-04	-3.3424e-02	8.0952e-01	-8.2118e+00	3.4140e+01	
spt	Roman Prism	0.22	-5.3463e-06	7.3440e-04	-3.7715e-02	8.8218e-01	-8.7326e+00	3.5123e+01	
spt	Roman Grism	0.22	-7.9558e-06	1.0338e-03	-5.0719e-02	1.1604e+00	-1.1920e+01	5.0993e+01	
spt	Euclid Y	0.21	-7.4184e-06	9.8267e-04	-4.8831e-02	1.1102e+00	-1.0709e+01	4.2012e+01	
spt	Euclid J	0.22	-5.8817e-06	7.9324e-04	-4.0115e-02	9.2721e-01	-9.1211e+00	3.5879e+01	
spt	Euclid H	0.22	-7.3423e-06	9.6595e-04	-4.7629e-02	1.0790e+00	-1.0600e+01	4.0518e+01	
spt	LSST g	0.46	1.8157e-05	-2.3958e-03	1.2860e-01	-3.5190e+00	4.9233e+01	-2.5970e+02	
spt	LSST r	0.58	3.9380e-05	-5.5472e-03	3.0853e-01	-8.4495e+00	1.1394e+02	-5.8695e+02	
spt	LSST i	0.53	8.8129e-06	-1.1733e-03	6.3224e-02	-1.7331e+00	2.4482e+01	-1.2725e+02	
spt	LSST z	0.37	2.5824e-06	-2.7472e-04	1.2816e-02	-3.5902e-01	6.1574e+00	-3.2887e+01	
spt	LSST y	0.38	7.2254e-06	-9.6995e-04	5.3125e-02	-1.4893e+00	2.1422e+01	-1.1296e+02	
spt	WFI R062	0.33	2.5317e-07	7.7007e-06	-2.9285e-04	-6.9568e-02	3.1308e+00	-2.0917e+01	
spt	WFI Z087	0.33	2.5317e-07	7.7007e-06	-2.9285e-04	-6.9568e-02	3.1308e+00	-2.0917e+01	
spt	WFI Y106	0.70	5.1851e-04	-5.2370e-02	2.1018e+00	-4.1912e+01	4.1587e+02	-1.6350e+03	
spt	WFI J129	0.34	1.8418e-05	-2.5040e-03	1.3462e-01	-3.5791e+00	4.7157e+01	-2.3515e+02	
spt	WFI H158	0.45	1.6587e-05	-2.3843e-03	1.3526e-01	-3.7787e+00	5.1923e+01	-2.6930e+02	
spt	WFI F184	0.50	2.6439e-05	-3.6844e-03	2.0229e-01	-5.4617e+00	7.2460e+01	-3.6673e+02	
spt	WFI Prism	0.40	1.6954e-05	-2.3947e-03	1.3362e-01	-3.6792e+00	5.0032e+01	-2.5688e+02	
spt	WFI Grism	0.41	1.9105e-05	-2.6913e-03	1.4957e-01	-4.0964e+00	5.5307e+01	-2.8307e+02	
spt	EUCLID Y	0.34	6.8506e-06	-8.4013e-04	4.1568e-02	-1.0567e+00	1.4114e+01	-6.6973e+01	
spt	EUCLID J	0.36	1.6312e-05	-2.2874e-03	1.2683e-01	-3.4742e+00	4.7058e+01	-2.3964e+02	
spt	EUCLID H	0.45	1.2314e-05	-1.8208e-03	1.0582e-01	-3.0148e+00	4.2073e+01	-2.1755e+02	
spt	LSST g	0.46	-1.2262e-05	1.6281e-03	-8.1213e-02	1.8518e+00	-1.8008e+01	6.7398e+01	
spt	LSST r	0.40	-1.7428e-05	2.2232e-03	-1.0533e-01	2.2598e+00	-2.0572e+01	6.7592e+01	
spt	LSST i	0.31	-2.3460e-05	3.2653e-03	-1.7543e-01	4.5311e+00	-5.5808e+01	2.7330e+02	
spt	LSST z	0.26	1.5019e-06	-2.2623e-04	1.4421e-02	-4.8266e-01	8.4052e+00	-4.6922e+01	
spt	LSST y	0.24	1.2067e-05	-1.6330e-03	8.6845e-02	-2.2791e+00	2.9779e+01	-1.4495e+02	
spt	WFI R062	0.23	9.9105e-06	-1.3802e-03	7.6023e-02	-2.0786e+00	2.8433e+01	-1.4429e+02	
spt	WFI Z087	0.23	9.9105e-06	-1.3802e-03	7.6023e-02	-2.0786e+00	2.8433e+01	-1.4429e+02	
spt	WFI Y106	19.00	1.3666e-05	-5.4975e-05	-4.5450e-03	-9.1041e-02	-3.2599e-01	5.5646e+01	
spt	WFI J129	0.35	1.2365e-05	-1.6706e-03	8.9626e-02	-2.3892e+00	3.1734e+01	-1.5809e+02	
spt	WFI H158	0.38	-9.3289e-06	1.1749e-03	-5.5407e-02	1.1962e+00	-1.1264e+01	4.2025e+01	
spt	WFI F184	0.49	-6.4902e-06	7.8450e-04	-3.3954e-02	6.1392e-01	-3.5150e+00	1.6935e+00	
spt	WFI Prism	0.34	1.9043e-07	-4.7284e-05	5.2094e-03	-2.5307e-01	5.4576e+00	-3.1995e+01	
spt	WFI Grism	0.36	1.5379e-06	-2.3830e-04	1.5911e-02	-5.4725e-01	9.3904e+00	-5.2745e+01	
spt	EUCLID Y	0.30	1.3961e-05	-1.9036e-03	1.0266e-01	-2.7415e+00	3.6385e+01	-1.8093e+02	
spt	EUCLID J	0.32	4.2540e-06	-6.1052e-04	3.5758e-02	-1.0611e+00	1.5842e+01	-8.3187e+01	
spt	EUCLID H	0.44	-8.5872e-06	1.0521e-03	-4.7621e-02	9.6133e-01	-7.9002e+00	2.5016e+01	

Decimal spectral type, with 10 = M0, 20 = L0, 30 = T0, etc. Empirical relations are computed as $y = \sum_{n=1}^{m} c_n x^n$ where m is the power of the polynomial. Coefficients are written in decimal exponent notation.

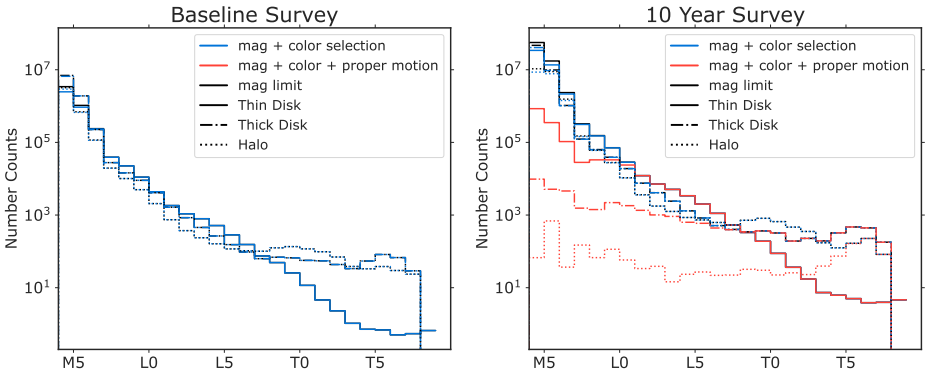

Figure 4.7 Expected number counts for the thin disk, thick disk and halo populations with the LSST baseline survey (left) and the full 10 year survey (right). While the 10 year survey is expected to have more UCDs, we imposed additional proper motions and parallax cuts on the 10 year. Overall, we should expect $> 10^5 > M5$ dwarfs with precise parallaxes and proper motions.

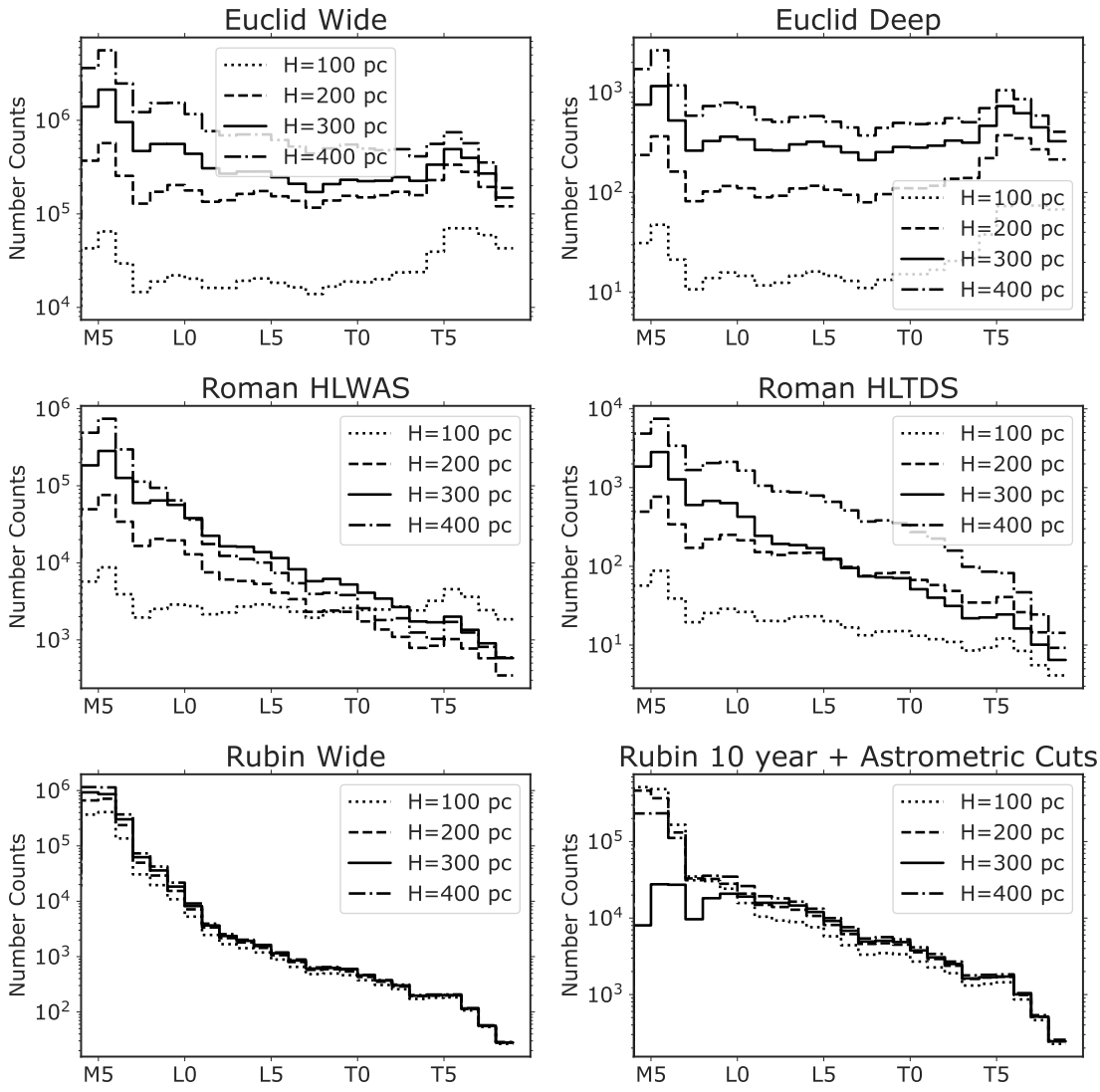

Figure 4.8 Expected number counts for thin disk UCDs for various surveys, assuming different scaleheights

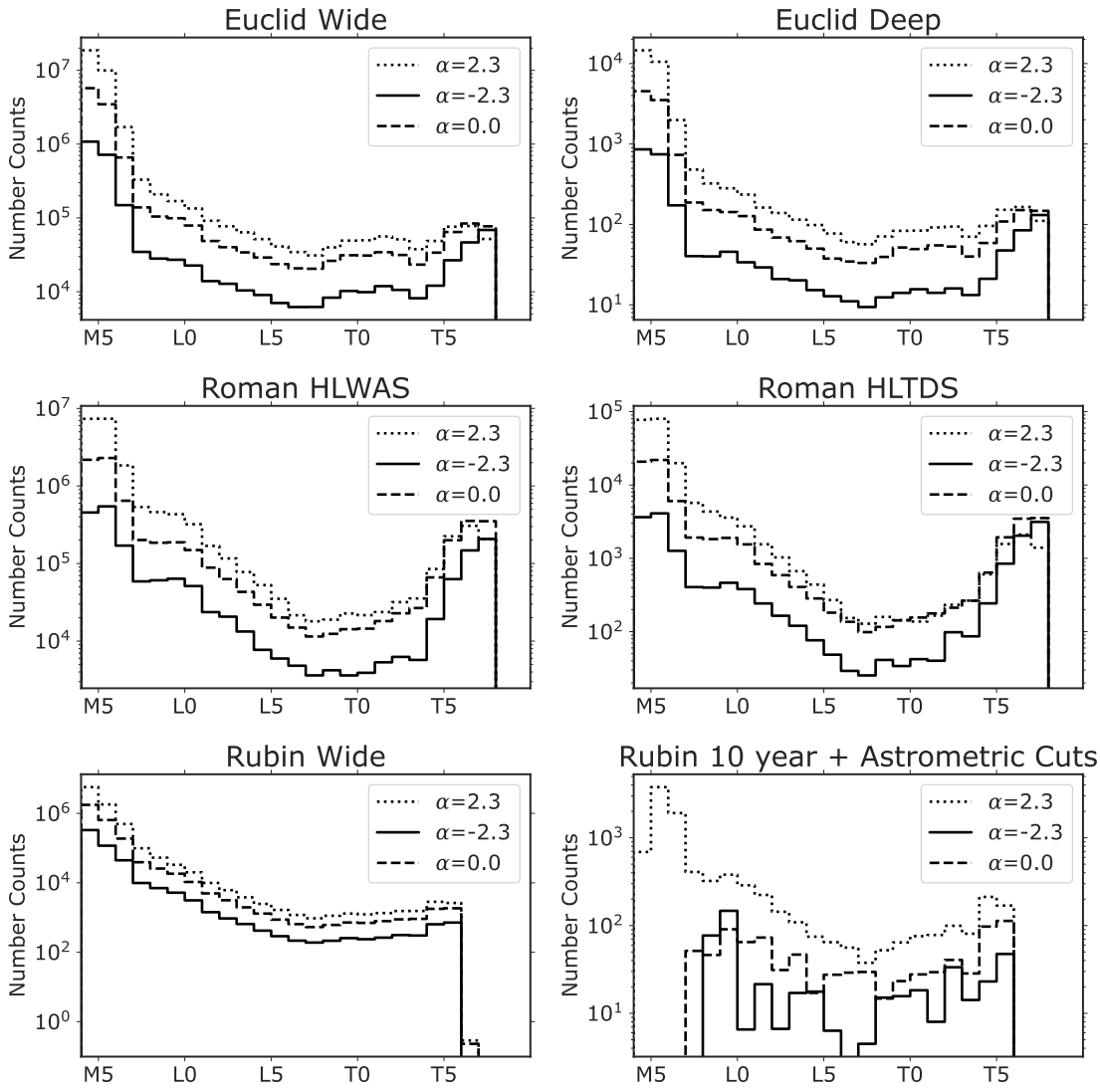

Figure 4.9 Expected number counts of halo UCDs for different surveys assuming different power-law exponent for the halo IMF

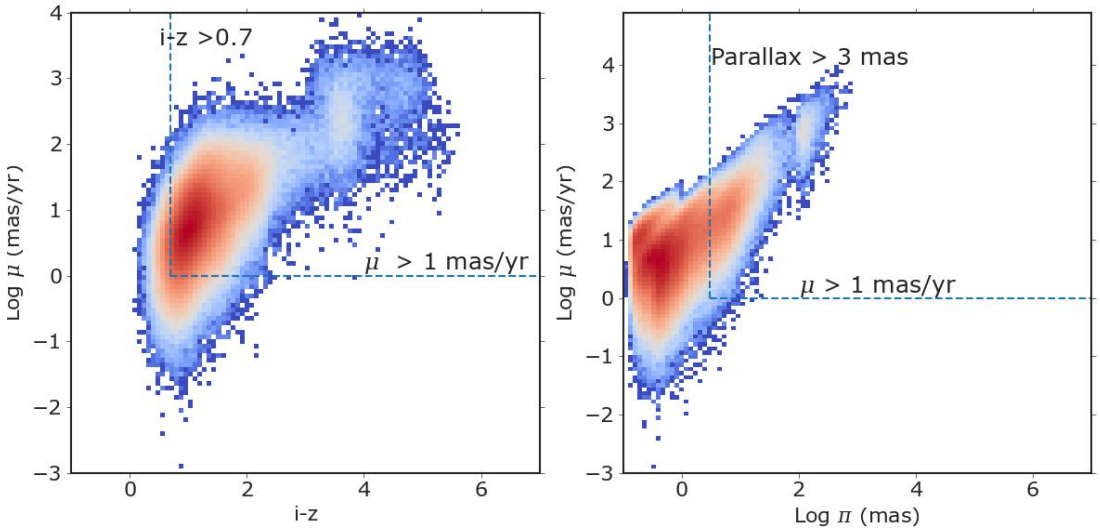

Figure 4.10 Distribution of $i-z$ colors, proper motions and parallaxes of UCDs within the magnitude limits of the LSST 10 year survey, the color scheme is the density of stars with an arbitrary normalization. A smaller set of the detectable sources will have measurable parallaxes over 10 years.

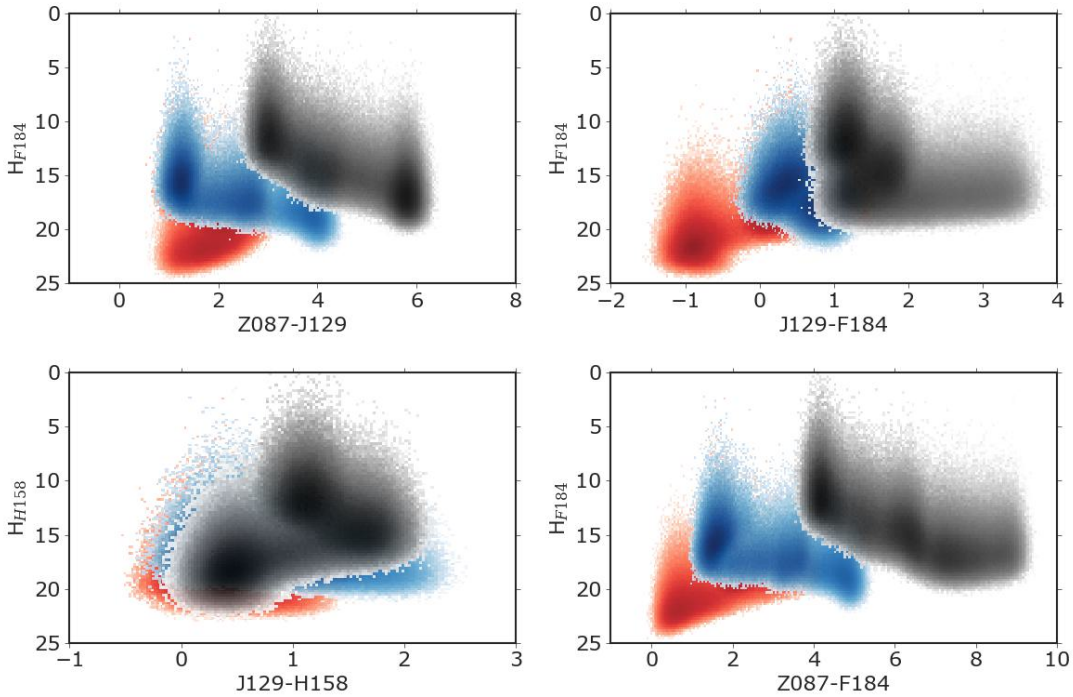

Figure 4.11 Reduced proper motion-color diagram for a sample Roman belonging to the thin disk (grey), thick disk (blue), and halo (red). The $Z087 - F184$ and $J129 - F184$ gives the best separation for these populations.

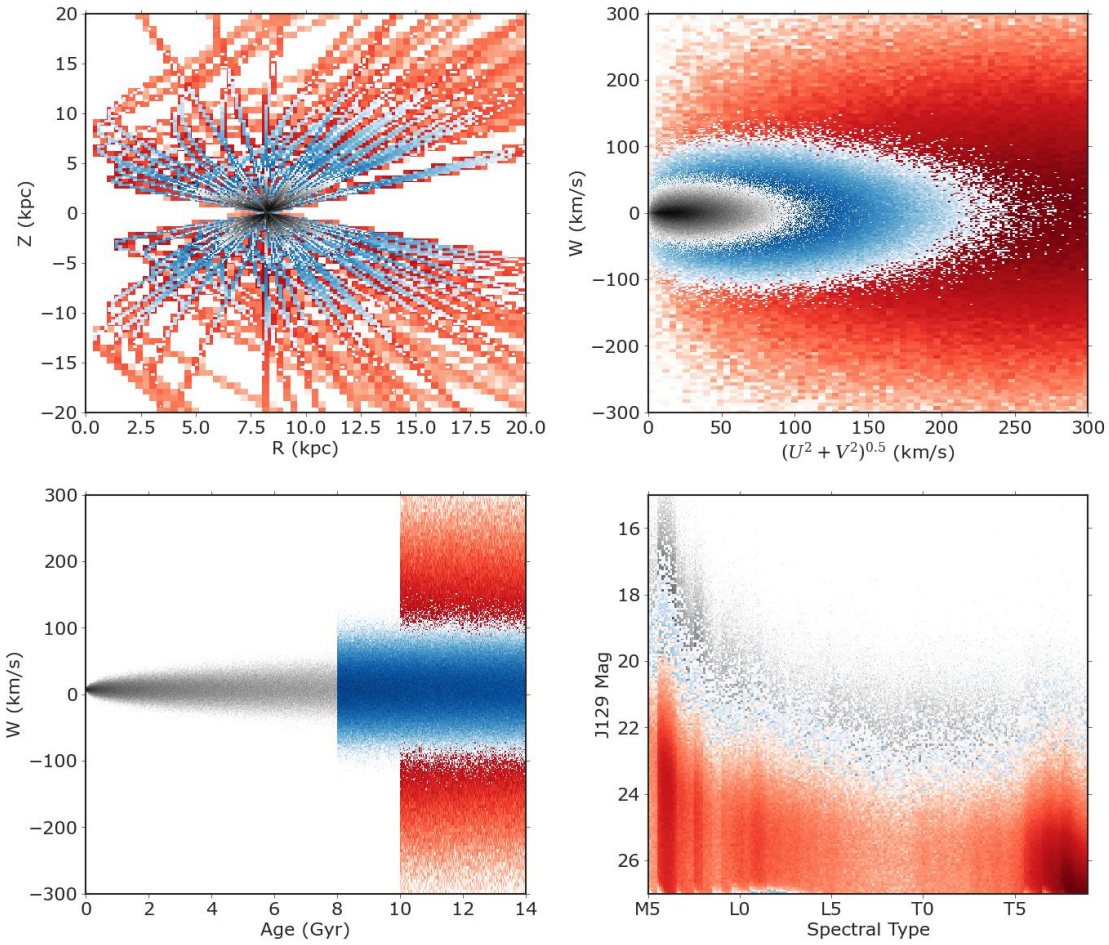

Figure 4.12 [Distribution of positions (top left), UVW velocities (top right), ages (bottom left), and magnitudes (bottom right) of sources in the Roman HLWAS survey. The number of objects and the normalization is arbitrary, but they are all within the magnitude limits of the survey. Thin disk sources are shown in black, thick disk are blue and halo stars are in blue. The density map follows the relative number of sources.

Chapter 4 is being prepared for submission to the Astrophysical Journal, authored by Christian Aganze, Roman Gerasimov, Adam Burgasser, Christopher Theissen, Chih-Chun Hsu. The thesis author was the primary investigator and author of this paper.

Chapter 5

Prospects for Detecting Gaps in Globular Cluster Stellar Streams in External Galaxies with the Nancy Grace Roman Space Telescope

5.1 Introduction

Large-scale cosmological simulations with cold dark matter (ΛCDM) predict hierarchical formation of dark matter halos and the existence of substructure at all scales (White & Rees, 1978; Blumenthal et al., 1984; Bullock et al., 2001; Springel et al., 2008; Fiacconi et al., 2016). To test ΛCDM predictions at small scales, previous studies have uncovered satellite galaxies around the Milky Way and dwarf galaxies in the local group with stellar masses down to 10^3 $M_\odot$ (Willman et al., 2005; Simon & Geha, 2007; Martin et al., 2008; Koposov et al., 2009; Willman et al., 2011; McConnachie, 2012; Bechtol et al., 2015; Drlica-Wagner et al., 2015; Geha et al., 2017; Mao et al., 2021). However,

in ΛCDM models, galaxies with halos of masses $\lesssim 10^8 M_\odot$ are more dominated by dark matter compared to higher-mass galaxies, which makes their detection difficult (Efstathiou, 1992; Okamoto et al., 2008; Bullock et al., 2000; Sawala et al., 2016). Other dark matter models differ from ΛCDM in their predictions for the masses and number densities of dark matter subhalos (subhalo mass functions). For instance, warm dark matter models (WDM, Bode et al. 2001) predict a similar hierarchical collapse at large scales, but this collapse is strongly suppressed at lower masses ($\lesssim 10^9 M_\odot$, depending on particle mass), resulting in a smaller fraction of low-mass subhalos (Bose et al., 2017). Similarly, some fuzzy cold dark matter models (Hu et al., 2000; Hui et al., 2017), predict a sharp cutoff at low masses ($\leq 10^7 M\odot$). Self-interacting dark matter (SIDM) models produce halos with pronounced cores with different tidal evolution, masses and densities compared to CDM halos (Spergel & Steinhardt, 2000; Rocha et al., 2013; Tulin & Yu, 2018; Glennon et al., 2022). Even in ΛCDM simulations, the survival and the properties of low-mass subhalos within a larger halo are poorly understood. The tidal field of the central galaxy, pre-existing substructure in the halo, and deviations from a smooth spherical halo density profile can all affect the tidal evolution of accreted subhalos (Garrison-Kimmel et al., 2017). On the other hand, analytical calculations, N-body simulations and high-resolution hydrodynamical simulations show that the central cores of subhalos are likely to survive for long periods of time, or even indefinitely (van den Bosch et al., 2018; van den Bosch & Ogiya, 2018; Errani & Peñarrubia, 2020).

All of these differences between different dark matter models can, in principle, be tested by statistical surveys of nearby low-mass subhalos. The key challenge is how to detect these invisible dark subhalos. Strong gravitational lensing offers an opportunity to validate predictions of dark matter models (Dalal & Kochanek, 2002; Amara et al., 2006; Nierenberg et al., 2014; Hezaveh et al., 2016; Nierenberg et al., 2017; Gilman et al., 2019). However, this technique probes all subhalos along the line of sight up to the

lensed luminous source, which complicates the inference of dark matter properties.

Globular cluster (GC) streams provide a complementary approach for detecting and measuring the spectrum of low-mass subhalos in the local volume (Johnston et al., 2002; Yoon et al., 2011; Bovy, 2016; Bovy et al., 2017). As GCs orbit the host galaxy, internal evolution and tidal stripping leads to the escape of stars from the central cluster, forming thin, elongated stellar streams which persist for billions of years (Johnston, 1998; Helmi & White, 1999). These streams can subsequently be perturbed by a free-floating dark matter subhalo, which can create a gap-like feature inside the stream (Yoon et al., 2011). Numerical and analytical calculations predict the morphology and frequency of these features in various types of GC streams (Yoon et al., 2011; Carlberg, 2012; Erkal et al., 2016; Sanderson et al., 2016; Koppelman & Helmi, 2021).

Photometric and spectroscopic surveys have identified and characterized $\approx$100 stellar streams in the Milky Way, with the majority being globular cluster streams (Odenkirchen et al., 2001; Newberg et al., 2002; Majewski et al., 2003; Odenkirchen et al., 2009; Newberg et al., 2009; Grillmair & Carlin, 2016; Shipp et al., 2018; Mateu et al., 2018; Ibata et al., 2019; Li et al., 2022; Martin et al., 2022; Mateu, 2023). A few of these GC streams show evidence of gap-like features that are predicted in numerical simulations of dark matter subhalo encounters (de Boer et al., 2018, 2020; Bonaca et al., 2020; Tavangar et al., 2022). In particular, Price-Whelan & Bonaca (2018) identified a spur and a gap in GD-1, which Bonaca et al. (2019) attributed to a likely encounter with a 10^6–10^7 dark matter subhalo $\sim$8 Gyr ago, after ruling out other types of perturbers.

Gaps in GC streams can be created through other processes, however. Previous studies have shown that baryonic matter perturbers (galactic bars, molecular clouds, black holes, spiral arms) can create similar features in GC streams (Amorisco et al., 2016; Hattori et al., 2016; Price-Whelan et al., 2016; Erkal et al., 2017; Pearson et al., 2017; Banik & Bovy, 2019; Bonaca et al., 2020), which makes gaps difficult to decipher, even

when they are detected. Moreover, since these streams have intrinsically low surface brightnesses, the detection of gaps has been limited to the Milky Way, which has resulted in relatively small samples.

Detecting gaps in globular cluster streams in external galaxies offers a new window into testing dark matter models by increasing the number and diversity of stream gaps. Previous studies have observed streams in external galaxies arising from tidally-disrupted satellites (Martínez-Delgado et al., 2010; Martinez-Delgado et al., 2021). While several candidate GC streams have been proposed in M31 (Pearson et al., 2022), these candidate detections require more sensitive and higher resolution data to be confirmed, and to eventually map both the streams and gap structures.

The upcoming *Nancy Grace Roman Space Telescope* (Spergel et al. 2015) will have a large field of view, high angular resolution and deep-imaging sensitivity. Pearson et al. (2019, 2022) demonstrated how this combination allows the detection of very low-surface brightness GC streams out to a couple of Mpcs. In this work, we examine the plausibility of detecting gaps in Pal 5-like GCs formed from interactions with dark matter subhalos by extending the predictions of Pearson et al. (2019). The paper is arranged as follows: Section 5.2 describes our methodology for simulating isolated, evolving streams with gaps; Section 5.3 discusses our simulations of mock observations with *Roman* including foreground and background star fields; and the feasibility of visual inspection to confirm gaps in simulated star count data. Section 5.4 discusses the application of an automatic gap-finding pipeline, `FindTheGap` (Contardo et al., 2022), to find gaps in simulated data. Section 5.5 discusses the implications and limitations of this work. We summarize our findings in Section 5.6.

5.2 Simulating Globular Cluster Streams with Gaps

Our goal is to simulate observations of gaps in GC streams, starting with the Palomar 5 stream (hereafter, Pal 5; Odenkirchen et al. 2001, 2003) as a test case, defined to have a present-day mass of 10^4 M$\odot$ (Ibata et al., 2017). Our work closely followed a similar methodology as Pearson et al. (2019), with additional modifications that are described herein. We conducted all numerical calculations with the `gala` package (Price-Whelan, 2017), which implements numerical integration techniques to model the orbits of stars in a pre-specified static potential.

5.2.1 Gravitational Potentials

In our analysis, we used M31 as the external host galaxy. Many groups have estimated the total mass and the potential of M31 by modeling the kinematics of satellites (Watkins et al., 2010); constraining the rotation curve (Chemin et al., 2009); modeling the velocity distributions using tracer particles such as stars, globular clusters, and planetary nebulae (Kafle et al., 2018); dynamical modeling of the giant southern stream (GSS) in M31 (Fardal et al., 2013); and the local group timing argument (González et al., 2014; Chamberlain et al., 2022). Additional references and trade-offs from these techniques are summarized by Fardal et al. (2013) and Kafle et al. (2018).

To set up an M31-like potential, we used the model by Kafle et al. (2018) composed of a central bulge, a disk, and a halo. The bulge potential follows a Hernquist profile (Hernquist, 1990) given by:

$$\Phi_b(r) = -\frac{GM_b}{r+q} \tag{5.1}$$

with a scale length (q) of 0.7 kpc and a bulge mass(M_b) of 3.4×10^{10} M$_\odot$. The disk

potential follows a Miyamoto-Nagai density profile (Miyamoto & Nagai, 1975) given by:

$$\Phi_d(R,z) = -\frac{GM_d}{\left(R^2 + \left(a + (z^2 + b^2)^{\frac{1}{2}}\right)^2\right)^{1/2}} \tag{5.2}$$

with a scale length (a) of 6.5 kpc, a scale height (b) of 0.26 kpc and a total disk mass (M_d) of 6.9 $\times 10^{10} \mathrm{M}_\odot$. These parameters for the disk and the bulge were adopted from a compilation of literature values (Bekki et al., 2001; Font et al., 2006; Geehan et al., 2006; Seigar et al., 2008; Chemin et al., 2009; Corbelli et al., 2010; Tamm et al., 2012). We assumed a Navarro-Frenk-White (NFW) profile (Navarro et al., 1996) for the halo given by:

$$\Phi_h(r) = -\frac{G\, M_{vir} \ln(1 + r\, c/r_{vir})}{g(c)\, r}, \tag{5.3}$$

$$\text{with } g(c) = \ln(1+c) - c/(1+c), \tag{5.4}$$

$$M_{vir} = \frac{4\pi}{3} r_{vir}^3 \Delta \rho_c, \tag{5.5}$$

$$\text{and } \rho_c = \frac{3H_0^2}{8\pi G} \tag{5.6}$$

Where M_{vir} is the virial mass, r_{vir} is the virial radius, c is the concentration parameter, Δ is the virial overdensity parameter and ρ_c is the critical density of the universe. As many of these parameters are interrelated, we used best-fit values for the halo virial mass at $\Delta = 200$ of $\mathrm{M}_{200} = 0.7 \times 10^{12} \mathrm{M}_\odot$, and $\log c = 1.5$ based on the inferred posterior distribution by Kafle et al. (2018). We note that the concentration parameter was poorly constrained in this work. We also assumed $H_0 = 67.7$ km/(Mpc s) based on Planck results (Planck Collaboration et al., 2020).

For the dark matter subhalo, we again assumed a Hernquist density profile with masses (M_h) and radii (r_h) determined by the scaling relation from Erkal et al. (2016):

$$r_h = 1005 \text{ pc} \times \left(\frac{M_h}{10^8 M_\odot} \right)^{0.5}. \tag{5.7}$$

5.2.2 Stream Progenitor Coordinates

As there are no currently-known globular cluster streams in M31, we used a Pal 5-like stream as an example. In the Milky Way, the Cartesian Galactocentric coordinates of Pal 5 are $(X,Y,Z) = (6.1 \text{ kpc}, 0.2 \text{ kpc}, 14.7 \text{ kpc})$ and $(V_X, V_Y, V_Z) = (-49.7 \text{ km/s}, -119.4 \text{ km/s}, -11.4 \text{ km/s})$ (Price-Whelan et al., 2019; Vasiliev, 2019)[1]. Our goal is to test the observability of gaps in streams located at various locations in galactic halos, hence, we also simulated streams to galactocentric radii of 35 kpc and 55 kpc. For simplicity, to simulate equivalent streams at 35 kpc and 55 kpc, we used positions that give approximately the desired Galactocentric radii, and we assumed that the velocities of the stream at 35 kpc and 55 kpc were the same as the velocity at 15 kpc. We used the same velocities (V_X, V_Y, V_Z) for all streams, but we note that this process results in different orbits compared to the stream at 15 kpc. These coordinates, along with additional parameters of our simulations are all summarized in Tables 5.1 and 5.2.

5.2.3 Generating a Gap in the Stream

We generated model streams using the "particle-spray" method described by Fardal et al. (2015) and implemented in `gala`. We assumed a uniform mass loss history and a progenitor mass (m_p) of 5×10^4 $M_\odot$ based on Bonaca et al. (2020). We simulated the direct impact of a dark matter subhalo and a stream using `gala`; specifically, the function

[1]We assumed that our GC progenitor lies at the present-day heliocentric equatorial coordinates of Pal 5, (α, δ) = (229022, $-$0112) at a distance of 22.5 kpc; and has a proper motion vector ($\mu_\alpha \cos\delta$, μ_δ) = ($-$2.736 mas/yr, $-$2.646 mas/yr) and radial velocity of $-$58.60 km/s. We assumed a galactocentric coordinate system with the local standard of rest velocity $\vec{V}_{lsr}$ = (8.4 km/s, 251.8 km/s, 8.4 km/s) and the Sun radial distance of 8.275 kpc from the Galactic center based on (Schönrich et al., 2010; Bovy et al., 2012b; GRAVITY Collaboration et al., 2019).

`MockStreamGenerator` which models the orbits of stars influenced by a massive body within an external potential. Throughout these calculations, individual stream stars were treated as non-interacting massless particles, and we did not include the stream's progenitor potential.

To ensure a direct impact between stream and subhalo, we first needed to determine the initial coordinates of both components given their positions and velocities at the moment of collision. We backward-integrated the present-day coordinates of the stream progenitor to a time t_1, initiated a stream at these coordinates, and then forward-integrated by Δt_2. At this point, the collision position was assumed to be at a position Δx away from the progenitor position. We adjusted the coordinates of the subhalo to achieve a fixed relative velocity ($|\vec{V_{\rm rel}}|$) between the stream stars and the subhalo perpendicular to the impact location. After we determined the position and velocity of the subhalo at the collision point, we backward-integrated its orbit by Δt_2 again to set the subhalo's initial conditions.

With the initial positions and velocities of the stream and subhalo determined, we forward-integrated the system for Δt_2, computing the stream particle/subhalo interaction using the `gala DirectNBody` routine, with an additional Δt_3 time period to allow the subhalo to pass completely through the stream. At this point, we removed the subhalo from the simulation to avoid potential multiple interactions, allowing for a more direct analysis of the observability of well-defined gaps in streams. We then forward-integrated the stream stars for the remaining $t_1 - (\Delta t_2 + \Delta t_3)$ to observe the growth of the gap over time.

These timescales ($t_1, \Delta t_2$ and Δt_3) were chosen to allow the stream to have similar lengths as that of Pal 5 in M31 (7–12 kpc at R_{GC}=15–55 kpc, based on estimates by Pearson et al. 2019). Additionally, after the subhalo encounter, we continued releasing stars into the mock stream to ensure that there isn't a gap at the location of the progenitor.

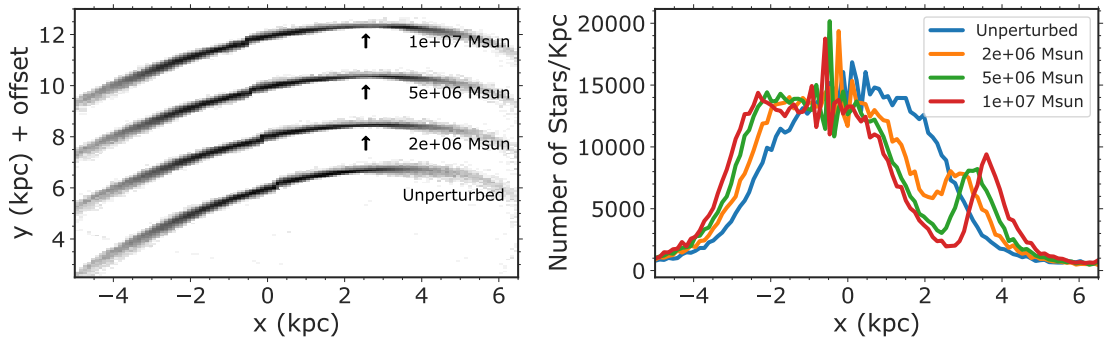

Figure 5.1 Results from our simulations of a gap in a stream at R_{GC}= 15 kpc. The total number of stars in each stream is ≈ 80,000 and the mass of the stream is 50,000 $M_{\odot}$. *Left* : Gaps are induced by collisions with dark matter subhalos of masses of $2-10\times10^{6}$ $M_{\odot}$. Each stream is offset by a constant displacement in the y-direction for display purposes and the relative velocity between the stream stars and the subhalo is 50 km/s. For comparison, we show an unperturbed stream of the same mass and trajectory. Arrows indicate the location of the gap, and we label the mass of the perturber. *Right* : Linear density of stars along the x-direction in each stream. In both plots, under-densities in perturbed streams can be identified by eye for subhalos with masses $\geq 2\times10^{6}$ $M_{\odot}$.

We later re-sampled the stream to match the number of stars observed in Pal 5 in the Milky Way based on Bonaca et al. (2020). Table 5.2 summarizes all parameters for streams at 15 kpc, 35 kpc and 55 kpc.

5.2.4 Quantifying the Size of the Simulated Gap

To estimate the size of the simulated gap, we fit a Gaussian near the visually-identifiable gap. To account for the density variation along the stream and the decrease in density near the wings of the stream, we measured both the density ratio and the density difference between the perturbed stream (with a gap) and an equivalent unperturbed stream. By averaging the full width at half maximum of the Gaussian fits to both the density ratios and density difference, we obtained gap sizes of 1.4 kpc, 1.8 kpc, and 1.8 kpc, at R_{GC}= 15 kpc, 35 kpc and 55 kpc, respectively for subhalo masses of 5×10^{6} $M_{\odot}$. We note that in our stream integration procedure, the orbits of the stream and the

subhalo, the total integration times, and the impact velocities were chosen to achieve the desired lengths (7–12 kpc) of the stream and to obtain approximately the same gap sizes at all galactocentric values.

Figure 5.1 depicts three simulated Pal 5-like streams at R_{GC}= 15 kpc with gaps induced by dark matter subhalos with masses of $2 \times 10^6 M_\odot$, $5 \times 10^6 M_\odot$, and $10^7 M_\odot$. The size of the gap increases with the mass of the subhalo, as previously shown by analytical and numerical simulations (Yoon et al., 2011; Erkal & Belokurov, 2015). Our results are consistent with numerical simulations by Yoon et al. (2011), who found that gaps induced by 10^5– $10^{7.5} M_\odot$ subhalos can be visually identified in Pal 5-like streams, although they used a higher relative impact velocity (>100 km/s), a single galactocentric radius ($R_{GC} \approx$ 25 kpc) and a longer integration times after the impact ($\approx$ 4.34 Gyr). In their simulations, they found that subhalo masses $\geq 10^6$ $M_\odot$ induce gaps with physical sizes of $\approx$ 1 kpc (visually), comparable to the observed gaps in our simulations. However, we note that even when using similar impact parameters and integration times, centrally-concentrated halo profiles (e.g NFW profiles) will result in larger gaps (Sanders et al., 2016).

5.3 Generating Mock Observations of Streams with Gaps in M31 and Other External Galaxies

In order to model the observability of both streams and gaps, we need to generate mock observations of our streams in external galaxies as they will appear with *Roman*, by taking into account sensitivity, resolution, and contamination from Milky Way foreground and the host galaxy halo background stellar populations. To address contaminant populations, we followed a method similar to Pearson et al. (2019) as applied to observations of the halo of M31. In these simulations, we assumed all stars are resolved down to our

assumed magnitude limits.

5.3.1 Simulating Mock Observations with *Roman*

We obtained M31 data from the Pan-Andromeda Archaeological Survey (PAndAS, McConnachie et al. 2009; Martin et al. 2016; McConnachie et al. 2018, Ibata et al., private communication). The PAndAS survey provides wide-field imaging data for the Milky Way, M31 and other nearby galaxies over a total area of 300 deg^2, with the 3.6-meter Canada-France-Hawaii Telescope (CFHT) MegaPrime/MegaCam camera in the optical and infrared u, g, r, i, and z filters. We used extinction-corrected CFHT AB magnitudes (denoted by g_0 and i_0) based on the corrections by Ibata et al. (2014). We selected three patches with projected areas of 10 kpc $\times$ 10 kpc at the distance of M31 at radial separations of 15 kpc, 35 kpc, and 55 kpc from its center, corresponding to regions of $\approx$0.5 deg^2 on the sky. To generate mock *Roman* observations, we assumed a total field of view of 0.28 deg^2 (not simulating the shape of the detector) and limiting Vega magnitudes of $Z(F087) = 27.15$ for 1000s exposures and $Z(F087) = 28.69$ for 1-hour exposures.[2] As in Pearson et al. (2019), we limited our analysis to $R(F062)$ and $Z(F087)$ bands.

Simulating Milky Way Foregrounds

We simulated foregrounds along the line of sight of M31 assuming a central coordinate of R.A.= 0.57 deg and decl.= 43.1 deg based on the central coordinates of the M31 PAndAS field. We used a Kroupa power-law initial mass function (IMF) (Kroupa, 2001) for stellar masses between 0.1 M$\odot$ and 120 M$_\odot$, isochrones from the PAdova and tRieste Stellar Evolution Code (Bressan et al., 2012, PARSEC) spanning ages of 4 Myr-13 Gyr, and metallicities $-2.0 \leq$ [Fe/H] ≤ 0.2 that realistically encompass

[2] https://roman.ipac.caltech.edu/sims/Param_db.html

the Milky Way thin and thick disks and halo populations. We sampled 10^6 stars with masses from the IMF, assigned ages and metallicities based on uniform distributions, and computed CFHT g_0 and i_0 and *Roman R* and *Z* absolute magnitudes by interpolating in initial mass–absolute magnitude space for every combination of metallicity and age.

We assigned distances drawn from a galactic density model composed of a thin disk, thick disk, and a halo based on Jurić et al. (2008). The total stellar density is given by:

$$\rho = \rho_{\text{thin disk}} + f_0 \times \rho_{\text{thick disk}} + f_1 \times \rho_{\text{halo}}, \tag{5.8}$$

where f_0 and f_1 are the relative fraction of thick disk and halo stars to the thin disk population at the position of the Sun, set to 0.12 and 0.005 respectively. Stellar densities for the disk were assumed to follow exponential profiles parameterized by a scale height (H) and scale length (L):

$$\rho_{\text{disk}} = \rho_{\odot} \exp\left(-\frac{R - R_{\odot}}{L}\right) \exp\left(-\frac{|z - Z_{\odot}|}{H}\right) \tag{5.9}$$

For the thin disk, we assumed $H = 300$ pc and $L = 2600$ pc. For the thick disk, we assumed $H = 900$ pc and $L = 3600$ pc. We also assumed $R_{\odot} = 8.3$ kpc and $Z_{\odot} = 0.027$ kpc (Jurić et al., 2008). While the scale height of a population varies with its main-sequence lifetime (Bovy, 2017), and dynamical evolution leads to asymmetries in the density profile (Reylé et al., 2009; Liu et al., 2017; Nitschai et al., 2021), these simple assumptions provide a reasonable first-order estimate of the broad stellar densities of present-day Milky Way stellar populations. For the halo stellar density, we used a flattened spheroid profile:

$$\rho_{\text{halo}} = \left(\frac{R_{\odot}}{(R^2 + (z/q)^2)^{\frac{1}{2}}}\right)^n \tag{5.10}$$

with $q = 0.64$ and $n = 2.77$. We drew distances from a probability distribution function $P(d) = d^2 \times \rho(R,z)$ out to 100 kpc.

After we estimated the distance distribution of Milky Way stars, we computed their observable apparent magnitudes. To model the magnitude uncertainty, we fit the magnitude dependence of the uncertainty (δmag) for CFHT g_0 and i_0 filters based on the McConnachie et al. (2018) point sources [3]. We then assigned apparent g_0 and i_0 magnitudes for the simulated population by drawing from a normal distribution with a scatter equal to the standard deviation of the estimated dependence. For all *Roman* magnitudes we assumed a constant uncertainty of 0.1 mag; but the true uncertainty will likely vary with magnitude and exposure time.

Finally, we determined the total number of stars that are observable by *Roman* at a given magnitude limit by scaling the simulated Milky Way foreground distribution to the observed PAndAS data within the region of the color-magnitude diagram bound by $2 < g_0 - i_0 < 3$ and $18 < i_0 < 21$. This region in the color-magnitude diagram is predominantly covered by Milky Way foreground isochrones, which makes it ideal for scaling our total number of foreground stars. We then applied the magnitude limit cut corresponding to 1 hour and 1000s exposure. While this scaling does not take into account exact selection effects, it provided a first-order estimate for the number of stars that can be observed by *Roman*. We obtained an agreement between our simulations and both the color-magnitude diagrams and the final g_0-band luminosity function from the PAndAS data in Figure 5.2; and we further discuss limitations in our foreground and background simulations in Section 5.5.2.

[3]We selected point sources from the McConnachie et al. (2018) catalog by restricting the morphology flags in the *g* and *i* bands to -1. The catalog can be accessed at https://www.cadc-ccda.hia-iha.nrc-cnrc.gc.ca/en/community/pandas/query.html

Simulating Background Stars in M31 and Other External Galaxies

We selected PARSEC isochrone tracks that span ages of 5 Gyr to 13 Gyr and metallicities $-2.0 \leq$ [Fe/H] $\leq +0.5$ to cover the approximate range of ages and metallicities of stars in the halo of M31 (Brown et al., 2003; Ibata et al., 2014). Similar to the Milky Way simulation, we assumed a Kroupa initial mass function for stellar masses between 0.1 $M_{\odot}$ and 120 M$\odot$, a uniform age distribution, and a uniform metallicity distribution in chosen patches of 10 kpc $\times$10 kpc at galactocentric radii (R_{GC}) of 15 kpc, 35 kpc and 55 kpc. The PAndAS survey and other previous studies have characterized the metallicity and abundance distributions (e.g. Escala et al. 2020) of small regions of M31's stellar halo in detail. As our goal is to estimate stellar number densities, assuming a general set of old and metal-poor stellar populations in all regions of the stellar halo was deemed sufficient. Throughout, we assumed the distance to M31 to be 770 kpc (distance modulus of 24.4, Ibata et al. 2014).

To assign distances to stars in the halo of M31, we modeled the stellar density as a flattened spheroid profile based on Ibata et al. (2014). The 3D stellar density is given by:

$$\rho_{\mathrm{M31}} = \left((\widetilde{R}^2 + (\widetilde{z}/q)^2)^{\frac{1}{2}} \right)^n \tag{5.11}$$

(cf. Eqn. 5.10), where $\widetilde{R}$ and $\widetilde{z}$ are the cylindrical radius and height starting from the center of M31, in the plane and perpendicular to its disk respectively, with $q = 1.11$, and $n = -3$. We drew distances assuming that the halo of M31 extends to $\approx$ 100 kpc (Chapman et al., 2006) and we assigned projected distances to M31 halo stars as $d = 770$ kpc $+ \widetilde{z}$, where $\widetilde{z}$ is the randomly-drawn cylindrical galactocentric height for simplicity.

Finally, we assigned apparent magnitudes and magnitude uncertainties in a similar manner as for Milky Way foreground stars. To obtain the correct normalization for the number of stars, we scaled the total number of stars to the observed number between

$0.5 < g_0 - i_0 < 2$ and $21.5 < i_0 < 23.5$ in the PAndAS data as there is a significant drop-off in the PAndAS magnitude completeness to below $\approx 70\%$ for $i_0, g_0 > 23.5$ (Martin et al., 2016). As a final check, we examined the simulated luminosity function (number of stars as a function of magnitude) in the CFHT g-band based on our CMD-based scaling, luminosity function inferred from PAndAS data.

Figure 5.2 the combined CHFT $g-band$ luminosity function of both components (M31 population and the Milky Way foregrounds) compared to the observed luminosity function from the PAndAS data, and it shows the simulated *Roman* color-magnitude diagram. This illustrates that Milky Way foreground stellar populations are dominated by sources with $Z < 25$, while M31 includes stars with $Z > 20$. In real *Roman* observations, it will be possible to separate most Milky Way foreground stars from M31 stars based on their positions on the CMD ($R-Z$ vs Z space, see Figure 5.2). We note that low-mass stars and brown dwarfs are lacking in our simulated foregrounds, hence they may introduce an additional source of contamination in the real data. Nevertheless, we found a general agreement between the simulated and the observed luminosity function in the CFHT bands. We further show a comparison between our simulations and the PAndAS data in Appendix 5.7. While the region corresponding to the Milky Way disk is reasonably well-matched, we could not reproduce all of the structures in the CFHT CMDs, perhaps due to an underestimation of the halo and thick disk fraction along this line of sight.

To further validate our methodology for simulating stellar populations, we compared our surface densities to the CFHT data and predictions of Pearson et al. (2019). For 1-hour exposure with *Roman*, we obtained stellar densities of 3.1×10^5 stars/degrees^2 at R_{GC}= 55 kpc, 3.1×10^5 stars/degrees^2 at R_{GC}= 35 kpc and 2.9×10^6 stars/degrees^2 at R_{GC}= 15 kpc for the halo of M31. These densities are $\approx$ 10 times higher than the densities obtained by Pearson et al. (2019) at the same radial distances and a similar *Roman* magnitude cut. We note that our methods for estimating the foregrounds significantly

deviate from the original methodology by Pearson et al. (2019), by incorporating a stellar density model and by scaling the stellar density to the brighter regions of the CMD where the PAndAS survey is most complete. In contrast, within the magnitude limits of the PAndAS data ($g_0, i_0 \approx 26$), our simulated densities of 2.0×10^4 stars/degrees^2, 2.2×10^4 stars/degrees^2 and 9×10^4 stars/degrees^2 at R_{GC}=55 kpc, 35 kpc, and 15 kpc, respectively, are in agreement with the observed densities in PAndAS at the same galactocentric radii. The agreement between our simulation and the observed data validates our assumptions about the background and foreground populations. We further discuss the limitations of our simulations in Section 5.5.

Simulating Observed Stars in Pal 5

We simulated the stream population in a similar manner to the backgrounds, but in this case, scaling to the observed properties of Pal 5. We generated a sample of 10^6 stars assuming a power-law IMF ($dN/dM \propto M^{-0.5}$, Grillmair & Smith 2001; Ibata et al. 2017). We then assigned CFHT *g* and *Roman R*, *Z* absolute magnitudes by interpolating the PARSEC isochrones for an age of 11.5 Gyr and [Fe/H]$= -1.3$. We applied a distance modulus corresponding to Pal 5 (d_{mod}= 16.85; Pearson et al. 2019), and then determined a population normalization factor by comparing the distribution of simulated CFHT *g* magnitudes to the 3000 stars with $20 \leq g \leq 23$ that are known members of the Pal 5 stream (Bonaca et al., 2019). With this normalization factor, we computed the number of stream stars detectable in a given host galaxy based on the corresponding distance modulus and *Roman* magnitude limit. Our number count predictions for Pal 5 match the predictions of Pearson et al. (2019).

To generate a final simulated *Roman* image, we re-sampled the simulated streams described in Section 5.2.3, drawing only the expected number of detectable stars for our *Roman Z*-band limits as a function of distance. We also drew foreground and background

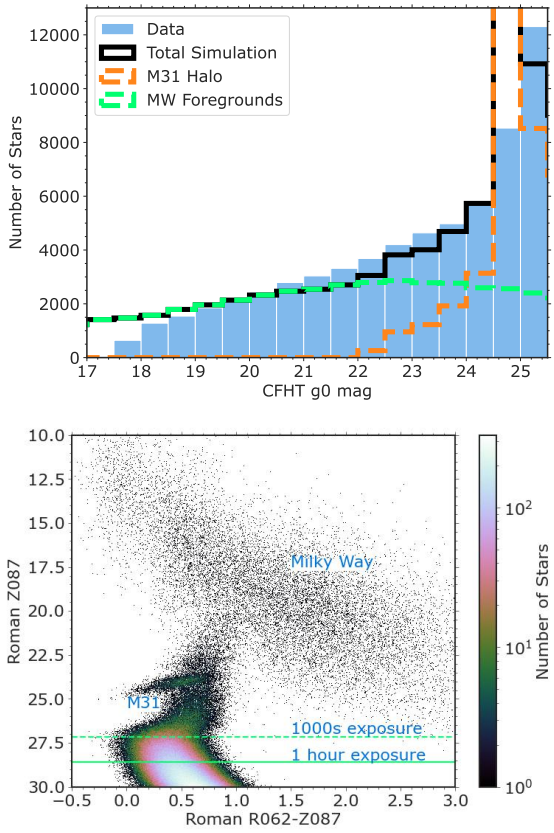

Figure 5.2 Colors and magnitude distributions of our simulations compared to the data. *(a)*: CFHT g_0 mag luminosity function based on the PAndAS data (blue filled-in histograms) and our simulations (black) for populations at R_{GC}= 35 kpc. The simulations are further divided into Milky Way foregrounds (light green) and M31 stars (orange). We are able to reproduce the CFHT *g*-band luminosity function based on our scaling to the CFHT CMD (more details in Appendix 5.7) *(b)*: Simulated color-magnitude diagram for *Roman R* and *Z* bands at R_{GC}= 35 kpc. CMD regions that are dominated by M31 stars or Milky Way foregrounds are labeled in blue text. The horizontal dashed and solid lines show the magnitude cuts for 1000 s and 1 hr exposures, respectively. With these magnitude cutoffs, the M31 halo population will be primarily dominated by horizontal-branch stars and giants.

stellar fields at the same Z-band limits, the latter sampling the three galactocentric radii from M31 PAndAS data, as well as different host galaxy distances. For simplicity, the positions of background and foreground stars were assumed to be uniformly distributed for a given 10 kpc by 10 kpc patch. As most background halo stars are of similar stellar populations as the stellar stream stars, the detection of these streams and their gaps depends mostly on density contrasts. We, therefore, focus our analysis on star count maps of these fields, rather than simulated images that incorporate brightness and instrumental point spread function effects. Figure 5.3 shows examples of our simulations of streams in M31. Henceforth, we will use “mock observations" or “density maps" to describe the results of our simulations.

5.3.2 Gap Identification by Visual Inspection of Density Maps

We now turn to examining gaps and quantifying their detection with distance and exposure times. Pearson et al. (2019, 2022) developed methods for finding Pal 5-like streams in *Roman* observations. Our primary goal is to investigate the detection of gaps, assuming the stream has already been identified. We present the visual inspection of gaps from simulated streams in M31 (Figure 5.3) and other external galaxies (Figure 5.4), centering the density maps on the gap region. For simplicity, we only considered gaps from interactions with subhalos of 5×10^6 $M_\odot$ as this mass is in the appropriate range for testing different dark matter models (Bullock & Boylan-Kolchin, 2017); and gaps that resulted from these interactions are clearly visible in mock streams (Figure 5.1). In all of our simulated observations, we applied a photometric metallicity constraint of [Fe/H]< -1, as GC streams are typically metal-poor (e.g. Martin et al., 2022), allowing us to reduce the number of background stars. In real *Roman* images, selecting low-metallicity stars will require fitting the foreground populations of a given galaxy to synthetic isochrones.

The angular lengths of Pal 5 streams for galaxies within a $\approx$ 1.2 Mpc volume are larger than the field of view of the *Roman* telescope; hence, only a portion of the stream will fit inside a *Roman* field for these distances. For an M31 distance of 770 kpc (d_{mod}= 24.4, Ibata et al. 2014), the projected angular distance is 13.4 kpc/degree, making the angular size of Pal 5-like streams in M31 (lengths of 7.8–12 kpc, Pearson et al. 2019) equal or larger than the expected 0.52 degree $\times$ 0.52-degree *Roman* field of view. Visually, the density contrast between the stream and background stars increases with galactocentric radius and with exposure time. Pearson et al. (2019) estimated that the width of a Pal 5-like stream in M31 would vary between 0.053 kpc–0.127 kpc at a galactocentric radius (R_{GC}) of 15 kpc–55 kpc, and the length would vary between 7.8 kpc and 12 kpc. We could best identify the gaps in the density maps for 1-hour exposure, otherwise, visual identification of the stream and gaps is difficult (see Figure 5.3).

To simulate streams in other external galaxies with distances spanning 0.5 Mpc to 10 Mpc (assuming a similar stellar composition and tidal field as M31), we offset the M31 background population in the *Roman* CMD space to the appropriate distance modulus, retaining the same Milky Way foreground populations. The number of stars in Pal 5 was re-sampled to match the pre-computed number of stars at the new galactic distance. We applied the same magnitude cuts as our simulated foreground and background models.

Figure 5.4 compares the simulated streams, all placed at a fixed galactocentric distance of 35 kpc. We display a fixed area in physical units of 7 kpc $\times$ 4 kpc in the figure (7 kpc is $\approx$ half the length of the stream), which corresponds to smaller angular scales in the total *Roman* field of view at larger distances. We display the streams at R_{GC}= 35 kpc because the combination of the density contrast and the thickness of the stream makes it easier to visually detect the gap in these mock observations compared to images at 15 kpc and 55 kpc. As the distance to the host galaxy is increased, the density of both background stars and the stream decrease. We note that the background stellar densities

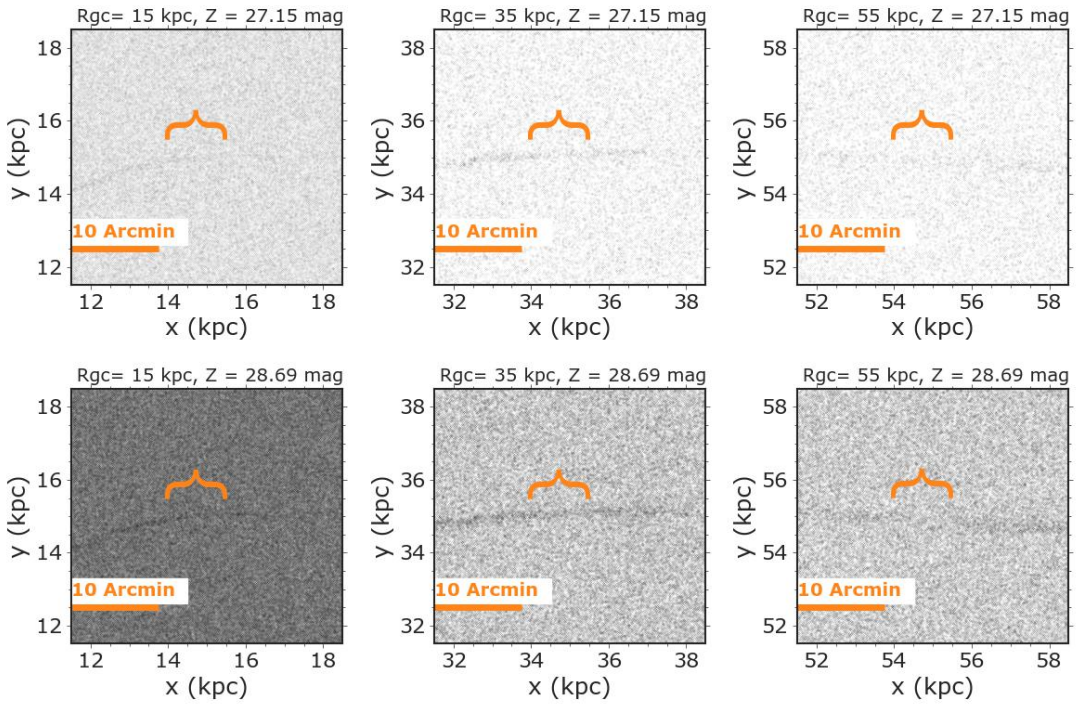

Figure 5.3 Simulated stellar density maps for a full *Roman* field of view of 0.28 deg^2 with M31 background stars and Milky Way foregrounds. The gap in the stellar stream is caused by an interaction with a subhalo with a mass of 5×10^6 $M_\odot$, and only a portion of the stream is shown here. The streams are injected at galactocentric distances of 15 kpc, 35 kpc and 55 kpc, and exposure times are 1000s ($Z = 27.15$, top panels) and 1 hr ($Z = 28.69$, bottom panels). We display these maps in physical coordinates to highlight the scale of the gap, indicated by curly brackets.The projected x and y coordinates in kpc were computed by assuming the distance to M31 is 770 kpc (an angular scale of 13.4 kpc/degree). We can visually see the gap for 1-hour exposure, otherwise, it becomes more obscured by the background population.

fall off faster than the density inside the stream with galaxy distance, due to the choice of isochrones and the metallicity cuts that we are applied to the data. We caution that in real observations, other external galaxies will have different sizes, and their halos will have a different composition compared to M31. All these caveats are further discussed in Section 5.5.

Through a visual inspection of streams with gaps in host galaxies spanning a distance of 0.5 to 10 Mpc, we find that the gap is visible by eye in external galaxies at distances out to $\approx$ 1.5 Mpc (see Figure 5.4).

5.4 Automating the Detection of a Gap

Visual confirmation alone can result in biased assessments of stream and gap detection, hence we now turn to quantifying detection using an automated tool. In Sections 5.4.1 and 5.4.2 we lay out methods for defining the gap and the stream region, and in Sections 5.4.3, 5.4.4, and 5.4.5 we outline a procedure for quantifying the detection of each gap and we provide a detection limit as a function of distance using a large sample of simulated mock streams.

5.4.1 Density Estimation and Detecting Gaps

Previous studies have developed algorithms to find and characterize stellar streams in the Milky Way (e.g., Mateu et al., 2017; Malhan & Ibata, 2018; Shih et al., 2022, 2023) and in external galaxies (e.g., Hendel et al., 2019; Pearson et al., 2022). Once such algorithms have determined a stream's presence, location, extent, and orientation, we can then search for gaps. We used the gap-finding tool (Contardo et al., 2022, `FindTheGap`), which is designed to evaluate under-densities in multi-dimensional data. Gaps, just like streams, can be detected by eye, but this tool provides an automated approach and serves

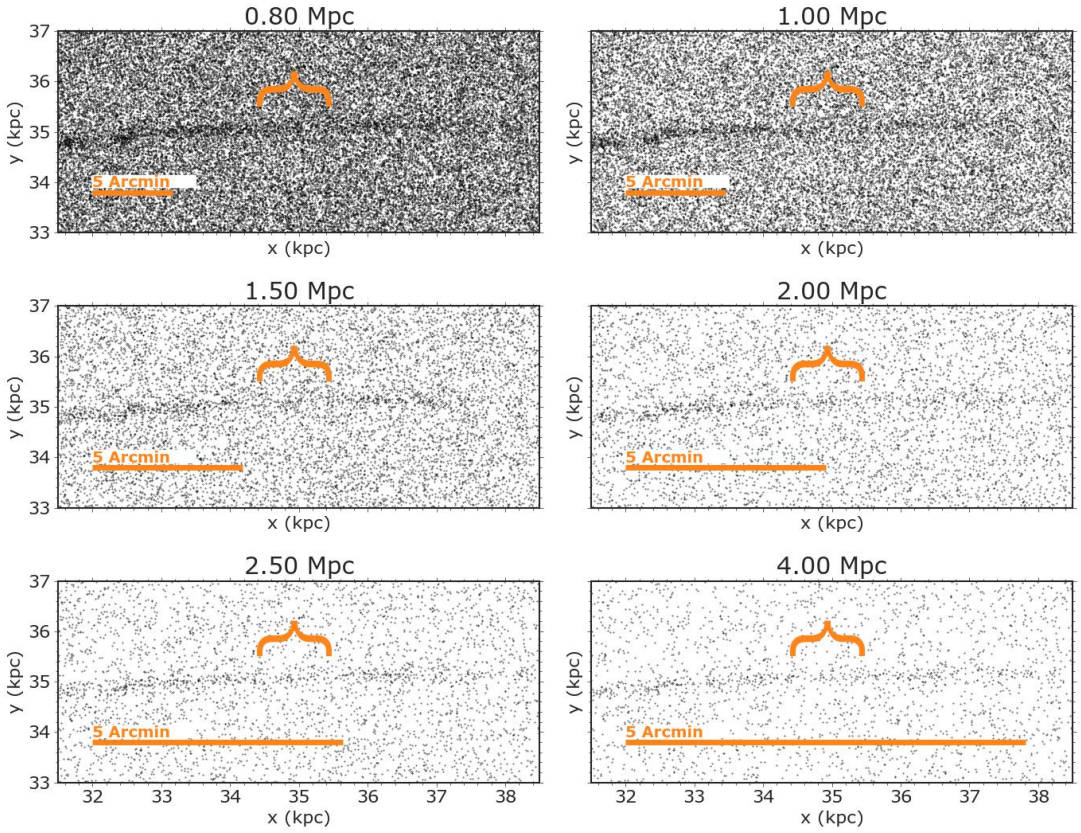

Figure 5.4 Mock observations of streams with gaps in a segment of the full *Roman* field of view. To generate these mock observations, streams were injected into pre-computed backgrounds. Stars are plotted with the same symbol size to facilitate comparison at various galaxy distances. The sizes of the images are 7 kpc $\times$ 4 kpc (about half the length of the stream), which would correspond to different angular sizes on the sky depending on the distance of the observed galaxy. The horizontal bar shows the scale of 5 arcmin (or 1/6 of the 32 arcmin$\times$32 arcmin full *Roman* field of view). We show the halo of the galaxy at $R_{GC} = 35$ kpc, assuming an exposure time of 1 hour ($Z = 28.69$) and a perturbation in the stream from 5×10^6 $M_\odot$ subhalo. We can see gaps to a distance of $\approx$ 1.5 Mpc.

as an additional method for confirmation or rejection in conjunction with visual detection.

`FindTheGap` uses the projection of the second derivatives (Hessian, H) of the density estimate onto the orthogonal subspace of the density gradient vector (g), denoted as $\Pi H \Pi$, where Π is a projection matrix defined as:

$$\Pi = 1 - \frac{gg^T}{g^T g} \tag{5.12}$$

The maximum eigenvalue of $\Pi H \Pi$ can then be used as a statistic to estimate if a point in the data space is "in a gap". Conversely, the minimum eigenvalue of $\Pi H \Pi$ can be used to highlight ridges and overdensities. The density estimation depends on a free parameter, the bandwidth, which relates the estimated density to the spacing between data points. In addition to the bandwidth, the stability of the gap detection also depends on the number of data points.

To apply this tool to simulated observations, we started with simulated density maps (Figures 5.3 and 5.4), making a cutout centered on the visually-identified gap. We did not use the full *Roman* field of view as the angular size of the stream becomes progressively smaller at larger galaxy distances, making it more difficult to identify gaps. We then created a grid of 50 by 20 points along each cutout with uniform spacing, covering an area of 5 kpc$\times$2 kpc that includes the main track of the stream and surrounding foreground and background stars.

The accuracy of this method relies on the choice of bandwidth. Large bandwidths tended to smooth over structures in the data, including the gap, but small bandwidths introduced gaps and other small-scale structures that were not necessarily present in the underlying true density. Additionally, the density estimation in `FindTheGap` assigns lower densities to regions near the edge of the simulated mock observations. To avoid these edge effects, we first ran an estimation of the stellar density and the values of $\Pi H \Pi$

on a slightly larger dataset, incorporating stars beyond the specified grid. Specifically, we required the data bounds to be larger than grid bounds to a factor of twice the bandwidth. For example, we used a 9 kpc by 6 kpc region for a bandwidth of 1 kpc, given our fixed grid size of 5 kpc by 2 kpc. After we fit the density estimator to the data, we predicted the values of density and $\Pi H \Pi$ on the smaller 5 kpc by 2 kpc grid (see Figure 5.5). To ensure the fidelity of each gap detection and to remove spurious gaps, we ran this estimation five times for every simulation, choosing the same number of randomly selected stars for each estimation (bootstrap re-sampling). In each iteration, the density, and the minimum and maximum eigenvalues of $\Pi H \Pi$ were scaled to span values of 0 and 1 to maintain a consistent range across bootstrap samples. We then computed the final $\Pi H \Pi$ map by taking the median over all bootstraps. Figure 5.5 shows the result of the application of this tool for simulated observations at a distance of 1 Mpc. The map of $\Pi H \Pi$ eigenvalues reliably locates the gap and the stream. We further discuss our determination of the optimal bandwidth in Section 5.4.4.

5.4.2 Further Outlining the Stream and Gap Regions with Indicator Points

In principle, it is possible to determine the stream path from the minimum eigenvalues of the $\Pi H \Pi$ matrix as the stream represents an overdensity. Nevertheless, our focus was solely on the detection of gaps within a stream. We constrained the stream region inside the density maps by fitting a second-degree polynomial to the pre-determined positions of the injected stream. To define the stream track, we fixed the size of the stream to be 0.2 kpc, which exceeds the real width of the stream (visually and based on analytical calculations by Pearson et al. 2019). This is to ensure that there were enough grid points to cover the full stream region. This step also allows us to measure the density of stars inside the stream, later discussed in Section 5.4.5. We note again that

our assumption is that the stream has been observed, and the approximate stream region is therefore known.

To outline the gap region, we selected points on the grid falling within the top 95-percentile of the distribution of minimum eigenvalues of $\Pi H \Pi$. We will refer to the regions on the grid that match this criterion as “gap indicator points". As shown in Figure 5.5, this criterion provided a first-order estimation of the location of the gap. We then further constrained the gap region to be centered around the median position of gap indicator points, with a width equal to the size of the stream region and a length equal to the gap size (see Section 5.2.4). This definition of the gap region along with gap indicator points was later used to develop metrics for distinguishing successful detections from noise.

Figure 5.5 illustrates the gap detection procedure. As all the mock observations were converted to physical projected coordinates, this assumption yielded consistent gap identification with galaxy distance. We further discuss our quantification of the breakdown of the gap identification procedure in the upcoming sections.

5.4.3 Defining Metrics for Gap Detections

We now turn to discuss our application of the gap detection method on a sample of mock streams in an automated fashion. We created an automatic pipeline using the methods described in Section 5.4.1 to search for gaps in simulated mock streams, and two metrics to quantify the detections. First, we computed $\Pi H \Pi$ maps and their eigenvalues for mock observations spanning distances between 0.5 Mpc and 10 Mpc and using bandwidths between 0.1 kpc and 2 kpc for all three R_{GC} values. We restricted the bandwidth range to 2 kpc as the metrics discussed below did not improve beyond this range. Ultimately bandwidths between 0.5 kpc and 1 kpc were optimal in finding the gap region. For each step, we repeated the generation of the stream, the generation of

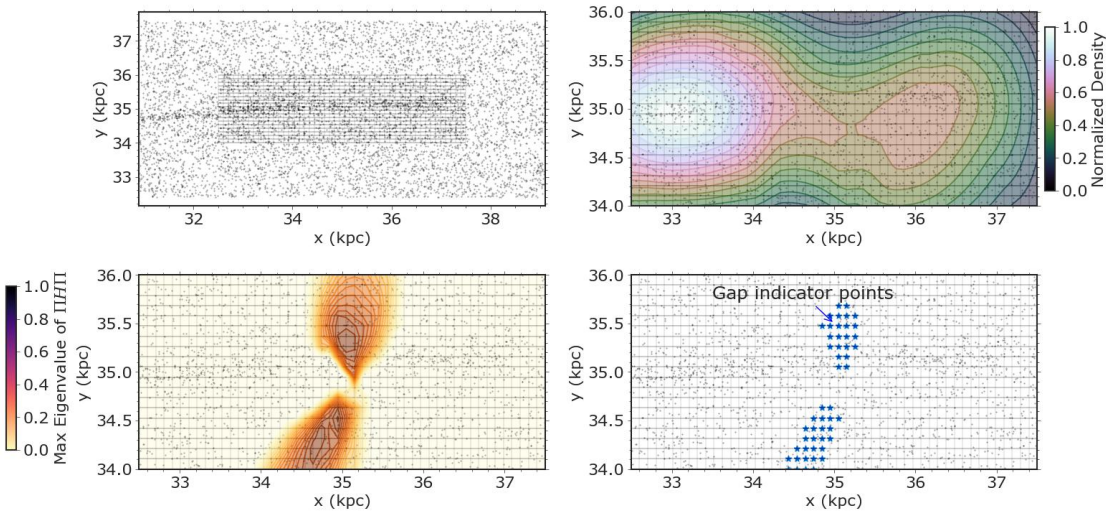

Figure 5.5 Illustration of the gap detection tool with a fixed bandwidth of 0.8 kpc applied to a stream at R_{GC} =35 kpc and a distance of $\approx$ 1 Mpc for a 1000 s exposure. Note that we assume all stars are resolved. *Top Left:* Black dots show the stream and uniformly-distributed background stars in the vicinity of the stream. We used a fixed grid of 5 kpc by 2 kpc indicated by black lines. *Top Right:* Contours show the stellar density which clearly shows an underdensity near the gap region and a decrease in density towards the edge of the stream. The density estimation is applied over the full range of the data to avoid edge effects at the end of the grid (see text for discussion). *Bottom Left:* Contours show a map of the maximum eigenvalues of $\Pi H \Pi$, which are maximized near the gap. We used this map to indicate the location of the gap along the stream. *Bottom Right:* Gap indicator points are shown in blue as defined to be where the maximum eigenvalues of $\Pi H \Pi$ are in the top 95 percentile. This procedure can locate underdensities inside the stream.

background populations, and the gap detection process to account for the scatter in the detection metrics at low stellar densities. This process resulted in 81,795 independent mock observations.

We used three metrics to quantify the significance of each detection. To quantify the uncertainty in the gap detection, we defined the spread of all the gap indicator points ($\mathscr{S}_g$) as the range of their x-positions (max-min). As a reminder, “gap indicator points" were defined as points on the grid in the top 95 % of maximum eigenvalues of $\Pi H \Pi$. We anticipate that a robust gap detection has low $\mathscr{S}_g$ values, as these gap points would be concentrated around one point near the stream (see blue markers in the lower right panel of Figure 5.5).

We then computed the median value of the absolute difference between the x-positions of gap indicator points to the center of the density maps denoted by Δ, computed for each stream separately. As we designed each simulated observation to be centered around the gap, we expect optimal detection to have a small value for Δ. Nevertheless, we show in Appendix 5.8.3, that our pipeline can also identify gaps located away from the center. After we defined $\mathscr{S}_g$ and Δ per stream, we used these metrics to determine which bandwidths were optimal for detecting gaps.

5.4.4 Determining the Optimal Bandwidth

The effects of bandwidth choice on the gap detection metrics as a function of distance are shown in Figure 5.6. We found that bandwidths between 0.5 kpc and 1 kpc resulted in the lowest values for the spread of gap indicator points ($\mathscr{S}_g$) and the deviation of the location of the gap from the center of the density maps (Δ). For large bandwidths, the estimated density on the grid is centrally concentrated and features are washed out. For small bandwidths, the stellar density was fragmented into small groups of spurious gaps, which also resulted in large values for $\mathscr{S}_g$ and Δ. We illustrate these effects in

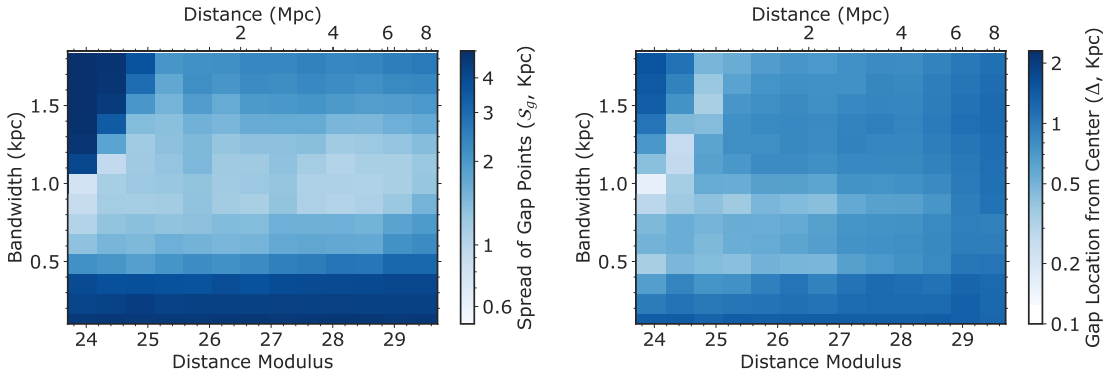

Figure 5.6 Distribution of detection metrics for a gap from a subhalo of mass equal to 5×10^6 $M_\odot$. *Left:* Distribution of the spread of gap indicator points ($\mathscr{S}_g$) defined as the range (max-min) of their x-values. There is an island of best bandwidths between 0.5 kpc and 1 kpc where this metric is the lowest, which defines our optimal set of bandwidths. *Right:* Map of the median deviation of gap indicator points with respect to their true location (Δ). The combination of Δ and $\mathscr{S}_g$ values show that the optimal bandwidth for locating the gap is between 0.5 kpc and 1 kpc.

Appendix 5.8.2. We inferred a middle value of $\approx$ 0.8 kpc as our optimal bandwidth.

To further evaluate the performance of the gap-detection tool and to ensure that our pipeline was robust, we also applied the gap-finding tool to mock observations with an intact stream (without a gap from an interaction with a subhalo) using our described methodology. As shown in Appendix 5.8.3, we could identify the drop off in density towards the edge of the stream, but we could not identify any gaps inside the track of the unperturbed stream for a bandwidths ranges of 0.5 to 0.9 kpc, further validating our method. In practice, when applying this tool to real *Roman* images, the optimal bandwidth may depend on the scale of underdensities in the backgrounds and a positive detection would require further characterization. Our goal in this study is to provide an additional methodology for detecting gaps in conjunction with visual inspections. While our pipeline could lead to false positives, it is unlikely to miss any real gaps in the data.

5.4.5 Distance Limits for Gap Detections

To determine a tentative detection limit, we used both the density of stars inside the gap region and the location of the gap region as a reference. We estimated the stellar density inside the stream and the gap by counting the number of stars inside each region and dividing this number by the physical area (in kpc^2) (see Section 5.4.4 for the definition of the gap and stream points/regions). To determine the area of the stream region, we multiplied the total area of the grid (10 kpc^2) by the fraction of grid points that fell within each respective region. Because the stream track did not follow a simple straight line, this procedure allowed us to obtain a more accurate measurement of each region's area. For the gap region and the background region, we approximated the area as a rectangle. For the gap, we used a width equal to the width of the stream, and the pre-computed length; and for the backgrounds, we used a width of 0.5 kpc and a length of 5 kpc.

Figure 5.7 shows the surface densities (number/kpc^2) inside the stream region, the gap, and the background for a fixed optimal bandwidth of 0.8 kpc. There is a monotonic decrease in the surface density inside the stream, inside the gap, and in the background with increasing galaxy distance, as expected. The stream density is generally higher than the gap density and the background. Additionally, streams at smaller R_{GC} values are denser than streams at larger R_{GC} values. However, it was still difficult to determine the detection limits from these densities alone.

To establish a tentative detection limit for our pipeline, we examined the evolution of the gap location with distance. We plot the median value of the location of gap points (Δ) for 5 random streams for each distance step in the bottom panels in Figure 5.7. Our expectation is that for robust detections of gaps, the central gap location will remain stable across several iterations. While there was a systematic offset between the center of the stream from the true center, we observed this "flaring" for the value of Δ at larger

distances. For both 1000 s and 1 hour exposure times, this effect translates to distance limits of 2 Mpc–3 Mpc. In Appendix 5.8.1, we show examples of gap detections in mock streams at R_{GC}=35 kpc which also indicates that the location of the gap inside the stream becomes progressively uncertain beyond these distance limits.

To summarize, we used the tool (`FindTheGap`) developed by Contardo et al. (2022) to evaluate the detection of gaps beyond a simple visual inspection and to quantify the distance limit with exposure time. We applied this tool to a set of $> 80,000$ mock observations for galaxy distances between 0.5–10 Mpc with M31-like stellar populations as background stars. For each mock observation, we defined “gap indicator points" based on gap statistic provided by `FindTheGap`. The gap detection method relies on the bandwidth as an additional parameter to compute the density of stars on a pre-defined grid. By changing this parameter uniformly between 0.1–2 kpc, we determined that the optimal bandwidth for detecting gaps was $\approx$0.8 kpc. We then evaluated the effectiveness of each detection by estimating the central location of gap indicator points with galaxy distance. Results from this procedure pipeline suggest that gaps from subhalos of 5×10^6 $M_\odot$ in the halo of M31-like galaxies will be detectable to 2–3 Mpc for exposure times between 1000s and 1 hour.

5.5 Discussion

In this Section, we revisit assumptions in our numerical simulations (Section 5.5.1), the observational limitations (Section 5.5.2), their implications, and how they affect our results. We also discuss future prospects of using extragalactic streams for dark matter science (Section 5.5.3).

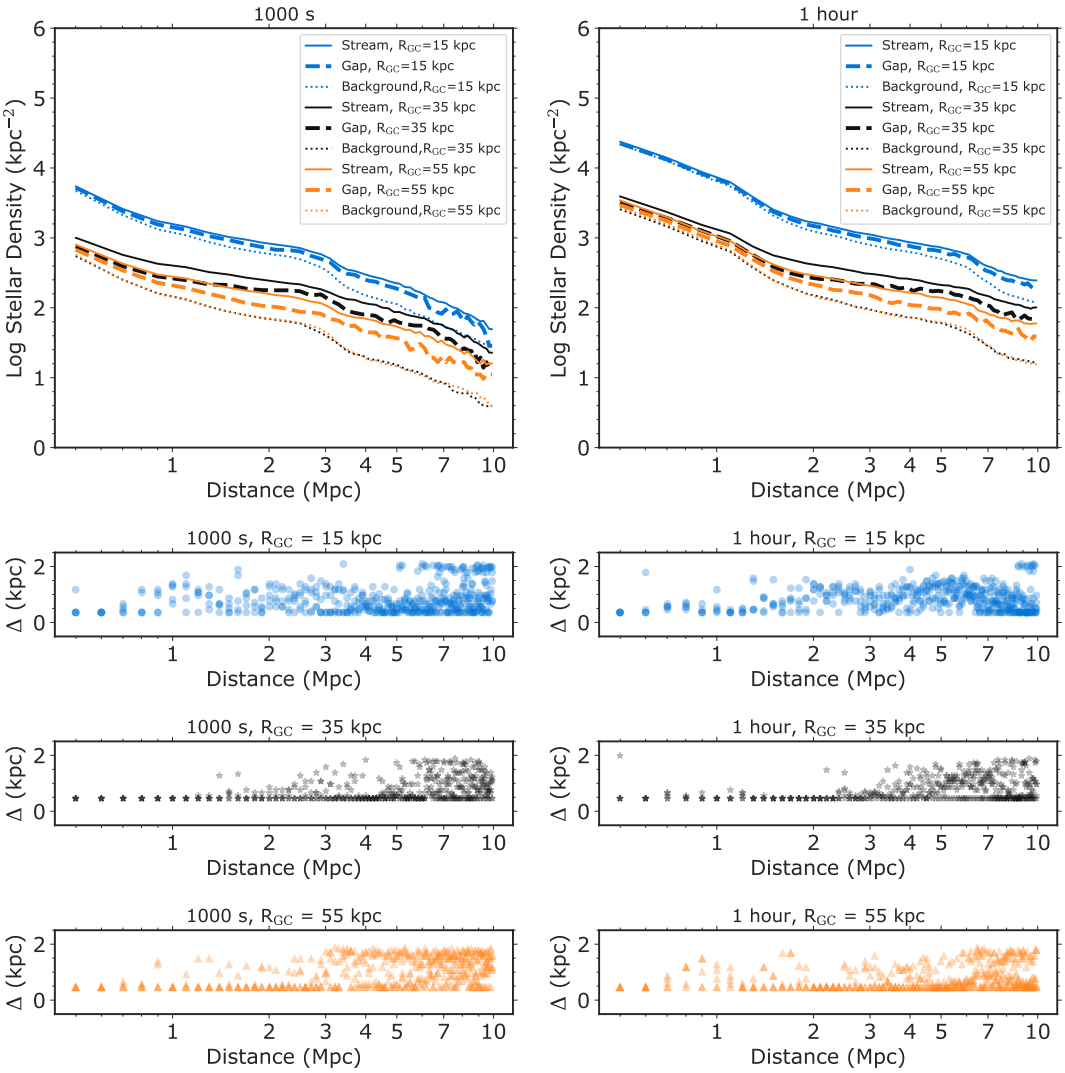

Figure 5.7 Testing the stability of gap detections with distance using the optimal bandwidth of 0.8 kpc. *First row*: Variation in the distribution of stellar densities inside the stream and the gap with distance. Gaps were created from subhalos of masses of 5×10^6 $M_\odot$. The density of stars in kpc^{-2} for the stream region is shown with solid lines, the gap is shown with dashed lines, and the background is shown with dotted lines a 1000 s (left) and 1-hour exposure (right) for galactocentric radii of 15 kpc (blue), 35 kpc (black) and 55 kpc (orange). As a general trend, the density inside the stream is higher than the gap, and the background density but it is difficult to establish a detection limit from densities alone. *Last 3 rows* : Value of the absolute difference between the x-positions of gap indicator points and the center of the density maps (Δ) as a function of distance for a 1000 s exposure (left) and 1-hour exposure (right). The color scheme follows the same pattern as the top panels. We defined our gap-detection limits to be where the median value of Δ starts to fluctuate, which corresponds to 2–3 Mpc.

5.5.1 Limitations in Our Simulation of a Gap

In our simulations, we have assumed that the galactic potential is smooth and static. However, previous studies of the Milky Way have shown that inhomogeneities in the global potential, including giant molecular clouds, galactic bars, streams, other globular clusters, and spiral arms can perturb GC streams (Amorisco et al., 2016; Hattori et al., 2016; Price-Whelan et al., 2016; Erkal et al., 2017; Pearson et al., 2017; Banik & Bovy, 2019; Doke & Hattori, 2022). To mitigate this effect, we can search for streams located at large galactocentric radii in external galaxies, and where the contrast between the stellar stream and background is more dramatic (see Figure 5.3). In addition, at large galactocentric radii, bars, spirals, and molecular clouds are less likely to cause dynamical perturbations in streams. Furthermore, with larger sample sizes we will be able to determine the frequencies, sizes, and locations of underdensities in streams, which gives us the ability to statistically evaluate signatures of perturbations from dark matter subhalos.

Global potentials in galaxies are also deformed by mergers and satellite interactions (Weinberg, 1998; Garavito-Camargo et al., 2019), and observations suggest that M31, in particular, has been largely shaped by a possibly recent minor (or major) merger (D'Souza & Bell, 2018; Escala et al., 2021; Dey et al., 2022; Bhattacharya et al., 2023). Merger events and interactions with satellites can distort present streams (Erkal et al., 2019b; Shipp et al., 2021; Lilleengen et al., 2023) and contribute to the accretion of new globular clusters that will eventually form streams (Kruijssen et al., 2020). The details of the formation and disruption of GC streams have not been extensively explored in large cosmological simulations.

Throughout this work, we have only considered one encounter between the stream and the subhalo. Old GC streams can undergo multiple collisions with subhalos, creating multiple observable density fluctuations and perturbations to the stream morphologies. In

fact, multiple under-densities have been observed in several Milky Way streams such as GD-1, (Bonaca & Hogg, 2018) and Pal 5 (Erkal et al., 2017). We do not further explore the effects of multiple encounters here, but based on our analysis of the detectability of a gap from a single subhalo encounter, we expect that streams, which have undergone multiple interactions with subhalos to have multiple observable gaps that can be detected using our methodology. Using realistic galaxy simulations that include baryonic physics, Barry et al. (2023) predicts that Pal-5-like streams in the Milky Way could undergo 2-3 interactions/Gyr with subhalos of masses $> 10^6$ $M_\odot$ before dissolution.

In our analysis, we limited our investigation of the observability of gaps with *Roman* to subhalo encounters between GC streams and dark matter subhalos with Hernquist profiles (Hernquist, 1990). Cuspier profiles for the dark matter subhalo can result in larger gaps for the same encounter properties (Sanders et al., 2016). Additionally, as gaps grow with time, the initial size and the growth of gaps will depend on the collision parameters, such as the mass and scale radius of the subhalo, the relative velocities of the subhalos to the stream, the impact parameter, the stream orbit, the time of the collision, the impact position, and others. These parameters have been extensively explored in numerical and analytical work (Yoon et al., 2011; Erkal & Belokurov, 2015; Sanders et al., 2016; Koppelman & Helmi, 2021). In external galaxies, these effects will be difficult to disentangle given the lack of kinematic information. However, large statistical sample sizes of observed gaps will allow for rigorous comparisons to predictions of gaps in streams evolved within various dark matter frameworks (e.g., warm, fuzzy, self-interacting).

5.5.2 Limitations in Our Simulation of Mock Observations

In this work, we have generated mock *Roman* observations to mimic stellar halos of external galaxies at various distances without accounting for observational biases due

to crowding, extinction, or star/galaxy separation. Pearson et al. (2019) discussed several of the limitations and considerations to take into account for such mock observations. In particular, they concluded that crowding effects will not affect the detection of thin GC streams in external galaxies with *Roman*. We can further minimize crowding effects by observing external galaxies with sight-lines pointing away from the Milky Way's galactic plane. Our method relies on estimating the underlying density of stars, thus measuring the density contrast between stream stars and background stars is the determining factor in the success of gap detections. Additionally, the effect of dust extinction will be minimal for the halo of M31 at infrared wavelengths (Dalcanton et al., 2015).

In addition, Pearson et al. (2019) evaluated the feasibility of star/galaxy separation detection on the detection limits of GC streams with *Roman*. They used the Space Telescope Image Product Simulator (STIPS) to inject known galaxy catalogs into simulated fields and applied quality cuts based on source shape. They concluded that including background galaxies would limit the detection of Pal 5 in M31-like galaxies to 1.1 Mpc–1.8 Mpc for an exposure time of 1 hour. There are ≈115 galaxies in this volume based on Karachentsev & Kaisina (2019), and gaps will be detectable to these distances based on the methodology presented in this work. Assuming "perfect" star/galaxy separation and investigating GC streams with $5-10$ times more massive than Pal 5, they estimated that thin GC streams could be detected in host galaxies out to $6.2-7.8$ Mpc with a 1-hour *Roman* exposure. This volume contains ≈ 660 galaxies (Karachentsev & Kaisina, 2019), with 25 galaxies that are 10% more luminous than the Milky Way; and the vast majority of galaxies within the 7.8 Mpc limit are dwarf galaxies. While we did not include such an analysis in this paper, we expect the feasibility of star/galaxy separation to have a similar effect as the predictions by Pearson et al. (2019) on the detection of gaps as the detection of streams because background galaxies will be randomly spread out throughout the image. We note that the formation of GC streams in dwarf galaxies has been explored

in simulations (e.g. Peñarrubia et al. 2009), but more work is needed to estimate their observability.

Finally, future large observing programs dedicated to searching for gaps in streams in external galaxies can extend to longer exposure times, which would allow for larger sample sizes and potential detection of GC streams in dwarf galaxies. Optimistically, it is likely that a full program that is dedicated to observing these gaps with *Roman* would extend over several hours of observing time, allowing the stacking of images from multiple visits to reach depths beyond our estimates.

5.5.3 Inference of Dark Matter Properties and Expected Sample Sizes

Our focus throughout this paper has been on the detectability of underdensities in extragalactic GC streams. Previous studies have explored pathways to isolate dark matter effects from baryonic effects and to infer dark matter properties (e.g. particle mass) from observations of gaps in streams. Using linear perturbation techniques, Bovy et al. (2017) constrained the number of dark matter subhalos of masses between $10^{6.5}$ and 10^{9} $M_{\odot}$ within 20 kpc of the Milky Way's galactic center by modeling Pal 5 data (see also Banik et al., 2021). Banik & Bovy (2019) provided a powerful method for disentangling under-densities caused by dark matter subhalos from baryonic perturbers (e.g. bars, molecular clouds, and spiral arms) in Pal 5 by computing the various perturbers' contributions to the stream's density power spectrum. They concluded that the contribution from spiral structure to Pal 5 substructure is low but that giant molecular clouds can create small-scale under-densities comparable to those from dark matter subhalos (Amorisco et al., 2016). Recently, Hermans et al. (2021) showed that simulation-based inference techniques with machine learning that map observed densities in streams to simulations can help constrain dark matter structure. They found that GD-1 stream data can be

used to constrain warm dark matter particle masses and distinguish between CDM and WDM models. Lovell et al. (2021) confirmed that the structure in GD-1 and Pal 5 can place limits on the fraction of WDM vs CDM subhalos within a 40 kpc distance from the Galactic center (see also discussion by Pearson et al. 2019, 2022). Searching for streams in the halos of external galaxies far from the bar and star-forming regions will increase the likelihood of finding gaps induced by gravitational perturbations from dark matter substructure, which can be compared to expectations from various dark matter candidates.

Even though we have shown that *Roman* will not be able to detect gaps in GC streams in external galaxies further than 2–3 Mpc away, in M31 alone there are ≈ 450 GCs (Galleti et al., 2006, 2007; Huxor et al., 2008, 2014; Caldwell & Romanowsky, 2016; Mackey et al., 2019), which is a factor of 3 more than the number of known GCs in the Milky Way (Harris, 1996, 2010). It is not unreasonable to assume that there is also a factor of 3 more, yet to be detected, GC streams in M31 than the ≈ 100 GC streams observed in the Milky Way (Malhan et al., 2018; Mateu, 2023; Martin et al., 2022) We know that GCs are also prevalent in other external galaxies (Harris et al., 2013). Thus, M31 and other galaxies could provide a diverse set of GC streams with gaps that can be used to constrain substructure within various frameworks of dark matter (Bovy et al., 2017).

While the full survey parameters of *Roman* is yet to be determined, the proposed high latitude survey (HLS) is expected to image high-latitude fields (Akeson et al., 2019). The WFI instrument can reach depths of ≈ 28 mag (AB) in R, Z, Y bands for exposure times of 1 hour. Furthermore, the instrument has slitless spectroscopic capabilities that cover (0.6 μ m-1.8 μ m), which will be beneficial in identifying resolved stellar populations, albeit at much shallower 1-hour sensitivity. Compared to previous M31 surveys with HST (e.g. the Panchromatic Hubble Andromeda Treasury Dalcanton

et al. 2012), *Roman* will offer an opportunity to observe M31 at higher efficiency and sensitivity.

Finally, in addition to the *Nancy Grace Roman Telescope*, other imaging and astrometric surveys, such as the Vera C. Rubin Observatory, will also help detect new gaps from dark matter subhalos down to $\approx 10^6$ $M_\odot$ in dozens of streams in the Milky Way (Drlica-Wagner et al., 2019). These detections will offer the possibility to constrain cold dark matter models at a 99 % confidence level, opening up an exciting era for using both Galactic and extra-galactic streams to constrain dark matter models.

5.6 Summary

5.7 Comparing Simulated Populations to PAndAS data

In Figure 5.8, we show the simulated color-magnitude diagram in CFHT g_0 and i_0 bands compared to the reddening-corrected PAndAS data, which reproduces a significant portion of the range of colors and magnitudes covered by the data. We also show the regions of the CMD that were used to scale the simulation to the data. While our simulations are a reasonable match to the data, we did not reproduce overdensities at $g_0 - i_0 \approx 1$ and $i_0 > 22$ which were labeled as Milky Way halo stars by Ibata et al. (2014), pointing to perhaps an underestimation of the fraction of Milky Way disk to halo stars in our simulations. Additionally, our simulations assume magnitude completeness down to the magnitude limits, which is not the case for the real data. As reported by Martin et al. (2016), the completeness of the PAndAS survey drops below 70 percent for $i_0 > 23$. Nevertheless, as discussed in the main text, this scaling provided a robust estimation of the CFHT *g*-band luminosity function and the total stellar density within the PAndAS fields.

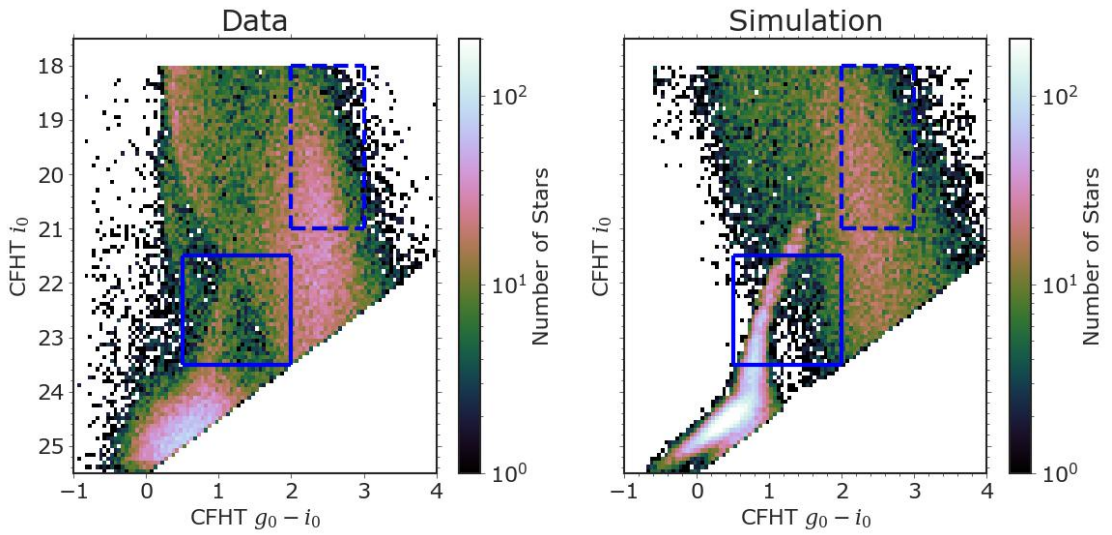

Figure 5.8 Comparison between simulated stellar populations and the PAndAS data. *Left:* Color-magnitude diagram of the CFHT data from the PAndAS survey covering distances 30–40 kpc from the center of M31. We used the regions shown by the dashed rectangles to scale the number of the Milky Way foreground stars, and the regions shown in solid rectangles to scale the total number of stars in our simulations. *Right:* Similar to the left but here, we show the simulated populations. Our simulated CMD reasonably matches the PAndAS observations.

5.8 Additional Checks for Gap Detection Pipeline

5.8.1 Visual Inspections of Gap Detections with Distance

Figure 5.9 shows additional examples of the density of stars in mock observations as a function of distance, and the identification of the gap. Here, we only show streams at R_{GC}= 35 kpc and 1 hour exposure time as the gaps are easier to detect (see discussion of Figure 5.7). The location of the gap is shown by arrows which become scattered beyond 2–3 Mpc, which indicates our detection limit.

5.8.2 Examples of Non-Detections of Gaps

We demonstrate where the detection of gap breaks down for a set of mock observations R_{GC}= 35 kpc and for 1 hour exposure times by showing three cases in Figure 5.10: (a) a case where the gap was detectable by eye but the bandwidth was much larger than our optimal bandwidth (b) a case where the bandwidth was much smaller than 0.8 kpc, and (c) a case where the bandwidth was optimal but the stellar density in the stream was low. For the first case and second cases, the spread in the location of gap points ($\mathscr{S}_g$) was large. In the last case, the deviation of gap points (Δ) from the center was large.

5.8.3 Comparing Streams with Gaps to Intact Streams and Backgrounds

We compare the performance of the gap detection tool to simulations of an intact stream with no perturbation from the dark matter subhalo for a bandwidth of 0.5 kpc and 0.8 kpc, and a stream with an off-centered gap with a bandwidth of 0.8 kpc in Figure 5.11. To generate mock observations, we followed the same methodology as highlighted in the

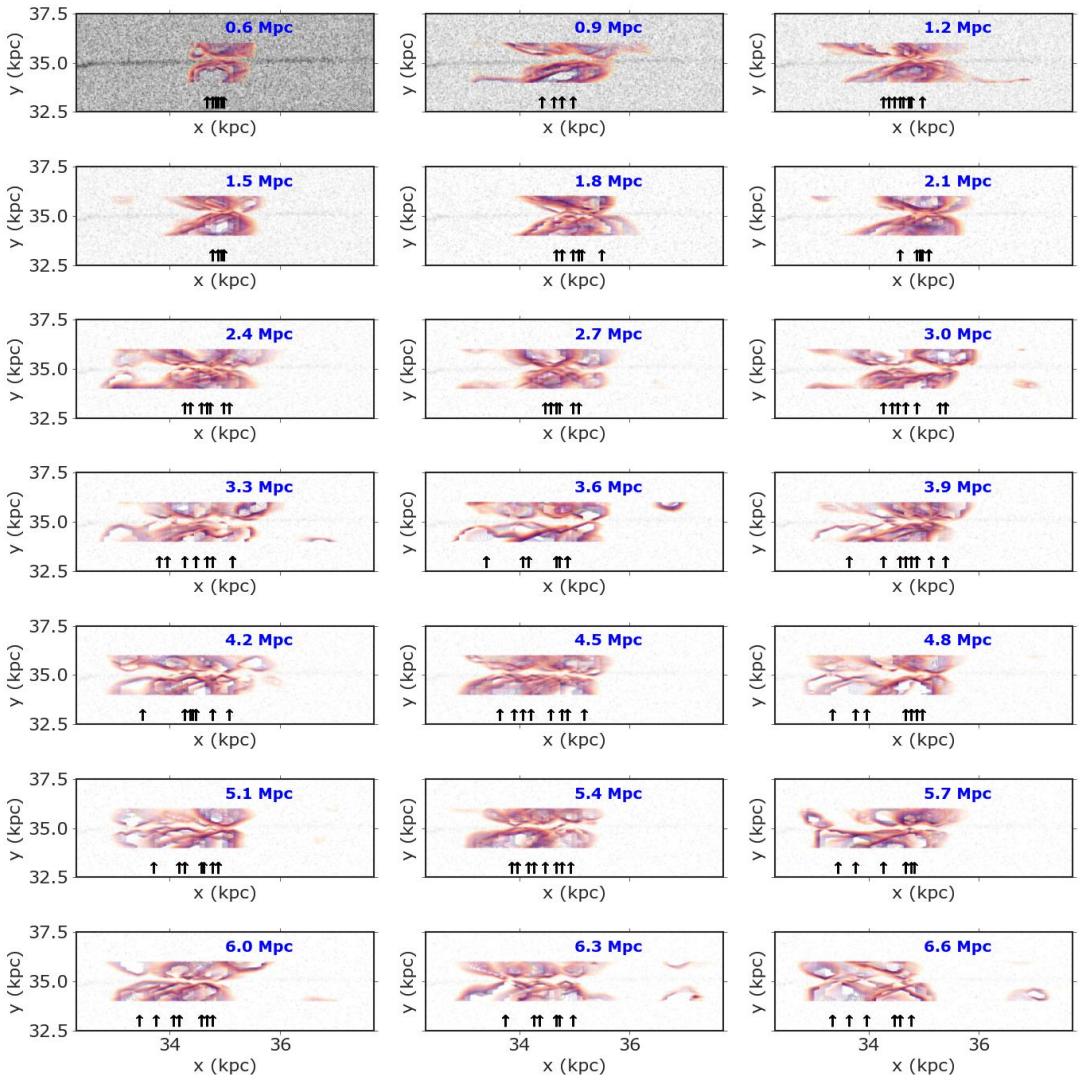

Figure 5.9 Additional simulation of a gap from a $5\times10^6 M_\odot$ subhalo at various distances of the host galaxy and for R_{GC}=35 kpc. Each panel is a composite of 10 mock observations, and all panels are centered around the gap. Contours show the distribution of the top 95 of the maximum eigenvalues of $\Pi H \Pi$values based on our density estimator with a bandwidth of 0.8 kpc. Simulated stars are shown as black points. Vertical arrows show the center gap area based on our pipeline for each iteration. Successful identifications of gaps were characterized by a centrally-located gap. Our method successfully identified gaps when the density of stars inside the stream was relatively high (distances $\approx 2-3$ Mpc). We discuss our characterization of potential failure modes of our pipeline in Appendix 5.8.2.

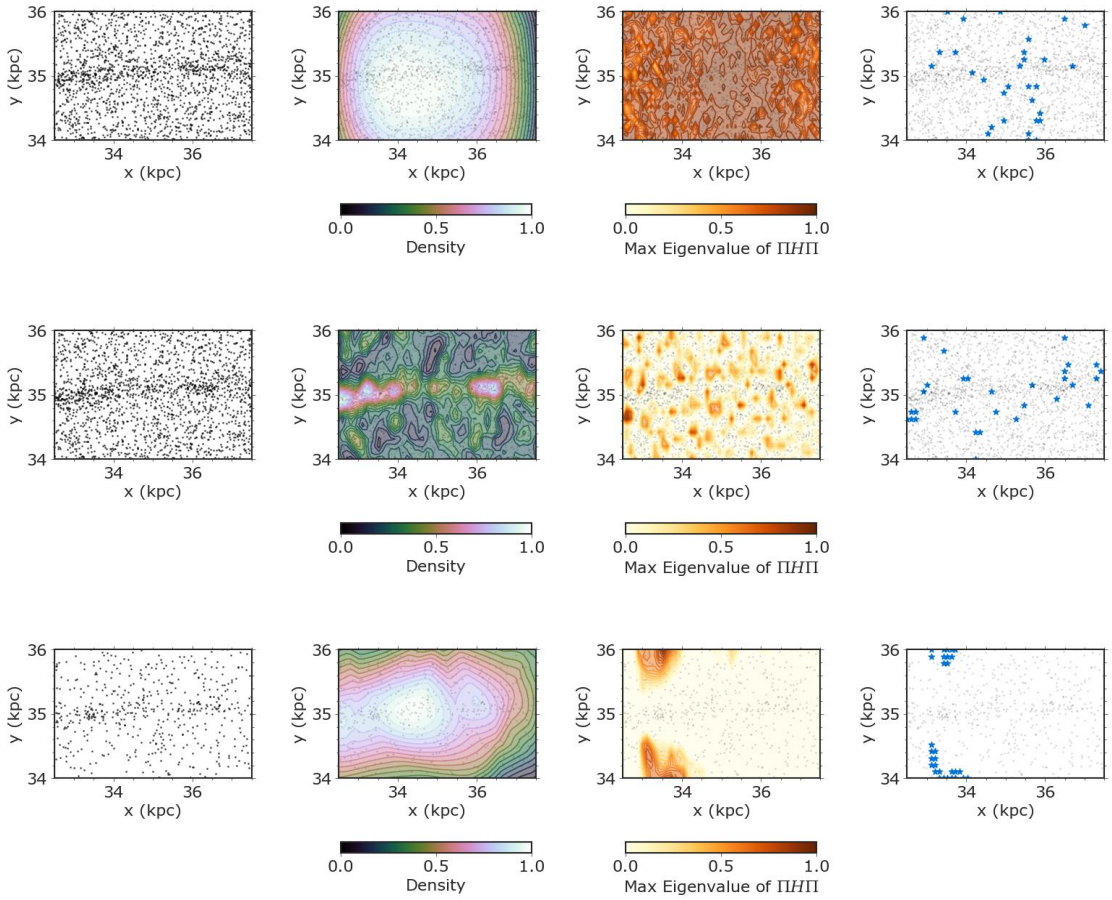

Figure 5.10 Illustration of different modes of failures for our detection pipeline. All images are for 1 hour exposures. In the left panels, we show the simulations. In the center panels, filled-in contours show the map of the density and the maximum eigenvalues of $\Pi H \Pi$ that we used to locate gaps. In the right panels, we show gap indicator points based on our percentile cuts. (a) Simulation of a stream at a distance of 0.8 Mpc using a large bandwidth of 1.5 kpc. The stream can still be identified, but the method could not detect the central gap. Using our pipeline selection metrics, this detection would be rejected on the basis that the spread in the location of gap points is large and that the absolute deviation of the predicted gap location from the center is large, consistent with our Δ metric (see Section 5.4.4). (b) Simulation of a stream at a distance of 0.8 Mpc using a bandwidth of 0.1 kpc. In this case, the predicted median location of gap points is close to the true location of the gap, but there are also spurious gaps in the background. Using our metrics defined in Section 5.4.4, this detection would have a small value for Δ, but a large value for $\mathscr{S}_g$. (c) Simulation of a stream at 6.5 Mpc with a bandwidth of 0.8 kpc. Due to the very low density in the image, the gap-finder tool detects an off-centered gap but it does not detect the real gap. This outcome motivates our claim that the gap detection pipeline works for distances < 3 Mpc.

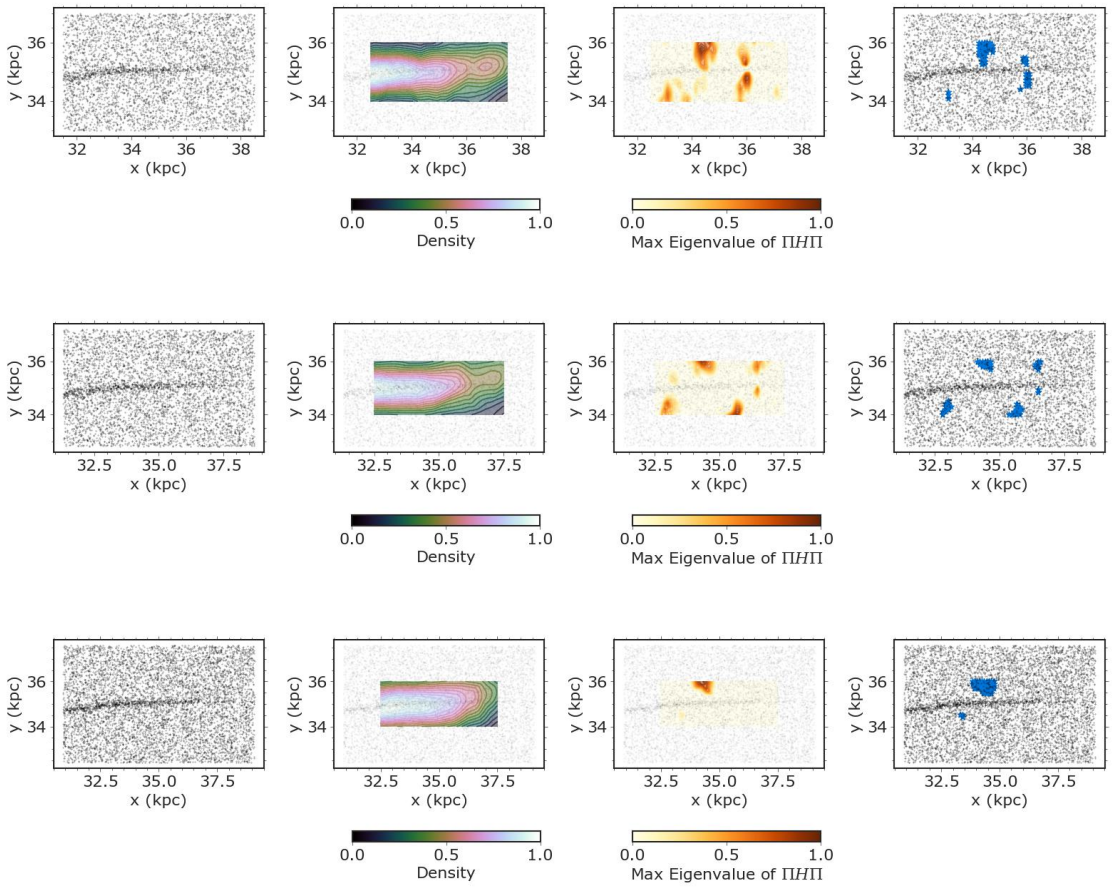

Figure 5.11 Additional tests of the gap detection tool on intact streams for a bandwidth of 0.5 kpc (a) and a bandwidth of 0.8 kpc (b). We also show a stream with off-centered gap (c), as an additional validation that our pipeline does not depend on the position of the gap. All simulated streams are at 1 Mpc at R_{GC}= 35 kpc, for 1000 s exposure.

main text. Spurious gaps were persistent in the backgrounds, but these detections can be ruled out by careful visual inspection. Additionally, the tool is able to detect off-centered gaps.

Table 5.1 Summary of simulation parameters for the stream and the subhalo

	Parameter	Description	Range of Values
Stream	m_p	progenitor mass	5×10^4 $M_\odot$
	–	number of particles	$\approx$ 80,000
Subhalo	M_h	mass	2×10^6 $M_\odot$–10^7 $M_\odot$
	r_s	scale radius	0.14 kpc–0.32 kpc
	–	potential	Hernquist[a]
Galaxy	–	potential	Hernquist bulge + Miyamoto-Nagai disk + NFW halo [b]

Hernquist (1990).
Profiles based on Miyamoto & Nagai (1975) and Navarro et al. (1996) with parameters based on Milky Way measurements by McMillan (2017).

Table 5.2 Summary of the stream, subhalo coordinates and resulting gap sizes

	Parameter and Description	R_{GC}= 15 kpc	R_{GC}= 35 kpc	R_{GC}= 55 kpc
Initial	progenitor position at t_1 ($\vec{x}_1$, kpc)	(6.1, 0.2, 14.7)	(6.1, 0.2, 34.7)	(6.1, 31.7, 44.7)
	progenitor velocity at t_1 ($\vec{v}_1$, km/s)	(-49.7, -119.4, -11.4)	(-49.7, -119.4, -11.4)	(-49.7, -119.4, -11.4)
	total integration time (t_1, Gyr)	2	3	3
collision	$\lvert\vec{V}_{\rm rel}\rvert$, km/s	50	70	50
	time before collision (Δt_2, Gyr)	0.7	1.7	1.5
	time during collision (Δt_3, Gyr)	0.5	0.5	0.1
	distance of impact from center (Δx, kpc)	0.5	0.7	0.8
result	size of the gap (kpc)	1.4	1.8	1.8

Table 5.3 Summary of Simulations Parameters for Resolved Stellar Populations

Population	Quantity	Distribution	Reference
Foregrounds & backgrounds	IMF	Kroupa[a]	Kroupa (2001)
Milky Way Thin Disk	age	Uniform (0, 8) Gyr	Jurić et al. (2008)
	[Fe/H]	Uniform (-1,0.5)	Mackereth et al. (2019a)
	spatial density	Exponential[b](H= 350 pc, L= 2600 pc)	Jurić et al. (2008)
Milky Way Thick Disk	age	Uniform (8, 10) Gyr	Kilic et al. (2017)
	[Fe/H]	Uniform (-1,0.5)	Hawkins et al. (2015)
	spatial density	Exponential (H= 900 pc, L= 3600 pc)	Jurić et al. (2008)
Milky Way Halo	age	Uniform (10, 13) Gyr	Jofré & Weiss (2011a)
	[Fe/H]	Uniform (-2.5, -1)	Mackereth et al. (2019a)
	spatial density	Spheroid[c](n= 0.64, q= 2.77)	Jurić et al. (2008)
M31 Halo	age	Uniform (5, 13) Gyr	Ibata et al. (2014)
	[Fe/H]	Uniform (-2.5, 0.5)	Ibata et al. (2014)
	spatial density	Spheroid[d](n= 1.11, q= 3)	Ibata et al. (2014)
Pal 5	age	11.5 Gyr	Ibata et al. (2017)
	[Fe/H]	-1.3	Ibata et al. (2017)
	IMF	dN/dM= $M^{-0.5}$	Grillmair & Smith (2001)

dN/dM= $M^{-\alpha}$, with $\alpha = 1.3$ for masses between 0.08 $M_\odot$ and 0.5 $M_\odot$, $\alpha = 2.3$ for masses > 0.5.
Exponential profile defined in Equation 5.9.
Spheroidal profile defined in Equation 5.10.
Profile given by Equation 5.11.

Chapter 5 has been submitted to the Astrophysical Journal and is currently in review, authored by Christian Aganze, Sarah Pearson, Tjitske Starkenburg ; Gabriella Contardo; Kathryn Johnston, Kiyan Tavangar, Adrian Price-Whelan, Burgasser, Adam J. The thesis author was the primary investigator and author of this paper.

Chapter 6

Summary

Chapter 2: Findings Distant UCDs in Deep HST Fields

- We have identified 164 late-M, L, and T dwarfs in 0.6 deg^2 of *HST*/WFC parallels grism spectra from the 3D-HST and WISPS samples. These objects were selected from over 250,000 sources using a combination of imaging morphology, spectral indices, template fitting, and visual confirmation.

- We evaluated three different methods for source identification: traditional spectral index-based selection, random forest classification, and deep neural network classification. The latter two provided a substantial reduction in source contamination while missing only a small number of late-M dwarfs, and provide a superior approach to the discovery of rare sources in large spectral samples.

- Spectral classification and empirical relations allow us to map the distances of these sources to up to 3 kpc, including many of the most distant spectroscopically-confirmed brown dwarfs currently known.

- The lack of detection of clear subddwarfs and/or Y dwarfs in the sample is expected due to the rarity of these populations and small area coverage of these surveys

This chapter provides an expansion of previous deep spectroscopic surveys, limited to only a handful of sources with $d \lesssim 1$ kpc. Nevertheless, the sample of distant L and T remains small. Fortunately, forthcoming wide-field spectral surveys achieved with the *James Webb Space Telescope* (*JWST*, Gardner et al. 2006), *SPHEREx* (Doré et al., 2014), and *Nancy Grace Roman Telescope* (Spergel et al., 2015), and deep multi-epoch, multi-color photometry and astrometry with the Vera Rubin Observatory (Ivezić et al., 2019) and the Euclid telescope (Laureijs et al., 2011), will allow us to probe to be greater depths ($J \approx 27$) and broader fields of view. Ryan & Reid (2016) has predicted a mean UCD surface density of ≈ 0.3 arcmin^{-2} (or 1080 deg^{-2}) in *JWST* down to a depth of $J = 24$. The recently-approved *JWST* Parallel Application of Slitless Spectroscopy to Analyze Galaxy Evolution survey (PASSAGE, Cycle 1 GO-1571, PI Malkan) will obtained slitless grism spectra over a total area of 7.5 deg^2 down to F115W & F200W $\approx$ 27 in a manner similar to 3D-HST and WISPS. We expect this survey to detect of order 10^4–10^5 thin disk UCDs, thousands of thick disk UCDs, and hundreds of halo UCDs out to distances of 10 kpc, with full 1–2.2 μm spectra enabling more robust segregation of contaminants and characterization of discoveries. In Paper II, we use this sample and a set of Monte-carlo simulations incorporating assumptions about the stellar mass function, star formation history, UCD evolutionary models and Galactic structure constrain the Galactic scale-height and population ages for these distant UCDs.

Chapter 3: Constraining Scaleheights and Population

- We attempted to reproduce the observed number counts in a deep spectral sample of UCDs from the WISP and 3D-HST *HST*/WFC3 surveys with Monte-Carlo population simulations that combine assumptions for the star formation history, mass function, local luminosity function, and spatial model of the Galactic UCD population.

- By comparing between simulations that varied the thin disk vertical scaleheight and choice of evolutionary model, we inferred the scaleheight distribution of UCDs as a function of spectral subclass, a proxy of population age and hence the star formation and evolutionary history of our mixed stellar and substellar sample.

- We found a late-M dwarf scaleheight of 249^{+48}_{-61} pc, a value smaller than but consistent with prior deep *HST* imaging samples and ground-based survey measurements. We also found an L dwarf scaleheight of 153^{+56}_{-30} pc and a T dwarf scaleheight of 175^{+149}_{-56} pc, both considerably smaller than prior space-based and ground-based deep imaging surveys.

- Using transformations between scaleheight, velocity dispersion, and age, we determined population ages of $3.6^{+0.8}_{-1.0}$ Gyr for late-M dwarfs, $2.1^{+0.9}_{-0.5}$ Gyr for L dwarfs, and $2.4^{+2.4}_{-0.8}$ Gyr for T dwarfs. While there is some variance between these spatially-based ages and velocity dispersion-based ages measured in the local UCD population, and systematic effects in age-velocity-scaleheight transformations contribute significantly to the uncertainties in the absolute ages (1–2 Gyr), the relative drop-off in age measured between late-M dwarfs and L and T dwarfs is consistent with predictions based on brown dwarf population simulations.

- We used our simulations to predict the expected UCD yield in the deep *JWST* PASSAGE spectral survey, which will reach distances of $\sim$40 kpc for late-M dwarfs, 10–30 kpc for L dwarfs, and 1-10 kpc for T dwarfs. The smaller area of PASSAGES compared to WISP and 3D-HST results in a comparably-sized spectral sample of 135-280 UCDs, but dominated by thick disk and halo objects. Thus, metallicity effects in evolution and observable properties will be more important in *JWST* surveys than *HST* equivalents.

This series provides a first glimpse into the utility and limitations of using deep

spectral samples of UCDs for investigations of the Galaxy at large. While the *HST* sample examined here greatly expands upon prior deep spectral surveys, and has far greater fidelity than comparable image-based surveys, sensitivity limits nevertheless restrict both the sample size (particularly for late-L, T and Y dwarfs) and accessibility to major Galactic populations (halo and thick disk subdwarfs). We also find important systematic differences between current evolutionary models, particularly for late-M and early-L dwarfs, which sample the largest distances in our survey. Hence, while our determinations for the scaleheights and ages of UCDs aligns with prior deep imaging and local kinematic studies, our uncertainties remain sufficiently large to limit our ability to critically assess evolution-induced age variations and explore star formation parameters in detail. Fortunately, larger and deeper spectral surveys are planned in the forthcoming space missions *JWST*, *SPHEREx* (Doré et al., 2014), the *Nancy Grace Roman Space Telescope* (Spergel et al., 2015), and the *Euclid* telescope (Laureijs et al., 2011; Solano et al., 2021). Our analysis of the *JWST* PASSAGE program predicts a UCD spectral sample extending to tens of kpc in distance, with a majority of thick disk and halo sources. For comparison, Solano et al. (2021) have predicted millions of UCDs in the *Euclid* wide field survey in multiple imaging filters, while the ground-based Vera Rubin Observatory's Legacy Survey of Space and Time (LSST; Ivezić et al. 2019) is expected to detect > 1 million UCDs with multi-epoch and multi-color photometry and astrometry. With these near-term improvements in sample size and fidelity, the full potential of UCD tracers for Galactic archaeology studies will be realized.

Chapter 4: Predictions for Euclid, Rubin and Roman In this chapter, our aim was to predict the expected number counts of UCDs and to design selection criteria with the Euclid Telescope, the Vera Rubin Observatory and the Nancy Grace Roman Space Telescope by incorporating the latest models of metal-poor thick disk and halo sources.

- Euclid will find millions of UCDs with spectral types $> M5$, with nearly similar number of the thin disk, thick disk and halo detectable in the NISP Y, J and H bands.

- The Roman high-latitude surveys will find a similar number of objects as Euclid, detectable in the Z, J, H and F bands.

- Rubin will find millions of late-M dwarfs but only thousands of L and T dwarfs with precise parallaxes and proper motion measurements are detectable over the next 10 years in the i,z and y bands.

- Samples from each individual survey are sufficient to constrain the thin disk scaleheights and to constrain the halo mass function (for power law IMFs between -2.3 and 2.3)

The combination of these surveys will allow us to study UCDs in the Galactic context.

Chapter 5: Prospects for Detecting Gaps in GC Streams with Roman In this chapter, our aim was to quantify the detection prospects of gaps in globular cluster streams in external galaxies with the *Nancy Grace Roman telescope* as tracers for dark matter structure. To do this, we simulated mock *Roman* observations of gaps in extra-galactic Pal 5-like streams produced by their interaction with dark matter subhalos. We generated mock streams and we simulated a direct encounter with dark matter subhalos with masses between $2\times10^6 M_\odot$ and $10^7 M_\odot$. Additionally, we simulated realistic mock observations of background of stars in the halo of M31 at galactocentric radii of 15 kpc, 35 kpc and 55 kpc, taking into account contamination from Milky Way foregrounds. To mimic observations of galaxies at distances that are further than M31, we moved the simulated M31 population to distances of 0.5–10 Mpc, retaining foreground Milky

Way populations. To search for gaps in the stream, we first visually inspected mock observations, then applied an analysis with the gap detection tool from Contardo et al. (2022), deriving several metrics to quantify the reliability of our detections with galaxy distance.

- We find that gaps formed by 5×10^6 $M_\odot$ subhalos gaps will be visually obvious in 1000 s and 1-hour photometric exposures in the halo of M31.
- Mock observations of the same stream at various distances from the Milky Way indicate that gaps can be seen out to distances of $\approx$1.5 Mpc by visual inspection.
- With the automated detection tool, we confirmed that gaps formed from 5×10^6 $M_\odot$ subhalos can be identified to distances of 2–3 Mpc, a volume which includes $\approx$ 200 galaxies.

While our analysis was limited to gaps from in Pal 5-like streams embedded in M31-like halos, it points to the potential of *Roman* to build a large and diverse set of GC stream gaps in multiple galaxies, which will contribute to constraining various dark matter models.

Bibliography

Abolfathi B., Aguado D. S., Aguilar G., Allende Prieto C., Almeida A., Ananna T. T., Anders F., Anderson S. F., Andrews B. H., Anguiano B., Aragón-Salamanca A., Argudo-Fernández M., Armengaud E., Ata M., Aubourg E., Avila-Reese V., Badenes C., Bailey S., Balland C., Barger K. A., Barrera-Ballesteros J., Bartosz C., Bastien F., Bates D., Baumgarten F., Bautista J., Beaton R., Beers T. C., Belfiore F., Bender C. F., Bernardi M., Bershady M. A., Beutler F., Bird J. C., Bizyaev D., Blanc G. A., Blanton M. R., Blomqvist M., Bolton A. S., Boquien M., Borissova J., Bovy J., Bradna Diaz C. A., Brandt W. N., Brinkmann J., Brownstein J. R., Bundy K., Burgasser A. J., Burtin E., Busca N. G., Cañas C. I., Cano-Díaz M., Cappellari M., Carrera R., Casey A. R., Cervantes Sodi B., Chen Y., Cherinka B., Chiappini C., Choi P. D., Chojnowski D., Chuang C.-H., Chung H., Clerc N., Cohen R. E., Comerford J. M., Comparat J., Correa do Nascimento J., da Costa L., Cousinou M.-C., Covey K., Crane J. D., Cruz-Gonzalez I., Cunha K., da Silva Ilha G., Damke G. J., Darling J., Davidson James W. J., Dawson K., de Icaza Lizaola M. A. C., de la Macorra A., de la Torre S., De Lee N., de Sainte Agathe V., Deconto Machado A., Dell'Agli F., Delubac T., Diamond-Stanic A. M., Donor J., Downes J. J., Drory N., du Mas des Bourboux H., Duckworth C. J., Dwelly T., Dyer J., Ebelke G., Davis Eigenbrot A., Eisenstein D. J., Elsworth Y. P., Emsellem E., Eracleous M., Erfanianfar G., Escoffier S., Fan X., Fernández Alvar E., Fernandez-Trincado J. G., Fernando Cirolini R., Feuillet D., Finoguenov A., Fleming

S. W., Font-Ribera A., Freischlad G., Frinchaboy P., Fu H., Gómez Maqueo Chew Y., Galbany L., García Pérez A. E., Garcia-Dias R., García-Hernández D. A., Garma Oehmichen L. A., Gaulme P., Gelfand J., Gil-Marín H., Gillespie B. A., Goddard D., González Hernández J. I., Gonzalez-Perez V., Grabowski K., Green P. J., Grier C. J., Gueguen A., Guo H., Guy J., Hagen A., Hall P., Harding P., Hasselquist S., Hawley S., Hayes C. R., Hearty F., Hekker S., Hernandez J., Hernandez Toledo H., Hogg D. W., Holley-Bockelmann K., Holtzman J. A., Hou J., Hsieh B.-C., Hunt J. A. S., Hutchinson T. A., Hwang H. S., Jimenez Angel C. E., Johnson J. A., Jones A., Jönsson H., Jullo E., Khan F. S., Kinemuchi K., Kirkby D., Kirkpatrick Charles C. I., Kitaura F.-S., Knapp G. R., Kneib J.-P., Kollmeier J. A., Lacerna I., Lane R. R., Lang D., Law D. R., Le Goff J.-M., Lee Y.-B., Li H., Li C., Lian J., Liang Y., Lima M., Lin L., Long D., Lucatello S., Lundgren B., Mackereth J. T., MacLeod C. L., Mahadevan S., Maia M. A. G., Majewski S., Manchado A., Maraston C., Mariappan V., Marques-Chaves R., Masseron T., Masters K. L., McDermid R. M., McGreer I. D., Melendez M., Meneses-Goytia S., Merloni A., Merrifield M. R., Meszaros S., Meza A., Minchev I., Minniti D., Mueller E.-M., Muller-Sanchez F., Muna D., Muñoz R. R., Myers A. D., Nair P., Nandra K., Ness M., Newman J. A., Nichol R. C., Nidever D. L., Nitschelm C., Noterdaeme P., O'Connell J., Oelkers R. J., Oravetz A., Oravetz D., Ortíz E. A., Osorio Y., Pace Z., Padilla N., Palanque-Delabrouille N., Palicio P. A., Pan H.-A., Pan K., Parikh T., Pâris I., Park C., Peirani S., Pellejero-Ibanez M., Penny S., Percival W. J., Perez-Fournon I., Petitjean P., Pieri M. M., Pinsonneault M., Pisani A., Prada F., Prakash A., Queiroz A. B. d. A., Raddick M. J., Raichoor A., Barboza Rembold S., Richstein H., Riffel R. A., Riffel R., Rix H.-W., Robin A. C., Rodríguez Torres S., Román-Zúñiga C., Ross A. J., Rossi G., Ruan J., Ruggeri R., Ruiz J., Salvato M., Sánchez A. G., Sánchez S. F., Sanchez Almeida J., Sánchez-Gallego J. R., Santana Rojas F. A., Santiago B. X., Schiavon R. P., Schimoia J. S., Schlafly E., Schlegel D.,

Schneider D. P., Schuster W. J., Schwope A., Seo H.-J., Serenelli A., Shen S., Shen Y., Shetrone M., Shull M., Silva Aguirre V., Simon J. D., Skrutskie M., Slosar A., Smethurst R., Smith V., Sobeck J., Somers G., Souter B. J., Souto D., Spindler A., Stark D. V., Stassun K., Steinmetz M., Stello D., Storchi-Bergmann T., Streblyanska A., Stringfellow G. S., Suárez G., Sun J., Szigeti L., Taghizadeh-Popp M., Talbot M. S., Tang B., Tao C., Tayar J., Tembe M., Teske J., Thakar A. R., Thomas D., Tissera P., Tojeiro R., Tremonti C., Troup N. W., Urry M., Valenzuela O., van den Bosch R., Vargas-González J., Vargas-Magaña M., Vazquez J. A., Villanova S., Vogt N., Wake D., Wang Y., Weaver B. A., Weijmans A.-M., Weinberg D. H., Westfall K. B., Whelan D. G., Wilcots E., Wild V., Williams R. A., Wilson J., Wood-Vasey W. M., Wylezalek D., Xiao T., Yan R., Yang M., Ybarra J. E., Yèche C., Zakamska N., Zamora O., Zarrouk P., Zasowski G., Zhang K., Zhao C., Zhao G.-B., Zheng Z., Zheng Z., Zhou Z.-M., Zhu G., Zinn J. C., Zou H. 2018, The Fourteenth Data Release of the Sloan Digital Sky Survey: First Spectroscopic Data from the Extended Baryon Oscillation Spectroscopic Survey and from the Second Phase of the Apache Point Observatory Galactic Evolution Experiment, ApJS, 235, 42, doi: 10.3847/1538-4365/aa9e8a

Ackerman A. S., Marley M. S. 2001, Precipitating Condensation Clouds in Substellar Atmospheres, ApJ, 556, 872, doi: 10.1086/321540

Aganze C., Burgasser A. J., Faherty J. K., Choban C., Escala I., Lopez M. A., Jin Y., Tamiya T., Tallis M., Rockward W. 2016, Characterization of the Very-low-mass Secondary in the GJ 660.1AB System, AJ, 151, 46, doi: 10.3847/0004-6256/151/2/46

Aganze C., Burgasser A. J., Malkan M., Theissen C. A., Tejada Arevalo R. A., Hsu C.-C., Bardalez Gagliuffi D. C., Ryan R. E., Holwerda B. 2022a, Beyond the Local Volume. I. Surface Densities of Ultracool Dwarfs in Deep HST/WFC3 Parallel Fields, ApJ, 924, 114, doi: 10.3847/1538-4357/ac35ea

Aganze C., Burgasser A. J., Malkan M., Theissen C. A., Tejada Arevalo R. A., Hsu C.-C., Bardalez Gagliuffi D. C., Ryan R. E., Holwerda B. 2022b, Beyond the Local Volume. I. Surface Densities of Ultracool Dwarfs in Deep HST/WFC3 Parallel Fields, ApJ, 924, 114, doi: 10.3847/1538-4357/ac35ea

Agertz O., Renaud F., Feltzing S., Read J. I., Ryde N., Andersson E. P., Rey M. P., Bensby T., Feuillet D. K. 2021, VINTERGATAN - I. The origins of chemically, kinematically, and structurally distinct discs in a simulated Milky Way-mass galaxy, MNRAS, 503, 5826, doi: 10.1093/mnras/stab322

Aguerri J. A. L., Balcells M., Peletier R. F. 2001, Growth of galactic bulges by mergers. I. Dense satellites, A&A, 367, 428, doi: 10.1051/0004-6361:20000441

Aihara H., Arimoto N., Armstrong R., Arnouts S., Bahcall N. A., Bickerton S., Bosch J., Bundy K., Capak P. L., Chan J. H. H., Chiba M., Coupon J., Egami E., Enoki M., Finet F., Fujimori H., Fujimoto S., Furusawa H., Furusawa J., Goto T., Goulding A., Greco J. P., Greene J. E., Gunn J. E., Hamana T., Harikane Y., Hashimoto Y., Hattori T., Hayashi M., Hayashi Y., Hełminiak K. G., Higuchi R., Hikage C., Ho P. T. P., Hsieh B.-C., Huang K., Huang S., Ikeda H., Imanishi M., Inoue A. K., Iwasawa K., Iwata I., Jaelani A. T., Jian H.-Y., Kamata Y., Karoji H., Kashikawa N., Katayama N., Kawanomoto S., Kayo I., Koda J., Koike M., Kojima T., Komiyama Y., Konno A., Koshida S., Koyama Y., Kusakabe H., Leauthaud A., Lee C.-H., Lin L., Lin Y.-T., Lupton R. H., Mand elbaum R., Matsuoka Y., Medezinski E., Mineo S., Miyama S., Miyatake H., Miyazaki S., Momose R., More A., More S., Moritani Y., Moriya T. J., Morokuma T., Mukae S., Murata R., Murayama H., Nagao T., Nakata F., Niida M., Niikura H., Nishizawa A. J., Obuchi Y., Oguri M., Oishi Y., Okabe N., Okamoto S., Okura Y., Ono Y., Onodera M., Onoue M., Osato K., Ouchi M., Price P. A., Pyo T.-S., Sako M., Sawicki M., Shibuya T., Shimasaku K., Shimono A., Shirasaki M.,

Silverman J. D., Simet M., Speagle J., Spergel D. N., Strauss M. A., Sugahara Y., Sugiyama N., Suto Y., Suyu S. H., Suzuki N., Tait P. J., Takada M., Takata T., Tamura N., Tanaka M. M., Tanaka M., Tanaka M., Tanaka Y., Terai T., Terashima Y., Toba Y., Tominaga N., Toshikawa J., Turner E. L., Uchida T., Uchiyama H., Umetsu K., Uraguchi F., Urata Y., Usuda T., Utsumi Y., Wang S.-Y., Wang W.-H., Wong K. C., Yabe K., Yamada Y., Yamanoi H., Yasuda N., Yeh S., Yonehara A., Yuma S. 2018, The Hyper Suprime-Cam SSP Survey: Overview and survey design, PASJ, 70, S4, doi: 10.1093/pasj/psx066

Akeson R., Armus L., Bachelet E., Bailey V., Bartusek L., Bellini A., Benford D., Bennett D., Bhattacharya A., Bohlin R., Boyer M., Bozza V., Bryden G., Calchi Novati S., Carpenter K., Casertano S., Choi A., Content D., Dayal P., Dressler A., Doré O., Fall S. M., Fan X., Fang X., Filippenko A., Finkelstein S., Foley R., Furlanetto S., Kalirai J., Gaudi B. S., Gilbert K., Girard J., Grady K., Greene J., Guhathakurta P., Heinrich C., Hemmati S., Hendel D., Henderson C., Henning T., Hirata C., Ho S., Huff E., Hutter A., Jansen R., Jha S., Johnson S., Jones D., Kasdin J., Kelly P., Kirshner R., Koekemoer A., Kruk J., Lewis N., Macintosh B., Madau P., Malhotra S., Mandel K., Massara E., Masters D., McEnery J., McQuinn K., Melchior P., Melton M., Mennesson B., Peeples M., Penny M., Perlmutter S., Pisani A., Plazas A., Poleski R., Postman M., Ranc C., Rauscher B., Rest A., Roberge A., Robertson B., Rodney S., Rhoads J., Rhodes J., Ryan Russell J., Sahu K., Sand D., Scolnic D., Seth A., Shvartzvald Y., Siellez K., Smith A., Spergel D., Stassun K., Street R., Strolger L.-G., Szalay A., Trauger J., Troxel M. A., Turnbull M., van der Marel R., von der Linden A., Wang Y., Weinberg D., Williams B., Windhorst R., Wollack E., Wu H.-Y., Yee J., Zimmerman N. 2019, The Wide Field Infrared Survey Telescope: 100 Hubbles for the 2020s, arXiv e-prints, arXiv:1902.05569. https://arxiv.org/abs/1902.05569

Allard F., Homeier D., Freytag B. 2012, Models of very-low-mass stars, brown dwarfs and exoplanets, Philosophical Transactions of the Royal Society of London Series A, 370, 2765, doi: 10.1098/rsta.2011.0269

Allers K., Jaffe D., Luhman K., Liu M., Wilson J., Skrutskie M., Nelson M., Peterson D., Smith J., Cushing M. 2007, Characterizing Young Brown Dwarfs Using Low-Resolution Near-Infrared Spectra, \apj, 657, 511, doi: 10.1086/510845

Amara A., Metcalf R. B., Cox T. J., Ostriker J. P. 2006, Simulations of strong gravitational lensing with substructure, MNRAS, 367, 1367, doi: 10.1111/j.1365-2966.2006.10053.x

Amorisco N. C., Gómez F. A., Vegetti S., White S. D. M. 2016, Gaps in globular cluster streams: giant molecular clouds can cause them too, MNRAS, 463, L17, doi: 10.1093/mnrasl/slw148

Antoja T., Helmi A., Romero-Gómez M., Katz D., Babusiaux C., Drimmel R., Evans D. W., Figueras F., Poggio E., Reylé C., Robin A. C., Seabroke G., Soubiran C. 2018, A dynamically young and perturbed Milky Way disk, Nature, 561, 360, doi: 10.1038/s41586-018-0510-7

Atek H., Malkan M., McCarthy P., Teplitz H., Scarlata C., Siana B., Henry A., Colbert J., Ross N., Bridge C., Bunker A., Dressler A., Fosbury R., Martin C., Shim H. 2010, The WFC3 Infrared Spectroscopic Parallel (WISP) Survey, \apj, 723, 104, doi: 10.1088/0004-637X/723/1/104

Aumer M., Binney J., Schönrich R. 2016, Age-velocity dispersion relations and heating histories in disc galaxies, MNRAS, 462, 1697, doi: 10.1093/mnras/stw1639

Aumer M., Binney J. J. 2009, Kinematics and history of the solar neighbourhood revisited, MNRAS, 397, 1286, doi: 10.1111/j.1365-2966.2009.15053.x

Bahcall J., Soneira R. 1981, Predicted star counts in selected fields and photometric bands Applications to galactic structure, the disk luminosity function, and the detection of a massive halo, \apjs, 47, 357, doi: 10.1086/190765

Bahcall J. N., Soneira R. M. 1980, The universe at faint magnitudes. I. Models for the Galaxy and the predicted star counts., ApJS, 44, 73, doi: 10.1086/190685

Banik N., Bovy J. 2019, Effects of baryonic and dark matter substructure on the Pal 5 stream, MNRAS, 484, 2009, doi: 10.1093/mnras/stz142

Banik N., Bovy J., Bertone G., Erkal D., de Boer T. J. L. 2021, Novel constraints on the particle nature of dark matter from stellar streams, , 2021, 043, doi: 10.1088/1475-7516/2021/10/043

Baraffe I., Chabrier G., Allard F., Hauschildt P. H. 1997, Evolutionary models for metal-poor low-mass stars. Lower main sequence of globular clusters and halo field stars, A&A, 327, 1054

Baraffe I., Chabrier G., Barman T., Allard F., Hauschildt P. 2003, Evolutionary models for cool brown dwarfs and extrasolar giant planets. The case of HD 209458, \aap, 402, 701, doi: 10.1051/0004-6361:20030252

Bardalez Gagliuffi D. C., Burgasser A. J., Schmidt S. J., Theissen C., Gagné J., Gillon M., Sahlmann J., Faherty J. K., Gelino C., Cruz K. L., Skrzypek N., Looper D. 2019, The Ultracool SpeXtroscopic Survey. I. Volume-limited Spectroscopic Sample and Luminosity Function of M7-L5 Ultracool Dwarfs, ApJ, 883, 205, doi: 10.3847/1538-4357/ab253d

Baron D. 2019, Machine Learning in Astronomy: a practical overview, arXiv e-prints, arXiv:1904.07248. https://arxiv.org/abs/1904.07248

Barry M., Wetzel A., Chapman S., Samuel J., Sanderson R., Arora A. 2023, The dark side of FIRE: predicting the population of dark matter subhaloes around Milky Way-mass galaxies, arXiv e-prints, arXiv:2303.05527. https://arxiv.org/abs/2303.05527

Basri G., Reiners A. 2006, A Survey for Spectroscopic Binaries among Very Low Mass Stars, AJ, 132, 663, doi: 10.1086/505198

Bastian N., Covey K. R., Meyer M. R. 2010, A Universal Stellar Initial Mass Function? A Critical Look at Variations, ARA&A, 48, 339, doi: 10.1146/annurev-astro-082708-101642

Bate M. R., Bonnell I. A. 2005, The origin of the initial mass function and its dependence on the mean Jeans mass in molecular clouds, MNRAS, 356, 1201, doi: 10.1111/j.1365-2966.2004.08593.x

Bechtol K., Drlica-Wagner A., Balbinot E., Pieres A., Simon J. D., Yanny B., Santiago B., Wechsler R. H., Frieman J., Walker A. R., Williams P., Rozo E., Rykoff E. S., Queiroz A., Luque E., Benoit-Lévy A., Tucker D., Sevilla I., Gruendl R. A., da Costa L. N., Fausti Neto A., Maia M. A. G., Abbott T., Allam S., Armstrong R., Bauer A. H., Bernstein G. M., Bernstein R. A., Bertin E., Brooks D., Buckley-Geer E., Burke D. L., Carnero Rosell A., Castander F. J., Covarrubias R., D'Andrea C. B., DePoy D. L., Desai S., Diehl H. T., Eifler T. F., Estrada J., Evrard A. E., Fernandez E., Finley D. A., Flaugher B., Gaztanaga E., Gerdes D., Girardi L., Gladders M., Gruen D., Gutierrez G., Hao J., Honscheid K., Jain B., James D., Kent S., Kron R., Kuehn K., Kuropatkin N., Lahav O., Li T. S., Lin H., Makler M., March M., Marshall J., Martini P., Merritt K. W., Miller C., Miquel R., Mohr J., Neilsen E., Nichol R., Nord B., Ogando R., Peoples J., Petravick D., Plazas A. A., Romer A. K., Roodman A., Sako M., Sanchez E., Scarpine V., Schubnell M., Smith R. C., Soares-Santos M., Sobreira F., Suchyta E., Swanson M. E. C., Tarle G., Thaler J., Thomas D., Wester W., Zuntz J., DES

Collaboration. 2015, Eight New Milky Way Companions Discovered in First-year Dark Energy Survey Data, ApJ, 807, 50, doi: 10.1088/0004-637X/807/1/50

Beers T. C., Carollo D., Ivezić Ž., An D., Chiba M., Norris J. E., Freeman K. C., Lee Y. S., Munn J. A., Re Fiorentin P., Sivarani T., Wilhelm R., Yanny B., York D. G. 2012, The Case for the Dual Halo of the Milky Way, ApJ, 746, 34, doi: 10.1088/0004-637X/746/1/34

Bekki K., Couch W. J., Drinkwater M. J., Gregg M. D. 2001, A New Formation Model for M32: A Threshed Early-Type Spiral Galaxy?, ApJ, 557, L39, doi: 10.1086/323075

Belokurov V., Erkal D., Evans N. W., Koposov S. E., Deason A. J. 2018, Co-formation of the disc and the stellar halo, MNRAS, 478, 611, doi: 10.1093/mnras/sty982

Belokurov V., Kravtsov A. 2022, From dawn till disc: Milky Way's turbulent youth revealed by the APOGEE+Gaia data, MNRAS, 514, 689, doi: 10.1093/mnras/stac1267

Bensby T., Feltzing S., Lundström I. 2003a, Elemental abundance trends in the Galactic thin and thick disks as traced by nearby F and G dwarf stars, A&A, 410, 527, doi: 10.1051/0004-6361:20031213

Bensby T., Feltzing S., Lundström I. 2003b, Elemental abundance trends in the Galactic thin and thick disks as traced by nearby F and G dwarf stars, A&A, 410, 527, doi: 10.1051/0004-6361:20031213

Bensby T., Feltzing S., Oey M. S. 2014, Exploring the Milky Way stellar disk. A detailed elemental abundance study of 714 F and G dwarf stars in the solar neighbourhood, A&A, 562, A71, doi: 10.1051/0004-6361/201322631

Bensby T., Yee J. C., Feltzing S., Johnson J. A., Gould A., Cohen J. G., Asplund M., Meléndez J., Lucatello S., Han C., Thompson I., Gal-Yam A., Udalski A., Bennett

D. P., Bond I. A., Kohei W., Sumi T., Suzuki D., Suzuki K., Takino S., Tristram P., Yamai N., Yonehara A. 2013, Chemical evolution of the Galactic bulge as traced by microlensed dwarf and subgiant stars. V. Evidence for a wide age distribution and a complex MDF, A&A, 549, A147, doi: 10.1051/0004-6361/201220678

Bergstra J., Bengio Y. 2012, Random Search for Hyper-Parameter Optimization, Journal of Machine Learning Research, 13, 281. http://jmlr.org/papers/v13/bergstra12a.html

Bertelli G., Girardi L., Marigo P., Nasi E. 2008, Scaled solar tracks and isochrones in a large region of the Z-Y plane. I. From the ZAMS to the TP-AGB end for 0.15-2.5 $\{M\}_{\odot}$ stars, A&A, 484, 815, doi: 10.1051/0004-6361:20079165

Bertin E., Arnouts S. 1996, SExtractor: Software for source extraction., \aaps, 117, 393

Best W. M. J., Liu M. C., Magnier E. A., Dupuy T. J. 2021, A Volume-limited Sample of Ultracool Dwarfs. I. Construction, Space Density, and a Gap in the L/T Transition, 161, 42, doi: 10.3847/1538-3881/abc893

Best W. M. J., Magnier E. A., Liu M. C., Aller K. M., Zhang Z., Burgett W. S., Chambers K. C., Draper P., Flewelling H., Kaiser N., Kudritzki R. P., Metcalfe N., Tonry J. L., Wainscoat R. J., Waters C. 2018, Photometry and Proper Motions of M, L, and T Dwarfs from the Pan-STARRS1 3π Survey, ApJS, 234, 1, doi: 10.3847/1538-4365/aa9982

Bhattacharya S., Arnaboldi M., Gerhard O., Caldwell N., Kobayashi C., Hammer F., Yang Y., Freeman K. C., Hartke J., McConnachie A. 2023, The Andromeda Galaxy's Last Major Merger: Constraints from the survey of Planetary Nebulae, arXiv e-prints, arXiv:2305.02761, doi: 10.48550/arXiv.2305.02761

Binney J., Gerhard O. E., Stark A. A., Bally J., Uchida K. I. 1991, Understanding the kinematics of Galactic Centre gas., MNRAS, 252, 210, doi: 10.1093/mnras/252.2.210

Binney J., Tremaine S. 2008, Galactic Dynamics: Second Edition

Binney J., Vasiliev E. 2023, Self-consistent models of our Galaxy, MNRAS, 520, 1832, doi: 10.1093/mnras/stad094

Bird J. C., Kazantzidis S., Weinberg D. H., Guedes J., Callegari S., Mayer L., Madau P. 2013, Inside out and Upside down: Tracing the Assembly of a Simulated Disk Galaxy Using Mono-age Stellar Populations, ApJ, 773, 43, doi: 10.1088/0004-637X/773/1/43

Blake C. H., Charbonneau D., White R. J. 2010, The NIRSPEC Ultracool Dwarf Radial Velocity Survey, ApJ, 723, 684, doi: 10.1088/0004-637X/723/1/684

Blancato K., Ness M., Huber D., Lu Y., Angus R. 2020, Data-driven derivation of stellar properties from photometric time series data using convolutional neural networks, arXiv e-prints, arXiv:2005.09682. https://arxiv.org/abs/2005.09682

Bland-Hawthorn J., Gerhard O. 2016, The Galaxy in Context: Structural, Kinematic, and Integrated Properties, ARA&A, 54, 529, doi: 10.1146/annurev-astro-081915-023441

Blitz L., Spergel D. N. 1991, Direct Evidence for a Bar at the Galactic Center, ApJ, 379, 631, doi: 10.1086/170535

Bloom J. S., Richards J. W., Nugent P. E., Quimby R. M., Kasliwal M. M., Starr D. L., Poznanski D., Ofek E. O., Cenko S. B., Butler N. R., Kulkarni S. R., Gal-Yam A., Law N. 2012, Automating Discovery and Classification of Transients and Variable Stars in the Synoptic Survey Era, PASP, 124, 1175, doi: 10.1086/668468

Blumenthal G. R., Faber S. M., Primack J. R., Rees M. J. 1984, Formation of galaxies and large-scale structure with cold dark matter., Nature, 311, 517, doi: 10.1038/311517a0

Bochanski J., Hawley S., Covey K., West A., Reid I., Golimowski D., Ivezić Ž. 2010,

The Luminosity and Mass Functions of Low-mass Stars in the Galactic Disk. II. The Field, \aj, 139, 2679, doi: 10.1088/0004-6256/139/6/2679

Bochanski J. J., West A. A., Hawley S. L., Covey K. R. 2007, Low-Mass Dwarf Template Spectra from the Sloan Digital Sky Survey, AJ, 133, 531, doi: 10.1086/510240

Bode P., Ostriker J. P., Turok N. 2001, Halo Formation in Warm Dark Matter Models, ApJ, 556, 93, doi: 10.1086/321541

Böker T., Laine S., van der Marel R. P., Sarzi M., Rix H.-W., Ho L. C., Shields J. C. 2002, A Hubble Space Telescope Census of Nuclear Star Clusters in Late-Type Spiral Galaxies. I. Observations and Image Analysis, AJ, 123, 1389, doi: 10.1086/339025

Bonaca A., Hogg D. W. 2018, The Information Content in Cold Stellar Streams, ApJ, 867, 101, doi: 10.3847/1538-4357/aae4da

Bonaca A., Hogg D. W., Price-Whelan A. M., Conroy C. 2019, The Spur and the Gap in GD-1: Dynamical Evidence for a Dark Substructure in the Milky Way Halo, ApJ, 880, 38, doi: 10.3847/1538-4357/ab2873

Bonaca A., Pearson S., Price-Whelan A. M., Dey A., Geha M., Kallivayalil N., Moustakas J., Muñoz R., Myers A. D., Schlegel D. J., Valdes F. 2020, Variations in the Width, Density, and Direction of the Palomar 5 Tidal Tails, ApJ, 889, 70, doi: 10.3847/1538-4357/ab5afe

Bond N. A., Ivezić Ž., Sesar B., Jurić M., Munn J. A., Kowalski A., Loebman S., Roškar R., Beers T. C., Dalcanton J., Rockosi C. M., Yanny B., Newberg H. J., Allende Prieto C., Wilhelm R., Lee Y. S., Sivarani T., Majewski S. R., Norris J. E., Bailer-Jones C. A. L., Re Fiorentin P., Schlegel D., Uomoto A., Lupton R. H., Knapp G. R., Gunn J. E., Covey K. R., Allyn Smith J., Miknaitis G., Doi M., Tanaka M., Fukugita M.,

Kent S., Finkbeiner D., Quinn T. R., Hawley S., Anderson S., Kiuchi F., Chen A., Bushong J., Sohi H., Haggard D., Kimball A., McGurk R., Barentine J., Brewington H., Harvanek M., Kleinman S., Krzesinski J., Long D., Nitta A., Snedden S., Lee B., Pier J. R., Harris H., Brinkmann J., Schneider D. P. 2010, The Milky Way Tomography with SDSS. III. Stellar Kinematics, ApJ, 716, 1, doi: 10.1088/0004-637X/716/1/1

Borucki W. J., Koch D., Basri G., Batalha N., Brown T., Caldwell D., Caldwell J., Christensen-Dalsgaard J., Cochran W. D., DeVore E., Dunham E. W., Dupree A. K., Gautier T. N., Geary J. C., Gilliland R., Gould A., Howell S. B., Jenkins J. M., Kondo Y., Latham D. W., Marcy G. W., Meibom S., Kjeldsen H., Lissauer J. J., Monet D. G., Morrison D., Sasselov D., Tarter J., Boss A., Brownlee D., Owen T., Buzasi D., Charbonneau D., Doyle L., Fortney J., Ford E. B., Holman M. J., Seager S., Steffen J. H., Welsh W. F., Rowe J., Anderson H., Buchhave L., Ciardi D., Walkowicz L., Sherry W., Horch E., Isaacson H., Everett M. E., Fischer D., Torres G., Johnson J. A., Endl M., MacQueen P., Bryson S. T., Dotson J., Haas M., Kolodziejczak J., Van Cleve J., Chandrasekaran H., Twicken J. D., Quintana E. V., Clarke B. D., Allen C., Li J., Wu H., Tenenbaum P., Verner E., Bruhweiler F., Barnes J., Prsa A. 2010, Kepler Planet-Detection Mission: Introduction and First Results, Science, 327, 977, doi: 10.1126/science.1185402

Bose S., Hellwing W. A., Frenk C. S., Jenkins A., Lovell M. R., Helly J. C., Li B., Gonzalez-Perez V., Gao L. 2017, Substructure and galaxy formation in the Copernicus Complexio warm dark matter simulations, MNRAS, 464, 4520, doi: 10.1093/mnras/stw2686

Boubert D., Guillochon J., Hawkins K., Ginsburg I., Evans N. W., Strader J. 2018, Revisiting hypervelocity stars after Gaia DR2, MNRAS, 479, 2789, doi: 10.1093/mnras/sty1601

Bouy H., Brandner W., Martín E. L., Delfosse X., Allard F., Basri G. 2003, Multiplicity of Nearby Free-Floating Ultracool Dwarfs: A Hubble Space Telescope WFPC2 Search for Companions, AJ, 126, 1526, doi: 10.1086/377343

Bovy J. 2016, Detecting the Disruption of Dark-Matter Halos with Stellar Streams, Phys. Rev. Lett., 116, 121301, doi: 10.1103/PhysRevLett.116.121301

Bovy J. 2017, Stellar inventory of the solar neighbourhood using Gaia DR1, MNRAS, 470, 1360, doi: 10.1093/mnras/stx1277

Bovy J., Erkal D., Sanders J. L. 2017, Linear perturbation theory for tidal streams and the small-scale CDM power spectrum, MNRAS, 466, 628, doi: 10.1093/mnras/stw3067

Bovy J., Rix H.-W. 2013, A Direct Dynamical Measurement of the Milky Way's Disk Surface Density Profile, Disk Scale Length, and Dark Matter Profile at 4 kpc <∼R <∼9 kpc, ApJ, 779, 115, doi: 10.1088/0004-637X/779/2/115

Bovy J., Rix H.-W., Hogg D. W. 2012a, The Milky Way Has No Distinct Thick Disk, ApJ, 751, 131, doi: 10.1088/0004-637X/751/2/131

Bovy J., Rix H.-W., Schlafly E. F., Nidever D. L., Holtzman J. A., Shetrone M., Beers T. C. 2016, The Stellar Population Structure of the Galactic Disk, ApJ, 823, 30, doi: 10.3847/0004-637X/823/1/30

Bovy J., Allende Prieto C., Beers T. C., Bizyaev D., da Costa L. N., Cunha K., Ebelke G. L., Eisenstein D. J., Frinchaboy P. M., García Pérez A. E., Girardi L., Hearty F. R., Hogg D. W., Holtzman J., Maia M. A. G., Majewski S. R., Malanushenko E., Malanushenko V., Mészáros S., Nidever D. L., O'Connell R. W., O'Donnell C., Oravetz A., Pan K., Rocha-Pinto H. J., Schiavon R. P., Schneider D. P., Schultheis M., Skrutskie M., Smith V. V., Weinberg D. H., Wilson J. C., Zasowski G. 2012b, The

Milky Way's Circular-velocity Curve between 4 and 14 kpc from APOGEE data, ApJ, 759, 131, doi: 10.1088/0004-637X/759/2/131

Brammer G., van Dokkum P., Franx M., Fumagalli M., Patel S., Rix H.-W., Skelton R., Kriek M., Nelson E., Schmidt K., Bezanson R., da Cunha E., Erb D., Fan X., Förster Schreiber N., Illingworth G., Labbé I., Leja J., Lundgren B., Magee D., Marchesini D., McCarthy P., Momcheva I., Muzzin A., Quadri R., Steidel C., Tal T., Wake D., Whitaker K., Williams A. 2012, 3D-HST: A Wide-field Grism Spectroscopic Survey with the Hubble Space Telescope, \apjs, 200, 13, doi: 10.1088/0067-0049/200/2/13

Breiman L. 1996, Bagging predictors, Machine Learning, 24, 123, doi: 10.1007/BF00058655

Breiman L. 2001, Random Forests, Machine Learning, 45, 5, doi: 10.1023/A:1010933404324

Bressan A., Marigo P., Girardi L., Salasnich B., Dal Cero C., Rubele S., Nanni A. 2012, PARSEC: stellar tracks and isochrones with the PAdova and TRieste Stellar Evolution Code, MNRAS, 427, 127, doi: 10.1111/j.1365-2966.2012.21948.x

Brink H., Richards J. W., Poznanski D., Bloom J. S., Rice J., Negahban S., Wainwright M. 2013, Using machine learning for discovery in synoptic survey imaging data, MNRAS, 435, 1047, doi: 10.1093/mnras/stt1306

Bromm V. 2013, Formation of the first stars, Reports on Progress in Physics, 76, 112901, doi: 10.1088/0034-4885/76/11/112901

Brown T. M., Ferguson H. C., Smith E., Kimble R. A., Sweigart A. V., Renzini A., Rich R. M., VandenBerg D. A. 2003, Evidence of a Significant Intermediate-Age Population in the M31 Halo from Main-Sequence Photometry, ApJ, 592, L17, doi: 10.1086/376935

Buck T., Obreja A., Macciò A. V., Minchev I., Dutton A. A., Ostriker J. P. 2020, NIHAO-UHD: the properties of MW-like stellar discs in high-resolution cosmological simulations, MNRAS, 491, 3461, doi: 10.1093/mnras/stz3241

Buder S., Sharma S., Kos J., Amarsi A. M., Nordlander T., Lind K., Martell S. L., Asplund M., Bland-Hawthorn J., Casey A. R., de Silva G. M., D'Orazi V., Freeman K. C., Hayden M. R., Lewis G. F., Lin J., Schlesinger K. J., Simpson J. D., Stello D., Zucker D. B., Zwitter T., Beeson K. L., Buck T., Casagrande L., Clark J. T., Čotar K., da Costa G. S., de Grijs R., Feuillet D., Horner J., Kafle P. R., Khanna S., Kobayashi C., Liu F., Montet B. T., Nandakumar G., Nataf D. M., Ness M. K., Spina L., Tepper-García T., Ting Y.-S., Traven G., Vogrinčič R., Wittenmyer R. A., Wyse R. F. G., Žerjal M., Galah Collaboration. 2021, The GALAH+ survey: Third data release, MNRAS, 506, 150, doi: 10.1093/mnras/stab1242

Bullock J. S., Boylan-Kolchin M. 2017, Small-Scale Challenges to the ΛCDM Paradigm, ARA&A, 55, 343, doi: 10.1146/annurev-astro-091916-055313

Bullock J. S., Johnston K. V. 2005, Tracing Galaxy Formation with Stellar Halos. I. Methods, ApJ, 635, 931, doi: 10.1086/497422

Bullock J. S., Kolatt T. S., Sigad Y., Somerville R. S., Kravtsov A. V., Klypin A. A., Primack J. R., Dekel A. 2001, Profiles of dark haloes: evolution, scatter and environment, MNRAS, 321, 559, doi: 10.1046/j.1365-8711.2001.04068.x

Bullock J. S., Kravtsov A. V., Weinberg D. H. 2000, Reionization and the Abundance of Galactic Satellites, ApJ, 539, 517, doi: 10.1086/309279

Burgasser A. 2004, T Dwarfs and the Substellar Mass Function. I. Monte Carlo Simulations, \apjs, 155, 191, doi: 10.1086/424386

Burgasser A., Blake C. 2009, An Age Constraint for the Very Low Mass Stellar/Brown Dwarf Binary 2MASS J03202839{\ndash}0446358AB, \aj, 137, 4621, doi: 10.1088/0004-6256/137/6/4621

Burgasser A., Looper D., Kirkpatrick J., Liu M. 2007, Discovery of a High Proper Motion L Dwarf Binary: 2MASS J15200224-4422419AB, \apj, 658, 557, doi: 10.1086/511518

Burgasser A., Kirkpatrick J., Burrows A., Liebert J., Reid I., Gizis J., McGovern M., Prato L., McLean I. 2003, The First Substellar Subdwarf? Discovery of a Metal-poor L Dwarf with Halo Kinematics, \apj, 592, 1186, doi: 10.1086/375813

Burgasser A. J. 2007, Binaries and the L Dwarf/T Dwarf Transition, ApJ, 659, 655, doi: 10.1086/511027

Burgasser A. J. 2014, in Astronomical Society of India Conference Series, Vol. 11, Astronomical Society of India Conference Series, 7–16. https://arxiv.org/abs/1406.4887

Burgasser A. J., Cruz K. L., Kirkpatrick J. D. 2007, Optical Spectroscopy of 2MASS Color-selected Ultracool Subdwarfs, ApJ, 657, 494, doi: 10.1086/510148

Burgasser A. J., Geballe T. R., Leggett S. K., Kirkpatrick J. D., Golimowski D. A. 2006a, A Unified Near-Infrared Spectral Classification Scheme for T Dwarfs, ApJ, 637, 1067, doi: 10.1086/498563

Burgasser A. J., Kirkpatrick J. D., Cruz K. L., Reid I. N., Leggett S. K., Liebert J., Burrows A., Brown M. E. 2006b, Hubble Space Telescope NICMOS Observations of T Dwarfs: Brown Dwarf Multiplicity and New Probes of the L/T Transition, ApJS, 166, 585, doi: 10.1086/506327

Burgasser A. J., Kirkpatrick J. D., Reid I. N., Brown M. E., Miskey C. L., Gizis J. E. 2003, Binarity in Brown Dwarfs: T Dwarf Binaries Discovered with the Hubble Space Telescope Wide Field Planetary Camera 2, ApJ, 586, 512, doi: 10.1086/346263

Burgasser A. J., Marley M. S., Ackerman A. S., Saumon D., Lodders K., Dahn C. C., Harris H. C., Kirkpatrick J. D. 2002, Evidence of Cloud Disruption in the L/T Dwarf Transition, ApJ, 571, L151, doi: 10.1086/341343

Burgasser A. J., McElwain M. W., Kirkpatrick J. D., Cruz K. L., Tinney C. G., Reid I. N. 2004, The 2MASS Wide-Field T Dwarf Search. III. Seven New T Dwarfs and Other Cool Dwarf Discoveries, AJ, 127, 2856, doi: 10.1086/383549

Burgasser A. J., Logsdon S. E., Gagné J., Bochanski J. J., Faherty J. K., West A. A., Mamajek E. E., Schmidt S. J., Cruz K. L. 2015, The Brown Dwarf Kinematics Project (BDKP). IV. Radial Velocities of 85 Late-M and L Dwarfs with MagE, ApJS, 220, 18, doi: 10.1088/0067-0049/220/1/18

Burningham B., Cardoso C., Smith L., Leggett S., Smart R., Mann A., Dhital S., Lucas P., Tinney C., Pinfield D., Zhang Z., Morley C., Saumon D., Aller K., Littlefair S., Homeier D., Lodieu N., Deacon N., Marley M., van Spaandonk L., Baker D., Allard F., Andrei A., Canty J., Clarke J., Day-Jones A., Dupuy T., Fortney J., Gomes J., Ishii M., Jones H., Liu M., Magazzú A., Marocco F., Murray D., Rojas-Ayala B., Tamura M. 2013, 76 T dwarfs from the UKIDSS LAS: benchmarks, kinematics and an updated space density, \mnras, 433, 457, doi: 10.1093/mnras/stt740

Burrows A., Hubbard W. B., Lunine J. I., Liebert J. 2001, The theory of brown dwarfs and extrasolar giant planets, Reviews of Modern Physics, 73, 719, doi: 10.1103/RevModPhys.73.719

Burrows A., Sudarsky D., Hubeny I. 2006, L and T Dwarf Models and the L to T Transition, ApJ, 640, 1063, doi: 10.1086/500293

Burrows A., Marley M., Hubbard W. B., Lunine J. I., Guillot T., Saumon D., Freedman R., Sudarsky D., Sharp C. 1997, A Nongray Theory of Extrasolar Giant Planets and Brown Dwarfs, ApJ, 491, 856, doi: 10.1086/305002

Caiazzo I., Heyl J. S., Richer H., Kalirai J. 2017, Globular cluster absolute ages from cooling brown dwarfs, ArXiv e-prints. https://arxiv.org/abs/1702.00091

Caldwell N., Romanowsky A. J. 2016, Star Clusters in M31. VII. Global Kinematics and Metallicity Subpopulations of the Globular Clusters, ApJ, 824, 42, doi: 10.3847/0004-637X/824/1/42

Carlberg R. G. 2012, Dark Matter Sub-halo Counts via Star Stream Crossings, ApJ, 748, 20, doi: 10.1088/0004-637X/748/1/20

Carneiro T., Medeiros Da NóBrega R. V., Nepomuceno T., Bian G., De Albuquerque V. H. C., Filho P. P. R. 2018, Performance Analysis of Google Colaboratory as a Tool for Accelerating Deep Learning Applications, IEEE Access, 6, 61677

Carnero Rosell A., Santiago B., dal Ponte M., Burningham B., da Costa L. N., James D. J., Marshall J. L., McMahon R. G., Bechtol K., De Paris L., Li T., Pieres A., García-Bellido J., Abbott T. M. C., Annis J., Avila S., Bernstein G. M., Brooks D., Burke D. L., Carrasco Kind M., Carretero J., De Vicente J., Drlica-Wagner A., Fosalba P., Frieman J., Gaztanaga E., Gruendl R. A., Gschwend J., Gutierrez G., Hollowood D. L., Maia M. A. G., Menanteau F., Miquel R., Plazas A. A., Roodman A., Sanchez E., Scarpine V., Schindler R., Serrano S., Sevilla-Noarbe I., Smith M., Sobreira F., Soares-Santos M., Suchyta E., Swanson M. E. C., Tarle G., Vikram V., Walker A. R., DES Collaboration. 2019, Brown dwarf census with the Dark Energy

Survey year 3 data and the thin disc scale height of early L types, MNRAS, 489, 5301, doi: 10.1093/mnras/stz2398

Carney B. W., Seitzer P. 1993, Optical detection of the Galaxy's Southern Stellar Warp and Outer Disk, AJ, 105, 2127, doi: 10.1086/116591

Carollo D., Beers T. C., Lee Y. S., Chiba M., Norris J. E., Wilhelm R., Sivarani T., Marsteller B., Munn J. A., Bailer-Jones C. A. L., Fiorentin P. R., York D. G. 2007, Two stellar components in the halo of the Milky Way, Nature, 450, 1020, doi: 10.1038/nature06460

Carollo D., Beers T. C., Chiba M., Norris J. E., Freeman K. C., Lee Y. S., Ivezić Ž., Rockosi C. M., Yanny B. 2010, Structure and Kinematics of the Stellar Halos and Thick Disks of the Milky Way Based on Calibration Stars from Sloan Digital Sky Survey DR7, ApJ, 712, 692, doi: 10.1088/0004-637X/712/1/692

Caruana R., Niculescu-Mizil A. 2006, in Proceedings of the 23rd International Conference on Machine Learning, ICML '06 (New York, NY, USA: Association for Computing Machinery), 161–168, doi: 10.1145/1143844.1143865

Chabrier G. 2005, in Astrophysics and Space Science Library, Vol. 327, The Initial Mass Function 50 Years Later, ed. E. Corbelli, F. Palla, H. Zinnecker, 41, doi: 10.1007/978-1-4020-3407-7_5

Chabrier G., Baraffe I. 2000, Theory of Low-Mass Stars and Substellar Objects, \araa, 38, 337, doi: 10.1146/annurev.astro.38.1.337

Chabrier G., Mera D. 1997, Determination of the globular cluster and halo stellar mass functions and stellar and brown dwarf densities, A&A, 328, 83. https://arxiv.org/abs/astro-ph/9705065

Chamberlain K., Price-Whelan A. M., Besla G., Cunningham E. C., Garavito-Camargo N., Peñarrubia J., Petersen M. S. 2022, Implications of the Milky Way travel velocity for dynamical mass estimates of the Local Group, arXiv e-prints, arXiv:2204.07173. https://arxiv.org/abs/2204.07173

Chambers K. C., Magnier E. A., Metcalfe N., Flewelling H. A., Huber M. E., Waters C. Z., Denneau L., Draper P. W., Farrow D., Finkbeiner D. P., Holmberg C., Koppenhoefer J., Price P. A., Rest A., Saglia R. P., Schlafly E. F., Smartt S. J., Sweeney W., Wainscoat R. J., Burgett W. S., Chastel S., Grav T., Heasley J. N., Hodapp K. W., Jedicke R., Kaiser N., Kudritzki R. P., Luppino G. A., Lupton R. H., Monet D. G., Morgan J. S., Onaka P. M., Shiao B., Stubbs C. W., Tonry J. L., White R., Bañados E., Bell E. F., Bender R., Bernard E. J., Boegner M., Boffi F., Botticella M. T., Calamida A., Casertano S., Chen W. P., Chen X., Cole S., Deacon N., Frenk C., Fitzsimmons A., Gezari S., Gibbs V., Goessl C., Goggia T., Gourgue R., Goldman B., Grant P., Grebel E. K., Hambly N. C., Hasinger G., Heavens A. F., Heckman T. M., Henderson R., Henning T., Holman M., Hopp U., Ip W. H., Isani S., Jackson M., Keyes C. D., Koekemoer A. M., Kotak R., Le D., Liska D., Long K. S., Lucey J. R., Liu M., Martin N. F., Masci G., McLean B., Mindel E., Misra P., Morganson E., Murphy D. N. A., Obaika A., Narayan G., Nieto-Santisteban M. A., Norberg P., Peacock J. A., Pier E. A., Postman M., Primak N., Rae C., Rai A., Riess A., Riffeser A., Rix H. W., Röser S., Russel R., Rutz L., Schilbach E., Schultz A. S. B., Scolnic D., Strolger L., Szalay A., Seitz S., Small E., Smith K. W., Soderblom D. R., Taylor P., Thomson R., Taylor A. N., Thakar A. R., Thiel J., Thilker D., Unger D., Urata Y., Valenti J., Wagner J., Walder T., Walter F., Watters S. P., Werner S., Wood-Vasey W. M., Wyse R. 2016, The Pan-STARRS1 Surveys, arXiv e-prints, arXiv:1612.05560. https://arxiv.org/abs/1612.05560

Chapman S. C., Ibata R., Lewis G. F., Ferguson A. M. N., Irwin M., McConnachie A., Tanvir N. 2006, A Kinematically Selected, Metal-poor Stellar Halo in the Outskirts of M31, ApJ, 653, 255, doi: 10.1086/508599

Chatzopoulos S., Fritz T. K., Gerhard O., Gillessen S., Wegg C., Genzel R., Pfuhl O. 2015, The old nuclear star cluster in the Milky Way: dynamics, mass, statistical parallax, and black hole mass, MNRAS, 447, 948, doi: 10.1093/mnras/stu2452

Chemin L., Carignan C., Foster T. 2009, H I Kinematics and Dynamics of Messier 31, ApJ, 705, 1395, doi: 10.1088/0004-637X/705/2/1395

Chen B., Stoughton C., Smith J. A., Uomoto A., Pier J. R., Yanny B., Ivezić Ž., York D. G., Anderson J. E., Annis J., Brinkmann J., Csabai I., Fukugita M., Hindsley R., Lupton R., Munn J. A., SDSS Collaboration. 2001, Stellar Population Studies with the SDSS. I. The Vertical Distribution of Stars in the Milky Way, ApJ, 553, 184, doi: 10.1086/320647

Chinchor N. 1992, in Proceedings of the 4th Conference on Message Understanding, MUC4 '92 (USA: Association for Computational Linguistics), 22–29, doi: 10.3115/1072064.1072067

Chollet F., et al. 2015, Keras, https://github.com/fchollet/keras, GitHub

Chrobáková Ž., Nagy R., López-Corredoira M. 2022, Warp and flare of the Galactic disc revealed with supergiants by Gaia EDR3, A&A, 664, A58, doi: 10.1051/0004-6361/202243296

Clarke A. O., Scaife A. M. M., Greenhalgh R., Griguta V. 2020, Identifying galaxies, quasars, and stars with machine learning: A new catalogue of classifications for 111 million SDSS sources without spectra, A&A, 639, A84, doi: 10.1051/0004-6361/201936770

Cohen M., Walker R. G., Barlow M. J., Deacon J. R. 1992, Spectral Irradiance Calibration in the Infrared. I. Ground-Based and IRAS Broadband Calibrations, AJ, 104, 1650, doi: 10.1086/116349

Combes F., Debbasch F., Friedli D., Pfenniger D. 1990, Box and peanut shapes generated by stellar bars., A&A, 233, 82

Combes F., Sanders R. H. 1981, Formation and properties of persisting stellar bars., A&A, 96, 164

Conroy C., Bonaca A., Cargile P., Johnson B. D., Caldwell N., Naidu R. P., Zaritsky D., Fabricant D., Moran S., Rhee J., Szentgyorgyi A., Berlind P., Calkins M. L., Kattner S., Ly C. 2019, Mapping the Stellar Halo with the H3 Spectroscopic Survey, ApJ, 883, 107, doi: 10.3847/1538-4357/ab38b8

Conroy C., Weinberg D. H., Naidu R. P., Buck T., Johnson J. W., Cargile P., Bonaca A., Caldwell N., Chandra V., Han J. J., Johnson B. D., Speagle J. S., Ting Y.-S., Woody T., Zaritsky D. 2022, Birth of the Galactic Disk Revealed by the H3 Survey, arXiv e-prints, arXiv:2204.02989, doi: 10.48550/arXiv.2204.02989

Contardo G., Hogg D. W., Hunt J. A. S., Peek J. E. G., Chen Y.-C. 2022, The emptiness inside: Finding gaps, valleys, and lacunae with geometric data analysis, arXiv e-prints, arXiv:2201.10674. https://arxiv.org/abs/2201.10674

Corbelli E., Lorenzoni S., Walterbos R., Braun R., Thilker D. 2010, A wide-field H I mosaic of Messier 31. II. The disk warp, rotation, and the dark matter halo, A&A, 511, A89, doi: 10.1051/0004-6361/200913297

Cruz K., Kirkpatrick J., Burgasser A., Looper D., Mohanty S., Prato L., Faherty J., Solomon A. 2007a, A New Population of Young Brown Dwarfs, ArXiv Astrophysics e-prints

Cruz K., Reid I., Kirkpatrick J., Burgasser A., Liebert J., Solomon A., Schmidt S., Allen P., Hawley S., Covey K. 2007b, Meeting the Cool Neighbors. IX. The Luminosity Function of M7-L8 Ultracool Dwarfs in the Field, \aj, 133, 439, doi: 10.1086/510132

Cruz K. L., Reid I. N., Liebert J., Kirkpatrick J. D., Lowrance P. J. 2003, Meeting the Cool Neighbors. V. A 2MASS-Selected Sample of Ultracool Dwarfs, AJ, 126, 2421, doi: 10.1086/378607

Cushing M., Rayner J., Vacca W. 2005, An Infrared Spectroscopic Sequence of M, L, and T Dwarfs, \apj, 623, 1115, doi: 10.1086/428040

Cushing M., Tokunaga A., Kobayashi N. 2000, H- and K-Band Spectra of Brown Dwarf Candidates in the Core of the {ρ} Ophiuchi Molecular Cloud Complex, \aj, 119, 3019, doi: 10.1086/301384

Cushing M. C., Roellig T. L., Marley M. S., Saumon D., Leggett S. K., Kirkpatrick J. D., Wilson J. C., Sloan G. C., Mainzer A. K., Van Cleve J. E., Houck J. R. 2006, A Spitzer Infrared Spectrograph Spectral Sequence of M, L, and T Dwarfs, ApJ, 648, 614, doi: 10.1086/505637

Cushing M. C., Kirkpatrick J. D., Gelino C. R., Griffith R. L., Skrutskie M. F., Mainzer A., Marsh K. A., Beichman C. A., Burgasser A. J., Prato L. A., Simcoe R. A., Marley M. S., Saumon D., Freedman R. S., Eisenhardt P. R., Wright E. L. 2011, The Discovery of Y Dwarfs using Data from the Wide-field Infrared Survey Explorer (WISE), ApJ, 743, 50, doi: 10.1088/0004-637X/743/1/50

Dalal N., Kochanek C. S. 2002, Direct Detection of Cold Dark Matter Substructure, ApJ, 572, 25, doi: 10.1086/340303

Dalcanton J. J., Williams B. F., Lang D., Lauer T. R., Kalirai J. S., Seth A. C., Dolphin A., Rosenfield P., Weisz D. R., Bell E. F., Bianchi L. C., Boyer M. L., Caldwell N.,

Dong H., Dorman C. E., Gilbert K. M., Girardi L., Gogarten S. M., Gordon K. D., Guhathakurta P., Hodge P. W., Holtzman J. A., Johnson L. C., Larsen S. S., Lewis A., Melbourne J. L., Olsen K. A. G., Rix H.-W., Rosema K., Saha A., Sarajedini A., Skillman E. D., Stanek K. Z. 2012, The Panchromatic Hubble Andromeda Treasury, ApJS, 200, 18, doi: 10.1088/0067-0049/200/2/18

Dalcanton J. J., Fouesneau M., Hogg D. W., Lang D., Leroy A. K., Gordon K. D., Sandstrom K., Weisz D. R., Williams B. F., Bell E. F., Dong H., Gilbert K. M., Gouliermis D. A., Guhathakurta P., Lauer T. R., Schruba A., Seth A. C., Skillman E. D. 2015, The Panchromatic Hubble Andromeda Treasury. VIII. A Wide-area, High-resolution Map of Dust Extinction in M31, ApJ, 814, 3, doi: 10.1088/0004-637X/814/1/3

Davis M., Guhathakurta P., Konidaris N. P., Newman J. A., Ashby M. L. N., Biggs A. D., Barmby P., Bundy K., Chapman S. C., Coil A. L., Conselice C. J., Cooper M. C., Croton D. J., Eisenhardt P. R. M., Ellis R. S., Faber S. M., Fang T., Fazio G. G., Georgakakis A., Gerke B. F., Goss W. M., Gwyn S., Harker J., Hopkins A. M., Huang J.-S., Ivison R. J., Kassin S. A., Kirby E. N., Koekemoer A. M., Koo D. C., Laird E. S., Floc'h E. L., Lin L., Lotz J. M., Marshall P. J., Martin D. C., Metevier A. J., Moustakas L. A., Nandra K., Noeske K. G., Papovich C., Phillips A. C., Rich R. M., Rieke G. H., Rigopoulou D., Salim S., Schiminovich D., Simard L., Smail I., Small T. A., Weiner B. J., Willmer C. N. A., Willner S. P., Wilson G., Wright E. L., Yan R. 2007, The All-Wavelength Extended Groth Strip International Survey (AEGIS) Data Sets, The Astrophysical Journal Letters, 660, L1. http://stacks.iop.org/1538-4357/660/i=1/a=L1

de Boer T. J. L., Belokurov V., Koposov S. E., Ferrarese L., Erkal D., Côté P., Navarro J. F. 2018, A deeper look at the GD1 stream: density variations and wiggles, MNRAS, 477, 1893, doi: 10.1093/mnras/sty677

de Boer T. J. L., Erkal D., Gieles M. 2020, A closer look at the spur, blob, wiggle, and gaps in GD-1, MNRAS, 494, 5315, doi: 10.1093/mnras/staa917

De Silva G. M., Freeman K. C., Bland-Hawthorn J., Martell S., de Boer E. W., Asplund M., Keller S., Sharma S., Zucker D. B., Zwitter T., Anguiano B., Bacigalupo C., Bayliss D., Beavis M. A., Bergemann M., Campbell S., Cannon R., Carollo D., Casagrande L., Casey A. R., Da Costa G., D'Orazi V., Dotter A., Duong L., Heger A., Ireland M. J., Kafle P. R., Kos J., Lattanzio J., Lewis G. F., Lin J., Lind K., Munari U., Nataf D. M., O'Toole S., Parker Q., Reid W., Schlesinger K. J., Sheinis A., Simpson J. D., Stello D., Ting Y. S., Traven G., Watson F., Wittenmyer R., Yong D., Žerjal M. 2015, The GALAH survey: scientific motivation, MNRAS, 449, 2604, doi: 10.1093/mnras/stv327

de Vaucouleurs G., Pence W. D. 1978, An outsider's view of the Galaxy: photometric parameters, scale lengths, and absolute magnitudes of the spheroidal and disk components of our Galaxy., AJ, 83, 1163, doi: 10.1086/112305

Deason A. J., Belokurov V., Koposov S. E., Lancaster L. 2018, Apocenter Pile-up: Origin of the Stellar Halo Density Break, ApJ, 862, L1, doi: 10.3847/2041-8213/aad0ee

Dey A., Najita J. R., Koposov S. E., Josephy-Zack J., Maxemin G., Bell E. F., Poppett C., Patel E., Beraldo e Silva L., Raichoor A., Schlegel D., Lang D., Meisner A., Myers A. D., Aguilar J., Ahlen S., Allende Prieto C., Brooks D., Cooper A. P., Dawson K. S., de la Macorra A., Doel P., Font-Ribera A., Garcia-Bellido J., Gontcho S. G. A., Guy J., Honscheid K., Kehoe R., Kisner T., Kremin A., Landriau M., Le Guillou L., Levi M. E., Li T. S., Martini P., Miquel R., Moustakas J., Nie J., Palanque-Delabrouille N., Prada F., Schlafly E. F., Sharples R. M., Tarle G., Ting Y.-S., Tyas L., Valluri M., Wechsler R. H., Zou H. 2022, DESI Observations of the Andromeda Galaxy: Revealing the Immigration History of our Nearest Neighbor, arXiv e-prints, arXiv:2208.11683, doi: 10.48550/arXiv.2208.11683

Doke Y., Hattori K. 2022, Probability of forming gaps in the GD-1 stream by close encounters of globular clusters, arXiv e-prints, arXiv:2203.15481. https://arxiv.org/abs/2203.15481

D'Onghia E., Vogelsberger M., Hernquist L. 2013, Self-perpetuating Spiral Arms in Disk Galaxies, ApJ, 766, 34, doi: 10.1088/0004-637X/766/1/34

Doré O., Bock J., Ashby M., Capak P., Cooray A., de Putter R., Eifler T., Flagey N., Gong Y., Habib S., Heitmann K., Hirata C., Jeong W.-S., Katti R., Korngut P., Krause E., Lee D.-H., Masters D., Mauskopf P., Melnick G., Mennesson B., Nguyen H., Öberg K., Pullen A., Raccanelli A., Smith R., Song Y.-S., Tolls V., Unwin S., Venumadhav T., Viero M., Werner M., Zemcov M. 2014, Cosmology with the SPHEREX All-Sky Spectral Survey, arXiv e-prints, arXiv:1412.4872. https://arxiv.org/abs/1412.4872

Doyon R., Hutchings J. B., Beaulieu M., Albert L., Lafrenière D., Willott C., Touahri D., Rowlands N., Maszkiewicz M., Fullerton A. W., Volk K., Martel A. R., Chayer P., Sivaramakrishnan A., Abraham R., Ferrarese L., Jayawardhana R., Johnstone D., Meyer M., Pipher J. L., Sawicki M. 2012, in Society of Photo-Optical Instrumentation Engineers (SPIE) Conference Series, Vol. 8442, Space Telescopes and Instrumentation 2012: Optical, Infrared, and Millimeter Wave, ed. M. C. Clampin, G. G. Fazio, H. A. MacEwen, J. Oschmann, Jacobus M., 84422R, doi: 10.1117/12.926578

Drimmel R., Spergel D. N. 2001, Three-dimensional Structure of the Milky Way Disk: The Distribution of Stars and Dust beyond 0.35 R_{solar}, ApJ, 556, 181, doi: 10.1086/321556

Drlica-Wagner A., Bechtol K., Rykoff E. S., Luque E., Queiroz A., Mao Y. Y., Wechsler R. H., Simon J. D., Santiago B., Yanny B., Balbinot E., Dodelson S., Fausti Neto A., James D. J., Li T. S., Maia M. A. G., Marshall J. L., Pieres A., Stringer K., Walker

A. R., Abbott T. M. C., Abdalla F. B., Allam S., Benoit-Lévy A., Bernstein G. M., Bertin E., Brooks D., Buckley-Geer E., Burke D. L., Carnero Rosell A., Carrasco Kind M., Carretero J., Crocce M., da Costa L. N., Desai S., Diehl H. T., Dietrich J. P., Doel P., Eifler T. F., Evrard A. E., Finley D. A., Flaugher B., Fosalba P., Frieman J., Gaztanaga E., Gerdes D. W., Gruen D., Gruendl R. A., Gutierrez G., Honscheid K., Kuehn K., Kuropatkin N., Lahav O., Martini P., Miquel R., Nord B., Ogando R., Plazas A. A., Reil K., Roodman A., Sako M., Sanchez E., Scarpine V., Schubnell M., Sevilla-Noarbe I., Smith R. C., Soares-Santos M., Sobreira F., Suchyta E., Swanson M. E. C., Tarle G., Tucker D., Vikram V., Wester W., Zhang Y., Zuntz J., DES Collaboration. 2015, Eight Ultra-faint Galaxy Candidates Discovered in Year Two of the Dark Energy Survey, ApJ, 813, 109, doi: 10.1088/0004-637X/813/2/109

Drlica-Wagner A., Mao Y.-Y., Adhikari S., Armstrong R., Banerjee A., Banik N., Bechtol K., Bird S., Boddy K. K., Bonaca A., Bovy J., Buckley M. R., Bulbul E., Chang C., Chapline G., Cohen-Tanugi J., Cuoco A., Cyr-Racine F.-Y., Dawson W. A., Díaz Rivero A., Dvorkin C., Erkal D., Fassnacht C. D., García-Bellido J., Giannotti M., Gluscevic V., Golovich N., Hendel D., Hezaveh Y. D., Horiuchi S., Jee M. J., Kaplinghat M., Keeton C. R., Koposov S. E., Lam C. Y., Li T. S., Lu J. R., Mandelbaum R., McDermott S. D., McNanna M., Medford M., Meyer M., Marc M., Murgia S., Nadler E. O., Necib L., Nuss E., Pace A. B., Peter A. H. G., Polin D. A., Prescod-Weinstein C., Read J. I., Rosenfeld R., Shipp N., Simon J. D., Slatyer T. R., Straniero O., Strigari L. E., Tollerud E., Tyson J. A., Wang M.-Y., Wechsler R. H., Wittman D., Yu H.-B., Zaharijas G., Ali-Haïmoud Y., Annis J., Birrer S., Biswas R., Blazek J., Brooks A. M., Buckley-Geer E., Caputo R., Charles E., Digel S., Dodelson S., Flaugher B., Frieman J., Gawiser E., Hearin A. P., Hložek R., Jain B., Jeltema T. E., Koushiappas S. M., Lisanti M., LoVerde M., Mishra-Sharma S., Newman J. A., Nord B., Nourbakhsh E., Ritz S., Robertson B. E., Sánchez-Conde M. A., Slosar A., Tait T. M. P., Verma A., Vilalta R.,

Walter C. W., Yanny B., Zentner A. R. 2019, Probing the Fundamental Nature of Dark Matter with the Large Synoptic Survey Telescope, arXiv e-prints, arXiv:1902.01055. https://arxiv.org/abs/1902.01055

D'Souza R., Bell E. F. 2018, The Andromeda galaxy's most important merger about 2 billion years ago as M32's likely progenitor, Nature Astronomy, 2, 737, doi: 10.1038/s41550-018-0533-x10.48550/arXiv.1807.08819

Dubath P., Rimoldini L., Süveges M., Blomme J., López M., Sarro L. M., De Ridder J., Cuypers J., Guy L., Lecoeur I., Nienartowicz K., Jan A., Beck M., Mowlavi N., De Cat P., Lebzelter T., Eyer L. 2011, Random forest automated supervised classification of Hipparcos periodic variable stars, MNRAS, 414, 2602, doi: 10.1111/j.1365-2966.2011.18575.x

Dupuy T., Liu M. 2012, The Hawaii Infrared Parallax Program. I. Ultracool Binaries and the L/T Transition, \apjs, 201, 19, doi: 10.1088/0067-0049/201/2/19

Efstathiou G. 1992, Suppressing the formation of dwarf galaxies via photoionization, MNRAS, 256, 43P, doi: 10.1093/mnras/256.1.43P

Efstathiou G., Silk J. 1983, The Formation of Galaxies, Fund. Cosmic Phys., 9, 1

Eggen O. J., Lynden-Bell D., Sandage A. R. 1962, Evidence from the motions of old stars that the Galaxy collapsed., ApJ, 136, 748, doi: 10.1086/147433

Eilers A.-C., Hogg D. W., Rix H.-W., Ness M. K. 2019, The Circular Velocity Curve of the Milky Way from 5 to 25 kpc, ApJ, 871, 120, doi: 10.3847/1538-4357/aaf648

Epchtein N., de Batz B., Capoani L., Chevallier L., Copet E., Fouqué P., Lacombe P., Le Bertre T., Pau S., Rouan D., Ruphy S., Simon G., Tiphène D., Burton W. B., Bertin E., Deul E., Habing H., Borsenberger J., Dennefeld M., Guglielmo F., Loup C., Mamon

G., Ng Y., Omont A., Provost L., Renault J.-C., Tanguy F., Kimeswenger S., Kienel C., Garzon F., Persi P., Ferrari-Toniolo M., Robin A., Paturel G., Vauglin I., Forveille T., Delfosse X., Hron J., Schultheis M., Appenzeller I., Wagner S., Balazs L., Holl A., Lépine J., Boscolo P., Picazzio E., Duc P.-A., Mennessier M.-O. 1997, The deep near-infrared southern sky survey (DENIS)., The Messenger, 87, 27

Erkal D., Belokurov V. 2015, Forensics of subhalo-stream encounters: the three phases of gap growth, MNRAS, 450, 1136, doi: 10.1093/mnras/stv655

Erkal D., Belokurov V., Bovy J., Sanders J. L. 2016, The number and size of subhalo-induced gaps in stellar streams, MNRAS, 463, 102, doi: 10.1093/mnras/stw1957

Erkal D., Belokurov V. A. 2020, Limit on the LMC mass from a census of its satellites, MNRAS, 495, 2554, doi: 10.1093/mnras/staa1238

Erkal D., Boubert D., Gualandris A., Evans N. W., Antonini F. 2019a, A hypervelocity star with a Magellanic origin, MNRAS, 483, 2007, doi: 10.1093/mnras/sty2674

Erkal D., Koposov S. E., Belokurov V. 2017, A sharper view of Pal 5's tails: discovery of stream perturbations with a novel non-parametric technique, MNRAS, 470, 60, doi: 10.1093/mnras/stx1208

Erkal D., Belokurov V., Laporte C. F. P., Koposov S. E., Li T. S., Grillmair C. J., Kallivayalil N., Price-Whelan A. M., Evans N. W., Hawkins K., Hendel D., Mateu C., Navarro J. F., del Pino A., Slater C. T., Sohn S. T., Orphan Aspen Treasury Collaboration. 2019b, The total mass of the Large Magellanic Cloud from its perturbation on the Orphan stream, MNRAS, 487, 2685, doi: 10.1093/mnras/stz1371

Errani R., Peñarrubia J. 2020, Can tides disrupt cold dark matter subhaloes?, MNRAS, 491, 4591, doi: 10.1093/mnras/stz3349

Escala I., Gilbert K. M., Kirby E. N., Wojno J., Cunningham E. C., Guhathakurta P. 2020, Elemental Abundances in M31: A Comparative Analysis of Alpha and Iron Element Abundances in the the Outer Disk, Giant Stellar Stream, and Inner Halo of M31, ApJ, 889, 177, doi: 10.3847/1538-4357/ab6659

Escala I., Gilbert K. M., Wojno J., Kirby E. N., Guhathakurta P. 2021, Elemental Abundances in M31: Gradients in the Giant Stellar Stream, AJ, 162, 45, doi: 10.3847/1538-3881/abfec410.48550/arXiv.2105.02339

Euclid Collaboration, Scaramella R., Amiaux J., Mellier Y., Burigana C., Carvalho C. S., Cuillandre J. C., Da Silva A., Derosa A., Dinis J., Maiorano E., Maris M., Tereno I., Laureijs R., Boenke T., Buenadicha G., Dupac X., Gaspar Venancio L. M., Gómez-Álvarez P., Hoar J., Lorenzo Alvarez J., Racca G. D., Saavedra-Criado G., Schwartz J., Vavrek R., Schirmer M., Aussel H., Azzollini R., Cardone V. F., Cropper M., Ealet A., Garilli B., Gillard W., Granett B. R., Guzzo L., Hoekstra H., Jahnke K., Kitching T., Maciaszek T., Meneghetti M., Miller L., Nakajima R., Niemi S. M., Pasian F., Percival W. J., Pottinger S., Sauvage M., Scodeggio M., Wachter S., Zacchei A., Aghanim N., Amara A., Auphan T., Auricchio N., Awan S., Balestra A., Bender R., Bodendorf C., Bonino D., Branchini E., Brau-Nogue S., Brescia M., Candini G. P., Capobianco V., Carbone C., Carlberg R. G., Carretero J., Casas R., Castander F. J., Castellano M., Cavuoti S., Cimatti A., Cledassou R., Congedo G., Conselice C. J., Conversi L., Copin Y., Corcione L., Costille A., Courbin F., Degaudenzi H., Douspis M., Dubath F., Duncan C. A. J., Dusini S., Farrens S., Ferriol S., Fosalba P., Fourmanoit N., Frailis M., Franceschi E., Franzetti P., Fumana M., Gillis B., Giocoli C., Grazian A., Grupp F., Haugan S. V. H., Holmes W., Hormuth F., Hudelot P., Kermiche S., Kiessling A., Kilbinger M., Kohley R., Kubik B., Kümmel M., Kunz M., Kurki-Suonio H., Lahav O., Ligori S., Lilje P. B., Lloro I., Mansutti O., Marggraf O., Markovic K., Marulli F.,

Massey R., Maurogordato S., Melchior M., Merlin E., Meylan G., Mohr J. J., Moresco M., Morin B., Moscardini L., Munari E., Nichol R. C., Padilla C., Paltani S., Peacock J., Pedersen K., Pettorino V., Pires S., Poncet M., Popa L., Pozzetti L., Raison F., Rebolo R., Rhodes J., Rix H. W., Roncarelli M., Rossetti E., Saglia R., Schneider P., Schrabback T., Secroun A., Seidel G., Serrano S., Sirignano C., Sirri G., Skottfelt J., Stanco L., Starck J. L., Tallada-Crespí P., Tavagnacco D., Taylor A. N., Teplitz H. I., Toledo-Moreo R., Torradeflot F., Trifoglio M., Valentijn E. A., Valenziano L., Verdoes Kleijn G. A., Wang Y., Welikala N., Weller J., Wetzstein M., Zamorani G., Zoubian J., Andreon S., Baldi M., Bardelli S., Boucaud A., Camera S., Di Ferdinando D., Fabbian G., Farinelli R., Galeotta S., Graciá-Carpio J., Maino D., Medinaceli E., Mei S., Neissner C., Polenta G., Renzi A., Romelli E., Rosset C., Sureau F., Tenti M., Vassallo T., Zucca E., Baccigalupi C., Balaguera-Antolínez A., Battaglia P., Biviano A., Borgani S., Bozzo E., Cabanac R., Cappi A., Casas S., Castignani G., Colodro-Conde C., Coupon J., Courtois H. M., Cuby J., de la Torre S., Desai S., Dole H., Fabricius M., Farina M., Ferreira P. G., Finelli F., Flose-Reimberg P., Fotopoulou S., Ganga K., Gozaliasl G., Hook I. M., Keihanen E., Kirkpatrick C. C., Liebing P., Lindholm V., Mainetti G., Martinelli M., Martinet N., Maturi M., McCracken H. J., Metcalf R. B., Morgante G., Nightingale J., Nucita A., Patrizii L., Potter D., Riccio G., Sánchez A. G., Sapone D., Schewtschenko J. A., Schultheis M., Scottez V., Teyssier R., Tutusaus I., Valiviita J., Viel M., Vriend W., Whittaker L. 2022, Euclid preparation. I. The Euclid Wide Survey, A&A, 662, A112, doi: 10.1051/0004-6361/202141938

Faherty J. K., Bochanski J. J., Gagne J., Nelson O., Coker K., Smithka I., Desir D., Vasquez C. 2018, New and Known Moving Groups And Clusters Identified in a Gaia Co-Moving Catalog, The Astrophysical Journal, 863, 91, doi: 10.3847/1538-4357/aac76e

Faherty J. K., Burgasser A. J., Cruz K. L., Shara M. M., Walter F. M., Gelino C. R. 2009, The Brown Dwarf Kinematics Project I. Proper Motions and Tangential Velocities for a Large Sample of Late-Type M, L, and T Dwarfs, AJ, 137, 1, doi: 10.1088/0004-6256/137/1/1

Faherty J. K., Burgasser A. J., West A. A., Bochanski J. J., Cruz K. L., Shara M. M., Walter F. M. 2010, The Brown Dwarf Kinematics Project. II. Details on Nine Wide Common Proper Motion Very Low Mass Companions to Nearby Stars, AJ, 139, 176, doi: 10.1088/0004-6256/139/1/176

Faherty J. K., Burgasser A. J., Walter F. M., Van der Bliek N., Shara M. M., Cruz K. L., West A. A., Vrba F. J., Anglada-Escudé G. 2012, The Brown Dwarf Kinematics Project (BDKP). III. Parallaxes for 70 Ultracool Dwarfs, ApJ, 752, 56, doi: 10.1088/0004-637X/752/1/56

Fardal M. A., Huang S., Weinberg M. D. 2015, Generation of mock tidal streams, MNRAS, 452, 301, doi: 10.1093/mnras/stv1198

Fardal M. A., Weinberg M. D., Babul A., Irwin M. J., Guhathakurta P., Gilbert K. M., Ferguson A. M. N., Ibata R. A., Lewis G. F., Tanvir N. R., Huxor A. P. 2013, Inferring the Andromeda Galaxy's mass from its giant southern stream with Bayesian simulation sampling, MNRAS, 434, 2779, doi: 10.1093/mnras/stt1121

Fiacconi D., Madau P., Potter D., Stadel J. 2016, Cold Dark Matter Substructures in Early-type Galaxy Halos, ApJ, 824, 144, doi: 10.3847/0004-637X/824/2/144

Font A. S., Johnston K. V., Guhathakurta P., Majewski S. R., Rich R. M. 2006, Dynamics and Stellar Content of the Giant Southern Stream in M31. II. Interpretation, AJ, 131, 1436, doi: 10.1086/499564

Fontanive C., Biller B., Bonavita M., Allers K. 2018, Constraining the multiplicity statistics of the coolest brown dwarfs: binary fraction continues to decrease with spectral type, MNRAS, 479, 2702, doi: 10.1093/mnras/sty1682

Fouesneau M., Rix H.-W., von Hippel T., Hogg D. W., Tian H. 2019, Precise Ages of Field Stars from White Dwarf Companions, ApJ, 870, 9, doi: 10.3847/1538-4357/aaee74

Freeman K., Bland-Hawthorn J. 2002, The New Galaxy: Signatures of Its Formation, ARA&A, 40, 487, doi: 10.1146/annurev.astro.40.060401.093840

Freeman K. C. 1987, The galactic spheroid and old disk., ARA&A, 25, 603, doi: 10.1146/annurev.aa.25.090187.003131

Gagné J., Faherty J. K., Cruz K. L., Lafreniére D., Doyon R., Malo L., Burgasser A. J., Naud M.-E., Artigau É., Bouchard S., Gizis J. E., Albert L. 2015, BANYAN. VII. A New Population of Young Substellar Candidate Members of Nearby Moving Groups from the BASS Survey, ApJS, 219, 33, doi: 10.1088/0067-0049/219/2/33

Gaia Collaboration, Brown A. G. A., Vallenari A., Prusti T., de Bruijne J. H. J., Babusiaux C., Bailer-Jones C. A. L., Biermann M., Evans D. W., Eyer L., Jansen F., Jordi C., Klioner S. A., Lammers U., Lindegren L., Luri X., Mignard F., Panem C., Pourbaix D., Randich S., Sartoretti P., Siddiqui H. I., Soubiran C., van Leeuwen F., Walton N. A., Arenou F., Bastian U., Cropper M., Drimmel R., Katz D., Lattanzi M. G., Bakker J., Cacciari C., Castañeda J., Chaoul L., Cheek N., De Angeli F., Fabricius C., Guerra R., Holl B., Masana E., Messineo R., Mowlavi N., Nienartowicz K., Panuzzo P., Portell J., Riello M., Seabroke G. M., Tanga P., Thévenin F., Gracia-Abril G., Comoretto G., Garcia-Reinaldos M., Teyssier D., Altmann M., Andrae R., Audard M., Bellas-Velidis I., Benson K., Berthier J., Blomme R., Burgess P., Busso G., Carry B., Cellino A., Clementini G., Clotet M., Creevey O., Davidson M., De Ridder J.,

Delchambre L., Dell'Oro A., Ducourant C., Fernández-Hernández J., Fouesneau M., Frémat Y., Galluccio L., García-Torres M., González-Núñez J., González-Vidal J. J., Gosset E., Guy L. P., Halbwachs J. L., Hambly N. C., Harrison D. L., Hernández J., Hestroffer D., Hodgkin S. T., Hutton A., Jasniewicz G., Jean-Antoine-Piccolo A., Jordan S., Korn A. J., Krone-Martins A., Lanzafame A. C., Lebzelter T., Löffler W., Manteiga M., Marrese P. M., Martín-Fleitas J. M., Moitinho A., Mora A., Muinonen K., Osinde J., Pancino E., Pauwels T., Petit J. M., Recio-Blanco A., Richards P. J., Rimoldini L., Robin A. C., Sarro L. M., Siopis C., Smith M., Sozzetti A., Süveges M., Torra J., van Reeven W., Abbas U., Abreu Aramburu A., Accart S., Aerts C., Altavilla G., Álvarez M. A., Alvarez R., Alves J., Anderson R. I., Andrei A. H., Anglada Varela E., Antiche E., Antoja T., Arcay B., Astraatmadja T. L., Bach N., Baker S. G., Balaguer-Núñez L., Balm P., Barache C., Barata C., Barbato D., Barblan F., Barklem P. S., Barrado D., Barros M., Barstow M. A., Bartholomé Muñoz S., Bassilana J. L., Becciani U., Bellazzini M., Berihuete A., Bertone S., Bianchi L., Bienaymé O., Blanco-Cuaresma S., Boch T., Boeche C., Bombrun A., Borrachero R., Bossini D., Bouquillon S., Bourda G., Bragaglia A., Bramante L., Breddels M. A., Bressan A., Brouillet N., Brüsemeister T., Brugaletta E., Bucciarelli B., Burlacu A., Busonero D., Butkevich A. G., Buzzi R., Caffau E., Cancelliere R., Cannizzaro G., Cantat-Gaudin T., Carballo R., Carlucci T., Carrasco J. M., Casamiquela L., Castellani M., Castro-Ginard A., Charlot P., Chemin L., Chiavassa A., Cocozza G., Costigan G., Cowell S., Crifo F., Crosta M., Crowley C., Cuypers J., Dafonte C., Damerdji Y., Dapergolas A., David P., David M., de Laverny P., De Luise F., De March R., de Martino D., de Souza R., de Torres A., Debosscher J., del Pozo E., Delbo M., Delgado A., Delgado H. E., Di Matteo P., Diakite S., Diener C., Distefano E., Dolding C., Drazinos P., Durán J., Edvardsson B., Enke H., Eriksson K., Esquej P., Eynard Bontemps G., Fabre C., Fabrizio M., Faigler S., Falcão A. J., Farràs Casas M., Federici

L., Fedorets G., Fernique P., Figueras F., Filippi F., Findeisen K., Fonti A., Fraile E., Fraser M., Frézouls B., Gai M., Galleti S., Garabato D., García-Sedano F., Garofalo A., Garralda N., Gavel A., Gavras P., Gerssen J., Geyer R., Giacobbe P., Gilmore G., Girona S., Giuffrida G., Glass F., Gomes M., Granvik M., Gueguen A., Guerrier A., Guiraud J., Gutiérrez-Sánchez R., Haigron R., Hatzidimitriou D., Hauser M., Haywood M., Heiter U., Helmi A., Heu J., Hilger T., Hobbs D., Hofmann W., Holland G., Huckle H. E., Hypki A., Icardi V., Janßen K., Jevardat de Fombelle G., Jonker P. G., Juhász Á. L., Julbe F., Karampelas A., Kewley A., Klar J., Kochoska A., Kohley R., Kolenberg K., Kontizas M., Kontizas E., Koposov S. E., Kordopatis G., Kostrzewa-Rutkowska Z., Koubsky P., Lambert S., Lanza A. F., Lasne Y., Lavigne J. B., Le Fustec Y., Le Poncin-Lafitte C., Lebreton Y., Leccia S., Leclerc N., Lecoeur-Taibi I., Lenhardt H., Leroux F., Liao S., Licata E., Lindstrøm H. E. P., Lister T. A., Livanou E., Lobel A., López M., Managau S., Mann R. G., Mantelet G., Marchal O., Marchant J. M., Marconi M., Marinoni S., Marschalkó G., Marshall D. J., Martino M., Marton G., Mary N., Massari D., Matijevič G., Mazeh T., McMillan P. J., Messina S., Michalik D., Millar N. R., Molina D., Molinaro R., Molnár L., Montegriffo P., Mor R., Morbidelli R., Morel T., Morris D., Mulone A. F., Muraveva T., Musella I., Nelemans G., Nicastro L., Noval L., O'Mullane W., Ordénovic C., Ordóñez-Blanco D., Osborne P., Pagani C., Pagano I., Pailler F., Palacin H., Palaversa L., Panahi A., Pawlak M., Piersimoni A. M., Pineau F. X., Plachy E., Plum G., Poggio E., Poujoulet E., Prša A., Pulone L., Racero E., Ragaini S., Rambaux N., Ramos-Lerate M., Regibo S., Reylé C., Riclet F., Ripepi V., Riva A., Rivard A., Rixon G., Roegiers T., Roelens M., Romero-Gómez M., Rowell N., Royer F., Ruiz-Dern L., Sadowski G., Sagristà Sellés T., Sahlmann J., Salgado J., Salguero E., Sanna N., Santana-Ros T., Sarasso M., Savietto H., Schultheis M., Sciacca E., Segol M., Segovia J. C., Ségransan D., Shih I. C., Siltala L., Silva A. F., Smart R. L., Smith K. W., Solano E., Solitro F., Sordo R., Soria Nieto S., Souchay J.,

Spagna A., Spoto F., Stampa U., Steele I. A., Steidelmüller H., Stephenson C. A., Stoev H., Suess F. F., Surdej J., Szabados L., Szegedi-Elek E., Tapiador D., Taris F., Tauran G., Taylor M. B., Teixeira R., Terrett D., Teyssand ier P., Thuillot W., Titarenko A., Torra Clotet F., Turon C., Ulla A., Utrilla E., Uzzi S., Vaillant M., Valentini G., Valette V., van Elteren A., Van Hemelryck E., van Leeuwen M., Vaschetto M., Vecchiato A., Veljanoski J., Viala Y., Vicente D., Vogt S., von Essen C., Voss H., Votruba V., Voutsinas S., Walmsley G., Weiler M., Wertz O., Wevers T., Wyrzykowski Ł., Yoldas A., Žerjal M., Ziaeepour H., Zorec J., Zschocke S., Zucker S., Zurbach C., Zwitter T. 2018, Gaia Data Release 2. Summary of the contents and survey properties, A&A, 616, A1, doi: 10.1051/0004-6361/201833051

Gallart C., Bernard E. J., Brook C. B., Ruiz-Lara T., Cassisi S., Hill V., Monelli M. 2019, Uncovering the birth of the Milky Way through accurate stellar ages with Gaia, Nature Astronomy, doi: 10.1038/s41550-019-0829-5

Galleti S., Bellazzini M., Federici L., Buzzoni A., Fusi Pecci F. 2007, An updated survey of globular clusters in M 31. II. Newly discovered bright and remote clusters, A&A, 471, 127, doi: 10.1051/0004-6361:20077788

Galleti S., Federici L., Bellazzini M., Buzzoni A., Fusi Pecci F. 2006, An updated survey of globular clusters in M 31. I. Classification and radial velocity for 76 candidate clusters, A&A, 456, 985, doi: 10.1051/0004-6361:20065309

Garavito-Camargo N., Besla G., Laporte C. F. P., Johnston K. V., Gómez F. A., Watkins L. L. 2019, Hunting for the Dark Matter Wake Induced by the Large Magellanic Cloud, ApJ, 884, 51, doi: 10.3847/1538-4357/ab32eb

Garavito-Camargo N., Besla G., Laporte C. F. P., Price-Whelan A. M., Cunningham E. C., Johnston K. V., Weinberg M., Gómez F. A. 2021, Quantifying the Impact of the

Large Magellanic Cloud on the Structure of the Milky Way's Dark Matter Halo Using Basis Function Expansions, ApJ, 919, 109, doi: 10.3847/1538-4357/ac0b44

Gardner J. P., Mather J. C., Clampin M., Doyon R., Greenhouse M. A., Hammel H. B., Hutchings J. B., Jakobsen P., Lilly S. J., Long K. S., Lunine J. I., McCaughrean M. J., Mountain M., Nella J., Rieke G. H., Rieke M. J., Rix H.-W., Smith E. P., Sonneborn G., Stiavelli M., Stockman H. S., Windhorst R. A., Wright G. S. 2006, The James Webb Space Telescope, Space Sci. Rev., 123, 485, doi: 10.1007/s11214-006-8315-7

Garrison-Kimmel S., Wetzel A., Bullock J. S., Hopkins P. F., Boylan-Kolchin M., Faucher-Giguère C.-A., Kereš D., Quataert E., Sanderson R. E., Graus A. S., Kelley T. 2017, Not so lumpy after all: modelling the depletion of dark matter subhaloes by Milky Way-like galaxies, MNRAS, 471, 1709, doi: 10.1093/mnras/stx1710

Geehan J. J., Fardal M. A., Babul A., Guhathakurta P. 2006, Investigating the Andromeda stream - I. Simple analytic bulge-disc-halo model for M31, MNRAS, 366, 996, doi: 10.1111/j.1365-2966.2005.09863.x

Geha M., Wechsler R. H., Mao Y.-Y., Tollerud E. J., Weiner B., Bernstein R., Hoyle B., Marchi S., Marshall P. J., Muñoz R., Lu Y. 2017, The SAGA Survey. I. Satellite Galaxy Populations around Eight Milky Way Analogs, ApJ, 847, 4, doi: 10.3847/1538-4357/aa8626

Gerasimov R., Burgasser A. J., Homeier D., Bedin L. R., Rees J. M., Scalco M., Anderson J., Salaris M. 2022, The HST large programme on ω Centauri – V. Exploring the Ultracool Dwarf Population with Stellar Atmosphere and Evolutionary Modelling, ApJ, in press. https://arxiv.org/abs/2111.10063

Gerasimov R., Homeier D., Burgasser A., Bedin L. R. 2020, A New Grid of Model

Atmospheres for Metal-poor Ultracool Brown Dwarfs, Research Notes of the American Astronomical Society, 4, 214, doi: 10.3847/2515-5172/abcf2c

Ghez A. M., Salim S., Weinberg N. N., Lu J. R., Do T., Dunn J. K., Matthews K., Morris M. R., Yelda S., Becklin E. E., Kremenek T., Milosavljevic M., Naiman J. 2008, Measuring Distance and Properties of the Milky Way's Central Supermassive Black Hole with Stellar Orbits, ApJ, 689, 1044, doi: 10.1086/592738

Giavalisco M., Ferguson H. C., Koekemoer A. M., Dickinson M., Alexander D. M., Bauer F. E., Bergeron J., Biagetti C., Brandt W. N., Casertano S., Cesarsky C., Chatzichristou E., Conselice C., Cristiani S., Da Costa L., Dahlen T., de Mello D., Eisenhardt P., Erben T., Fall S. M., Fassnacht C., Fosbury R., Fruchter A., Gardner J. P., Grogin N., Hook R. N., Hornschemeier A. E., Idzi R., Jogee S., Kretchmer C., Laidler V., Lee K. S., Livio M., Lucas R., Madau P., Mobasher B., Moustakas L. A., Nonino M., Padovani P., Papovich C., Park Y., Ravindranath S., Renzini A., Richardson M., Riess A., Rosati P., Schirmer M., Schreier E., Somerville R. S., Spinrad H., Stern D., Stiavelli M., Strolger L., Urry C. M., Vandame B., Williams R., Wolf C. 2004, The Great Observatories Origins Deep Survey: Initial Results from Optical and Near-Infrared Imaging, The Astrophysical Journal, 600, L93, doi: 10.1086/379232

Gillessen S., Eisenhauer F., Trippe S., Alexand er T., Genzel R., Martins F., Ott T. 2009, Monitoring Stellar Orbits Around the Massive Black Hole in the Galactic Center, ApJ, 692, 1075, doi: 10.1088/0004-637X/692/2/1075

Gilman D., Birrer S., Treu T., Nierenberg A., Benson A. 2019, Probing dark matter structure down to 10^7 solar masses: flux ratio statistics in gravitational lenses with line-of-sight haloes, MNRAS, 487, 5721, doi: 10.1093/mnras/stz1593

Gilmore G., Reid N. 1983, New light on faint stars - III. Galactic structure towards the

South Pole and the Galactic thick disc., MNRAS, 202, 1025, doi: 10.1093/mnras/202.4.1025

Gilmore G., Wyse R. F. G., Jones J. B. 1995, A Determination of the Thick Disk Chemical Abundance Distribution: Implications for Galaxy Evolution, AJ, 109, 1095, doi: 10.1086/117344

Gizis J. E., Reid I. N., Knapp G. R., Liebert J., Kirkpatrick J. D., Koerner D. W., Burgasser A. J. 2003, Hubble Space Telescope Observations of Binary Very Low Mass Stars and Brown Dwarfs, AJ, 125, 3302, doi: 10.1086/374991

Glennon N., Nadler E. O., Musoke N., Banerjee A., Prescod-Weinstein C., Wechsler R. H. 2022, Tidal disruption of solitons in self-interacting ultralight axion dark matter, Phys. Rev. D, 105, 123540, doi: 10.1103/PhysRevD.105.123540

Goldreich P., Lynden-Bell D. 1965, II. Spiral arms as sheared gravitational instabilities, MNRAS, 130, 125, doi: 10.1093/mnras/130.2.125

Gonzales E. C., Faherty J. K., Gagné J., Artigau É., Bardalez Gagliuffi D. 2018, Understanding Fundamental Properties and Atmospheric Features of Subdwarfs via a Case Study of SDSS J125637.13-022452.4, 864, 100, doi: 10.3847/1538-4357/aad3c7

González R. E., Kravtsov A. V., Gnedin N. Y. 2014, On the Mass of the Local Group, ApJ, 793, 91, doi: 10.1088/0004-637X/793/2/91

Gould A., Bahcall J., Flynn C. 1997, M Dwarfs from Hubble Space Telescope Star Counts. III. The Groth Strip, \apj, 482, 913, doi: 10.1086/304194

GRAVITY Collaboration, Abuter R., Amorim A., Bauböck M., Berger J. P., Bonnet H., Brandner W., Clénet Y., Coudé Du Foresto V., de Zeeuw P. T., Dexter J., Duvert G., Eckart A., Eisenhauer F., Förster Schreiber N. M., Garcia P., Gao F., Gendron

E., Genzel R., Gerhard O., Gillessen S., Habibi M., Haubois X., Henning T., Hippler S., Horrobin M., Jiménez-Rosales A., Jocou L., Kervella P., Lacour S., Lapeyrère V., Le Bouquin J. B., Léna P., Ott T., Paumard T., Perraut K., Perrin G., Pfuhl O., Rabien S., Rodriguez Coira G., Rousset G., Scheithauer S., Sternberg A., Straub O., Straubmeier C., Sturm E., Tacconi L. J., Vincent F., von Fellenberg S., Waisberg I., Widmann F., Wieprecht E., Wiezorrek E., Woillez J., Yazici S. 2019, A geometric distance measurement to the Galactic center black hole with 0.3% uncertainty, A&A, 625, L10, doi: 10.1051/0004-6361/201935656

Grillmair C. J., Carlin J. L. 2016, in Astrophysics and Space Science Library, Vol. 420, Tidal Streams in the Local Group and Beyond, ed. H. J. Newberg, J. L. Carlin, 87, doi: 10.1007/978-3-319-19336-6_4

Grillmair C. J., Smith G. H. 2001, The Main-Sequence Luminosity Function of Palomar 5 from THE HUBBLE SPACE TELESCOPE, AJ, 122, 3231, doi: 10.1086/323916

Grogin N. A., Kocevski D. D., Faber S. M., Ferguson H. C., Koekemoer A. M., Riess A. G., Acquaviva V., Alexander D. M., Almaini O., Ashby M. L. N., Barden M., Bell E. F., Bournaud F., Brown T. M., Caputi K. I., Casertano S., Cassata P., Castellano M., Challis P., Chary R.-R., Cheung E., Cirasuolo M., Conselice C. J., Roshan Cooray A., Croton D. J., Daddi E., Dahlen T., Davé R., de Mello D. F., Dekel A., Dickinson M., Dolch T., Donley J. L., Dunlop J. S., Dutton A. A., Elbaz D., Fazio G. G., Filippenko A. V., Finkelstein S. L., Fontana A., Gardner J. P., Garnavich P. M., Gawiser E., Giavalisco M., Grazian A., Guo Y., Hathi N. P., Häussler B., Hopkins P. F., Huang J.-S., Huang K.-H., Jha S. W., Kartaltepe J. S., Kirshner R. P., Koo D. C., Lai K., Lee K.-S., Li W., Lotz J. M., Lucas R. A., Madau P., McCarthy P. J., McGrath E. J., McIntosh D. H., McLure R. J., Mobasher B., Moustakas L. A., Mozena M., Nandra K., Newman J. A., Niemi S.-M., Noeske K. G., Papovich C. J., Pentericci L., Pope

A., Primack J. R., Rajan A., Ravindranath S., Reddy N. A., Renzini A., Rix H.-W., Robaina A. R., Rodney S. A., Rosario D. J., Rosati P., Salimbeni S., Scarlata C., Siana B., Simard L., Smidt J., Somerville R. S., Spinrad H., Straughn A. N., Strolger L.-G., Telford O., Teplitz H. I., Trump J. R., van der Wel A., Villforth C., Wechsler R. H., Weiner B. J., Wiklind T., Wild V., Wilson G., Wuyts S., Yan H.-J., Yun M. S. 2011, CANDELS: The Cosmic Assembly Near-infrared Deep Extragalactic Legacy Survey, ApJS, 197, 35, doi: 10.1088/0067-0049/197/2/35

Gunn J. E., Knapp G. R., Tremaine S. D. 1979, The global properties of the Galaxy. II. The galactic rotation parameters from 21-cm H I observations., AJ, 84, 1181, doi: 10.1086/112525

Gunn J. E., Siegmund W. A., Mannery E. J., Owen R. E., Hull C. L., Leger R. F., Carey L. N., Knapp G. R., York D. G., Boroski W. N., Kent S. M., Lupton R. H., Rockosi C. M., Evans M. L., Waddell P., Anderson J. E., Annis J., Barentine J. C., Bartoszek L. M., Bastian S., Bracker S. B., Brewington H. J., Briegel C. I., Brinkmann J., Brown Y. J., Carr M. A., Czarapata P. C., Drennan C. C., Dombeck T., Federwitz G. R., Gillespie B. A., Gonzales C., Hansen S. U., Harvanek M., Hayes J., Jordan W., Kinney E., Klaene M., Kleinman S. J., Kron R. G., Kresinski J., Lee G., Limmongkol S., Lindenmeyer C. W., Long D. C., Loomis C. L., McGehee P. M., Mantsch P. M., Neilsen Eric H. J., Neswold R. M., Newman P. R., Nitta A., Peoples John J., Pier J. R., Prieto P. S., Prosapio A., Rivetta C., Schneider D. P., Snedden S., Wang S.-i. 2006, The 2.5 m Telescope of the Sloan Digital Sky Survey, AJ, 131, 2332, doi: 10.1086/500975

Guo J.-C., Zhang H.-W., Huang Y., Liu X.-W., Liu J.-F., Xiang M.-S., Chen B.-Q., Yuan H.-B., Tian Z.-J., Huo Z.-Y., Wang C. 2019, Galactic halo age estimated from LAMOST DR4 and Gaia DR1, Research in Astronomy and Astrophysics, 19, 008, doi: 10.1088/1674-4527/19/1/8

Hammersley P. L., Garzón F., Mahoney T. J., López-Corredoira M., Torres M. A. P. 2000, Detection of the old stellar component of the major Galactic bar, MNRAS, 317, L45, doi: 10.1046/j.1365-8711.2000.03858.x

Hardegree-Ullman K. K., Cushing M. C., Muirhead P. S., Christiansen J. L. 2019, Kepler Planet Occurrence Rates for Mid-type M Dwarfs as a Function of Spectral Type, AJ, 158, 75, doi: 10.3847/1538-3881/ab21d2

Harris W. E. 1996, A Catalog of Parameters for Globular Clusters in the Milky Way, AJ, 112, 1487, doi: 10.1086/118116

Harris W. E. 2010, A New Catalog of Globular Clusters in the Milky Way, arXiv e-prints, arXiv:1012.3224. https://arxiv.org/abs/1012.3224

Harris W. E., Harris G. L. H., Alessi M. 2013, A Catalog of Globular Cluster Systems: What Determines the Size of a Galaxy's Globular Cluster Population?, ApJ, 772, 82, doi: 10.1088/0004-637X/772/2/82

Hastie T., Tibshirani R., Friedman J. 2009, The Elements of Statistical Learning: Data Mining, Inference, and Prediction, Springer series in statistics (Springer). https://books.google.com/books?id=eBSgoAEACAAJ

Hattori K., Erkal D., Sanders J. L. 2016, Shepherding tidal debris with the Galactic bar: the Ophiuchus stream, MNRAS, 460, 497, doi: 10.1093/mnras/stw1006

Hauschildt P. H., Baron E., Allard F. 1997, Parallel Implementation of the PHOENIX Generalized Stellar Atmosphere Program, ApJ, 483, 390, doi: 10.1086/304233

Hawkins K., Jofré P., Masseron T., Gilmore G. 2015, Using chemical tagging to redefine the interface of the Galactic disc and halo, MNRAS, 453, 758, doi: 10.1093/mnras/stv1586

Hawley S. L., Covey K. R., Knapp G. R., Golimowski D. A., Fan X., Anderson S. F., Gunn J. E., Harris H. C., Ivezić Ž., Long G. M., Lupton R. H., McGehee P. M., Narayanan V., Peng E., Schlegel D., Schneider D. P., Spahn E. Y., Strauss M. A., Szkody P., Tsvetanov Z., Walkowicz L. M., Brinkmann J., Harvanek M., Hennessy G. S., Kleinman S. J., Krzesinski J., Long D., Neilsen E. H., Newman P. R., Nitta A., Snedden S. A., York D. G. 2002, Characterization of M, L, and T Dwarfs in the Sloan Digital Sky Survey, AJ, 123, 3409, doi: 10.1086/340697

Hayashi C., Nakano T. 1963, Evolution of Stars of Small Masses in the Pre-Main-Sequence Stages, Progress of Theoretical Physics, 30, 460, doi: 10.1143/PTP.30.460

Hayden M. R., Bovy J., Holtzman J. A., Nidever D. L., Bird J. C., Weinberg D. H., Andrews B. H., Majewski S. R., Allende Prieto C., Anders F., Beers T. C., Bizyaev D., Chiappini C., Cunha K., Frinchaboy P., García-Herńandez D. A., García Pérez A. E., Girardi L., Harding P., Hearty F. R., Johnson J. A., Mészáros S., Minchev I., O'Connell R., Pan K., Robin A. C., Schiavon R. P., Schneider D. P., Schultheis M., Shetrone M., Skrutskie M., Steinmetz M., Smith V., Wilson J. C., Zamora O., Zasowski G. 2015, Chemical Cartography with APOGEE: Metallicity Distribution Functions and the Chemical Structure of the Milky Way Disk, ApJ, 808, 132, doi: 10.1088/0004-637X/808/2/132

Haywood M. 2006, Revisiting two local constraints of the Galactic chemical evolution, MNRAS, 371, 1760, doi: 10.1111/j.1365-2966.2006.10802.x

Haywood M., Di Matteo P., Lehnert M. D., Katz D., Gómez A. 2013a, The age structure of stellar populations in the solar vicinity. Clues of a two-phase formation history of the Milky Way disk, A&A, 560, A109, doi: 10.1051/0004-6361/201321397

Haywood M., Di Matteo P., Lehnert M. D., Katz D., Gómez A. 2013b, The age structure

of stellar populations in the solar vicinity. Clues of a two-phase formation history of the Milky Way disk, A&A, 560, A109, doi: 10.1051/0004-6361/201321397

Haywood M., Di Matteo P., Lehnert M. D., Snaith O., Khoperskov S., Gómez A. 2018, In Disguise or Out of Reach: First Clues about In Situ and Accreted Stars in the Stellar Halo of the Milky Way from Gaia DR2, ApJ, 863, 113, doi: 10.3847/1538-4357/aad235

Helling C., Ackerman A., Allard F., Dehn M., Hauschildt P., Homeier D., Lodders K., Marley M., Rietmeijer F., Tsuji T., Woitke P. 2008, A comparison of chemistry and dust cloud formation in ultracool dwarf model atmospheres, MNRAS, 391, 1854, doi: 10.1111/j.1365-2966.2008.13991.x

Helmi A., Babusiaux C., Koppelman H. H., Massari D., Veljanoski J., Brown A. G. A. 2018, The merger that led to the formation of the Milky Way's inner stellar halo and thick disk, Nature, 563, 85, doi: 10.1038/s41586-018-0625-x

Helmi A., White S. D. M. 1999, Building up the stellar halo of the Galaxy, MNRAS, 307, 495, doi: 10.1046/j.1365-8711.1999.02616.x

Helmi A., White S. D. M., de Zeeuw P. T., Zhao H. 1999, Debris streams in the solar neighbourhood as relicts from the formation of the Milky Way, Nature, 402, 53, doi: 10.1038/46980

Hendel D., Johnston K. V., Patra R. K., Sen B. 2019, A machine-vision method for automatic classification of stellar halo substructure, MNRAS, 486, 3604, doi: 10.1093/mnras/stz1107

Hermans J., Banik N., Weniger C., Bertone G., Louppe G. 2021, Towards constraining warm dark matter with stellar streams through neural simulation-based inference, MNRAS, 507, 1999, doi: 10.1093/mnras/stab2181

Hernquist L. 1990, An Analytical Model for Spherical Galaxies and Bulges, ApJ, 356, 359, doi: 10.1086/168845

Hezaveh Y., Dalal N., Holder G., Kisner T., Kuhlen M., Perreault Levasseur L. 2016, Measuring the power spectrum of dark matter substructure using strong gravitational lensing, , 2016, 048, doi: 10.1088/1475-7516/2016/11/048

Holmberg J., Nordström B., Andersen J. 2007, The Geneva-Copenhagen survey of the Solar neighbourhood II. New uvby calibrations and rediscussion of stellar ages, the G dwarf problem, age-metallicity diagram, and heating mechanisms of the disk, A&A, 475, 519, doi: 10.1051/0004-6361:20077221

Holwerda B. W., Trenti M., Clarkson W., Sahu K., Bradley L., Stiavelli M., Pirzkal N., De Marchi G., Andersen M., Bouwens R., Ryan R. J. 2014, Milky Way Red Dwarfs in the BoRG Survey; Galactic Scale-height and the Distribution of Dwarf Stars in WFC3 Imaging, ApJ, 788, 77, doi: 10.1088/0004-637X/788/1/77

Holwerda B. W., Bridge J. S., Ryan R. J., Kenworthy M. A., Pirzkal N., Andersen M., Wilkins S., Smit R., Bernard S. R., Meshkat T., Steele R., Bouwens R. C. 2018, Substellar and low-mass dwarf identification with near-infrared imaging space observatories, A&A, 620, A132, doi: 10.1051/0004-6361/201832838

Hopkins P. F., Hernquist L., Cox T. J., Younger J. D., Besla G. 2008, The Radical Consequences of Realistic Satellite Orbits for the Heating and Implied Merger Histories of Galactic Disks, ApJ, 688, 757, doi: 10.1086/592087

Hopkins P. F., Kereš D., Oñorbe J., Faucher-Giguère C.-A., Quataert E., Murray N., Bullock J. S. 2014, Galaxies on FIRE (Feedback In Realistic Environments): stellar feedback explains cosmologically inefficient star formation, MNRAS, 445, 581, doi: 10.1093/mnras/stu1738

Howell S. B., Sobeck C., Haas M., Still M., Barclay T., Mullally F., Troeltzsch J., Aigrain S., Bryson S. T., Caldwell D., Chaplin W. J., Cochran W. D., Huber D., Marcy G. W., Miglio A., Najita J. R., Smith M., Twicken J. D., Fortney J. J. 2014, The K2 Mission: Characterization and Early Results, PASP, 126, 398, doi: 10.1086/676406

Hsu C.-C., Burgasser A. J., Theissen C. A., Gelino C. R., Birky J. L., Diamant S. J. M., Bardalez Gagliuffi D. C., Aganze C., Blake C. H., Faherty J. K. 2021, The Brown Dwarf Kinematics Project (BDKP). V. Radial and Rotational Velocities of T Dwarfs from Keck/NIRSPEC High-resolution Spectroscopy, ApJS, 257, 45, doi: 10.3847/1538-4365/ac1c7d

Hu W., Barkana R., Gruzinov A. 2000, Fuzzy Cold Dark Matter: The Wave Properties of Ultralight Particles, Phys. Rev. Lett., 85, 1158, doi: 10.1103/PhysRevLett.85.1158

Hui L., Ostriker J. P., Tremaine S., Witten E. 2017, Ultralight scalars as cosmological dark matter, Phys. Rev. D, 95, 043541, doi: 10.1103/PhysRevD.95.043541

Hunt J. A. S., Price-Whelan A. M., Johnston K. V., Darragh-Ford E. 2022, Multiple phase spirals suggest multiple origins in Gaia DR3, MNRAS, 516, L7, doi: 10.1093/mnrasl/slac082

Huxor A. P., Tanvir N. R., Ferguson A. M. N., Irwin M. J., Ibata R., Bridges T., Lewis G. F. 2008, Globular clusters in the outer halo of M31: the survey, MNRAS, 385, 1989, doi: 10.1111/j.1365-2966.2008.12882.x

Huxor A. P., Mackey A. D., Ferguson A. M. N., Irwin M. J., Martin N. F., Tanvir N. R., Veljanoski J., McConnachie A., Fishlock C. K., Ibata R., Lewis G. F. 2014, The outer halo globular cluster system of M31 - I. The final PAndAS catalogue, MNRAS, 442, 2165, doi: 10.1093/mnras/stu771

Ibata R. A., Gilmore G., Irwin M. J. 1994, A dwarf satellite galaxy in Sagittarius, Nature, 370, 194, doi: 10.1038/370194a0

Ibata R. A., Lewis G. F., Thomas G., Martin N. F., Chapman S. 2017, Feeling the Pull: A Study of Natural Galactic Accelerometers. II. Kinematics and Mass of the Delicate Stellar Stream of the Palomar 5 Globular Cluster, ApJ, 842, 120, doi: 10.3847/1538-4357/aa7514

Ibata R. A., Malhan K., Martin N. F. 2019, The Streams of the Gaping Abyss: A Population of Entangled Stellar Streams Surrounding the Inner Galaxy, ApJ, 872, 152, doi: 10.3847/1538-4357/ab0080

Ibata R. A., Lewis G. F., McConnachie A. W., Martin N. F., Irwin M. J., Ferguson A. M. N., Babul A., Bernard E. J., Chapman S. C., Collins M., Fardal M., Mackey A. D., Navarro J., Peñarrubia J., Rich R. M., Tanvir N., Widrow L. 2014, The Large-scale Structure of the Halo of the Andromeda Galaxy. I. Global Stellar Density, Morphology and Metallicity Properties, ApJ, 780, 128, doi: 10.1088/0004-637X/780/2/128

Ivezić Ž., Beers T. C., Jurić M. 2012, Galactic Stellar Populations in the Era of the Sloan Digital Sky Survey and Other Large Surveys, ARA&A, 50, 251, doi: 10.1146/annurev-astro-081811-125504

Ivezić Ž., Sesar B., Jurić M., Bond N., Dalcanton J., Rockosi C. M., Yanny B., Newberg H. J., Beers T. C., Allende Prieto C., Wilhelm R., Lee Y. S., Sivarani T., Norris J. E., Bailer-Jones C. A. L., Re Fiorentin P., Schlegel D., Uomoto A., Lupton R. H., Knapp G. R., Gunn J. E., Covey K. R., Allyn Smith J., Miknaitis G., Doi M., Tanaka M., Fukugita M., Kent S., Finkbeiner D., Munn J. A., Pier J. R., Quinn T., Hawley S., Anderson S., Kiuchi F., Chen A., Bushong J., Sohi H., Haggard D., Kimball A., Barentine J., Brewington H., Harvanek M., Kleinman S., Krzesinski J., Long D.,

Nitta A., Snedden S., Lee B., Harris H., Brinkmann J., Schneider D. P., York D. G. 2008, The Milky Way Tomography with SDSS. II. Stellar Metallicity, ApJ, 684, 287, doi: 10.1086/589678

Ivezić Ž., Kahn S. M., Tyson J. A., Abel B., Acosta E., Allsman R., Alonso D., AlSayyad Y., Anderson S. F., Andrew J., Angel J. R. P., Angeli G. Z., Ansari R., Antilogus P., Araujo C., Armstrong R., Arndt K. T., Astier P., Aubourg É., Auza N., Axelrod T. S., Bard D. J., Barr J. D., Barrau A., Bartlett J. G., Bauer A. E., Bauman B. J., Baumont S., Bechtol E., Bechtol K., Becker A. C., Becla J., Beldica C., Bellavia S., Bianco F. B., Biswas R., Blanc G., Blazek J., Blandford R. D., Bloom J. S., Bogart J., Bond T. W., Booth M. T., Borgland A. W., Borne K., Bosch J. F., Boutigny D., Brackett C. A., Bradshaw A., Brandt W. N., Brown M. E., Bullock J. S., Burchat P., Burke D. L., Cagnoli G., Calabrese D., Callahan S., Callen A. L., Carlin J. L., Carlson E. L., Chandrasekharan S., Charles-Emerson G., Chesley S., Cheu E. C., Chiang H.-F., Chiang J., Chirino C., Chow D., Ciardi D. R., Claver C. F., Cohen-Tanugi J., Cockrum J. J., Coles R., Connolly A. J., Cook K. H., Cooray A., Covey K. R., Cribbs C., Cui W., Cutri R., Daly P. N., Daniel S. F., Daruich F., Daubard G., Daues G., Dawson W., Delgado F., Dellapenna A., de Peyster R., de Val-Borro M., Digel S. W., Doherty P., Dubois R., Dubois-Felsmann G. P., Durech J., Economou F., Eifler T., Eracleous M., Emmons B. L., Fausti Neto A., Ferguson H., Figueroa E., Fisher-Levine M., Focke W., Foss M. D., Frank J., Freemon M. D., Gangler E., Gawiser E., Geary J. C., Gee P., Geha M., Gessner C. J. B., Gibson R. R., Gilmore D. K., Glanzman T., Glick W., Goldina T., Goldstein D. A., Goodenow I., Graham M. L., Gressler W. J., Gris P., Guy L. P., Guyonnet A., Haller G., Harris R., Hascall P. A., Haupt J., Hernandez F., Herrmann S., Hileman E., Hoblitt J., Hodgson J. A., Hogan C., Howard J. D., Huang D., Huffer M. E., Ingraham P., Innes W. R., Jacoby S. H., Jain B., Jammes F., Jee M. J., Jenness T., Jernigan G., Jevremović D., Johns K., Johnson A. S., Johnson M. W. G.,

Jones R. L., Juramy-Gilles C., Jurić M., Kalirai J. S., Kallivayalil N. J., Kalmbach B., Kantor J. P., Karst P., Kasliwal M. M., Kelly H., Kessler R., Kinnison V., Kirkby D., Knox L., Kotov I. V., Krabbendam V. L., Krughoff K. S., Kubánek P., Kuczewski J., Kulkarni S., Ku J., Kurita N. R., Lage C. S., Lambert R., Lange T., Langton J. B., Le Guillou L., Levine D., Liang M., Lim K.-T., Lintott C. J., Long K. E., Lopez M., Lotz P. J., Lupton R. H., Lust N. B., MacArthur L. A., Mahabal A., Mandelbaum R., Markiewicz T. W., Marsh D. S., Marshall P. J., Marshall S., May M., McKercher R., McQueen M., Meyers J., Migliore M., Miller M., Mills D. J., Miraval C., Moeyens J., Moolekamp F. E., Monet D. G., Moniez M., Monkewitz S., Montgomery C., Morrison C. B., Mueller F., Muller G. P., Muñoz Arancibia F., Neill D. R., Newbry S. P., Nief J.-Y., Nomerotski A., Nordby M., O'Connor P., Oliver J., Olivier S. S., Olsen K., O'Mullane W., Ortiz S., Osier S., Owen R. E., Pain R., Palecek P. E., Parejko J. K., Parsons J. B., Pease N. M., Peterson J. M., Peterson J. R., Petravick D. L., Libby Petrick M. E., Petry C. E., Pierfederici F., Pietrowicz S., Pike R., Pinto P. A., Plante R., Plate S., Plutchak J. P., Price P. A., Prouza M., Radeka V., Rajagopal J., Rasmussen A. P., Regnault N., Reil K. A., Reiss D. J., Reuter M. A., Ridgway S. T., Riot V. J., Ritz S., Robinson S., Roby W., Roodman A., Rosing W., Roucelle C., Rumore M. R., Russo S., Saha A., Sassolas B., Schalk T. L., Schellart P., Schindler R. H., Schmidt S., Schneider D. P., Schneider M. D., Schoening W., Schumacher G., Schwamb M. E., Sebag J., Selvy B., Sembroski G. H., Seppala L. G., Serio A., Serrano E., Shaw R. A., Shipsey I., Sick J., Silvestri N., Slater C. T., Smith J. A., Smith R. C., Sobhani S., Soldahl C., Storrie-Lombardi L., Stover E., Strauss M. A., Street R. A., Stubbs C. W., Sullivan I. S., Sweeney D., Swinbank J. D., Szalay A., Takacs P., Tether S. A., Thaler J. J., Thayer J. G., Thomas S., Thornton A. J., Thukral V., Tice J., Trilling D. E., Turri M., Van Berg R., Vanden Berk D., Vetter K., Virieux F., Vucina T., Wahl W., Walkowicz L., Walsh B., Walter C. W., Wang D. L., Wang S.-Y., Warner M., Wiecha

O., Willman B., Winters S. E., Wittman D., Wolff S. C., Wood-Vasey W. M., Wu X., Xin B., Yoachim P., Zhan H. 2019, LSST: From Science Drivers to Reference Design and Anticipated Data Products, ApJ, 873, 111, doi: 10.3847/1538-4357/ab042c

Jahreiß H., Wielen R. 1997, in ESA Special Publication, Vol. 402, Hipparcos - Venice '97, ed. R. M. Bonnet, E. Høg, P. L. Bernacca, L. Emiliani, A. Blaauw, C. Turon, J. Kovalevsky, L. Lindegren, H. Hassan, M. Bouffard, B. Strim, D. Heger, M. A. C. Perryman, L. Woltjer, 675–680

Jeffries R., Oliveira J. 2005, The lithium depletion boundary in NGC 2547 as a test of pre-main-sequence evolutionary models, \mnras, 358, 13, doi: 10.1111/j.1365-2966.2005.08820.x

Jofré P., Weiss A. 2011a, The age of the Milky Way halo stars from the Sloan Digital Sky Survey, A&A, 533, A59, doi: 10.1051/0004-6361/201117131

Jofré P., Weiss A. 2011b, The age of the Milky Way halo stars from the Sloan Digital Sky Survey, A&A, 533, A59, doi: 10.1051/0004-6361/201117131

Johnston K. V. 1998, A Prescription for Building the Milky Way's Halo from Disrupted Satellites, ApJ, 495, 297, doi: 10.1086/305273

Johnston K. V., Spergel D. N., Haydn C. 2002, How Lumpy Is the Milky Way's Dark Matter Halo?, ApJ, 570, 656, doi: 10.1086/339791

Julian W. H., Toomre A. 1966, Non-Axisymmetric Responses of Differentially Rotating Disks of Stars, ApJ, 146, 810, doi: 10.1086/148957

Jurić M., Ivezić Ž., Brooks A., Lupton R. H., Schlegel D., Finkbeiner D., Padmanabhan N., Bond N., Sesar B., Rockosi C. M., Knapp G. R., Gunn J. E., Sumi T., Schneider D. P., Barentine J. C., Brewington H. J., Brinkmann J., Fukugita M., Harvanek M.,

Kleinman S. J., Krzesinski J., Long D., Neilsen Eric H. J., Nitta A., Snedden S. A., York D. G. 2008, The Milky Way Tomography with SDSS. I. Stellar Number Density Distribution, ApJ, 673, 864, doi: 10.1086/523619

Just A., Jahreiß H. 2010, Towards a fully consistent Milky Way disc model - I. The local model based on kinematic and photometric data, MNRAS, 402, 461, doi: 10.1111/j.1365-2966.2009.15893.x

Kafle P. R., Sharma S., Lewis G. F., Robotham A. S. G., Driver S. P. 2018, The need for speed: escape velocity and dynamical mass measurements of the Andromeda galaxy, MNRAS, 475, 4043, doi: 10.1093/mnras/sty082

Kakazu Y., Hu E. M., Liu M. C., Wang W.-H., Wainscoat R. J., Capak P. L. 2010, Hawaii Quasar and T Dwarf Survey. I. Method and Discovery of Faint Field Ultracool Dwarfs, ApJ, 723, 184, doi: 10.1088/0004-637X/723/1/184

Karachentsev I. D., Kaisina E. I. 2019, Dwarf Galaxies in the Local Volume, Astrophysical Bulletin, 74, 111, doi: 10.1134/S1990341319020019

Kazantzidis S., Zentner A. R., Kravtsov A. V., Bullock J. S., Debattista V. P. 2009, Cold Dark Matter Substructure and Galactic Disks. II. Dynamical Effects of Hierarchical Satellite Accretion, ApJ, 700, 1896, doi: 10.1088/0004-637X/700/2/1896

Kereš D., Katz N., Weinberg D. H., Davé R. 2005, How do galaxies get their gas?, MNRAS, 363, 2, doi: 10.1111/j.1365-2966.2005.09451.x

Kerins E. 1997, Low-mass stars and star clusters in the dark Galactic halo, \aap, 328, 5

Kiefer J., Wolfowitz J. 1952, Stochastic Estimation of the Maximum of a Regression Function, Ann. Math. Statist., 23, 462, doi: 10.1214/aoms/1177729392

Kilic M., Munn J. A., Harris H. C., von Hippel T., Liebert J. W., Williams K. A., Jeffery E., DeGennaro S. 2017, The Ages of the Thin Disk, Thick Disk, and the Halo from Nearby White Dwarfs, ApJ, 837, 162, doi: 10.3847/1538-4357/aa62a5

Kimble R. A., MacKenty J. W., O'Connell R. W., Townsend J. A. 2008, Wide Field Camera 3: a powerful new imager for the Hubble Space Telescope, doi: 10.1117/12.789581

Kingma D. P., Ba J. 2014, Adam: A Method for Stochastic Optimization, arXiv e-prints, arXiv:1412.6980. https://arxiv.org/abs/1412.6980

Kirkpatrick J., Looper D., Burgasser A., Schurr S., Cutri R., Cushing M., Cruz K., Sweet A., Knapp G., Barman T., Bochanski J., Roellig T., McLean I., McGovern M., Rice E. 2010, Discoveries from a Near-infrared Proper Motion Survey Using Multi-epoch Two Micron All-Sky Survey Data, \apjs, 190, 100, doi: 10.1088/0067-0049/190/1/100

Kirkpatrick J., Schneider A., Fajardo-Acosta S., Gelino C., Mace G., Wright E., Logsdon S., McLean I., Cushing M., Skrutskie M., Eisenhardt P., Stern D., Baloković M., Burgasser A., Faherty J., Lansbury G., Rich J., Skrzypek N., Fowler J., Cutri R., Masci F., Conrow T., Grillmair C., McCallon H., Beichman C., Marsh K. 2014, The AllWISE Motion Survey and the Quest for Cold Subdwarfs, \apj, 783, 122, doi: 10.1088/0004-637X/783/2/122

Kirkpatrick J. D. 2005, New Spectral Types L and T, ARA&A, 43, 195, doi: 10.1146/annurev.astro.42.053102.134017

Kirkpatrick J. D., Reid I. N., Liebert J., Cutri R. M., Nelson B., Beichman C. A., Dahn C. C., Monet D. G., Gizis J. E., Skrutskie M. F. 1999, Dwarfs Cooler than "M": The Definition of Spectral Type "L" Using Discoveries from the 2 Micron All-Sky Survey (2MASS), ApJ, 519, 802, doi: 10.1086/307414

Kirkpatrick J. D., Reid I. N., Liebert J., Gizis J. E., Burgasser A. J., Monet D. G., Dahn C. C., Nelson B., Williams R. J. 2000, 67 Additional L Dwarfs Discovered by the Two Micron All Sky Survey, AJ, 120, 447, doi: 10.1086/301427

Kirkpatrick J. D., Gelino C. R., Cushing M. C., Mace G. N., Griffith R. L., Skrutskie M. F., Marsh K. A., Wright E. L., Eisenhardt P. R., McLean I. S., Mainzer A. K., Burgasser A. J., Tinney C. G., Parker S., Salter G. 2012, Further Defining Spectral Type "Y" and Exploring the Low-mass End of the Field Brown Dwarf Mass Function, ApJ, 753, 156, doi: 10.1088/0004-637X/753/2/156

Kirkpatrick J. D., Martin E. C., Smart R. L., Cayago A. J., Beichman C. A., Marocco F., Gelino C. R., Faherty J. K., Cushing M. C., Schneider A. C. 2019, Preliminary Trigonometric Parallaxes of 184 Late-T and Y Dwarfs and an Analysis of the Field Substellar Mass Function into the "Planetary" Mass Regime, ApJS, 240, 19, doi: 10.3847/1538-4365/aaf6af

Kirkpatrick J. D., Gelino C. R., Faherty J. K., Meisner A. M., Caselden D., Schneider A. C., Marocco F., Cayago A. J., Smart R. L., Eisenhardt P. R., Kuchner M. J., Wright E. L., Cushing M. C., Allers K. N., Bardalez Gagliuffi D. C., Burgasser A. J., Gagné J., Logsdon S. E., Martin E. C., Ingalls J. G., Lowrance P. J., Abrahams E. S., Aganze C., Gerasimov R., Gonzales E. C., Hsu C.-C., Kamraj N., Kiman R., Rees J., Theissen C., Ammar K., Andersen N. S., Beaulieu P., Colin G., Elachi C. A., Goodman S. J., Gramaize L., Hamlet L. K., Hong J., Jonkeren A., Khalil M., Martin D. W., Pendrill W., Pumphrey B., Rothermich A., Sainio A., Stenner A., Tanner C., Thévenot M., Voloshin N. V., Walla J., Wędracki Z., Backyard Worlds: Planet 9 Collaboration. 2021, The Field Substellar Mass Function Based on the Full-sky 20 pc Census of 525 L, T, and Y Dwarfs, ApJS, 253, 7, doi: 10.3847/1538-4365/abd107

Koekemoer A. M., Faber S. M., Ferguson H. C., Grogin N. A., Kocevski D. D., Koo D. C.,

Lai K., Lotz J. M., Lucas R. A., McGrath E. J., Ogaz S., Rajan A., Riess A. G., Rodney S. A., Strolger L., Casertano S., Castellano M., Dahlen T., Dickinson M., Dolch T., Fontana A., Giavalisco M., Grazian A., Guo Y., Hathi N. P., Huang K.-H., van der Wel A., Yan H.-J., Acquaviva V., Alexander D. M., Almaini O., Ashby M. L. N., Barden M., Bell E. F., Bournaud F., Brown T. M., Caputi K. I., Cassata P., Challis P. J., Chary R.-R., Cheung E., Cirasuolo M., Conselice C. J., Roshan Cooray A., Croton D. J., Daddi E., Davé R., de Mello D. F., de Ravel L., Dekel A., Donley J. L., Dunlop J. S., Dutton A. A., Elbaz D., Fazio G. G., Filippenko A. V., Finkelstein S. L., Frazer C., Gardner J. P., Garnavich P. M., Gawiser E., Gruetzbauch R., Hartley W. G., Häussler B., Herrington J., Hopkins P. F., Huang J.-S., Jha S. W., Johnson A., Kartaltepe J. S., Khostovan A. A., Kirshner R. P., Lani C., Lee K.-S., Li W., Madau P., McCarthy P. J., McIntosh D. H., McLure R. J., McPartland C., Mobasher B., Moreira H., Mortlock A., Moustakas L. A., Mozena M., Nandra K., Newman J. A., Nielsen J. L., Niemi S., Noeske K. G., Papovich C. J., Pentericci L., Pope A., Primack J. R., Ravindranath S., Reddy N. A., Renzini A., Rix H.-W., Robaina A. R., Rosario D. J., Rosati P., Salimbeni S., Scarlata C., Siana B., Simard L., Smidt J., Snyder D., Somerville R. S., Spinrad H., Straughn A. N., Telford O., Teplitz H. I., Trump J. R., Vargas C., Villforth C., Wagner C. R., Wand ro P., Wechsler R. H., Weiner B. J., Wiklind T., Wild V., Wilson G., Wuyts S., Yun M. S. 2011, CANDELS: The Cosmic Assembly Near-infrared Deep Extragalactic Legacy Survey—The Hubble Space Telescope Observations, Imaging Data Products, and Mosaics, ApJS, 197, 36, doi: 10.1088/0067-0049/197/2/36

Koposov S. E., Yoo J., Rix H.-W., Weinberg D. H., Macciò A. V., Escudé J. M. 2009, A Quantitative Explanation of the Observed Population of Milky Way Satellite Galaxies, ApJ, 696, 2179, doi: 10.1088/0004-637X/696/2/2179

Koppelman H. H., Helmi A. 2021, Time evolution of gaps in stellar streams in axisym-

metric Stäckel potentials, A&A, 649, A55, doi: 10.1051/0004-6361/202039968

Koppelman H. H., Helmi A., Massari D., Price-Whelan A. M., Starkenburg T. K. 2019a, Multiple retrograde substructures in the Galactic halo: A shattered view of Galactic history, arXiv e-prints, arXiv:1909.08924. https://arxiv.org/abs/1909.08924

Koppelman H. H., Helmi A., Massari D., Price-Whelan A. M., Starkenburg T. K. 2019b, Multiple retrograde substructures in the Galactic halo: A shattered view of Galactic history, A&A, 631, L9, doi: 10.1051/0004-6361/201936738

Kormendy J., Cornell M. E., Block D. L., Knapen J. H., Allard E. L. 2006, Pseudobulges in the Disk Galaxies NGC 7690 and NGC 4593, ApJ, 642, 765, doi: 10.1086/501341

Kroupa P. 2001, On the variation of the initial mass function, MNRAS, 322, 231, doi: 10.1046/j.1365-8711.2001.04022.x

Kruijssen J. M. D., Pfeffer J. L., Chevance M., Bonaca A., Trujillo-Gomez S., Bastian N., Reina-Campos M., Crain R. A., Hughes M. E. 2020, Kraken reveals itself - the merger history of the Milky Way reconstructed with the E-MOSAICS simulations, MNRAS, 498, 2472, doi: 10.1093/mnras/staa2452

Kumar S. S. 1962, Study of Degeneracy in Very Light Stars., AJ, 67, 579, doi: 10.1086/108658

Kumar S. S. 1963, The Structure of Stars of Very Low Mass., ApJ, 137, 1121, doi: 10.1086/147589

Kümmel M., Walsh J. R., Pirzkal N., Kuntschner H., Pasquali A. 2009, The Slitless Spectroscopy Data Extraction Software aXe, Publications of the Astronomical Society of the Pacific, 121, 59, doi: 10.1086/596715

Kurucz R. L. 1993, VizieR Online Data Catalog: Model Atmospheres (Kurucz, 1979), VizieR Online Data Catalog, VI/39

Lacey C. G. 1984, The influence of massive gas clouds on stellar velocity dispersions in galactic discs, MNRAS, 208, 687, doi: 10.1093/mnras/208.4.687

Lane J., Bovy J., Mackereth T. 2023, The stellar mass of the Gaia-Sausage/Enceladus accretion remnant, arXiv e-prints, arXiv:2306.03084, doi: 10.48550/arXiv.2306.03084

Laporte C. F. P., Minchev I., Johnston K. V., Gómez F. A. 2018, Footprints of the Sagittarius dwarf galaxy in the *Gaia* data set, arXiv e-prints, arXiv:1808.00451, doi: 10.48550/arXiv.1808.00451

Laporte C. F. P., Minchev I., Johnston K. V., Gómez F. A. 2019, Footprints of the Sagittarius dwarf galaxy in the Gaia data set, MNRAS, 485, 3134, doi: 10.1093/mnras/stz583

Laughlin G., Bodenheimer P., Adams F. 1997, The End of the Main Sequence, \apj, 482, 420, doi: 10.1086/304125

Launhardt R., Zylka R., Mezger P. G. 2002, The nuclear bulge of the Galaxy. III. Large-scale physical characteristics of stars and interstellar matter, A&A, 384, 112, doi: 10.1051/0004-6361:20020017

Laureijs R., Amiaux J., Arduini S., Augueres J. L., Brinchmann J., Cole R., Cropper M., Dabin C., Duvet L., Ealet A., Garilli B., Gondoin P., Guzzo L., Hoar J., Hoekstra H., Holmes R., Kitching T., Maciaszek T., Mellier Y., Pasian F., Percival W., Rhodes J., Saavedra Criado G., Sauvage M., Scaramella R., Valenziano L., Warren S., Bender R., Castander F., Cimatti A., Le Fèvre O., Kurki-Suonio H., Levi M., Lilje P., Meylan G., Nichol R., Pedersen K., Popa V., Rebolo Lopez R., Rix H. W., Rottgering H.,

Zeilinger W., Grupp F., Hudelot P., Massey R., Meneghetti M., Miller L., Paltani S., Paulin-Henriksson S., Pires S., Saxton C., Schrabback T., Seidel G., Walsh J., Aghanim N., Amendola L., Bartlett J., Baccigalupi C., Beaulieu J. P., Benabed K., Cuby J. G., Elbaz D., Fosalba P., Gavazzi G., Helmi A., Hook I., Irwin M., Kneib J. P., Kunz M., Mannucci F., Moscardini L., Tao C., Teyssier R., Weller J., Zamorani G., Zapatero Osorio M. R., Boulade O., Foumond J. J., Di Giorgio A., Guttridge P., James A., Kemp M., Martignac J., Spencer A., Walton D., Blümchen T., Bonoli C., Bortoletto F., Cerna C., Corcione L., Fabron C., Jahnke K., Ligori S., Madrid F., Martin L., Morgante G., Pamplona T., Prieto E., Riva M., Toledo R., Trifoglio M., Zerbi F., Abdalla F., Douspis M., Grenet C., Borgani S., Bouwens R., Courbin F., Delouis J. M., Dubath P., Fontana A., Frailis M., Grazian A., Koppenhöfer J., Mansutti O., Melchior M., Mignoli M., Mohr J., Neissner C., Noddle K., Poncet M., Scodeggio M., Serrano S., Shane N., Starck J. L., Surace C., Taylor A., Verdoes-Kleijn G., Vuerli C., Williams O. R., Zacchei A., Altieri B., Escudero Sanz I., Kohley R., Oosterbroek T., Astier P., Bacon D., Bardelli S., Baugh C., Bellagamba F., Benoist C., Bianchi D., Biviano A., Branchini E., Carbone C., Cardone V., Clements D., Colombi S., Conselice C., Cresci G., Deacon N., Dunlop J., Fedeli C., Fontanot F., Franzetti P., Giocoli C., Garcia-Bellido J., Gow J., Heavens A., Hewett P., Heymans C., Holland A., Huang Z., Ilbert O., Joachimi B., Jennins E., Kerins E., Kiessling A., Kirk D., Kotak R., Krause O., Lahav O., van Leeuwen F., Lesgourgues J., Lombardi M., Magliocchetti M., Maguire K., Majerotto E., Maoli R., Marulli F., Maurogordato S., McCracken H., McLure R., Melchiorri A., Merson A., Moresco M., Nonino M., Norberg P., Peacock J., Pello R., Penny M., Pettorino V., Di Porto C., Pozzetti L., Quercellini C., Radovich M., Rassat A., Roche N., Ronayette S., Rossetti E., Sartoris B., Schneider P., Semboloni E., Serjeant S., Simpson F., Skordis C., Smadja G., Smartt S., Spano P., Spiro S., Sullivan M., Tilquin A., Trotta R., Verde L., Wang Y., Williger G., Zhao G., Zoubian

J., Zucca E. 2011, Euclid Definition Study Report, arXiv e-prints, arXiv:1110.3193. https://arxiv.org/abs/1110.3193

Lawrence A., Others. 2007, The UKIRT Infrared Deep Sky Survey (UKIDSS), \mnras, 379, 1599, doi: 10.1111/j.1365-2966.2007.12040.x

LeCun Y., Bengio Y., Hinton G. 2015, Deep learning, Nature, 521, 436, doi: 10.1038/nature14539

Leggett S., Ruiz M., Bergeron P. 1998, The Cool White Dwarf Luminosity Function and the Age of the Galactic Disk, \apj, 497, 294, doi: 10.1086/305463

Lépine S., Scholz R.-D. 2008, Twenty-Three New Ultracool Subdwarfs from the Sloan Digital Sky Survey, \apjl, 681, L33, doi: 10.1086/590183

Li J., Liu C., Zhang Z.-Y., Tian H., Fu X., Li J., Yan Z.-Q. 2023, Stellar initial mass function varies with metallicity and time, Nature, 613, 460, doi: 10.1038/s41586-022-05488-1

Li T. S., Ji A. P., Pace A. B., Erkal D., Koposov S. E., Shipp N., Da Costa G. S., Cullinane L. R., Kuehn K., Lewis G. F., Mackey D., Simpson J. D., Zucker D. B., Ferguson P. S., Martell S. L., Bland-Hawthorn J., Balbinot E., Tavangar K., Drlica-Wagner A., De Silva G. M., Simon J. D. 2022, S ^{5}: The Orbital and Chemical Properties of One Dozen Stellar Streams, ApJ, 928, 30, doi: 10.3847/1538-4357/ac46d3

Lilleengen S., Petersen M. S., Erkal D., Peñarrubia J., Koposov S. E., Li T. S., Cullinane L. R., Ji A. P., Kuehn K., Lewis G. F., Mackey D., Pace A. B., Shipp N., Zucker D. B., Bland-Hawthorn J., Hilmi T., S5 Collaboration. 2023, The effect of the deforming dark matter haloes of the Milky Way and the Large Magellanic Cloud on the Orphan-Chenab stream, MNRAS, 518, 774, doi: 10.1093/mnras/stac3108

Lin C. C., Shu F. H. 1964, On the Spiral Structure of Disk Galaxies., ApJ, 140, 646, doi: 10.1086/147955

Lin C. C., Shu F. H. 1966, On the Spiral Structure of Disk Galaxies, II. Outline of a Theory of Density Waves, Proceedings of the National Academy of Science, 55, 229, doi: 10.1073/pnas.55.2.229

Line M. R., Fortney J. J., Marley M. S., Sorahana S. 2014, A Data-driven Approach for Retrieving Temperatures and Abundances in Brown Dwarf Atmospheres, 793, 33, doi: 10.1088/0004-637X/793/1/33

Linsky J. L. 1969, On the Pressure-Induced Opacity of Molecular Hydrogen in Late-Type Stars, ApJ, 156, 989, doi: 10.1086/150030

Liu C., Xu Y., Wan J.-C., Wang H.-F., Carlin J. L., Deng L.-C., Newberg H. J., Cao Z.-H., Hou Y.-H., Wang Y.-F., Zhang Y. 2017, Mapping the Milky Way with LAMOST I: method and overview, Research in Astronomy and Astrophysics, 17, 096, doi: 10.1088/1674-4527/17/9/96

Liu M. C., Leggett S. K., Golimowski D. A., Chiu K., Fan X., Geballe T. R., Schneider D. P., Brinkmann J. 2006, SDSS J1534+1615AB: A Novel T Dwarf Binary Found with Keck Laser Guide Star Adaptive Optics and the Potential Role of Binarity in the L/T Transition, ApJ, 647, 1393, doi: 10.1086/505561

Lodieu N., Burgasser A. J., Pavlenko Y., Rebolo R. 2015, A search for lithium in metal-poor L dwarfs, A&A, 579, A58, doi: 10.1051/0004-6361/201425551

Lodieu N., Espinoza Contreras M., Zapatero Osorio M. R., Solano E., Aberasturi M., Martín E. L., Rodrigo C. 2017, New ultracool subdwarfs identified in large-scale surveys using Virtual Observatory tools, Astronomy & Astrophysics, 598, A92, doi: 10.1051/0004-6361/201629410

Lodieu N., Zapatero Osorio M. R., Martín E. L., Solano E., Aberasturi M. 2010, GTC/OSIRIS Spectroscopic Identification of a Faint L Subdwarf in the UKIRT Infrared Deep Sky Survey, ApJ, 708, L107, doi: 10.1088/2041-8205/708/2/L107

Loebman S. R., Roškar R., Debattista V. P., Ivezić Ž., Quinn T. R., Wadsley J. 2011, The Genesis of the Milky Way's Thick Disk Via Stellar Migration, ApJ, 737, 8, doi: 10.1088/0004-637X/737/1/8

Looper D. L., Gelino C. R., Burgasser A. J., Kirkpatrick J. D. 2008, Discovery of a T Dwarf Binary with the Largest Known J-Band Flux Reversal, ApJ, 685, 1183, doi: 10.1086/590382

López-Corredoira M., Cabrera-Lavers A., Garzón F., Hammersley P. L. 2002, Old stellar Galactic disc in near-plane regions according to 2MASS: Scales, cut-off, flare and warp, A&A, 394, 883, doi: 10.1051/0004-6361:20021175

Lopez-Santiago J., Montes D., Crespo-Chacon I., Fernandez-Figueroa M. J. 2006, The Nearest Young Moving Groups, The Astrophysical Journal, 643, 1160, doi: 10.1086/503183

Lovell M. R., Cautun M., Frenk C. S., Hellwing W. A., Newton O. 2021, The spatial distribution of Milky Way satellites, gaps in streams, and the nature of dark matter, MNRAS, 507, 4826, doi: 10.1093/mnras/stab2452

LSST Science Collaboration, Abell P. A., Allison J., Anderson S. F., Andrew J. R., Angel J. R. P., Armus L., Arnett D., Asztalos S. J., Axelrod T. S., Bailey S., Ballantyne D. R., Bankert J. R., Barkhouse W. A., Barr J. D., Barrientos L. F., Barth A. J., Bartlett J. G., Becker A. C., Becla J., Beers T. C., Bernstein J. P., Biswas R., Blanton M. R., Bloom J. S., Bochanski J. J., Boeshaar P., Borne K. D., Bradac M., Brandt W. N., Bridge C. R., Brown M. E., Brunner R. J., Bullock J. S., Burgasser A. J., Burge J. H., Burke D. L.,

Cargile P. A., Chandrasekharan S., Chartas G., Chesley S. R., Chu Y.-H., Cinabro D., Claire M. W., Claver C. F., Clowe D., Connolly A. J., Cook K. H., Cooke J., Cooray A., Covey K. R., Culliton C. S., de Jong R., de Vries W. H., Debattista V. P., Delgado F., Dell'Antonio I. P., Dhital S., Di Stefano R., Dickinson M., Dilday B., Djorgovski S. G., Dobler G., Donalek C., Dubois-Felsmann G., Durech J., Eliasdottir A., Eracleous M., Eyer L., Falco E. E., Fan X., Fassnacht C. D., Ferguson H. C., Fernandez Y. R., Fields B. D., Finkbeiner D., Figueroa E. E., Fox D. B., Francke H., Frank J. S., Frieman J., Fromenteau S., Furqan M., Galaz G., Gal-Yam A., Garnavich P., Gawiser E., Geary J., Gee P., Gibson R. R., Gilmore K., Grace E. A., Green R. F., Gressler W. J., Grillmair C. J., Habib S., Haggerty J. S., Hamuy M., Harris A. W., Hawley S. L., Heavens A. F., Hebb L., Henry T. J., Hileman E., Hilton E. J., Hoadley K., Holberg J. B., Holman M. J., Howell S. B., Infante L., Ivezic Z., Jacoby S. H., Jain B., R, Jedicke, Jee M. J., Garrett Jernigan J., Jha S. W., Johnston K. V., Jones R. L., Juric M., Kaasalainen M., Styliani, Kafka, Kahn S. M., Kaib N. A., Kalirai J., Kantor J., Kasliwal M. M., Keeton C. R., Kessler R., Knezevic Z., Kowalski A., Krabbendam V. L., Krughoff K. S., Kulkarni S., Kuhlman S., Lacy M., Lepine S., Liang M., Lien A., Lira P., Long K. S., Lorenz S., Lotz J. M., Lupton R. H., Lutz J., Macri L. M., Mahabal A. A., Mandelbaum R., Marshall P., May M., McGehee P. M., Meadows B. T., Meert A., Milani A., Miller C. J., Miller M., Mills D., Minniti D., Monet D., Mukadam A. S., Nakar E., Neill D. R., Newman J. A., Nikolaev S., Nordby M., O'Connor P., Oguri M., Oliver J., Olivier S. S., Olsen J. K., Olsen K., Olszewski E. W., Oluseyi H., Padilla N. D., Parker A., Pepper J., Peterson J. R., Petry C., Pinto P. A., Pizagno J. L., Popescu B., Prsa A., Radcka V., Raddick M. J., Rasmussen A., Rau A., Rho J., Rhoads J. E., Richards G. T., Ridgway S. T., Robertson B. E., Roskar R., Saha A., Sarajedini A., Scannapieco E., Schalk T., Schindler R., Schmidt S., Schmidt S., Schneider D. P., Schumacher G., Scranton R., Sebag J., Seppala L. G., Shemmer O., Simon J. D., Sivertz M., Smith H. A., Allyn

Smith J., Smith N., Spitz A. H., Stanford A., Stassun K. G., Strader J., Strauss M. A., Stubbs C. W., Sweeney D. W., Szalay A., Szkody P., Takada M., Thorman P., Trilling D. E., Trimble V., Tyson A., Van Berg R., Vanden Berk D., VanderPlas J., Verde L., Vrsnak B., Walkowicz L. M., Wandelt B. D., Wang S., Wang Y., Warner M., Wechsler R. H., West A. A., Wiecha O., Williams B. F., Willman B., Wittman D., Wolff S. C., Wood-Vasey W. M., Wozniak P., Young P., Zentner A., Zhan H. 2009, LSST Science Book, Version 2.0, arXiv e-prints, arXiv:0912.0201, doi: 10.48550/arXiv.0912.0201

Ma X., Hopkins P. F., Wetzel A. R., Kirby E. N., Anglés-Alcázar D., Faucher-Giguère C.-A., Kereš D., Quataert E. 2017, The structure and dynamical evolution of the stellar disc of a simulated Milky Way-mass galaxy, MNRAS, 467, 2430, doi: 10.1093/mnras/stx273

Mackereth J. T., Bovy J., Schiavon R. P., Zasowski G., Cunha K., Frinchaboy P. M., García Perez A. E., Hayden M. R., Holtzman J., Majewski S. R., Mészáros S., Nidever D. L., Pinsonneault M., Shetrone M. D. 2017, The age-metallicity structure of the Milky Way disc using APOGEE, MNRAS, 471, 3057, doi: 10.1093/mnras/stx1774

Mackereth J. T., Schiavon R. P., Pfeffer J., Hayes C. R., Bovy J., Anguiano B., Allende Prieto C., Hasselquist S., Holtzman J., Johnson J. A., Majewski S. R., O'Connell R., Shetrone M., Tissera P. B., Fernández-Trincado J. G. 2019a, The origin of accreted stellar halo populations in the Milky Way using APOGEE, Gaia, and the EAGLE simulations, MNRAS, 482, 3426, doi: 10.1093/mnras/sty2955

Mackereth J. T., Bovy J., Leung H. W., Schiavon R. P., Trick W. H., Chaplin W. J., Cunha K., Feuillet D. K., Majewski S. R., Martig M., Miglio A., Nidever D., Pinsonneault M. H., Aguirre V. S., Sobeck J., Tayar J., Zasowski G. 2019b, Dynamical heating across the Milky Way disc using APOGEE and Gaia, MNRAS, 489, 176, doi: 10.1093/mnras/stz1521

Mackey A. D., Ferguson A. M. N., Huxor A. P., Veljanoski J., Lewis G. F., McConnachie A. W., Martin N. F., Ibata R. A., Irwin M. J., Côté P., Collins M. L. M., Tanvir N. R., Bate N. F. 2019, The outer halo globular cluster system of M31 - III. Relationship to the stellar halo, MNRAS, 484, 1756, doi: 10.1093/mnras/stz072

Majewski S. R., Skrutskie M. F., Weinberg M. D., Ostheimer J. C. 2003, A Two Micron All Sky Survey View of the Sagittarius Dwarf Galaxy. I. Morphology of the Sagittarius Core and Tidal Arms, ApJ, 599, 1082, doi: 10.1086/379504

Majewski S. R., Schiavon R. P., Frinchaboy P. M., Allende Prieto C., Barkhouser R., Bizyaev D., Blank B., Brunner S., Burton A., Carrera R., Chojnowski S. D., Cunha K., Epstein C., Fitzgerald G., García Pérez A. E., Hearty F. R., Henderson C., Holtzman J. A., Johnson J. A., Lam C. R., Lawler J. E., Maseman P., Mészáros S., Nelson M., Nguyen D. C., Nidever D. L., Pinsonneault M., Shetrone M., Smee S., Smith V. V., Stolberg T., Skrutskie M. F., Walker E., Wilson J. C., Zasowski G., Anders F., Basu S., Beland S., Blanton M. R., Bovy J., Brownstein J. R., Carlberg J., Chaplin W., Chiappini C., Eisenstein D. J., Elsworth Y., Feuillet D., Fleming S. W., Galbraith-Frew J., García R. A., García-Hernández D. A., Gillespie B. A., Girardi L., Gunn J. E., Hasselquist S., Hayden M. R., Hekker S., Ivans I., Kinemuchi K., Klaene M., Mahadevan S., Mathur S., Mosser B., Muna D., Munn J. A., Nichol R. C., O'Connell R. W., Parejko J. K., Robin A. C., Rocha-Pinto H., Schultheis M., Serenelli A. M., Shane N., Silva Aguirre V., Sobeck J. S., Thompson B., Troup N. W., Weinberg D. H., Zamora O. 2017, The Apache Point Observatory Galactic Evolution Experiment (APOGEE), AJ, 154, 94, doi: 10.3847/1538-3881/aa784d

Malhan K., Ibata R. A. 2018, STREAMFINDER - I. A new algorithm for detecting stellar streams, MNRAS, 477, 4063, doi: 10.1093/mnras/sty912

Malhan K., Ibata R. A., Martin N. F. 2018, Ghostly tributaries to the Milky Way:

charting the halo's stellar streams with the Gaia DR2 catalogue, MNRAS, 481, 3442, doi: 10.1093/mnras/sty2474

Malkan M. A., Alavi A., Atek H., Baronchelli I., Battisti A. J., Bradac M., Bruton S. T., Bunker A., Burgasser A. J., Colbert J., Dai S., Hayes M. J., Henry A. L., Jones T., Leethochawalit N., Mason C., Mehta V., Morishita T., Rafelski M., Roberts-Borsani G., Rutkowski M. J., Scarlata C., Schmidt K. B., Teplitz H., Trenti M., Treu T. L., Vulcani B., Wang X. 2021, PASSAGE-Parallel Application of Slitless Spectroscopy to Analyze Galaxy Evolution, JWST Proposal. Cycle 1

Mamajek E. E. 2015, A Pre-Gaia Census of Nearby Stellar Groups, Proceedings of the International Astronomical Union, 10, 21, doi: 10.1017/S1743921315006250

Manjavacas E., Apai D., Zhou Y., Karalidi T., Lew B. W. P., Schneider G., Cowan N., Metchev S., Miles-Páez P. A., Burgasser A. J., Radigan J., Bedin L. R., Lowrance P. J., Marley M. S. 2017, Cloud Atlas: Discovery of Rotational Spectral Modulations in a Low-mass, L-type Brown Dwarf Companion to a Star, The Astronomical Journal, 155, 11, doi: 10.3847/1538-3881/aa984f

Manjavacas E., Apai D., Zhou Y., Lew B. W. P., Schneider G., Metchev S., Miles-Páez P. A., Radigan J., Marley M. S., Cowan N., Karalidi T., Burgasser A. J., Bedin L. R., Lowrance P. J., Kauffmann P. 2019, Cloud Atlas: Hubble Space Telescope Near-infrared Spectral Library of Brown Dwarfs, Planetary-mass Companions, and Hot Jupiters, AJ, 157, 101, doi: 10.3847/1538-3881/aaf88f

Mao Y.-Y., Geha M., Wechsler R. H., Weiner B., Tollerud E. J., Nadler E. O., Kallivayalil N. 2021, The SAGA Survey. II. Building a Statistical Sample of Satellite Systems around Milky Way-like Galaxies, ApJ, 907, 85, doi: 10.3847/1538-4357/abce58

Marley M., Saumon D., Morley C., Fortney J. 2018, Sonora 2018: Cloud-free, solar composition, solar C/O substellar atmosphere models and spectra, nc_m+0.0_co1.0_v1.0, Zenodo, doi: 10.5281/zenodo.1309035

Marley M. S., Saumon D., Visscher C., Lupu R., Freedman R., Morley C., Fortney J. J., Seay C., Smith A. J. R. W., Teal D. J., Wang R. 2021, The Sonora Brown Dwarf Atmosphere and Evolution Models. I. Model Description and Application to Cloudless Atmospheres in Rainout Chemical Equilibrium, ApJ, 920, 85, doi: 10.3847/1538-4357/ac141d

Márquez-Neila P., Fisher C., Sznitman R., Heng K. 2018, Supervised machine learning for analysing spectra of exoplanetary atmospheres, Nature Astronomy, 2, 719, doi: 10.1038/s41550-018-0504-2

Martell S. L., Sharma S., Buder S., Duong L., Schlesinger K. J., Simpson J., Lind K., Ness M., Marshall J. P., Asplund M., Bland-Hawthorn J., Casey A. R., De Silva G., Freeman K. C., Kos J., Lin J., Zucker D. B., Zwitter T., Anguiano B., Bacigalupo C., Carollo D., Casagrande L., Da Costa G. S., Horner J., Huber D., Hyde E. A., Kafle P. R., Lewis G. F., Nataf D., Navin C. A., Stello D., Tinney C. G., Watson F. G., Wittenmyer R. 2017, The GALAH survey: observational overview and Gaia DR1 companion, MNRAS, 465, 3203, doi: 10.1093/mnras/stw2835

Martig M., Minchev I., Flynn C. 2014, Dissecting simulated disc galaxies - II. The age-velocity relation, MNRAS, 443, 2452, doi: 10.1093/mnras/stu1322

Martín E. L., Lodieu N., Pavlenko Y., Béjar V. J. S. 2018, The Lithium Depletion Boundary and the Age of the Hyades Cluster, ApJ, 856, 40, doi: 10.3847/1538-4357/aaaeb8

Martin N. F., de Jong J. T. A., Rix H.-W. 2008, A Comprehensive Maximum Likelihood

Analysis of the Structural Properties of Faint Milky Way Satellites, ApJ, 684, 1075, doi: 10.1086/590336

Martin N. F., Ibata R. A., Lewis G. F., McConnachie A., Babul A., Bate N. F., Bernard E., Chapman S. C., Collins M. M. L., Conn A. R., Crnojević D., Fardal M. A., Ferguson A. M. N., Irwin M., Mackey A. D., McMonigal B., Navarro J. F., Rich R. M. 2016, The PAndAS View of the Andromeda Satellite System. II. Detailed Properties of 23 M31 Dwarf Spheroidal Galaxies, ApJ, 833, 167, doi: 10.3847/1538-4357/833/2/167

Martin N. F., Ibata R. A., Starkenburg E., Yuan Z., Malhan K., Bellazzini M., Viswanathan A., Aguado D., Arentsen A., Bonifacio P., Carlberg R., González Hernández J. I., Hill V., Jablonka P., Kordopatis G., Lardo C., McConnachie A. W., Navarro J., Sánchez-Janssen R., Sestito F., Thomas G. F., Venn K. A., Vitali S., Voggel K. T. 2022, The Pristine survey - XVI. The metallicity of 26 stellar streams around the Milky Way detected with the STREAMFINDER in Gaia EDR3, MNRAS, 516, 5331, doi: 10.1093/mnras/stac2426

Martínez-Delgado D., Gabany R. J., Crawford K., Zibetti S., Majewski S. R., Rix H.-W., Fliri J., Carballo-Bello J. A., Bardalez-Gagliuffi D. C., Peñarrubia J., Chonis T. S., Madore B., Trujillo I., Schirmer M., McDavid D. A. 2010, Stellar Tidal Streams in Spiral Galaxies of the Local Volume: A Pilot Survey with Modest Aperture Telescopes, AJ, 140, 962, doi: 10.1088/0004-6256/140/4/962

Martinez-Delgado D., Cooper A. P., Roman J., Pillepich A., Erkal D., Pearson S., Moustakas J., Laporte C. F. P., Laine S., Akhlaghi M., Lang D., Makarov D., Borlaff A. S., Donatiello G., Pearson W. J., Miro-Carretero J., Cuillandre J.-C., Dominguez H., Roca-Fabrega S., Frenk C. S., Schmidt J., Gomez-Flechoso M. A., Guzman R., Libeskind N. I., Dey A., Weaver B. A., Schlegel D., Myers A. D., Valdes F. G. 2021,

Hidden depths in the local Universe: The Stellar Stream Legacy Survey, arXiv e-prints, arXiv:2104.06071. https://arxiv.org/abs/2104.06071

Masters D., McCarthy P., Burgasser A., Hathi N., Malkan M., Ross N., Siana B., Scarlata C., Henry A., Colbert J., Atek H., Rafelski M., Teplitz H., Bunker A., Dressler A. 2012, Discovery of Three Distant, Cold Brown Dwarfs in the WFC3 Infrared Spectroscopic Parallels Survey, \apjl, 752, L14, doi: 10.1088/2041-8205/752/1/L14

Mateu C. 2023, galstreams: A Library of Milky Way Stellar Stream Footprints and Tracks, MNRAS, doi: 10.1093/mnras/stad321

Mateu C., Cooper A. P., Font A. S., Aguilar L., Frenk C., Cole S., Wang W., McCarthy I. G. 2017, Predictions for the detection of tidal streams with Gaia using great-circle methods, MNRAS, 469, 721, doi: 10.1093/mnras/stx872

Mateu C., Read J. I., Kawata D. 2018, Fourteen candidate RR Lyrae star streams in the inner Galaxy, MNRAS, 474, 4112, doi: 10.1093/mnras/stx2937

McConnachie A. W. 2012, The Observed Properties of Dwarf Galaxies in and around the Local Group, AJ, 144, 4, doi: 10.1088/0004-6256/144/1/4

McConnachie A. W., Irwin M. J., Ibata R. A., Dubinski J., Widrow L. M., Martin N. F., Côté P., Dotter A. L., Navarro J. F., Ferguson A. M. N., Puzia T. H., Lewis G. F., Babul A., Barmby P., Bienaymé O., Chapman S. C., Cockcroft R., Collins M. L. M., Fardal M. A., Harris W. E., Huxor A., Mackey A. D., Peñarrubia J., Rich R. M., Richer H. B., Siebert A., Tanvir N., Valls-Gabaud D., Venn K. A. 2009, The remnants of galaxy formation from a panoramic survey of the region around M31, Nature, 461, 66, doi: 10.1038/nature08327

McConnachie A. W., Ibata R., Martin N., Ferguson A. M. N., Collins M., Gwyn S., Irwin M., Lewis G. F., Mackey A. D., Davidge T., Arias V., Conn A., Côté P., Crnojevic D.,

Huxor A., Penarrubia J., Spengler C., Tanvir N., Valls-Gabaud D., Babul A., Barmby P., Bate N. F., Bernard E., Chapman S., Dotter A., Harris W., McMonigal B., Navarro J., Puzia T. H., Rich R. M., Thomas G., Widrow L. M. 2018, The Large-scale Structure of the Halo of the Andromeda Galaxy. II. Hierarchical Structure in the Pan-Andromeda Archaeological Survey, ApJ, 868, 55, doi: 10.3847/1538-4357/aae8e7

McKee C. F., Ostriker E. C. 2007, Theory of Star Formation, ARA&A, 45, 565, doi: 10.1146/annurev.astro.45.051806.110602

McMillan P. J. 2017, The mass distribution and gravitational potential of the Milky Way, MNRAS, 465, 76, doi: 10.1093/mnras/stw2759

Medan I., Lépine S. 2023, Chemodynamical ages of small-scale kinematic structures of the galactic disc in the solar neighbourhood from 250 000 K and M dwarfs, MNRAS, 521, 208, doi: 10.1093/mnras/stad435

Metchev S., Kirkpatrick J., Berriman G., Looper D. 2008, A Cross-Match of 2MASS and SDSS: Newly Found L and T Dwarfs and an Estimate of the Space Density of T Dwarfs, \apj, 676, 1281, doi: 10.1086/524721

Miller A. A., Kulkarni M. K., Cao Y., Laher R. R., Masci F. J., Surace J. A. 2017, Preparing for Advanced LIGO: A Star-Galaxy Separation Catalog for the Palomar Transient Factory, The Astronomical Journal, 153, 73, doi: 10.3847/1538-3881/153/2/73

Miller G. E., Scalo J. M. 1979, The Initial Mass Function and Stellar Birthrate in the Solar Neighborhood, ApJS, 41, 513, doi: 10.1086/190629

Minchev I., Martig M., Streich D., Scannapieco C., de Jong R. S., Steinmetz M. 2015, On the Formation of Galactic Thick Disks, ApJL, 804, L9, doi: 10.1088/2041-8205/804/1/L9

Miyamoto M., Nagai R. 1975, Three-dimensional models for the distribution of mass in galaxies., PASJ, 27, 533

Momcheva I. G., Brammer G. B., van Dokkum P. G., Skelton R. E., Whitaker K. E., Nelson E. J., Fumagalli M., Maseda M. V., Leja J., Franx M., Rix H.-W., Bezanson R., Cunha E. D., Dickey C., Schreiber N. M. F., Illingworth G., Kriek M., Labbé I., Lange J. U., Lundgren B. F., Magee D., Marchesini D., Oesch P., Pacifici C., Patel S. G., Price S., Tal T., Wake D. A., van der Wel A., Wuyts S. 2016, THE 3D-HST SURVEY: HUBBLE SPACE TELESCOPE WFC3/G141 GRISM SPECTRA, REDSHIFTS, AND EMISSION LINE MEASUREMENTS FOR 100,000 GALAXIES, The Astrophysical Journal Supplement Series, 225, 27, doi: 10.3847/0067-0049/225/2/27

Morgan W. W., Sharpless S., Osterbrock D. 1952, Some features of galactic structure in the neighborhood of the Sun., AJ, 57, 3, doi: 10.1086/106673

Myeong G. C., Evans N. W., Belokurov V., Sand ers J. L., Koposov S. E. 2018, The Milky Way Halo in Action Space, ApJL, 856, L26, doi: 10.3847/2041-8213/aab613

Myeong G. C., Vasiliev E., Iorio G., Evans N. W., Belokurov V. 2019, Evidence for two early accretion events that built the Milky Way stellar halo, MNRAS, 488, 1235, doi: 10.1093/mnras/stz1770

Naidu R. P., Conroy C., Bonaca A., Johnson B. D., Ting Y.-S., Caldwell N., Zaritsky D., Cargile P. A. 2020, Evidence from the H3 Survey That the Stellar Halo Is Entirely Comprised of Substructure, ApJ, 901, 48, doi: 10.3847/1538-4357/abaef4

Nair V., Hinton G. E. 2010, in ICML, 807–814. https://icml.cc/Conferences/2010/papers/432.pdf

Nakajima T., Oppenheimer B. R., Kulkarni S. R., Golimowski D. A., Matthews K.,

Durrance S. T. 1995, Discovery of a cool brown dwarf, Nature, 378, 463, doi: 10.1038/378463a0

Navarro J. F., Benz W. 1991, Dynamics of Cooling Gas in Galactic Dark Halos, ApJ, 380, 320, doi: 10.1086/170590

Navarro J. F., Eke V. R., Frenk C. S. 1996, The cores of dwarf galaxy haloes, MNRAS, 283, L72, doi: 10.1093/mnras/283.3.L72

Ness M., Freeman K., Athanassoula E., Wylie-de-Boer E., Bland-Hawthorn J., Asplund M., Lewis G. F., Yong D., Lane R. R., Kiss L. L. 2013, ARGOS - III. Stellar populations in the Galactic bulge of the Milky Way, MNRAS, 430, 836, doi: 10.1093/mnras/sts629

Newberg H. J., Yanny B., Willett B. A. 2009, Discovery of a New, Polar-Orbiting Debris Stream in the Milky Way Stellar Halo, ApJ, 700, L61, doi: 10.1088/0004-637X/700/2/L61

Newberg H. J., Yanny B., Rockosi C., Grebel E. K., Rix H.-W., Brinkmann J., Csabai I., Hennessy G., Hindsley R. B., Ibata R., Ivezić Z., Lamb D., Nash E. T., Odenkirchen M., Rave H. A., Schneider D. P., Smith J. A., Stolte A., York D. G. 2002, The Ghost of Sagittarius and Lumps in the Halo of the Milky Way, ApJ, 569, 245, doi: 10.1086/338983

Nierenberg A. M., Treu T., Wright S. A., Fassnacht C. D., Auger M. W. 2014, Detection of substructure with adaptive optics integral field spectroscopy of the gravitational lens B1422+231, MNRAS, 442, 2434, doi: 10.1093/mnras/stu862

Nierenberg A. M., Treu T., Brammer G., Peter A. H. G., Fassnacht C. D., Keeton C. R., Kochanek C. S., Schmidt K. B., Sluse D., Wright S. A. 2017, Probing dark matter substructure in the gravitational lens HE 0435-1223 with the WFC3 grism, MNRAS, 471, 2224, doi: 10.1093/mnras/stx1400

Nitschai M. S., Eilers A.-C., Neumayer N., Cappellari M., Rix H.-W. 2021, Dynamical Model of the Milky Way Using APOGEE and Gaia Data, ApJ, 916, 112, doi: 10.3847/1538-4357/ac04b5

Nordström B., Mayor M., Andersen J., Holmberg J., Pont F., Jørgensen B. R., Olsen E. H., Udry S., Mowlavi N. 2004, The Geneva-Copenhagen survey of the Solar neighbourhood. Ages, metallicities, and kinematic properties of ~14 000 F and G dwarfs, A&A, 418, 989, doi: 10.1051/0004-6361:20035959

Odenkirchen M., Grebel E. K., Kayser A., Rix H.-W., Dehnen W. 2009, Kinematics of the Tidal Debris of the Globular Cluster Palomar 5, AJ, 137, 3378, doi: 10.1088/0004-6256/137/2/3378

Odenkirchen M., Grebel E. K., Rockosi C. M., Dehnen W., Ibata R., Rix H.-W., Stolte A., Wolf C., Anderson John E. J., Bahcall N. A., Brinkmann J., Csabai I., Hennessy G., Hindsley R. B., Ivezić Ž., Lupton R. H., Munn J. A., Pier J. R., Stoughton C., York D. G. 2001, Detection of Massive Tidal Tails around the Globular Cluster Palomar 5 with Sloan Digital Sky Survey Commissioning Data, ApJ, 548, L165, doi: 10.1086/319095

Odenkirchen M., Grebel E. K., Dehnen W., Rix H.-W., Yanny B., Newberg H. J., Rockosi C. M., Martínez-Delgado D., Brinkmann J., Pier J. R. 2003, The Extended Tails of Palomar 5: A 10° Arc of Globular Cluster Tidal Debris, AJ, 126, 2385, doi: 10.1086/378601

Okamoto T., Gao L., Theuns T. 2008, Mass loss of galaxies due to an ultraviolet background, MNRAS, 390, 920, doi: 10.1111/j.1365-2966.2008.13830.x

Oreshenko M., Kitzmann D., Márquez-Neila P., Malik M., Bowler B. P., Burgasser A. J., Sznitman R., Fisher C. E., Heng K. 2020, Supervised Machine Learning for

Intercomparison of Model Grids of Brown Dwarfs: Application to GJ 570D and the Epsilon Indi B Binary System, AJ, 159, 6, doi: 10.3847/1538-3881/ab5955

Oser L., Ostriker J. P., Naab T., Johansson P. H., Burkert A. 2010, The Two Phases of Galaxy Formation, ApJ, 725, 2312, doi: 10.1088/0004-637X/725/2/2312

Parzen E. 1962, On Estimation of a Probability Density Function and Mode, Ann. Math. Statist., 33, 1065, doi: 10.1214/aoms/1177704472

Peñarrubia J., Walker M. G., Gilmore G. 2009, Tidal disruption of globular clusters in dwarf galaxies with triaxial dark matter haloes, MNRAS, 399, 1275, doi: 10.1111/j.1365-2966.2009.15027.x

Pearson S., Clark S. E., Demirjian A. J., Johnston K. V., Ness M. K., Starkenburg T. K., Williams B. F., Ibata R. A. 2022, The Hough Stream Spotter: A New Method for Detecting Linear Structure in Resolved Stars and Application to the Stellar Halo of M31, ApJ, 926, 166, doi: 10.3847/1538-4357/ac4496

Pearson S., Price-Whelan A. M., Johnston K. V. 2017, Gaps and length asymmetry in the stellar stream Palomar 5 as effects of Galactic bar rotation, Nature Astronomy, 1, 633, doi: 10.1038/s41550-017-0220-3

Pearson S., Starkenburg T. K., Johnston K. V., Williams B. F., Ibata R. A., Khan R. 2019, Detecting Thin Stellar Streams in External Galaxies: Resolved Stars and Integrated Light, ApJ, 883, 87, doi: 10.3847/1538-4357/ab3e06

Pecaut M. J., Mamajek E. E. 2013, Intrinsic Colors, Temperatures, and Bolometric Corrections of Pre-Main-Sequence Stars, The Astrophysical Journal Supplement Series, 208, doi: 10.1088/0067-0049/208/1/9

Pecaut M. J., Mamajek E. E. 2013, Intrinsic Colors, Temperatures, and Bolometric Corrections of Pre-main-sequence Stars, ApJS, 208, 9, doi: 10.1088/0067-0049/208/1/9

Pedregosa F., Varoquaux G., Gramfort A., Michel V., Thirion B., Grisel O., Blondel M., Prettenhofer P., Weiss R., Dubourg V., Vanderplas J., Passos A., Cournapeau D., Brucher M., Perrot M., Duchesnay E. 2011, Scikit-learn: Machine Learning in Python, Journal of Machine Learning Research, 12, 2825

Phillips M. W., Tremblin P., Baraffe I., Chabrier G., Allard N. F., Spiegelman F., Goyal J. M., Drummond B., Hébrard E. 2020, A new set of atmosphere and evolution models for cool T-Y brown dwarfs and giant exoplanets, A&A, 637, A38, doi: 10.1051/0004-6361/201937381

Piddington J. H., Minnett H. C. 1951, Observations of Galactic Radiation at Frequencies of 1200 and 3000 Mc/s., Australian Journal of Scientific Research A Physical Sciences, 4, 459, doi: 10.1071/CH9510459

Pirzkal N., Xu C., Malhotra S., Rhoads J. E., Koekemoer A. M., Moustakas L. A., Walsh J. R., Windhorst R. A., Daddi E., Cimatti A., Ferguson H. C., Gardner J. P., Gronwall C., Haiman Z., Kümmel M., Panagia N., Pasquali A., Stiavelli M., di Serego Alighieri S., Tsvetanov Z., Vernet J., Yan H. 2004, GRAPES, Grism Spectroscopy of the Hubble Ultra Deep Field: Description and Data Reduction, ApJS, 154, 501, doi: 10.1086/422582

Pirzkal N., Sahu K., Burgasser A., Moustakas L., Xu C., Malhotra S., Rhoads J., Koekemoer A., Nelan E., Windhorst R., Panagia N., Gronwall C., Pasquali A., Walsh J. 2005, Stars in the Hubble Ultra Deep Field, \apj, 622, 319, doi: 10.1086/427896

Pirzkal N., Burgasser A., Malhotra S., Holwerda B., Sahu K., Rhoads J., Xu C., Bochanski

J., Walsh J., Windhorst R., Hathi N., Cohen S. 2009, Spectrophotometrically Identified Stars in the PEARS-N and PEARS-S Fields, \apj, 695, 1591, doi: 10.1088/0004-637X/695/2/1591

Planck Collaboration, Aghanim N., Akrami Y., Ashdown M., Aumont J., Baccigalupi C., Ballardini M., Banday A. J., Barreiro R. B., Bartolo N., Basak S., Battye R., Benabed K., Bernard J. P., Bersanelli M., Bielewicz P., Bock J. J., Bond J. R., Borrill J., Bouchet F. R., Boulanger F., Bucher M., Burigana C., Butler R. C., Calabrese E., Cardoso J. F., Carron J., Challinor A., Chiang H. C., Chluba J., Colombo L. P. L., Combet C., Contreras D., Crill B. P., Cuttaia F., de Bernardis P., de Zotti G., Delabrouille J., Delouis J. M., Di Valentino E., Diego J. M., Doré O., Douspis M., Ducout A., Dupac X., Dusini S., Efstathiou G., Elsner F., Enßlin T. A., Eriksen H. K., Fantaye Y., Farhang M., Fergusson J., Fernandez-Cobos R., Finelli F., Forastieri F., Frailis M., Fraisse A. A., Franceschi E., Frolov A., Galeotta S., Galli S., Ganga K., Génova-Santos R. T., Gerbino M., Ghosh T., González-Nuevo J., Górski K. M., Gratton S., Gruppuso A., Gudmundsson J. E., Hamann J., Handley W., Hansen F. K., Herranz D., Hildebrandt S. R., Hivon E., Huang Z., Jaffe A. H., Jones W. C., Karakci A., Keihänen E., Keskitalo R., Kiiveri K., Kim J., Kisner T. S., Knox L., Krachmalnicoff N., Kunz M., Kurki-Suonio H., Lagache G., Lamarre J. M., Lasenby A., Lattanzi M., Lawrence C. R., Le Jeune M., Lemos P., Lesgourgues J., Levrier F., Lewis A., Liguori M., Lilje P. B., Lilley M., Lindholm V., López-Caniego M., Lubin P. M., Ma Y. Z., Macías-Pérez J. F., Maggio G., Maino D., Mandolesi N., Mangilli A., Marcos-Caballero A., Maris M., Martin P. G., Martinelli M., Martínez-González E., Matarrese S., Mauri N., McEwen J. D., Meinhold P. R., Melchiorri A., Mennella A., Migliaccio M., Millea M., Mitra S., Miville-Deschênes M. A., Molinari D., Montier L., Morgante G., Moss A., Natoli P., Nørgaard-Nielsen H. U., Pagano L., Paoletti D., Partridge B., Patanchon G., Peiris H. V., Perrotta F., Pettorino V., Piacentini F., Polastri L., Polenta

G., Puget J. L., Rachen J. P., Reinecke M., Remazeilles M., Renzi A., Rocha G., Rosset C., Roudier G., Rubiño-Martín J. A., Ruiz-Granados B., Salvati L., Sandri M., Savelainen M., Scott D., Shellard E. P. S., Sirignano C., Sirri G., Spencer L. D., Sunyaev R., Suur-Uski A. S., Tauber J. A., Tavagnacco D., Tenti M., Toffolatti L., Tomasi M., Trombetti T., Valenziano L., Valiviita J., Van Tent B., Vibert L., Vielva P., Villa F., Vittorio N., Wandelt B. D., Wehus I. K., White M., White S. D. M., Zacchei A., Zonca A. 2020, Planck 2018 results. VI. Cosmological parameters, A&A, 641, A6, doi: 10.1051/0004-6361/201833910

Price-Whelan A. M. 2017, Gala: A Python package for galactic dynamics, The Journal of Open Source Software, 2, doi: 10.21105/joss.00388

Price-Whelan A. M., Bonaca A. 2018, Off the Beaten Path: Gaia Reveals GD-1 Stars outside of the Main Stream, ApJ, 863, L20, doi: 10.3847/2041-8213/aad7b5

Price-Whelan A. M., Johnston K. V., Sheffield A. A., Laporte C. F. P., Sesar B. 2015, A reinterpretation of the Triangulum-Andromeda stellar clouds: a population of halo stars kicked out of the Galactic disc, MNRAS, 452, 676, doi: 10.1093/mnras/stv1324

Price-Whelan A. M., Johnston K. V., Valluri M., Pearson S., Küpper A. H. W., Hogg D. W. 2016, Chaotic dispersal of tidal debris, MNRAS, 455, 1079, doi: 10.1093/mnras/stv2383

Price-Whelan A. M., Mateu C., Iorio G., Pearson S., Bonaca A., Belokurov V. 2019, Kinematics of the Palomar 5 Stellar Stream from RR Lyrae Stars, AJ, 158, 223, doi: 10.3847/1538-3881/ab4cef

Quillen A. C. 2002, Prospecting for Spiral Structure in the Flocculent Outer Milky Way Disk with Color-Magnitude Star Counts from the Two Micron All Sky Survey, AJ, 124, 924, doi: 10.1086/341379

Quillen A. C., Minchev I., Bland-Hawthorn J., Haywood M. 2009, Radial mixing in the outer Milky Way disc caused by an orbiting satellite, MNRAS, 397, 1599, doi: 10.1111/j.1365-2966.2009.15054.x

Quillen A. C., Carrillo I., Anders F., McMillan P., Hilmi T., Monari G., Minchev I., Chiappini C., Khalatyan A., Steinmetz M. 2018, Spiral arm crossings inferred from ridges in Gaia stellar velocity distributions, MNRAS, 480, 3132, doi: 10.1093/mnras/sty2077

Rayner J. T., Toomey D. W., Onaka P. M., Denault A. J., Stahlberger W. E., Vacca W. D., Cushing M. C., Wang S. 2003, SpeX: A Medium-Resolution 0.8-5.5 Micron Spectrograph and Imager for the NASA Infrared Telescope Facility, PASP, 115, 362

Reid I. 2003, Meeting the Cool Neighbors. VI. A Search for Nearby Ultracool Dwarfs in the Galactic Plane, \aj, 126, 2449, doi: 10.1086/378907

Reid I., Kirkpatrick J., Liebert J., Burrows A., Gizis J., Burgasser A., Dahn C., Monet D., Cutri R., Beichman C., Skrutskie M. 1999, L Dwarfs and the Substellar Mass Function, \apj, 521, 613, doi: 10.1086/307589

Reid I. N., Yan L., Majewski S., Thompson I., Smail I. 1996, Starcounts Redivivus II: Deep Starcounts With Keck and HST and the Luminosity Function of the Galactic Halo, AJ, 112, 1472, doi: 10.1086/118115

Reylé C., Jardine K., Fouqué P., Caballero J. A., Smart R. L., Sozzetti A. 2021, The 10 parsec sample in the Gaia era, A&A, 650, A201, doi: 10.1051/0004-6361/202140985

Reylé C., Marshall D. J., Robin A. C., Schultheis M. 2009, The Milky Way's external disc constrained by 2MASS star counts, A&A, 495, 819, doi: 10.1051/0004-6361/200811341

Reyle C., Delorme P., Willott C. J., Albert L., Delfosse X., Forveille T., Artigau E., Malo L., Hill G. J., Doyon R. 2010, The ultracool-field dwarf luminosity-function and space density from the Canada-France Brown Dwarf Survey, Astronomy and Astrophysics, Volume 522, id.A112, 15 pp., 522, doi: 10.1051/0004-6361/200913234

Reylé C., Delorme P., Willott C. J., Albert L., Delfosse X., Forveille T., Artigau É., Malo L., Hill G. J., Doyon R. 2010, The ultracool field dwarf luminosity function and space density from the Canada-France Brown Dwarf Survey, A&A, 522, A112+

Richards J. W., Starr D. L., Butler N. R., Bloom J. S., Brewer J. M., Crellin-Quick A., Higgins J., Kennedy R., Rischard M. 2011, On Machine-learned Classification of Variable Stars with Sparse and Noisy Time-series Data, ApJ, 733, 10, doi: 10.1088/0004-637X/733/1/10

Ricker G. R., Winn J. N., Vanderspek R., Latham D. W., Bakos G. Á., Bean J. L., Berta-Thompson Z. K., Brown T. M., Buchhave L., Butler N. R., Butler R. P., Chaplin W. J., Charbonneau D., Christensen-Dalsgaard J., Clampin M., Deming D., Doty J., De Lee N., Dressing C., Dunham E. W., Endl M., Fressin F., Ge J., Henning T., Holman M. J., Howard A. W., Ida S., Jenkins J., Jernigan G., Johnson J. A., Kaltenegger L., Kawai N., Kjeldsen H., Laughlin G., Levine A. M., Lin D., Lissauer J. J., MacQueen P., Marcy G., McCullough P. R., Morton T. D., Narita N., Paegert M., Palle E., Pepe F., Pepper J., Quirrenbach A., Rinehart S. A., Sasselov D., Sato B., Seager S., Sozzetti A., Stassun K. G., Sullivan P., Szentgyorgyi A., Torres G., Udry S., Villasenor J. 2014, in Society of Photo-Optical Instrumentation Engineers (SPIE) Conference Series, Vol. 9143, Space Telescopes and Instrumentation 2014: Optical, Infrared, and Millimeter Wave, ed. J. Oschmann, Jacobus M., M. Clampin, G. G. Fazio, H. A. MacEwen, 914320, doi: 10.1117/12.2063489

Robertson B. E. 2021, Galaxy Formation and Reionization: Key Unknowns and Expected

Breakthroughs by the James Webb Space Telescope, arXiv e-prints, arXiv:2110.13160. https://arxiv.org/abs/2110.13160

Robin A. C., Reylé C., Derrière S., Picaud S. 2003, A synthetic view on structure and evolution of the Milky Way, A&A, 409, 523, doi: 10.1051/0004-6361:20031117

Rocha M., Peter A. H. G., Bullock J. S., Kaplinghat M., Garrison-Kimmel S., Oñorbe J., Moustakas L. A. 2013, Cosmological simulations with self-interacting dark matter - I. Constant-density cores and substructure, MNRAS, 430, 81, doi: 10.1093/mnras/sts514

Rojas-Ayala B., Covey K. R., Muirhead P. S., Lloyd J. P. 2012, Metallicity and Temperature Indicators in M Dwarf K-band Spectra: Testing New and Updated Calibrations with Observations of 133 Solar Neighborhood M Dwarfs, ApJ, 748, 93, doi: 10.1088/0004-637X/748/2/93

Roman N. G. 1950, A Correlation Between the Spectroscopic and Dynamical Characteristics of the Late F - and Early G - Type Stars., ApJ, 112, 554, doi: 10.1086/145367

Rubin V. C., Ford W. K. J., Thonnard N. 1980, Rotational properties of 21 SC galaxies with a large range of luminosities and radii, from NGC 4605 (R=4kpc) to UGC 2885 (R=122kpc)., ApJ, 238, 471, doi: 10.1086/158003

Ruphy S., Robin A. C., Epchtein N., Copet E., Bertin E., Fouque P., Guglielmo F. 1996, New determination of the disc scale length and the radial cutoff in the anticenter with DENIS data., A&A, 313, L21

Ryan R. E. J., Reid I. N. 2016, The Surface Densities of Disk Brown Dwarfs in JWST Surveys, AJ, 151, 92, doi: 10.3847/0004-6256/151/4/92

Ryan R. E. J., Thorman P. A., Yan H., Fan X., Yan L., Mechtley M. R., Hathi N. P., Cohen S. H., Windhorst R. A., McCarthy P. J., Wittman D. M. 2011, HUBBLE

SPACE TELESCOPE OBSERVATIONS OF FIELD ULTRACOOL DWARFS AT HIGH GALACTIC LATITUDE, The Astrophysical Journal, 739, 83, doi: 10.1088/0004-637X/739/2/83

Ryan R.˜E. J., Hathi N., Cohen S., Windhorst R. 2005, Constraining the Distribution of L and T Dwarfs in the Galaxy, \apjl, 631, L159, doi: 10.1086/497368

Ryan Russell E. J., Thorman P. A., Schmidt S. J., Cohen S. H., Hathi N. P., Holwerda B. W., Lunine J. I., Pirzkal N., Windhorst R. A., Young E. 2017, The Effect of Atmospheric Cooling on Vertical Velocity Dispersion and Density Distribution of Brown Dwarfs, The Astrophysical Journal, 847, 53, doi: 10.3847/1538-4357/aa85ea

Salpeter E. E. 1955, The Luminosity Function and Stellar Evolution., ApJ, 121, 161, doi: 10.1086/145971

Sanders J. L., Binney J. 2015, Extended distribution functions for our Galaxy, MNRAS, 449, 3479, doi: 10.1093/mnras/stv578

Sanders J. L., Bovy J., Erkal D. 2016, Dynamics of stream-subhalo interactions, MNRAS, 457, 3817, doi: 10.1093/mnras/stw232

Sanders J. L., Das P. 2018, Isochrone ages for $\sim$3 million stars with the second Gaia data release, MNRAS, 481, 4093, doi: 10.1093/mnras/sty2490

Sanderson R. E., Vera-Ciro C., Helmi A., Heit J. 2016, Stream-subhalo interactions in the Aquarius simulations, arXiv e-prints, arXiv:1608.05624, doi: 10.48550/arXiv.1608.05624

Saumon D., Marley M. 2008, The Evolution of L and T Dwarfs in Color-Magnitude Diagrams, \apj, 689, 1327, doi: 10.1086/592734

Sawala T., Frenk C. S., Fattahi A., Navarro J. F., Theuns T., Bower R. G., Crain R. A., Furlong M., Jenkins A., Schaller M., Schaye J. 2016, The chosen few: the low-mass haloes that host faint galaxies, MNRAS, 456, 85, doi: 10.1093/mnras/stv2597

Schawinski K., Zhang C., Zhang H., Fowler L., Santhanam G. K. 2017, Generative adversarial networks recover features in astrophysical images of galaxies beyond the deconvolution limit, MNRAS, 467, L110, doi: 10.1093/mnrasl/slx008

Schmidhuber J. 2014, Deep Learning in Neural Networks: An Overview, arXiv e-prints, arXiv:1404.7828. https://arxiv.org/abs/1404.7828

Schneider A. C., Cushing M. C., Kirkpatrick J. D., Gelino C. R., Mace G. N., Wright E. L., Eisenhardt P. R., Skrutskie M. F., Griffith R. L., Marsh K. A. 2015, Hubble Space Telescope Spectroscopy of Brown Dwarfs Discovered with the Wide-field Infrared Survey Explorer, ApJ, 804, 92, doi: 10.1088/0004-637X/804/2/92

Schneider A. C., Burgasser A. J., Gerasimov R., Marocco F., Gagné J., Goodman S., Beaulieu P., Pendrill W., Rothermich A., Sainio A., Kuchner M. J., Caselden D., Meisner A. M., Faherty J. K., Mamajek E. E., Hsu C.-C., Greco J. J., Cushing M. C., Kirkpatrick J. D., Bardalez-Gagliuffi D., Logsdon S. E., Allers K., Debes J. H., Backyard Worlds: Planet 9 Collaboration. 2020, WISEA J041451.67-585456.7 and WISEA J181006.18-101000.5: The First Extreme T-type Subdwarfs?, ApJ, 898, 77, doi: 10.3847/1538-4357/ab9a40

Schönrich R., Binney J. 2009, Origin and structure of the Galactic disc(s), MNRAS, 399, 1145, doi: 10.1111/j.1365-2966.2009.15365.x

Schönrich R., Binney J., Dehnen W. 2010, Local kinematics and the local standard of rest, MNRAS, 403, 1829, doi: 10.1111/j.1365-2966.2010.16253.x

Scoville N., Aussel H., Brusa M., Capak P., Carollo C. M., Elvis M., Giavalisco M., Guzzo L., Hasinger G., Impey C., Kneib J., LeFevre O., Lilly S. J., Mobasher B., Renzini A., Rich R. M., Sanders D. B., Schinnerer E., Schminovich D., Shopbell P., Taniguchi Y., Tyson N. D. 2007, The Cosmic Evolution Survey (COSMOS): Overview, The Astrophysical Journal Supplement Series, 172, 1, doi: 10.1086/516585

Searle L., Zinn R. 1978, Composition of halo clusters and the formation of the galactic halo., ApJ, 225, 357, doi: 10.1086/156499

Seigar M. S., Barth A. J., Bullock J. S. 2008, A revised Λ CDM mass model for the Andromeda Galaxy, MNRAS, 389, 1911, doi: 10.1111/j.1365-2966.2008.13732.x

Sellwood J. A. 2014, Secular evolution in disk galaxies, Reviews of Modern Physics, 86, 1, doi: 10.1103/RevModPhys.86.1

Sellwood J. A., Binney J. J. 2002, Radial mixing in galactic discs, MNRAS, 336, 785, doi: 10.1046/j.1365-8711.2002.05806.x

Sellwood J. A., Wilkinson A. 1993, Dynamics of barred galaxies, Reports on Progress in Physics, 56, 173, doi: 10.1088/0034-4885/56/2/001

Semenov V. A., Conroy C., Chandra V., Hernquist L., Nelson D. 2023, Formation of Galactic Disks I: Why did the Milky Way's Disk Form Unusually Early?, arXiv e-prints, arXiv:2306.09398, doi: 10.48550/arXiv.2306.09398

Shallue C. J., Vanderburg A. 2018, Identifying Exoplanets with Deep Learning: A Five-planet Resonant Chain around Kepler-80 and an Eighth Planet around Kepler-90, AJ, 155, 94, doi: 10.3847/1538-3881/aa9e09

Sharma S., Stello D., Buder S., Kos J., Bland-Hawthorn J., Asplund M., Duong L., Lin J., Lind K., Ness M., Huber D., Zwitter T., Traven G., Hon M., Kafle P. R., Khanna

S., Saddon H., Anguiano B., Casey A. R., Freeman K., Martell S., De Silva G. M., Simpson J. D., Wittenmyer R. A., Zucker D. B. 2018, The TESS-HERMES survey data release 1: high-resolution spectroscopy of the TESS southern continuous viewing zone, MNRAS, 473, 2004, doi: 10.1093/mnras/stx2582

Sharma S., Stello D., Bland-Hawthorn J., Hayden M. R., Zinn J. C., Kallinger T., Hon M., Asplund M., Buder S., De Silva G. M., D'Orazi V., Freeman K., Kos J., Lewis G. F., Lin J., Lind K., Martell S., Simpson J. D., Wittenmyer R. A., Zucker D. B., Zwitter T., Bedding T. R., Chen B., Cotar K., Esdaile J., Horner J., Huber D., Kafle P. R., Khanna S., Li T., Ting Y.-S., Nataf D. M., Nordlander T., Saadon M. H. M., Traven G., Wright D., Wyse R. F. G. 2019, The K2-HERMES Survey: age and metallicity of the thick disc, MNRAS, 490, 5335, doi: 10.1093/mnras/stz2861

Sharma S., Hayden M. R., Bland-Hawthorn J., Stello D., Buder S., Zinn J. C., Kallinger T., Asplund M., De Silva G. M., D'Orazi V., Freeman K., Kos J., Lewis G. F., Lin J., Lind K., Martell S., Simpson J. D., Wittenmyer R. A., Zucker D. B., Zwitter T., Chen B., Cotar K., Esdaile J., Hon M., Horner J., Huber D., Kafle P. R., Khanna S., Ting Y.-S., Nataf D. M., Nordlander T., Saadon M. H. M., Tepper-Garcia T., Tinney C. G., Traven G., Watson F., Wright D., Wyse R. F. G. 2021, Fundamental relations for the velocity dispersion of stars in the Milky Way, MNRAS, 506, 1761, doi: 10.1093/mnras/stab1086

Sheinis A., Anguiano B., Asplund M., Bacigalupo C., Barden S., Birchall M., Bland-Hawthorn J., Brzeski J., Cannon R., Carollo D., Case S., Casey A., Churilov V., Warrick C., Dean R., De Silva G., D'Orazi V., Duong L., Farrell T., Fiegert K., Freeman K., Gabriella F., Gers L., Goodwin M., Gray D., Green A., Heald R., Heijmans J., Ireland M., Jones D., Kafle P., Keller S., Klauser U., Kondrat Y., Kos J., Lawrence J., Lee S., Mali S., Martell S., Mathews D., Mayfield D., Miziarski S., Muller R., Pai N.,

Patterson R., Penny E., Orr D., Schlesinger K., Sharma S., Shortridge K., Simpson J., Smedley S., Smith G., Stafford D., Staszak N., Vuong M., Waller L., de Boer E. W., Xavier P., Zheng J., Zhelem R., Zucker D., Zwitter T. 2015, First light results from the High Efficiency and Resolution Multi-Element Spectrograph at the Anglo-Australian Telescope, Journal of Astronomical Telescopes, Instruments, and Systems, 1, 035002, doi: 10.1117/1.JATIS.1.3.035002

Shih D., Buckley M. R., Necib L. 2023, Via Machinae 2.0: Full-Sky, Model-Agnostic Search for Stellar Streams in Gaia DR2, arXiv e-prints, arXiv:2303.01529, doi: 10.48550/arXiv.2303.01529

Shih D., Buckley M. R., Necib L., Tamanas J. 2022, VIA MACHINAE: Searching for stellar streams using unsupervised machine learning, MNRAS, 509, 5992, doi: 10.1093/mnras/stab3372

Shipp N., Drlica-Wagner A., Balbinot E., Ferguson P., Erkal D., Li T. S., Bechtol K., Belokurov V., Buncher B., Carollo D., Carrasco Kind M., Kuehn K., Marshall J. L., Pace A. B., Rykoff E. S., Sevilla-Noarbe I., Sheldon E., Strigari L., Vivas A. K., Yanny B., Zenteno A., Abbott T. M. C., Abdalla F. B., Allam S., Avila S., Bertin E., Brooks D., Burke D. L., Carretero J., Castander F. J., Cawthon R., Crocce M., Cunha C. E., D'Andrea C. B., da Costa L. N., Davis C., De Vicente J., Desai S., Diehl H. T., Doel P., Evrard A. E., Flaugher B., Fosalba P., Frieman J., García-Bellido J., Gaztanaga E., Gerdes D. W., Gruen D., Gruendl R. A., Gschwend J., Gutierrez G., Hartley W., Honscheid K., Hoyle B., James D. J., Johnson M. D., Krause E., Kuropatkin N., Lahav O., Lin H., Maia M. A. G., March M., Martini P., Menanteau F., Miller C. J., Miquel R., Nichol R. C., Plazas A. A., Romer A. K., Sako M., Sanchez E., Santiago B., Scarpine V., Schindler R., Schubnell M., Smith M., Smith R. C., Sobreira F., Suchyta E., Swanson M. E. C., Tarle G., Thomas D., Tucker D. L., Walker A. R.,

Wechsler R. H., DES Collaboration. 2018, Stellar Streams Discovered in the Dark Energy Survey, ApJ, 862, 114, doi: 10.3847/1538-4357/aacdab

Shipp N., Erkal D., Drlica-Wagner A., Li T. S., Pace A. B., Koposov S. E., Cullinane L. R., Da Costa G. S., Ji A. P., Kuehn K., Lewis G. F., Mackey D., Simpson J. D., Wan Z., Zucker D. B., Bland-Hawthorn J., Ferguson P. S., Lilleengen S., Lilleengen S. 2021, Measuring the Mass of the Large Magellanic Cloud with Stellar Streams Observed by S ^{5}, ApJ, 923, 149, doi: 10.3847/1538-4357/ac2e93

Shrestha A., Mahmood A. 2019, Review of Deep Learning Algorithms and Architectures, IEEE Access, 7, 53040, doi: 10.1109/ACCESS.2019.2912200

Simon J. D., Geha M. 2007, The Kinematics of the Ultra-faint Milky Way Satellites: Solving the Missing Satellite Problem, ApJ, 670, 313, doi: 10.1086/521816

Skelton R. E., Whitaker K. E., Momcheva I. G., Brammer G. B., van Dokkum P. G., Labbé I., Franx M., van der Wel A., Bezanson R., Da Cunha E., Fumagalli M., Förster Schreiber N., Kriek M., Leja J., Lundgren B. F., Magee D., Marchesini D., Maseda M. V., Nelson E. J., Oesch P., Pacifici C., Patel S. G., Price S., Rix H.-W., Tal T., Wake D. A., Wuyts S. 2014, 3D-HST WFC3-SELECTED PHOTOMETRIC CATALOGS IN THE FIVE CANDELS/3D-HST FIELDS: PHOTOMETRY, PHOTOMETRIC REDSHIFTS, AND STELLAR MASSES, The Astrophysical Journal Supplement Series, 214, 24, doi: 10.1088/0067-0049/214/2/24

Skrutskie M. F., Cutri R. M., Stiening R., Weinberg M. D., Schneider S., Carpenter J. M., Beichman C., Capps R., Chester T., Elias J., Huchra J., Liebert J., Lonsdale C., Monet D. G., Price S., Seitzer P., Jarrett T., Kirkpatrick J. D., Gizis J. E., Howard E., Evans T., Fowler J., Fullmer L., Hurt R., Light R., Kopan E. L., Marsh K. A., McCallon H. L.,

Tam R., Van Dyk S., Wheelock S. 2006, The Two Micron All Sky Survey (2MASS), AJ, 131, 1163, doi: 10.1086/498708

Skrzypek N., Warren S. J., Faherty J. K. 2016, Photometric brown-dwarf classification. II. A homogeneous sample of 1361 L and T dwarfs brighter than J = 17.5 with accurate spectral types, A&A, 589, A49, doi: 10.1051/0004-6361/201527359

Solano E., Gálvez-Ortiz M. C., Martín E. L., Gómez Muñoz I. M., Rodrigo C., Burgasser A. J., Lodieu N., Béjar V. J. S., Huélamo N., Morales-Calderón M., Bouy H. 2021, Ultracool dwarfs in deep extragalactic surveys using the virtual observatory: ALHAMBRA and COSMOS, MNRAS, 501, 281, doi: 10.1093/mnras/staa3423

Somerville R. S., Davé R. 2015, Physical Models of Galaxy Formation in a Cosmological Framework, ARA&A, 53, 51, doi: 10.1146/annurev-astro-082812-140951

Song I., Bessell M., Zuckerman B. 2002, Lithium Depletion Boundary in a Pre-Main-Sequence Binary System, \apjl, 581, L43, doi: 10.1086/345927

Sorahana S., Nakajima T., Matsuoka Y. 2019, Evaluation of the Vertical Scale Height of L Dwarfs in the Galactic Thin Disk, ApJ, 870, 118, doi: 10.3847/1538-4357/aaf1a7

Spergel D., Gehrels N., Baltay C., Bennett D., Breckinridge J., Donahue M., Dressler A., Gaudi B. S., Greene T., Guyon O., Hirata C., Kalirai J., Kasdin N. J., Macintosh B., Moos W., Perlmutter S., Postman M., Rauscher B., Rhodes J., Wang Y., Weinberg D., Benford D., Hudson M., Jeong W. S., Mellier Y., Traub W., Yamada T., Capak P., Colbert J., Masters D., Penny M., Savransky D., Stern D., Zimmerman N., Barry R., Bartusek L., Carpenter K., Cheng E., Content D., Dekens F., Demers R., Grady K., Jackson C., Kuan G., Kruk J., Melton M., Nemati B., Parvin B., Poberezhskiy I., Peddie C., Ruffa J., Wallace J. K., Whipple A., Wollack E., Zhao F. 2015, Wide-Field

InfrarRed Survey Telescope-Astrophysics Focused Telescope Assets WFIRST-AFTA 2015 Report, arXiv e-prints, arXiv:1503.03757. https://arxiv.org/abs/1503.03757

Spergel D. N., Steinhardt P. J. 2000, Observational Evidence for Self-Interacting Cold Dark Matter, Phys. Rev. Lett., 84, 3760, doi: 10.1103/PhysRevLett.84.3760

Spitzer Lyman J., Schwarzschild M. 1953, The Possible Influence of Interstellar Clouds on Stellar Velocities. II., ApJ, 118, 106, doi: 10.1086/145730

Springel V., Wang J., Vogelsberger M., Ludlow A., Jenkins A., Helmi A., Navarro J. F., Frenk C. S., White S. D. M. 2008, The Aquarius Project: the subhaloes of galactic haloes, MNRAS, 391, 1685, doi: 10.1111/j.1365-2966.2008.14066.x

Stauffer J., Schultz G., Kirkpatrick J. 1998, Keck Spectra of Pleiades Brown Dwarf Candidates and a Precise Determination of the Lithium Depletion Edge in the Pleiades, \apjl, 499, L199+, doi: 10.1086/311379

Tamm A., Tempel E., Tenjes P., Tihhonova O., Tuvikene T. 2012, Stellar mass map and dark matter distribution in M 31, A&A, 546, A4, doi: 10.1051/0004-6361/201220065

Tavangar K., Ferguson P., Shipp N., Drlica-Wagner A., Koposov S., Erkal D., Balbinot E., García-Bellido J., Kuehn K., Lewis G. F., Li T. S., Mau S., Pace A. B., Riley A. H., Abbott T. M. C., Aguena M., Allam S., Andrade-Oliveira F., Annis J., Bertin E., Brooks D., Burke D. L., Carnero Rosell A., Carrasco Kind M., Carretero J., Costanzi M., da Costa L. N., Pereira M. E. S., De Vicente J., Diehl H. T., Everett S., Ferrero I., Flaugher B., Frieman J., Gaztanaga E., Gerdes D. W., Gruen D., Gruendl R. A., Gschwend J., Gutierrez G., Hinton S. R., Hollowood D. L., Honscheid K., James D. J., Kuropatkin N., Maia M. A. G., Marshall J. L., Menanteau F., Miquel R., Morgan R., Ogando R. L. C., Palmese A., Paz-Chinchón F., Pieres A., Plazas Malagón A. A., Rodriguez-Monroy M., Sanchez E., Scarpine V., Serrano S., Sevilla-Noarbe I., Smith M., Suchyta

E., Swanson M. E. C., Tarle G., To C., Varga T. N., Walker A. R. 2022, From the Fire: A Deeper Look at the Phoenix Stream, ApJ, 925, 118, doi: 10.3847/1538-4357/ac399b

Testi L., D'Antona F., Ghinassi F., Licandro J., Magazzù A., Maiolino R., Mannucci F., Marconi A., Nagar N., Natta A., Oliva E. 2001, NICS-TNG Low-Resolution 0.85-2.45 micron Spectra of L Dwarfs: A Near-Infrared Spectral Classification Scheme for Faint Dwarfs, ApJ, 552, L147, doi: 10.1086/320348

The Dark Energy Survey Collaboration. 2005, The Dark Energy Survey, arXiv e-prints, astro. https://arxiv.org/abs/astro-ph/0510346

Tinsley B. M., Larson R. B. 1979, Stellar population explosions in proto-elliptical galaxies., MNRAS, 186, 503, doi: 10.1093/mnras/186.3.503

Tokunaga A., Kobayashi N. 1999, K-Band Spectra and Narrowband Photometry of DENIS Field Brown Dwarfs, \aj, 117, 1010, doi: 10.1086/300732

Tolstoy E., Hill V., Tosi M. 2009, Star-Formation Histories, Abundances, and Kinematics of Dwarf Galaxies in the Local Group, ARA&A, 47, 371, doi: 10.1146/annurev-astro-082708-101650

Toth G., Ostriker J. P. 1992, Galactic Disks, Infall, and the Global Value of Omega, ApJ, 389, 5, doi: 10.1086/171185

Tremblin P., Amundsen D. S., Mourier P., Baraffe I., Chabrier G., Drummond B., Homeier D., Venot O. 2015, Fingering Convection and Cloudless Models for Cool Brown Dwarf Atmospheres, ApJ, 804, L17, doi: 10.1088/2041-8205/804/1/L17

Tulin S., Yu H.-B. 2018, Dark matter self-interactions and small scale structure, Phys. Rep., 730, 1, doi: 10.1016/j.physrep.2017.11.004

van den Bosch F. C., Ogiya G. 2018, Dark matter substructure in numerical simulations: a tale of discreteness noise, runaway instabilities, and artificial disruption, MNRAS, 475, 4066, doi: 10.1093/mnras/sty084

van den Bosch F. C., Ogiya G., Hahn O., Burkert A. 2018, Disruption of dark matter substructure: fact or fiction?, MNRAS, 474, 3043, doi: 10.1093/mnras/stx2956

van der Kruit P. C. 1988, The three-dimensional distribution of light and mass in disks of spiral galaxies., A&A, 192, 117

van Leeuwen F. 2007, Validation of the new Hipparcos reduction, A&A, 474, 653, doi: 10.1051/0004-6361:20078357

van Vledder I., van der Vlugt D., Holwerda B. W., Kenworthy M. A., Bouwens R. J., Trenti M. 2016, The size and shape of the Milky Way disc and halo from M-type brown dwarfs in the BoRG survey, MNRAS, 458, 425, doi: 10.1093/mnras/stw258

Vasiliev E. 2019, Proper motions and dynamics of the Milky Way globular cluster system from Gaia DR2, MNRAS, 484, 2832, doi: 10.1093/mnras/stz171

Veyette M. J., Muirhead P. S., Mann A. W., Brewer J. M., Allard F., Homeier D. 2017, A Physically Motivated and Empirically Calibrated Method to Measure the Effective Temperature, Metallicity, and Ti Abundance of M Dwarfs, ApJ, 851, 26, doi: 10.3847/1538-4357/aa96aa

Vivas A. K., Zinn R. 2006, The QUEST RR Lyrae Survey. II. The Halo Overdensities in the First Catalog, AJ, 132, 714, doi: 10.1086/505200

Walcher C. J., Böker T., Charlot S., Ho L. C., Rix H. W., Rossa J., Shields J. C., van der Marel R. P. 2006, Stellar Populations in the Nuclei of Late-Type Spiral Galaxies, ApJ, 649, 692, doi: 10.1086/505166

Walcher C. J., van der Marel R. P., McLaughlin D., Rix H. W., Böker T., Häring N., Ho L. C., Sarzi M., Shields J. C. 2005, Masses of Star Clusters in the Nuclei of Bulgeless Spiral Galaxies, ApJ, 618, 237, doi: 10.1086/425977

Warren S. J., Ahmed S., Laithwaite R. C. 2021, The local vertical density distribution of ultracool dwarfs M7 to L2.5 and their luminosity function, The Open Journal of Astrophysics, 4, 4, doi: 10.21105/astro.2010.11093

Watkins L. L., Evans N. W., An J. H. 2010, The masses of the Milky Way and Andromeda galaxies, MNRAS, 406, 264, doi: 10.1111/j.1365-2966.2010.16708.x

Weinberg M. D. 1998, Dynamics of an interacting luminous disc, dark halo and satellite companion, MNRAS, 299, 499, doi: 10.1046/j.1365-8711.1998.01790.x

White S. D. M., Frenk C. S. 1991, Galaxy Formation through Hierarchical Clustering, ApJ, 379, 52, doi: 10.1086/170483

White S. D. M., Rees M. J. 1978, Core condensation in heavy halos: a two-stage theory for galaxy formation and clustering., MNRAS, 183, 341, doi: 10.1093/mnras/183.3.341

Wielen R. 1977, The Diffusion of Stellar Orbits Derived from the Observed Age-Dependence of the Velocity Dispersion, A&A, 60, 263

Willman B., Geha M., Strader J., Strigari L. E., Simon J. D., Kirby E., Ho N., Warres A. 2011, Willman 1—A Probable Dwarf Galaxy with an Irregular Kinematic Distribution, AJ, 142, 128, doi: 10.1088/0004-6256/142/4/128

Willman B., Blanton M. R., West A. A., Dalcanton J. J., Hogg D. W., Schneider D. P., Wherry N., Yanny B., Brinkmann J. 2005, A New Milky Way Companion: Unusual Globular Cluster or Extreme Dwarf Satellite?, AJ, 129, 2692, doi: 10.1086/430214

Willott C. J., Doyon R., Albert L., Brammer G. B., Dixon W. V., Muzic K., Ravindranath S., Scholz A., Abraham R., Artigau É., Bradač M., Goudfrooij P., Hutchings J. B., Iyer K. G., Jayawardhana R., LaMassa S., Martis N., Meyer M. R., Morishita T., Mowla L., Muzzin A., Noirot G., Pacifici C., Rowlands N., Sarrouh G., Sawicki M., Taylor J. M., Volk K., Zabl J. 2022, The Near-infrared Imager and Slitless Spectrograph for the James Webb Space Telescope. II. Wide Field Slitless Spectroscopy, PASP, 134, 025002, doi: 10.1088/1538-3873/ac5158

Wright E. L., Eisenhardt P. R. M., Mainzer A. K., Ressler M. E., Cutri R. M., Jarrett T., Kirkpatrick J. D., Padgett D., McMillan R. S., Skrutskie M., Stanford S. A., Cohen M., Walker R. G., Mather J. C., Leisawitz D., Gautier Thomas N. I., McLean I., Benford D., Lonsdale C. J., Blain A., Mendez B., Irace W. R., Duval V., Liu F., Royer D., Heinrichsen I., Howard J., Shannon M., Kendall M., Walsh A. L., Larsen M., Cardon J. G., Schick S., Schwalm M., Abid M., Fabinsky B., Naes L., Tsai C.-W. 2010, The Wide-field Infrared Survey Explorer (WISE): Mission Description and Initial On-orbit Performance, AJ, 140, 1868, doi: 10.1088/0004-6256/140/6/1868

Wu J. F., Peek J. E. G. 2020, Predicting galaxy spectra from images with hybrid convolutional neural networks, arXiv e-prints, arXiv:2009.12318. https://arxiv.org/abs/2009.12318

Yanny B., Rockosi C., Newberg H. J., Knapp G. R., Adelman-McCarthy J. K., Alcorn B., Allam S., Allende Prieto C., An D., Anderson K. S. J., Anderson S., Bailer-Jones C. A. L., Bastian S., Beers T. C., Bell E., Belokurov V., Bizyaev D., Blythe N., Bochanski J. J., Boroski W. N., Brinchmann J., Brinkmann J., Brewington H., Carey L., Cudworth K. M., Evans M., Evans N. W., Gates E., Gänsicke B. T., Gillespie B., Gilmore G., Nebot Gomez-Moran A., Grebel E. K., Greenwell J., Gunn J. E., Jordan C., Jordan W., Harding P., Harris H., Hendry J. S., Holder D., Ivans I. I., Ivezič Ž., Jester S., Johnson

J. A., Kent S. M., Kleinman S., Kniazev A., Krzesinski J., Kron R., Kuropatkin N., Lebedeva S., Lee Y. S., French Leger R., Lépine S., Levine S., Lin H., Long D. C., Loomis C., Lupton R., Malanushenko O., Malanushenko V., Margon B., Martinez-Delgado D., McGehee P., Monet D., Morrison H. L., Munn J. A., Neilsen Eric H. J., Nitta A., Norris J. E., Oravetz D., Owen R., Padmanabhan N., Pan K., Peterson R. S., Pier J. R., Platson J., Re Fiorentin P., Richards G. T., Rix H.-W., Schlegel D. J., Schneider D. P., Schreiber M. R., Schwope A., Sibley V., Simmons A., Snedden S. A., Allyn Smith J., Stark L., Stauffer F., Steinmetz M., Stoughton C., SubbaRao M., Szalay A., Szkody P., Thakar A. R., Sivarani T., Tucker D., Uomoto A., Vanden Berk D., Vidrih S., Wadadekar Y., Watters S., Wilhelm R., Wyse R. F. G., Yarger J., Zucker D. 2009, SEGUE: A Spectroscopic Survey of 240,000 Stars with g = 14-20, AJ, 137, 4377, doi: 10.1088/0004-6256/137/5/4377

Yoon J. H., Johnston K. V., Hogg D. W. 2011, Clumpy Streams from Clumpy Halos: Detecting Missing Satellites with Cold Stellar Structures, ApJ, 731, 58, doi: 10.1088/0004-637X/731/1/58

York D. G., Adelman J., Anderson Jr. J. E., Anderson S. F., Annis J., Bahcall N. A., Bakken J. A., Barkhouser R., Bastian S., Berman E., Boroski W. N., Bracker S., Briegel C., Briggs J. W., Brinkmann J., Brunner R., Burles S., Carey L., Carr M. A., Castander F. J., Chen B., Colestock P. L., Connolly A. J., Crocker J. H., Csabai I., Czarapata P. C., Davis J. E., Doi M., Dombeck T., Eisenstein D., Ellman N., Elms B. R., Evans M. L., Fan X., Federwitz G. R., Fiscelli L., Friedman S., Frieman J. A., Fukugita M., Gillespie B., Gunn J. E., Gurbani V. K., de Haas E., Haldeman M., Harris F. H., Hayes J., Heckman T. M., Hennessy G. S., Hindsley R. B., Holm S., Holmgren D. J., Huang C.-h., Hull C., Husby D., Ichikawa S.-I., Ichikawa T., Ivezić Ž., Kent S., Kim R. S. J., Kinney E., Klaene M., Kleinman A. N., Kleinman S., Knapp G. R., Korienek J., Kron

R. G., Kunszt P. Z., Lamb D. Q., Lee B., Leger R. F., Limmongkol S., Lindenmeyer C., Long D. C., Loomis C., Loveday J., Lucinio R., Lupton R. H., MacKinnon B., Mannery E. J., Mantsch P. M., Margon B., McGehee P., McKay T. A., Meiksin A., Merelli A., Monet D. G., Munn J. A., Narayanan V. K., Nash T., Neilsen E., Neswold R., Newberg H. J., Nichol R. C., Nicinski T., Nonino M., Okada N., Okamura S., Ostriker J. P., Owen R., Pauls A. G., Peoples J., Peterson R. L., Petravick D., Pier J. R., Pope A., Pordes R., Prosapio A., Rechenmacher R., Quinn T. R., Richards G. T., Richmond M. W., Rivetta C. H., Rockosi C. M., Ruthmansdorfer K., Sandford D., Schlegel D. J., Schneider D. P., Sekiguchi M., Sergey G., Shimasaku K., Siegmund W. A., Smee S., Smith J. A., Snedden S., Stone R., Stoughton C., Strauss M. A., Stubbs C., SubbaRao M., Szalay A. S., Szapudi I., Szokoly G. P., Thakar A. R., Tremonti C., Tucker D. L., Uomoto A., Vanden Berk D., Vogeley M. S., Waddell P., Wang S.-i., Watanabe M., Weinberg D. H., Yanny B., Yasuda N., SDSS Collaboration. 2000, The Sloan Digital Sky Survey: Technical Summary, AJ, 120, 1579, doi: 10.1086/301513

Yu S., Bullock J. S., Gurvich A. B., Hafen Z., Stern J., Boylan-Kolchin M., Faucher-Giguère C.-A., Wetzel A., Hopkins P. F., Moreno J. 2022, Born this way: thin disc, thick disc, and isotropic spheroid formation in FIRE-2 Milky-Way-mass galaxy simulations, arXiv e-prints, arXiv:2210.03845, doi: 10.48550/arXiv.2210.03845

Yuan Z., Myeong G. C., Beers T. C., Evans N. W., Lee Y. S., Banerjee P., Gudin D., Hattori K., Li H., Matsuno T., Placco V. M., Smith M. C., Whitten D. D., Zhao G. 2020, Dynamical Relics of the Ancient Galactic Halo, ApJ, 891, 39, doi: 10.3847/1538-4357/ab6ef7

Zapatero Osorio M. R., Martín E. L., Béjar V. J. S., Bouy H., Deshpande R., Wainscoat R. J. 2007, Space Velocities of L- and T-Type Dwarfs, ApJ, 666, 1205, doi: 10.1086/520673

Zhang Z. H., Burgasser A. J., Gálvez-Ortiz M. C., Lodieu N., Zapatero Osorio M. R., Pinfield D. J., Allard F. 2019, Primeval very low-mass stars and brown dwarfs - VI. Population properties of metal-poor degenerate brown dwarfs, MNRAS, 486, 1260, doi: 10.1093/mnras/stz777

Zhang Z. H., Pinfield D. J., Gálvez-Ortiz M. C., Burningham B., Lodieu N., Marocco F., Burgasser A. J., Day-Jones A. C., Allard F., Jones H. R. A., Homeier D., Gomes J., Smart R. L. 2017, Primeval very low-mass stars and brown dwarfs - I. Six new L subdwarfs, classification and atmospheric properties, MNRAS, 464, 3040, doi: 10.1093/mnras/stw2438

Zhang Z. H., Galvez-Ortiz M. C., Pinfield D. J., Burgasser A. J., Lodieu N., Jones H. R. A., Martín E. L., Burningham B., Homeier D., Allard F., Zapatero Osorio M. R., Smith L. C., Smart R. L., López Martí B., Marocco F., Rebolo R. 2018, Primeval very low-mass stars and brown dwarfs - IV. New L subdwarfs, Gaia astrometry, population properties, and a blue brown dwarf binary, MNRAS, 480, 5447, doi: 10.1093/mnras/sty2054

Zhao G., Zhao Y.-H., Chu Y.-Q., Jing Y.-P., Deng L.-C. 2012, LAMOST spectral survey — An overview, Research in Astronomy and Astrophysics, 12, 723, doi: 10.1088/1674-4527/12/7/002

Zoccali M., Hill V., Lecureur A., Barbuy B., Renzini A., Minniti D., Gómez A., Ortolani S. 2008, The metal content of bulge field stars from FLAMES-GIRAFFE spectra. I. Stellar parameters and iron abundances, A&A, 486, 177, doi: 10.1051/0004-6361:200809394